Non-contact Measurement Machine

for Freeform Optics

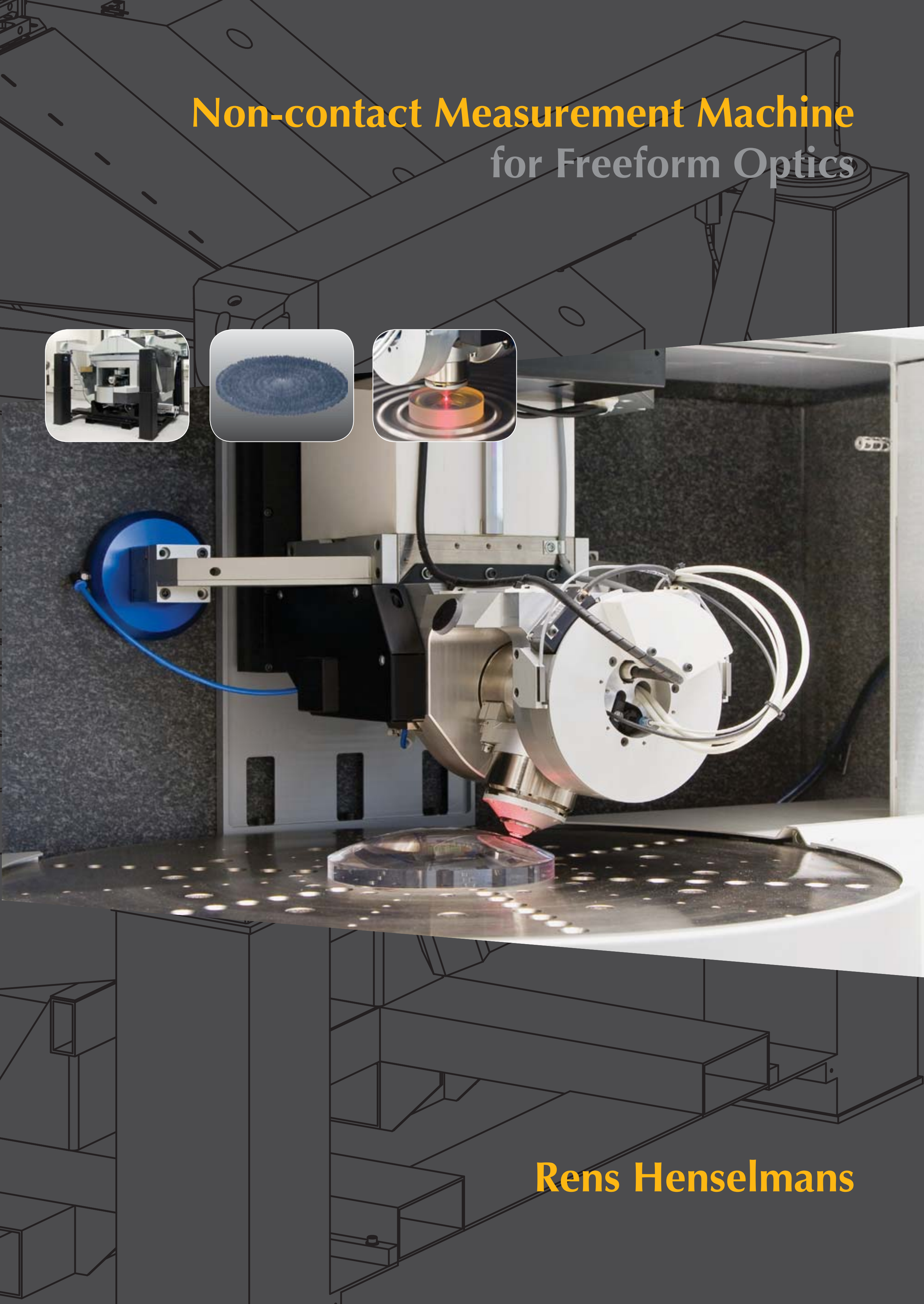

Rens Henselmans

Non-contact Measurement Machine for Freeform Optics

Non-contact Measurement Machine for Freeform Optics

PROEFONTWERP

ter verkrijging van de graad van doctor aan de
Technische Universiteit Eindhoven, op gezag van de
Rector Magnificus, prof.dr.ir. C.J. van Duijn, voor een
commissie aangewezen door het College voor
Promoties in het openbaar te verdedigen
op donderdag 2 april 2009 om 16.00 uur

door

Rens Henselmans

geboren te Gouda

De documentatie van het proefontwerp is goedgekeurd door de promotor:

prof.dr.ir. M. Steinbuch

Copromotor:
dr.ir. P.C.J.N. Rosielle

A catalogue record is available from the Eindhoven University of Technology Library

Non-contact Measurement machine for Freeform Optics / by Rens Henselmans – Eindhoven: Technische Universiteit Eindhoven, 2009, Proefschrift

ISBN: 978-90-386-1607-0

Printed by Ponsen & Looijen b.v., Wageningen, the Netherlands

Cover design by R. Verhoeven, photos by L. Ploeg

This research is funded by TNO Science & Industry, Technische Universiteit Eindhoven, NMi Van Swinden Laboratory, and the IOP Precision Technology program of the Dutch Ministry of Economic Affairs.

Summary

The performance of high-precision optical systems using spherical optics is limited by aberrations. By applying aspherical and freeform optics, the geometrical aberrations can be reduced or eliminated while at the same time also reducing the required number of components, the size and the weight of the system. New manufacturing techniques enable creation of high-precision freeform surfaces. Suitable metrology (high accuracy, universal, non-contact, large measurement volume and short measurement time) is key in the manufacturing and application of these surfaces, but not yet available. In this thesis, the design, realization and testing of a new metrology instrument is described. This measurement machine is capable of universal, non-contact and fast measurement of freeform optics up to ∅500 mm, with an uncertainty of 30 nm (2σ).

A cylindrical scanning setup with an optical distance probe has been designed. This concept is non-contact, universal and fast. With a probe with 5 mm range, circular tracks on freeform surfaces can be measured rapidly with minimal dynamics. By applying a metrology frame relative to which the position of the probe and the product are measured, most stage errors are eliminated from the metrology loop. Because the probe is oriented perpendicular to the aspherical best-fit of the surface, the sensitivity to tangential errors is reduced. This allows for the metrology system to be 2D. The machine design can be split into three parts: the motion system, the metrology system and: the non-contact probe.

The motion system positions the probe relative to the product in 4 degrees of freedom. The product is mounted on an air bearing spindle (θ), and the probe is positioned over it in radial (r), vertical (z) and inclination (ψ) direction by the R-stage, Z-stage and Ψ-axis, respectively. The motion system provides a sub-micrometer repeatable plane of motion to the probe. The Z-stage is hereto aligned to a vertical plane of the granite base using three air bearings, to obtain a parallel bearing stage configuration. To minimize distortions and hysteresis, the stages have separate position and preload frames. Direct drive motors and high resolution optical scales and encoders are used for positioning. Mechanical brakes are applied while measuring a track, to minimize power dissipation and to exclude encoder, amplifier and EMC noise. The motors, brakes and weight compensation are aligned to the centres of gravity of the R and Z-stage. Stabilizing controllers have been designed based on frequency response measurements.

The metrology system measures the position of the probe relative to the product in the six critical directions in the plane of motion of the probe (the measurement plane). By focussing a vertical and horizontal interferometer onto the Ψ-axis rotor, the displacement of the probe is measured relative to the reference mirrors on the upper

metrology frame. Due to the reduced sensitivity in tangential direction at the probe tip, the Abbe criterion is still satisfied. Silicon Carbide is the material of choice for the upper metrology frame, due to its excellent thermal and mechanical properties. Mechanical and thermal analysis of this frame shows nanometer-level stabilities under the expected thermal loads. Simulations of the multi-probe method show capabilities of in process separation of the spindle reference edge profile and the spindle error motion with sub-nanometer uncertainty.

The non-contact probe measures the distance between the Ψ-axis rotor and the surface under test. A dual stage design is applied, which has 5 mm range, nanometer resolution and 5° unidirectional acceptance angle. This enables the R and Z-stage and Ψ-axis to be stationary during the measurement of a circular track on a freeform surface. The design consists of a compact integration of the differential confocal method with an interferometer. The focussing objective is positioned by a flexure guidance with a voice coil actuator. A motion controller finds the surface and keeps the objective focused onto it with some tens of nanometers servo error.

The electronics and software are designed to safely operate the 5 axes of the machine and to acquire the signals of all measurement channels. The electronics cabinet contains a real-time processor with many in and outputs, control units for all 5 axes, a safety control unit, a probe laser unit and an interferometry interface. The software consists of three main elements: the trajectory planning, the machine control and the data processing. Emphasis has been on the machine control, in order to safely validate the machine performance and perform basic data-processing.

The performance of the machine assembly has been tested by stability, single track and full surface measurements. The measurements focus on repeatability, since this is a key condition before achieving low measurement uncertainty by calibration. The measurements are performed on a ∅100 mm optical flat, which was calibrated by NMi VSL to be flat within 7 nm rms. At standstill, the noise level of the metrology loop is 0.9 nm rms over 0.1 s. When measuring a single track at 1 rev/s, 10 revolutions overlap within 10 nm PV. The repeatability of three measurements of the flat, tilted by 13 μm, is 2 nm rms. The flatness measured by the uncalibrated machine matches the NMi data well. Ten measurements of the flat tilted by 1.6 mm repeat to 3.4 nm rms.

A new non-contact measurement machine prototype for freeform optics has been developed. The characteristics desired for a high-end, single piece, freeform optics production environment (high accuracy, universal, non-contact, large measurement volume and short measurement time) have been incorporated into one instrument. The validation measurement results exceed the expectations, especially since they are basically raw data. Future calibrations and development of control and data-processing software will certainly further improve these results.

Samenvatting

De prestaties van high-end optische systemen met sferische optiek worden begrensd door aberraties. Door toepassing van asferische en freeform optiek kunnen geometrische aberraties worden verminderd of geëlimineerd, terwijl het aantal componenten, de afmetingen en de massa van het systeem sterk kunnen worden gereduceerd. Nieuwe bewerkingstechnieken zijn in staat om hoognauwkeurige oppervlakken te fabriceren. Geschikte metrologie (hoge nauwkeurigheid, universeel, contactloos, groot meetvolume en korte meettijd), is essentieel bij de fabricage en toepassing van deze oppervlakken, maar nog niet beschikbaar. In dit proefschrift wordt het ontwerp, de realisatie en het testen van een nieuw metrologie instrument beschreven. Deze meetmachine is geschikt voor het universeel, contactloos en snel meten van freeform optiek tot ∅500 mm, met een meetonzekerheid van 30 nm (2σ).

Een cilindrische scannende opstelling met een optische afstandsprobe is contactloos, universeel en snel. Met een probe met 5 mm bereik kunnen cirkelvormige sporen op freeform oppervlakken gemeten worden met minimale dynamica. Door toepassing van een metrologieframe ten opzichte waarvan de positie van de probe en het product worden gemeten, worden de meeste sledeafwijkingen geëlimineerd uit de metrologie lus. Omdat de probe loodrecht op de asferische best-fit van het oppervlak wordt georiënteerd, wordt de gevoeligheid voor tangentiële positioneerfouten gereduceerd. Hierdoor kan het metrologie systeem 2D zijn. Het machine ontwerp bestaat uit een motion systeem, een metrologie systeem en een contactloze taster.

Het motion systeem positioneert de probe ten opzichte van het product in vier vrijheidsgraden. Het product wordt op een luchtgelagerde spil geplaatst (θ), en de probe wordt erboven gepositioneerd in radiale (r), verticale (z) en hellingsrichting (ψ) door respectievelijk de R-slede, de Z-slede en de Ψ-as. Het motion systeem biedt de probe een sub-µm vlak van beweging. De Z-slede is hiertoe direct tegen een verticaal vlak van de basis gelagerd met 3 luchtlagers, wat in een parallelle sledeconfiguratie resulteert. Om vervormingen en hysteresis te minimaliseren hebben de sledes gescheiden positie- en voorspanframes. Direct drive motoren en hoge resolutie optische linialen en encoders worden toegepast voor de positionering. Mechanische remmen fixeren de sledes tijdens het meten van een cirkelvormig spoor, om warmteontwikkeling te minimaliseren en ruis van encoders, versterkers en elektromagnetische storing uit te sluiten. De motoren, remmen en gewichtscompensatie liggen in lijn met de zwaartepunten van de sledes. Op basis van frequentie respons metingen zijn stabiliserende regelaars ontworpen.

Het metrologie system meet de positie van de probe ten opzichte van het product in de 6 kritische richtingen in het vlak van beweging van de probe (het meetvlak). Door een horizontale en verticale interferometer te focusseren op de Ψ-as rotor, wordt de

verplaatsing van de probe ten opzichte van referentiespiegels op het bovenste metrologieframe gemeten. Door de verminderde gevoeligheid voor tangentiële positioneerfouten bij de probe tip, wordt nog steeds voldaan aan het Abbe criterium. SiliciumCarbide is gekozen voor het metrologieframe, vanwege de uitstekende thermische en mechanische eigenschappen. Thermische en mechanische analyse van dit frame voorspellen nanometer stabiliteit voor de verwachtte thermische verstoringen. Simulaties van de multi-probe methode laten zien dat het mogelijk is om de rondheid van de referentierand en de spil afwijkingen in-process te scheiden met sub-nanometer meetonzekerheid.

De contactloze taster meet de afstand tussen de Ψ-as rotor en het te meten oppervlak. Een tweetraps ontwerp is toegepast met 5 mm bereik, nanometer resolutie en 5° hoekbereik. Dit zorgt ervoor dat de R en Z-slede en de Ψ-as op de rem kunnen tijdens het meten van een cirkelvormig spoor op een freeform oppervlak. Het ontwerp bestaat uit een compacte integratie van de differentiële confocaal methode met een interferometer. Het objectief wordt gepositioneerd door een elastische rechtgeleiding met een duikspoel actuator. Een regelaar zoekt het oppervlak en houdt het objectief erop gefocusseerd met enkele tientallen nanometers volgfout.

De elektronica en software is ontworpen voor veilige besturing van de 5 assen van de machine en data acquisitie van alle meetkanalen. Het elektronicakabinet bevat een real-time processor met vele in- en uitgangen, besturingen voor de 5 assen, een veiligheidsbesturing, een probe laser kast en een interface voor de interferometers. De software bestaat uit drie hoofdelementen: de trajectplanner, de machine besturing en de dataverwerking. De nadruk ligt op de machine besturing, zodat de machine validatie veilig uitgevoerd kan worden en basis dataverwerking kan worden gedaan.

De machine is getest middels stabiliteits-, enkelspoors- en volledige oppervlak metingen. De nadruk ligt op reproduceerbaarheid omdat dit een voorwaarde is voor het bereiken van lage meetonzekerheid middels kalibratie. De metingen zijn gedaan op een door NMi VSL gekalibreerd ∅100 mm vlak proefglas dat een vlakheidsafwijking heeft van 7 nm rms. Bij stilstand is het ruisniveau van de meetlus 0.9 nm rms over 0.1 s. Bij het meten van een enkel cirkelvormig spoor bij 1 omw/s zijn 10 omwentelingen binnen 10 nm PV gelijk. De reproduceerbaarheid van drie metingen met het proefglas 13 µm scheef is 2 nm rms. De door de ongekalibreerde machine gemeten vlakheid komt overeen met de metingen van het NMi. Tien metingen met het proefglas 1.6 mm scheef reproduceren op 3.4 nm rms.

Een prototype van een contactloze meetmachine voor freeform optiek is ontwikkeld. De gewenste eigenschappen van een meetinstrument (hoge nauwkeurigheid, universeel, contactloos, groot meetvolume en korte meettijd), zijn verenigd in één instrument. De validatiemetingen overtreffen de verwachtingen, te meer omdat dit nagenoeg onbewerkte data betreft. Toekomstige kalibraties en ontwikkelingen van besturing en software zullen deze resultaten daarom zeker nog verder verbeteren.

Nomenclature

Symbol	*Description*	*Unit*
A	Amplitude	[m]
A, A_S, A_p	Area, Surface area, Porous plug surface area	[m^2]
A	Jones matrix	-
B	Beam width	[m]
B	Magnetic flux density	[T]
D	Diameter	[m]
D_0, D_{ph}, D_z	Beam waist diameter, Pinhole diameter, e^{-2} diameter	[m]
E	Young's modulus	[N/m^2]
$\vec{E}_x, \vec{E}_y$	Electric field vector	[-]
E_c	Contact modulus	[N/m^2]
F	Force	[N]
F_c, F_g, F_a	Spring force, gravity force, acceleration force	[N]
$F_{1,2}$	View factor	[-]
G	Shear modulus	[N/m^2]
G_c	Contact shear modulus	[N/m^2]
H	Beam height	[m]
H	Partial water vapour pressure	[Pa]
$\vec{H}$	Complex transfer coefficient column	[-]
I	Current	[A]
I	Irradiance	[W/m^2]
I	Planar moment of inertia against bending	[m^4]
J, $J_{i,j}$	Moment of inertia (of part *i* in direction *j*)	[kgm^2]
L	Length	[m]
L_P	Probe length	[m]
M	Moment	[Nm]
$\dot{M}$	Mass flow	[kg/s]
P	Pressure	[Pa]
P_S, P_A, P_R	Bearing pressure (supply, atmospheric, restriction)	[Pa]
P	Line load	[N/m]
P	Power	[W]
P_{ax}, P_{rad}	Profile (axial and radial)	[m]
Q	Normalized volume flow rate	[l/min]
R	Radius	[m]
R	Radial position	[m]
R	Flow resistance	[Pa.s/m^3]
R	Gas constant	[J/(kmol·K)]
R	Rotation matrix	[-]

Ra	Raleigh number	[-]
R_a	Roughness	[m]
R_c	Radius of curvature	[m]
R_c	Contact radius	[m]
S_{ax}, S_{rad}	Sum signal (axial, radial)	[m]
T	Temperature	[K] or [°C]
T	Tangential force	[N]
V	Volume	[m^3]
Z	Height, Vertical position	[m]

$a,b,c,\alpha,\beta,\gamma$	Local probe coordinate system	[m]
a,b,c,d,e,f,g	Sum factors	[-]
a	Major contact radius	[m]
b	Minor contact radius	[m]
b	Half contact width	[m]
b	Beam wall thickness	[m]
b	Gap width	[m]
c, $c_{i,j}$	Stiffness (of part i in direction j)	[N/m]
c_p	Specific heat	[J/kg/K]
e	Relative radial bearing eccentricity	[-]
$\vec{e}_{ax}, \vec{e}_{rad}$	Phase vector	[-]
f, f_e	Frequency, eigenfrequency	[Hz]
f	Focal length	[m]
g	Gravitational acceleration	[m/s^2]
g	Geometry factor	[m^{-3}]
h	Hinge thickness	[m]
h	Bearing gap height	[m]
h	Convection coefficient	[W/m^2/K]
h_{ax}, h_{rad}	Complex transfer coefficient	[-]
j	Complex number	[-]
k, $k_{i,j}$	Rotation stiffness (of part i in direction j)	[Nm/rad]
k	Thermal conductivity	[W/m/K]
k, k_{limit}	Harmonic number, harmonic limit	[upr]
k_F	Motor force constant	[N/A]
k_m	Motor constant	[N/√W]
k_p	Permeability	[m^2]
k_T	Motor torque constant	[Nm/A]
l	Length	[m]
m	Mass	[kg]
m_i	Measurement signal of probe i	[m]
n	Refractive index	[-]
n	Number of coil windings	[-]
$\vec{n}$	Normal vector	[-]

$\vec{n}$	Noise level column	[m]
q	Heat transfer rate	[W]
q''	Heat flux	[W/m^2]
r	Radius	[m]
$r,y,z,\varphi,\psi,\theta$	Modified Cartesian coordinate system as used in this thesis	[m]
s	Bearing porous plug thickness	[m]
t	Time	[s]
t	Thickness	[m]
t	Hinge width	[m]
$\vec{t}$	Tangential vector	[-]
u	Position from focus along optical axis	[m]
w	Relative beam displacement (walk-off)	[m]
w	Width	[m]
z	Distance from focus along optical axis	[m]
z_r	Rayleigh range	[m]
z_g	Floor vibration amplitude	[m]
x,y,z	Cartesian coordinate system	[m]

Greek	***Description***	***Unit***
Δ_n, Δ_t, Δ_s,	Resulting error (normal, tangential, slope)	[m]
Φ	Contact tangential displacement correction factor	[-]
α	Thermal expansion coefficient	[m/m/K]
α,β,γ	Rotations in a,b,c coordinate system	[rad]
δ	Deflection	[m]
$\delta_{i,j}$	Position error of part i in direction j	[m]
δ_n, δ_t	Position error at probe tip (normal, tangential)	[m]
δ	Vibration amplitude at probe	[m]
ε	Emissivity	[-]
ε	Wavefront alignment difference	[rad]
ζ	Rotation in polar coordinate system	[rad]
η	Dynamic viscosity	[Pa.s]
η	Local surface slope	[°]
θ	Divergence	[rad]
θ_i	Angular position of probe i	[°]
κ	Wavefront curvature difference	[m]
λ	Wavelength	[m]
μ	Friction coefficient	[-]
ν	Poisson’s ration	[-]

ρ	Density	[kg/m^3]
ρ_c	Resistivity	[Ωm]
σ	Stress	[N/m^2]
σ	Boltzmann constant	[W/m^2/K^4]
σ	Standard deviation (= rms)	[m] or [rad]
σ_{Hz}	Hertzian contact stress	[N/m^2]
τ	Shear stress	[N/m^2]
ϕ, ϕ_t, ϕ_κ	Optical phase error from wavefront tilt or curvature	[rad]
φ, ψ, θ	Rotations in r,y,z coordinate system	[rad]
ω	Angular frequency	[rad/s]

Subscript	***Description***
CG	Centre of gravity
P	Probe
R	R-stage
S	Spindle
SUT	Surface under test
Z	Z-stage
Ψ	Ψ-axis
a,b,c	In direction of local coordinate system
ax	Axial
dl	Dimensionless
e	Erroneous component
enc	Encircled
eq	Equivalent
f	Frame
g	Floor
i	Index
i,j	Property of part i in direction j
$isol$	Isolator
max	Maximum
mov	Moving
$norm$	Normalized
ph	Pinhole
rad	Radial
s	Shield
$stat$	Stationary
t	True component
$t\text{-}b$	Top – Bottom

tilt	Tip – tilt (no axial rotation)
tot	Total
0	Nominal
∞	Bulk

Abbreviation	***Description***
ADC	Analog to Digital Converter
C	Controller
CC	Corner Cube (retro reflector)
CL	Cylinder lens
DAC	Digital to Analog Converter
DOF	Degree of freedom
FES	Focus Error Signal
FJP	Fluid Jet Polishing
FL	Force Linearization
FM	Fold mirror
FTP	Fractional Transferred Power
IF	Interferometer
I/O	Digital input / output
MZC	Minimum Zone Circle
NA	Numerical Aperture
NPBS	Non-polarizing beamsplitter
P	Plant
PBS	Polarizing beamsplitter
PD	Photo Diode
PH	Pinhole
PSD	Position Sensitive Detector
PTH	Pressure, Temperature, Humidity
PU	Pickup
PV	Peak-to-valley
QWP	Quarter wave plate
SH	Sample & Hold
SPDT	Single Point Diamond Turning
SSiC	Sintered Silicon Carbide
SUT	Surface under test
TG	Traject Generator
TIR	Total Indicator Reading
rms	Root-mean-square
upr	Undulations per revolution

Table of contents

Chapter 1

Introduction

The performance of high-precision optical systems using spherical optics is limited by aberrations. By applying aspherical and freeform optics, the geometrical aberrations can be reduced or eliminated while at the same time also reducing the required number of components, the size and the weight of the system. New manufacturing techniques enable creation of high-precision freeform surfaces. Suitable metrology is key in the manufacturing and application of these surfaces, but not yet available. Objective of the NANOMEFOS project is to realize a new metrology method to complete the freeform surface manufacturing value chain.

1.1 Aspherical and freeform optics

High-precision optical systems can for instance be found in space, science and lithography applications. Well known examples are various earth and space observation satellites, lithography projection systems, astronomical telescopes and optical microscopes. Consumer products increasingly also incorporate precision optical systems, such as digital cameras, multi-media projectors and car head-up displays. Miniature optics are found in optical storage and camera phones.

The requirements for these systems are ever increasing towards better, lighter, cheaper, smaller and also larger. Most optical systems employ flat and spherical optics due to the relative ease of manufacturing and measuring. Their performance is, however, limited by aberrations. Applying aspherical and freeform surfaces allows for elimination of these aberrations, combined with many other advantages. Their application requires new techniques for optical designing, manufacturing and measuring. This thesis describes the development of a new metrology method for aspherical and freeform optical surfaces.

1.1.1 Advantages of aspherical and freeform optics

Geometrical optical aberrations are inherent to the use of spherical optics. Figure 1.1 (top) schematically shows spherical aberration of a spherical lens. The outer rays are deflected more than the inner rays, giving a distorted focus. Currently, aberrations are mostly reduced by applying multiple spherical elements in series. A more elegant way to reduce aberrations is by applying aspherical and freeform optics, as illustrated by Figure 1.1 (bottom).

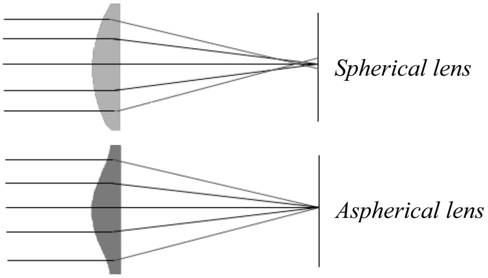

Figure 1.1: Elimination of spherical aberration with an asphere

Besides improving the optical quality of a system, application of aspheres and freeforms also allows for a reduction of the required number of components, and with that also a decrease of stray light and of system size and mass (ASPE, 2004; OptoNet 2006; OptoNet 2008). In (Winsor et al., 2004) and (Garrard et al., 2005) it is for instance reported that an order of magnitude size reduction of the ground based infrared IRMOS spectrometer is obtained by utilizing freeform surfaces. They further report reduced alignment efforts due to the fewer number of elements. Dynamic optical motion systems, such as optical storage focusing objectives, also benefit from reduced size and weight, but these optics are generally very small and are not the subject of this thesis.

Freeform optics allow for more design flexibility. Since there are relatively few degrees of freedom in a spherical system (such as the radii of curvature, thickness and diameter, the distance between the elements and the materials used), the boundary conditions for the mechanical design are usually dictated by the optical layout. This is especially the case in for instance satellite instruments, where a maximum functionality is required in a minimum of design volume, combined with harsh launching and environmental conditions. By applying aspherical and freeform optics, the optical layout becomes more flexible, enabling it for instance to depart from rotational symmetry. This allows for a more optimal opto-mechatronic design. In retrofitting it is the other way around; the mechanics dictate the optical design space.

An example is the SCUBA-2 instrument (Atad-Ettedgui et al., 2006), where the optical requirements in combination with the available design volume led to a freeform optical design.

The increased number of degrees of freedom in the surface shape however also has an almost infinite number of solutions with minimal aberrations. The challenge here is now no longer in minimizing the aberrations of the nominal system, but in optimizing the alignment and manufacturing tolerances (Garrard et al., 2005), to truly benefit from the extra design freedom.

Another field where freeform optics have advantages is in illumination optics (Ries and Muschaweck, 2002), such as car headlight reflectors. Here, freeform optics allow for far more effective tuning of the spatial illumination distribution than with aspherical optics.

1.1.2 Applications and trend

The evolution of aspherical optics is described in (Heynacher, 1979). The concept of using aspherical optics was first suggested by Kepler in 1611, and given a theoretical foundation by Descartes in 1638. This has mainly remained theoretical practice until the arrival of computer-controlled manufacturing techniques. The development of CNC machining processes has enabled generation of aspheres with sufficient accuracy for early applications, especially in large volume production and dies for moulded optics. The advantages are now widely recognized, but due to the fabrication and metrology issues, optical designers are still reluctant to apply aspheres and freeforms (Garrard et al., 2005).

Aspheres

Moderate precision aspheres are currently becoming widely adopted in mass production consumer applications, such as (semi-)professional camera objectives. Figure 1.2 (left) for example shows an objective where the application of an asphere led to half the size and weight and increased image quality (Schuhmann, 2007).

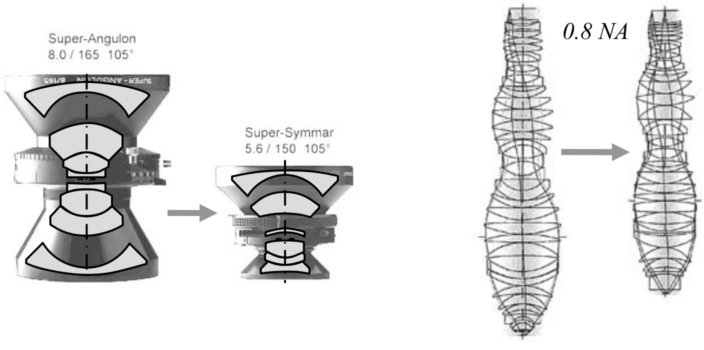

Figure 1.2: Improvement with aspheres of a camera objective (Schuhmann, 2007) and DUV projection system (Ulrich et al., 2003)

High-precision aspheres are mainly being applied in single-piece and small series diffraction limited applications, such as science and lithography instruments. Figure 1.2 (right) for example shows the size and number of elements reduction that was achieved by using aspheres for a DUV lithography projection system (Ulrich et al., 2003). In the next generation Extreme UV lithography systems aspherical off-axis mirrors are applied for which accuracies of better than 1 nm are required (Dörband and Seitz, 2001). Large high-precision aspheres are increasingly applied in astronomical telescope designs, such as the Hubble space telescope (Allen et al., 1990) and the European Extremely Large Telescope (Gilmozzi and Spiromilio, 2007).

Freeforms

The ophtalmics industry already commonly applies freeform optics in the form of multi-focal and cylinder corrected spectacle glasses. The required accuracy in this case is in the micrometer range, since the human eye is able to compensate the remaining error. Together with illumination optics, these are probably the most common example of freeform optics, but they are not subject in this thesis since the challenge in producing these optics is more in cost and speed, rather than in form accuracy.

Figure 1.3: Freeform optics in the Polaroid SX-70

One of the earliest applications of imaging freeform optics is the Polaroid SX-70 folding Single Lens Reflex camera (Figure 1.3), introduced in 1972 (Plummer, 1982). Here, the foldable design and the off-axis viewing optical system required two freeform lenses to provide a well corrected system. A more recent example where the mechanics dictated the optical layout is the SCUBA-2 instrument (Atad-Ettedgui et al., 2006; Saunders et al., 2005). For this infrared instrument the required accuracy was 3-15 μm. In the visible spectrum, moderate precision freeform surfaces are starting to be applied in for instance head-up and helmet mounted displays (Zänkert, 2008), where size and weight are critical. Applications of high-precision (diffraction limited) freeform optics for visible spectrum imaging systems are still rare.

Trend

As observed by (Beckstette, 2008), the trend for freeform optics is repeating the history of aspherical optics. The first applications are now found in low accuracy high volume (moulded) optics in reflectors and spectacle glasses, and high-end specialties such as spectrometers and off-axis telescopes. The same drivers that stimulated the development of aspheres (size, mass, number of components etc.) now continue to do the same freeforms. The development of new technical capabilities in design, manufacturing and metrology will lead to more high precision single piece and small series applications. With aspheres, the paradigm has recently changed from *"Only use aspheres if you have no other way"* to *"Keep in mind aspheres can help! Learn how to use them"*. According to (Beckstette, 2008), comparison of conventional and freeform design examples shows that freeforms are *"The winner under all aspects"*. Freeform optics are therefore expected to eventually become a commodity just as aspheres.

Further supporting the observed trend is the increasing number of scientific conferences and publications dedicated to all aspects of aspherical and freeform optics, by among others ASPE (ASPE, 2004), OptoNet (OptoNet, 2006; OptoNet 2008), Euspen (Euspen, 2009), and various SPIE conferences. Large companies such as Carl Zeiss (Beckstette, 2008), EADS Astrium (Holota, 2008), Berliner Glass (Schuhmann, 2007), ASML (ASML, 2004) also increasingly recognize the potential of aspherical and freeform optics. The Freeform Fabrication & Metrology program of TNO (Saunders et al., 2005) is also an example of this development.

Metrology

Application of high-precision aspherical and freeform optics requires new technologies to be developed in all fields of opto-mechanical system development: in the area of optical design, fabrication, metrology, alignment and assembly. Manufacturing technologies are available now (see section 1.1.4), but metrology is currently believed to be a lacking key enabling technology. Many fabricators at the conferences mentioned before, find that there is no suitable metrology method for aspherical and freeform surfaces, especially for surfaces with large departures from spherical. Citing the recent (NIST, 2008): *"Measuring aspheric surfaces poses formidable metrology problems because of the difficulty of obtaining a reference wavefront that closely matches the desired form of the asphere. No single, widely recognized, general, validated way exists for calibrating or measuring complex surfaces with nm-level uncertainties"*.

Suitable metrology will enable generation of the optics to the required accuracy, which in turn will encourage optical designers to incorporate them into new designs. This will generate expertise and trust, and lowers manufacturing cost, towards the more common application of aspheres and freeforms.

1.1.3 Surface properties and definitions

Many types of optical surfaces exist, with many different describing terminologies. In (ISO, 2006), standards for spherical optics are described extensively, but aspherical optics are only briefly addressed. No unified terminology is yet defined for freeforms. This section defines the surface properties and terminology as used in this thesis.

Surface types

In Figure 1.4 the different surface shape types are defined. The departure from spherical is exaggerated for explanatory purposes. The term asphere is used by some for all non-spherical optics, leading to confusion on rotational symmetry. In this thesis aspherical surfaces are therefore defined as rotationally symmetric but non-spherical. Examples are parabolic, elliptical and higher order rotationally symmetric surfaces.

A freeform surface is non-rotationally symmetric and can thus be virtually any shape. Generally, they can be approximated by smooth waves superimposed on an aspherical best-fit. Surface form is usually expressed in *x,y,z* coordinates, a polynomial description or Zernike coefficients. Flats, spheres and aspheres can be considered limit cases of a freeform surface; the ability to measure freeforms also enables measurement of rotationally symmetric surfaces.

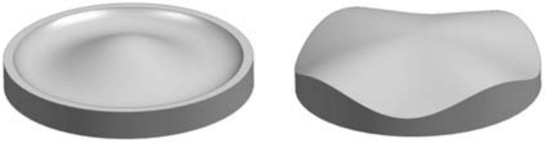

Asphere *Freeform*

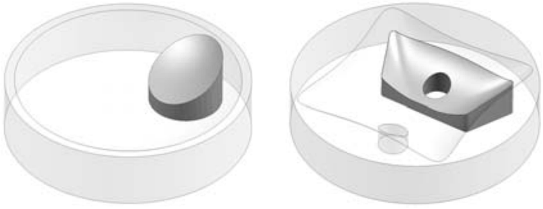

Off-axis *Off-axis freeform*

Figure 1.4: Aspherical, freeform and off-axis surface examples (departure from spherical exaggerated for explanatory purposes)

An off-axis surface is a part of a larger surface that fits one of the previous surface types. An off-axis surface can be considered to be rotationally symmetric or freeform, depending on the chosen position of the axis of rotation.

The circumference of any of the surface types can be non-circular, such as square or elliptical. There can be holes in the surface, for instance for light to pass into or out of the system. For illustration purposes, an extreme example of an off-axis freeform with an off-axis hole is shown in Figure 1.4, together with the original on-axis surface it was a part of.

Dimensions

Optics manufacturing machines are available roughly up to ∅200 mm, up to ∅500 mm (www14, 15, 16 and 22) and custom machines for diameters as large as 8.4 meters (Martin et al., 2003).

Departure from spherical

Currently, a departure from the best-fit-sphere of several tens of micrometers results in an unresolvable amount of fringes on a Phase-Shifting Interferometer (section 1.1.5 and Appendix B) and is therefore currently considered large. It is suspected that the lack of a metrology method is restricting the departure currently applied by optical designers, so larger departures are expected in future applications. The aspherical departure is chosen to be virtually unlimited, and the Peak-to-Valley freeform departure is chosen to be limited to 5 mm. These large departures may especially occur with infrared optics and off-axis optics that are measured on-axis.
It is expected that approximately 80% of the surfaces will have less than a few millimeters aspherical, and less than a few tenths of a millimeter freeform departure. For illustrational purposes: (Chang et al., 1997) surveyed thousands of lens designs and patents, showing that about 85% has an aspherical departure of the best-fit-sphere of less than 3000 waves, or about 1.8 mm in the visible spectrum (λ =600 nm).

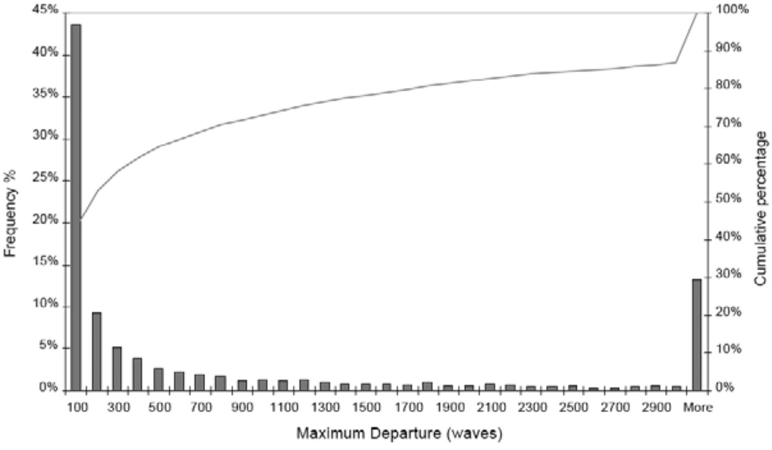

Figure 1.5: Aspherical departure from best-fit-sphere (Chang et al., 1997)

Global and local surface slope

Surfaces can be convex as well as concave. The global slope can range up to 90° for a hemispherical or cylindrical surface, but generally amounts up to 30°. The waves superimposed on the aspherical best-fit, cause local slope variations on top of the global slope. Depending on the typical wavelength and amplitude, unidirectional local slope variations up to 5° are expected.

This typically means that that a sine with 20 mm wavelength can have 0.55 mm PV, and that at the outer edge of a ∅500 mm part almost 9 waves with 5 mm PV are allowed. Most optics, however, will have less local slope, in the order of a few tenths of a degree.

Local radius of curvature

Optical surfaces as meant in this thesis are generally very smoothly curved. Besides the holes there are no discontinuities such as steps present. The global radius of curvature (R_c) is usually limited to several tens of millimeters for small lenses, as is the local radius of curvature for high order surface form components.

Materials and reflectivity

Transmission optics can be made from a large variety of glass and other transparent ceramics. Reflectivity of the uncoated optics is generally around 4% for visible light. Reflective optics can either be a metal-coated glass or ceramic substrate, or a mirror machined directly onto a metallic substrate. Reflectivity then ranges from 60 to (theoretically) 100%. Form measurements on surfaces during production are performed on surfaces without a (multi-layer) anti-reflection or protective coating.

Form, waviness and roughness

According to (Whitehouse, 1994), surface topography can be split in the spatial frequency domain into form, waviness and roughness. Form refers to the macroscopic shape, and for optics covers spatial wavelengths down to about 1 mm. Waviness, caused by for instance tool marks and instabilities in the machining process is in the range of approximately 1 mm down to 20 µm. Roughness is covered by the spatial frequency range below 20 µm.

Expressing the surface topography in a PSD spectrum is increasingly applied to characterize the surface (Duparré et al., 2002; Youngworth et al., 2005). For high-end freeform surfaces, the content of the form range is in the order of millimeters, while the content of the waviness and roughness range decreases from micrometers to nanometers during production. Especially waviness (mid-spatials) is undesirable in an optical surface.

The required form accuracy for moderate precision optics is around λ/4, where λ/20 is required for high precision diffraction limited optics. For visible light this correlates to 150 nm and 30 nm, respectively. DUV and EUV optics require an even higher accuracy (λ/100). These are beyond the scope of this thesis.

Scratch / dig

A commonly used method to specify surface defects is by a scratch/dig number (MIL-PRF-13830B). This number quantifies the allowable amount of scratches and digs in a surface, and has a more aesthetic meaning rather than functional. Scratches typically have a width in the order of tens of micrometers, and pits have a typical diameter in the order of tenths of millimeters. The scratch/dig number is usually determined visually.

1.1.4 Current manufacturing methods

Classical polishing methods used for spherical surfaces (see also Appendix A), are not applicable to general aspheres and freeforms (Karow, 1993). New computer-controlled local polishing methods enable the generation of precision complex surfaces. Examples are the Zeeko Precessions process (Walker et al., 2001), the QED MRF process (Dumas et al., 2004), and ion- and plasma beam machining (Frost et al., 2003). These processes have a deterministic influence function, allowing for rapid iteration in corrective polishing to the desired form.

For non-ferro metals and some ceramics, single point diamond turning (SPDT) is applied for generating aspheres. Non-rotationally symmetric surfaces can be made by SPDT with a slow- or fast-tool-servo or by precision grinding (Wanders, 2006). Diamond turning or precision grinding is also applied to manufacture moulds for glass pressing or hot embossing techniques, with which large series of complex optics can be manufactured cost effectively (Allen et al., 2006).

1.1.5 Current metrology methods

In every fabrication process the achievable precision is only as good as the measurement method. For a high-end, single piece, freeform optics production environment, important characteristics of a measurement method are:

- high accuracy
- universal
- non-contact
- large measurement volume
- short measurement time

Many techniques, experimental as well as commercial, exist for measuring optics. A recent overview of measuring general freeform surfaces, ranging from car body parts to turbine blades to optics, is given by (Savio et al., 2007). In Appendix B the existing methods are assessed with respect to the above characteristics and the properties defined in section 1.1.3. A brief summary is given here.

The metrology methods can be separated in imaging and scanning techniques. The main imaging technique is Phase-Shifting Interferometry and the main scanning techniques are stylus profilers and coordinate measuring machines. Some experimental methods are also discussed.

Interferometry

Phase-Shifting Interferometry (Figure 1.6) currently is the work horse for measuring flat and spherical optics. An extensive overview of many interferometry based techniques is given in (Malacara, 2007). The entire surface is imaged at once, measuring it in seconds. With a calibrated reference surface and proper measurement conditions, uncertainty can be of (sub)nanometer order (Dörband and Seitz, 2001). Apertures are generally around 100 mm, but some larger setups exist.

Figure 1.6: Phase-Shifting Interferometer (www26)

If the departure from spherical of the surface under test exceeds several micrometers, the fringes become too dense to resolve, limiting the applicability for aspheres and freeforms. Applying null optics or computer generated holograms (Burge and Wyant, 2004), resolves this issue but at the cost of traceability and universality. Stitching sub-apertures is sometimes done (Dumas et al., 2004), but large departures require many sub-apertures which gives the risk of stitching errors.

Stylus profilometers

Scanning methods generally provide a more universal measurement compared to imaging techniques. A stylus profilometer (Figure 1.7) performs a 2D line scan with a diamond or ruby tipped stylus (Whitehouse, 1994). This is currently the most commonly applied method for measuring aspheres. For measuring freeforms, a transverse stage is added. In 2D mode, the uncertainty can be in the order of several tens of nanometers.

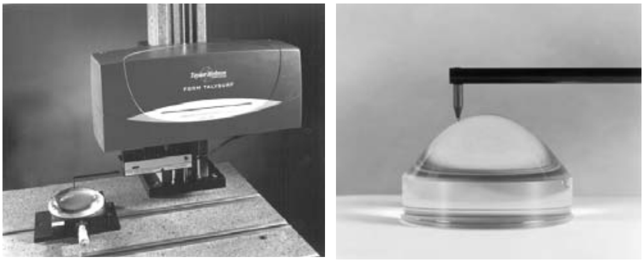

Figure 1.7: Stylus profilometer (www20)

The measurement length is limited to about 200 mm, and the allowed sag is in the order of 20 mm (www20). The contact stylus requires slow scanning speeds (~10 mm/s) and has the risk of damaging the surface. Transverse inclined surfaces further give rise to torsional deflection errors in the stylus arm and bending of the stylus itself.

Coordinate Measuring Machines

Truly universal 3D measurements are done with Coordinate Measuring Machines (CMM). Conventional portal CMMs are limited by Abbe errors (Abbe, 1890). Intermediate bodies can be introduced in the guidance setup to keep the linear scales aligned to the probe tip and thus eliminate the Abbe offset in the horizontal plane (Vermeulen, M., 1999; Van Seggelen, 2007).

In (Ruijl, 2001; Jäger et al., 2001) laser interferometers are used that are orthogonally aligned to a stationary probe tip, and are measuring to a moving mirror block on which the product is mounted. In (Becker and Heynacher, 1987) fixed reference mirrors are applied and the laser interferometers emanate from the moving probe.

The measurement volume of these CMMs is generally less than 1 dm^3, except (Becker and Heynacher, 1987), and uncertainties in the order of several tens of nanometers are reported. Contact trigger probes (Weckenmann et al., 2006) are employed. The orthogonal setup makes application of an optical non-contact probe difficult for surfaces with slopes of more than a few degrees.

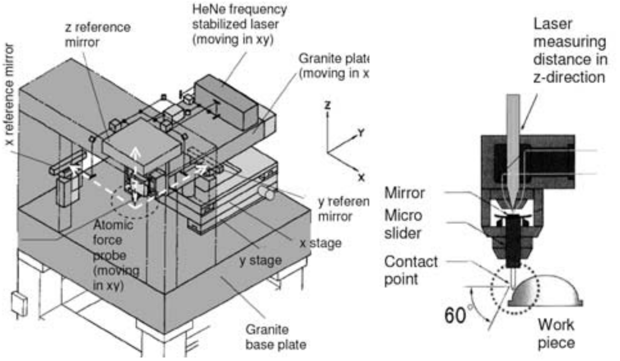

Figure 1.8: CMM with AFM probe (Takeuchi et al., 2004)

In (Takeuchi et al., 2004) an Atomic Force Probe is used (Figure 1.8), in combination with interferometers and stationary reference mirrors. Although the surface is not contacted, scanning speeds are still limited to mm/s, leading to measurement times of many hours for large surfaces. Due to the orthogonal setup, measurement uncertainty rapidly increases with surface inclination (Figure 1.8, right).

Experimental methods

Swing-arm profilometry (Anderson and Burge, 1995; Callender et al., 2006) is able to scan a spherical surface using only two axes of rotation whilst also keeping the probe perpendicular to the best-fit-sphere. Slope measurement (Qian et al., 1995; Van der Beek et al., 2002), slope difference measurement (Geckeler and Weingärtner, 2002) and curvature scanning (Schulz and Weingärtner, 2002; Machkour et al., 2006) determine surface form from integrating surface slope and local curvature, respectively. The latter two properties can be measured independently from an outside reference. Fringe projection calculates the local surface slope and integrates that to height data from a fringe pattern that is deformed after reflecting on a surface under test (Knauer et al., 2004). Advantages and disadvantages of these methods are further discussed in Appendix B and throughout the conceptual design in Chapter 2.

Conclusion

No single method yet incorporates the previously mentioned five characteristics desired for measuring single piece high precision freeform surfaces as described in section 1.1.3. This lack of a suitable metrology method is currently holding back the common application of high-precision aspherical and freeform optics.

1.2 The NANOMEFOS project

1.2.1 Objective

The objective of the NANOMEFOS[1] project is to realize a new measurement machine prototype for measuring high-end single piece freeform surfaces as defined in section 1.1.3. Hereto, the design goals for this method are formulated as follows.

1. Universal measurement of:
    a) Flat, spherical, aspherical, freeform and off-axis surfaces
    b) Convex and concave surfaces
    c) Transmission and reflection optics
2. Product dimensions up to ∅500 x 100 mm
3. Measurement uncertainty 30 nm (2σ)
4. Non-contact
5. Measure form
6. Fast (~15 min.)

---

[1] *NANOMEFOS is an acronym for Nanometer Accuracy NOn-contact MEasurement of Freeform Optical Surfaces. This project was a continuation of the research done in the authors' M.Sc. graduation (Henselmans, 2003). It is a collaboration of TNO Science & Industry, Technische Universiteit Eindhoven and the Netherlands Metrology institute Van Swinden Laboratory. Subsidy was provided by the SenterNovem IOP Precision Technology program of the Dutch Ministry of Economic Affairs. The machine has been realized at the TU/e GTD workshop.*

Recapitulating from section 1.1.3, the aspherical departure from spherical is not limited, and the PV freeform departure is 5 mm. The global slope ranges from -45° to +90°, and the unidirectional local slope may amount up to 5°. The reflectivity may range from 4% to 100% and surfaces are not (multi-layer) coated. The chosen product dimensions match the capabilities of the TNO facilities (Appendix A). The measurement uncertainty corresponds with diffraction limited performance for the visible spectrum (λ/20). Measuring form requires a point spacing in the order of 1 mm. Aim is to measure a ∅500 mm surface within 15 minutes. The instrument will be placed in a conditioned metrology laboratory, with an expected temperature stability of 20±0.2°C.

A few further objectives are optional. During production, the roughness decreases from opaque to optical quality. Measuring rough surfaces, probably with less accuracy, would therefore be a useful option. Measuring small areas with µm point spacing would provide valuable information on roughness and waviness. This would result in a single measurement method that can be applied throughout the entire production process, from roughly ground to finely polished, and from µm to m spatial frequency range.

Ideally, the method would be applicable as an on-machine method. This has been considered, but the boundary conditions of existing manufacturing machines are not quite optimal for metrology (e.g. stage constructions, abrasive slurries, temperature and humidity).

1.2.2 Methods

The focus in this thesis is on the combination of the previously mentioned five properties into one instrument. The measurement volume of ∅500 x 100 mm, combined with an uncertainty of 30 nm, requires a dynamic range that is one to two orders of magnitude larger compared to state-of-the-art 3D CMMs. The non-contact and fast measurement requires a long range optical probe, which does not yet exist. The application of an optical probe in combination with the large surface slopes requires a departure from the orthogonal setup for the metrology as well as the structural loop design.

Numerous papers on precision instrument design principles have been published over the years, of which an overview is published in (Schellekens et al., 1998). Summarizing, the following principles are applied in the design of the new instrument.

Design for repeatability

As in many precision instruments, emphasis is on design for repeatability in combination with calibration. To achieve the desired measurement uncertainty, the surface measurement repeatability should be in the order of a few nanometers rms.

In this case, repeatability is not as important in positioning as it is in measuring. Since the intended method is non-contact, a position error is not a problem as long as the actual position is measured correctly. This in contrast to for instance a diamond turning machine, where a position error of the tool is immediately copied into the work piece surface.

By applying statically determined design, hysteresis and backlash are minimized. Distortions resulting from varying loads on the structural loop should also be minimized, since these may give rise to hysteresis and other possible measurement errors. This is done by applying separate preload, position and metrology frames.

Minimize metrology loop error sensitivity

According to the Abbe principle (Abbe, 1890), the measurement systems are to be aligned with the point of interest to avoid sensitivity to angular displacements. Measurement is further to be done as directly to the point of interest as possible, to obtain a short metrology loop and thus exclude possible error sources from the measurement. Thermal sensitivity of the metrology loop is first of all reduced by minimizing internal and external heat sources. Second, materials with low thermal sensitivity, high thermal diffusivity or low thermal expansion are applied to minimize deformation due to thermal influences.

Minimize system dynamics effects

Applying the minimal number of moving axes generally improves machine accuracy. Light and stiff structural loop design minimizes the required actuation force, increases bandwidth and allows for higher speed and shorter measurement time. By aligning the actuators with the centre of gravity of the stages, parasitic angular displacements are minimized.

Traceability

The required uncertainty level can only be obtained by repeatability in combination with calibration. Calibration can be done by either measuring a reference artefact (which is difficult to obtain to the required accuracy in this case), or by characterizing all error sources of the metrology loop, either individually or in groups. Care must thus be taken that the complete metrology loop can be calibrated. By taking the necessary calibration procedures into account early in the design phase, traceability is assured.

1.3 Thesis outline

The conceptual design is explained in Chapter 2. Here the cylindrical machine concept is explained after some conceptual considerations and evaluations of existing principles. Next the error budget is determined and a machine design overview is given. The air bearing motion system, with the vertical stage directly aligned to a vertical base plane, is explained in Chapter 3. The overall concept is explained first, after which the design, realization and testing of each motion axis is shown. The chapter is concluded with test results of the assembled motion system. In Chapter 4 the metrology system is explained, starting with the metrology concept, followed by the design, analysis and realization of the interferometry system. Next, the design, realization and testing of the Silicon Carbide metrology frame and multi-probe spindle error measurement are explained. This chapter ends with test results of the metrology system and motion system assembly. Chapter 5 explains the optical probe design. The differential confocal measurement method is explained first, followed by the optical design with the integration of an interferometer and PSD. Next, the opto-mechanical design is shown, followed by the realization and stand-alone test results.

Chapter 6 explains the functionality of the machine control electronics and software. The safety precautions implemented are also addressed. The test results of the machine prototype are shown in Chapter 7, from stability measurements to full surface measurements. Calibration is addressed, and the chapter closes with an achievable uncertainty estimation. Final conclusions and recommendations will be drawn in Chapter 8.

Chapter 2

Conceptual design

A cylindrical scanning setup with an optical distance probe is non-contact, universal and fast. With a probe with 5 mm range, circular tracks on freeform surfaces can be measured rapidly with minimized system dynamics. By applying a metrology frame relative to which the position of the probe and the product are measured, most stage errors are eliminated from the metrology loop. Because the probe is oriented perpendicular to the aspherical best-fit of the surface, the sensitivity to tangential errors is reduced. This allows for the metrology system to be 2D. The machine design consists of the motion system, the metrology system and the non-contact probe.

2.1 Conceptual considerations

Based on the review of existing measurement methods, some fundamental choices can be made with regard to the characteristics of the measurement method.

Method

Although imaging techniques such as phase-shifting interferometry provide accurate, non-contact and very fast measurement, they are not universal and are difficult to scale to the required dimensions. Single point scanning methods are slower and the moving of components generally requires more effort to obtain high accuracy, but they are in principle capable of universal measurement in a large volume. With a suitable probe, fast non-contact measurement is possible.

Probe type

Several principles can be used for probing the surface, as summarized in (Schwenke et al., 2002; Weckenmann et al., 2006). Optical probes are truly non-contact and especially single point sensors allow for scanning speeds in the order of meters per second. Care must be taken when applying an optical technique, since measurement relies on reflection of the surface under test, which generally is sensitive to imperfections such as dust and scratches.

Semi-contact scanning probe microscopy principles, such as Atomic Force Probes, can be used to measure the distance to a surface by keeping the stylus at constant distance or using it tapping mode. Since the tip is extremely fragile, scanning speeds are much smaller than one millimeter per second, which is similar to contact probes.

Capacitive probes are capable of high-accuracy, but can only be applied to metallic surfaces and are thus not suitable for transmission optics. The same goes for other non-contact sensors such as Eddy-current sensors. Ultrasonic sensors have not been found to provide the required resolution.

Only optical probes are truly non-contact, have sufficient accuracy and allow for high scanning speeds. Hence, they are the probe type of choice. The global surface slope can amount up to 45° or even 90°. This requires the optical probe to be oriented perpendicular to the surface by the scanning system to recollect the beam that is reflected by the surface.

Measurand

When scanning a surface point by point, the position, slope, slope difference, curvature or a combination thereof can be measured at each point (Figure 2.1). Slope, slope difference and curvature have to be integrated once and twice, respectively, to obtain the surface form. Optically, the slope is the functional parameter since this changes the propagation direction of light by refraction or reflection. In manufacturing practice, however, the surface form is specified. Form is also required to determine the amount of material that is to be removed during the iterative corrective machining process.

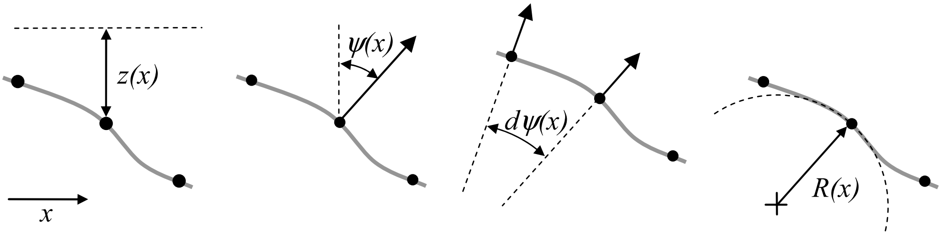

Figure 2.1: Measurement of position, slope, slope difference and curvature

Measuring position (i.e. surface coordinates) gives similar measurement versatility as current CMMs. It allows for true universal measurement, also for discontinuous parts, reference markers and quick alignment checks. Further, each individual measurement point can be directly traced back to a point on the surface, which is not the case when measuring other measurands.
Optically measuring distance is relatively difficult. It generally requires a spot to be focused onto the surface. To obtain high axial resolution, a high NA and thus a small spot (micrometer order) is necessary. This makes it very sensitive to local defects. Furthermore, measuring position requires the position of the sensor relative to the product to be known at similar accuracy level, which yields high requirements for the scanning system.

Slope can optically be measured relatively easily and accurately, for instance with a deflectometer (miniature autocollimator). In (Szwedowicz, 2006) remarkable results have been obtained in wafer measurement, also because of a multi-path integration algorithm that suppresses random measurement errors. The spot size can range from 0.1 - 1 mm, which makes it relatively insensitive to local surface defects. With this setup nanometer height resolution has been shown for wafer measurements.
There also are some disadvantages. First of all, due to the required integration of the data, discontinuous surfaces (such as multiple optical surfaces on one part or reference markers on the product carrier) can not be measured. To reconstruct a surface, a high density data set is always required. A quick check to confirm coarse surface form or alignment for instance by measuring some specific points on the surface, is thus not possible.
Due to the slope measurement, the positioning requirements of the sensor relative to the product are somewhat relieved, but the angular position of the sensor is still critical to prevent systematic integration errors. Because the distance between the surface and the sensor is not known, the actual point of measurement in space is difficult to determine, which leads to uncertainties for the absolute dimensions and location of the part (radius of curvature, diameter etc.), especially for strongly curved parts.

Instead of measuring slope, the slope difference between two points (Geckeler and Weingärtner, 2002) or the local curvature at a point (Schulz and Weingärtner, 2002) can also be measured. These properties are intrinsic properties of a surface, which can be measured independently of the object’s orientation relative to an outside reference. This relieves the positioning requirements of the sensor relative to the product. By dual integration, the surface form can be calculated. Due to the required integration, these methods suffer from the same disadvantages as slope measurement. Further, curvature ranges from convex to concave with local radii of curvature down to some tens of millimeters. No curvature sensor yet has sufficient dynamic range to universally satisfy these demands. The curvature sensor commonly used is a miniature interferometer using a CCD, which does not allow for continuous scanning.

Traceability

The measurand of choice also depends on the traceability. Traceability can be provided by either verifying the process with a large series of reference artefacts that cover the range of products to be measured, or by characterizing the grouped or individual elements of the entire metrology loop of the instrument. Besides tilted flats and off-axis spheres, no true freeforms calibrated to the required uncertainty are yet available (Savio et al., 2007). Hence, the metrology loop will have to be characterized. When measuring positions, this is relatively straightforward since each individual measurement can be directly traced to a point on the surface. Further, measuring form from position data is standard practice at the National Metrology Institutes.

When measuring slope, slope difference or curvature, the individual measurements can be calibrated using autocollimators, angle gauges or reference spheres. Correct individual measurements do not necessarily guarantee that the reconstructed form is correct due to the data integration. Proving traceability of this process is thus less straightforward since it is dependent on the entire slope data set.

Regarding the above, measuring position is believed to result in the most versatile and traceable measurement method. Therefore, a distance measuring optical probe will be scanned over the surface.

Setup

To position the probe over the surface, an orthogonal, cylindrical or polar setup can be used. Conventional coordinate measurement machines use an orthogonal setup as shown in Figure 2.2. The probe is translated in 3 directions (*x, y* and *z*). To orient the probe perpendicular to the surface, this setup can be extended with two rotations (φ and ψ). For high speed scanning all axes are thus continuously in motion resulting in large moving masses and accelerations. The 3 translations and 2 rotations further result in a fully 3D metrology loop. The required strokes are approximately 700 x 700 x 150 mm and rotations up to 180° depending on the chosen rotation axis setup.

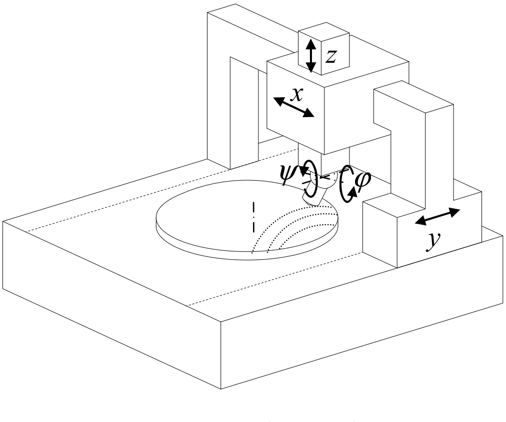

Figure 2.2: Orthogonal setup

Since the surfaces are more or less rotationally symmetric (within 5 mm PV), a cylindrical setup appears to be the obvious choice. The product can be mounted on a continuously rotating spindle *(θ)*, while the probe is positioned in radial *(r)* and vertical *(z)* direction. To align the probe to the global surface slope, one rotation *(ψ)* is required. Here, the spindle can be rotating continuously, while the probe is positioned over the surface in circular or spiral tracks. The stages move in small slow steps, so system dynamics is improved compared to the orthogonal setup. Due to the large difference between the displacement in the plane of motion and perpendicular to it, the metrology loop generally referred to as 2½D.

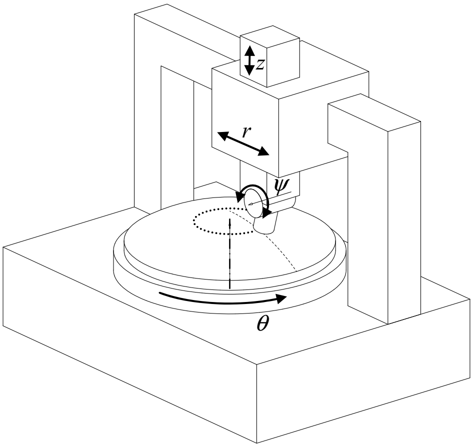

Figure 2.3: Cylindrical setup

The surfaces are not only more or less rotationally symmetric; they will also be more or less spherical. A polar or swing arm setup (Figure 2.4) might therefore also be applied (Anderson and Burge, 1995; Callender et al., 2006). When the rotation axis of the arm coincides with the centre of curvature of the surface, the entire surface can be measured with only two rotations (ζ and θ). The probe inherently stays perpendicular with the best-fit-sphere of the surface. This setup also allows for fast scanning of circular tracks.

When measuring different radii of curvature (especially with changing from convex to concave), the inclination angle of the bearing of the arm has to be adjusted. Also, for small radii, in the order of several tens of millimeters, the physical dimensions of the arm and bearing become a problem. Due to the required adjustments, this setup is thus not universal. Aligning the rotation axis and the probe to the (non-physical) centre of curvature of the surface is difficult, especially when the surface is non-spherical. This leads to uncertainty in the absolute surface dimensions and position. Further, the influence of gravity on the arm is continuously changing, and the metrology problem for this setup is fully 3D again. Provided that calibration issues are resolved, this setup is more suitable for near constant radius measurements of large series of large surfaces.

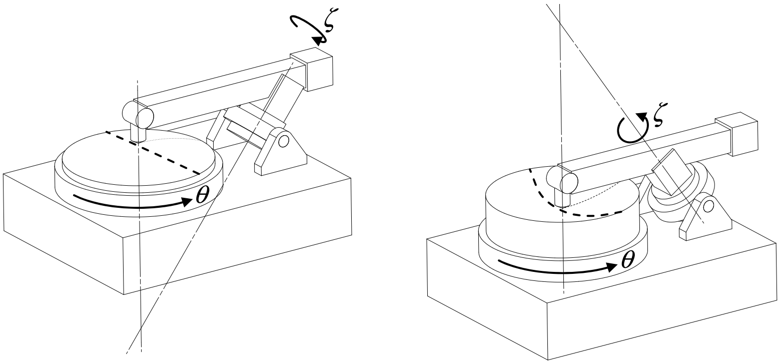

Figure 2.4: Polar setup for convex and concave surfaces

Concluding from the above, the cylindrical setup of Figure 2.3 is the obvious choice. It is truly universal, can be fast with relatively little system dynamics, uses only four axes of motion and it has a 2½ D metrology loop.

Stage layout

Some variations are possible to the cylindrical setup of Figure 2.3, similarly to the considerations of (Vermeulen, J., 1999). The spindle can be oriented vertically and horizontally. The vertical orientation is preferred due to the large product mass and diameter of 500 mm. This way the accessibility and visibility for loading, aligning and fixing of a product is most convenient. Further the spindle is loaded axially, preventing mass dependent bending forces and eccentricity of the spindle rotor.
The ψ-rotation can best be done with the probe, since it is the smallest mass and thus is least affected by the changing direction of gravity. The remaining 2 translations (r and z) can be performed with the spindle, the probe or a combination of the two. Due to the large spindle and product mass (~200 kg), moving the lightest component (i.e. the probe) will result in the best dynamic behaviour. Furthermore, this setup will lead to the shortest metrology loop as will be shown in Chapter 4. The cylindrical setup of Figure 2.3 is thus the preferred stacking sequence of the stages.

2.2 Machine concept

The chosen cylindrical concept is shown in Figure 2.5. The product is mounted on an air-bearing spindle, which is rotating continuously at for instance 1 rev/s. An optical distance probe is mounted on a rotation axis (Ψ-axis) which positions it perpendicular to the rotationally symmetric best-fit of the product. The probe can be moved in radial and vertical direction by an R and Z-stage, respectively.

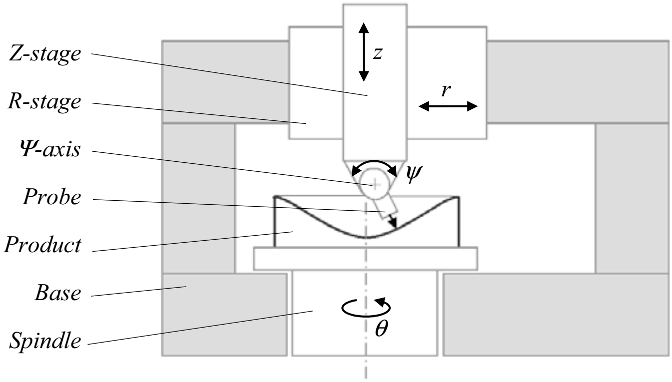

Figure 2.5: Cylindrical machine concept

The probe will be positioned on a circular track on the product and the stages will be locked. This improves the positioning stability of the stages since the electronic noise of the motors and encoders is cancelled. The track can be measured multiple times with little extra effort, to obtain redundant data, for instance for averaging. After this, the stages are moved about 1 mm further to the next track and the process is repeated. This allows for measurement times in the order of 15 minutes for large surfaces.

When a freeform surface is rotating on the spindle, the surface may vary between the continuous and dotted line in Figure 2.6 by 5 mm PV. As will be explained in Chapter 5, optical probes generally only have a focal depth of a few micrometers. Keeping the probe in focus by actuating the R and Z-stage requires large accelerations of these heavy stages, resulting in undesirable dynamics. To avoid this, a probe with 5 mm range is required. This way the stages can be held stationary even when measuring a freeform track. This reduces the dynamically moving mass from a few hundred kg for the stages to only 50 g of the probe objective. This improves system dynamics and allows for maintained high scanning speed for freeforms surfaces.

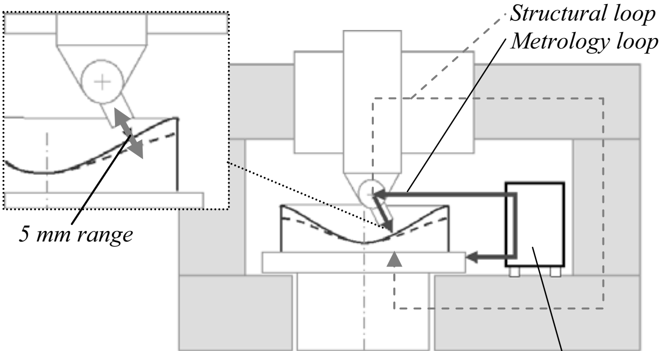

Figure 2.6: Addition of probe with 5 mm range and metrology frame

The total measurement uncertainty is composed of many factors, such as probe position, product position, probe-surface interaction, form stability of the surface under test, the data-acquisition and the data-processing software.
The largest contribution is expected to be determined by the metrology loop between the probe and the product. In Figure 2.5, this loop was equal to the structural loop and thus included the stages, bearings, base etc. By applying a metrology frame relative to which the probe and product position are measured as directly as possible, most stage errors can be eliminated from the metrology loop, as shown in Figure 2.6.

The spindle is intended to rotate at 1 rev/s. The worst case deformation of the surface under test due to the centrifugal force was estimated using FEM for a ∅500 mm flat, concave and convex surface with material properties similar to aluminium or glass. Depending on the boundary conditions (e.g. fixed backside, three-point mount, fixed centre), the deformation varied between 3 and 40 nm. Part of this deformation is of the less-sensitive type (see section 2.3.2). by modelling the effect in FEM, this deformation can be compensated for in the data-processing.

The required stroke is shown in Figure 2.7. The length of the probe is 100 mm. To be able to orient the probe at + and –45° throughout the measurement volume, the range of the R-stage has to be 400 mm (–75 to +325 mm), and range of the Z-stage has to be 125 mm. To optionally incorporate an intermediate body as a product carrier, the Z-stage range is further increased to 150 mm. It is further convenient to have a ψ-range of –45° to +120° for calibration and nulling purposes, as further explained in section 7.3.

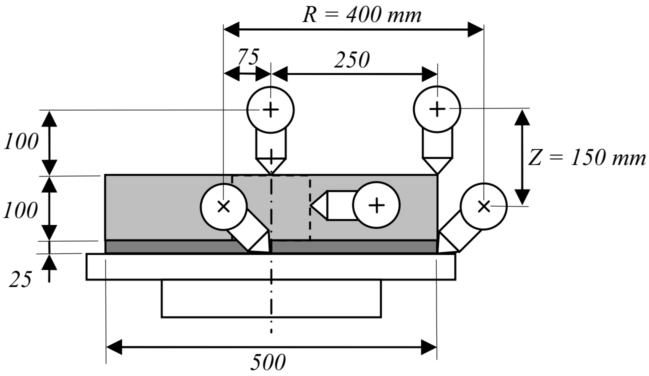

Figure 2.7: Required stroke for the stages

This concept can meet the design goals. The Ψ-axis enables application of an optical probe. By increasing the measurement range of this probe to 5 mm and combining it with a cylindrical machine setup, freeforms can be measured universally with high scanning speeds and minimal dynamics. The separate 2D metrology loop somewhat relieves the requirements on the structural loop. Due to the non-contact nature, measurement is more important than actual positioning. This may allow for achieving the desired uncertainty.

2.3 Error budget

2.3.1 Coordinate system definition

To emphasize the cylindrical nature of the machine, an *r,y,z* coordinate system has been adopted (Figure 2.8). The origin of the system is located at the spindle surface centre, the *z*-direction is coaxial with the spindle centre line and the *r*-direction ('radial') is parallel to the plane of motion of the probe. This plane is also referred to as the '*measurement plane*'. The rotations around the *r*, *y* and *z* axis are φ, ψ and θ, respectively.

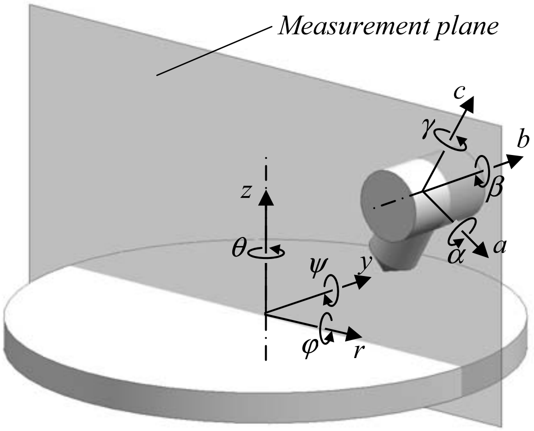

Figure 2.8: Global and local coordinate system definition.

As will become clear, it is convenient to also define a local coordinate system that rotates with the probe. In this system, the *c*-direction is aligned with the probe axial direction and the *b*-direction is parallel to the *y*-direction of the global coordinate system. Rotations around the *a*, *b* and *c* axes are called α, β and γ, respectively. The β-direction coincides with the ψ-direction. The origin is located at the Ψ-axis centre line.

2.3.2 Error sensitivity

The probe is aligned to the rotationally symmetric best-fit of the surface. When measuring a flat, sphere or asphere, the probe will always be nominally perpendicular to the surface, and the local curvature and slope equal the global curvature and slope. With freeform surfaces, the 5 mm PV departure from rotationally symmetry inherently results in a departure of local slope and curvature from global values. Since the probe will not be actively controlled perpendicular to the surface during the measurement of an individual track, the local slope variations cause a misalignment between probe and surface in α as well as β direction of up to 5° (see section 1.1.3).

The metrology loop is composed of three main elements: the distance measured by the probe, the measured position of the probe relative to the metrology frame and the measured position of the product relative to the metrology frame. To model the sensitivity of errors in these three elements, they are interpreted as displacements of the probe relative to the product. The error in the distance measured by the probe as a result of this displacement δ is the measurement error Δ..

As illustrated in Figure 2.9 A, a distance measurement error of the probe, and a position measurement error δ_n with its resulting vector in normal direction $\vec{n}$ of the surface, both result in a direct measurement error Δ_n.

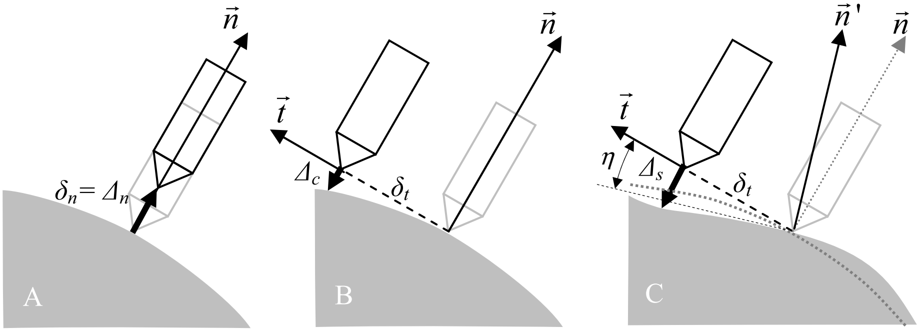

Figure 2.9: Distance measurement error Δ resulting from displacement in normal (δ_n) and tangential (δ_t) direction.

A position measurement error δ_t in tangential direction $\vec{t}$ of the surface, results in an error Δ_c that is dependent on local surface geometry. Since the surfaces are smoothly curved and have low roughness, only local curvature and tilt have to be taken into account here. When measuring rotationally symmetric surfaces (flats, spheres and aspheres), the probe is always nominally perpendicular to the surface (Figure 2.9 B). Therefore only local curvature can cause an error here. A position measurement error in tangential direction only results in a second order error Δ_c. Figure 2.10 (left) shows this error up to an R_c of 10 mm and a δ_t of 2 µm, to be only 0.2 nm. Errors due to local curvature are thus negligible.

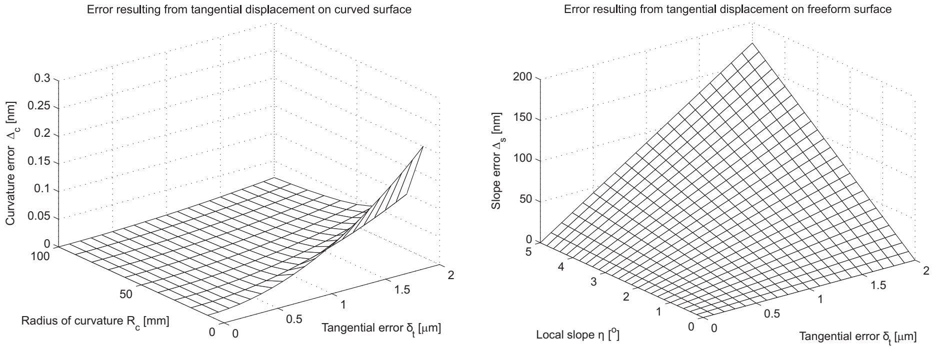
Error resulting from tangential displacement on curved surface

Error resulting from tangential displacement on freeform surface

Figure 2.10: Error as a function of curvature (left) and local slope (right)

Local surface slopes of 5° are expected (section 1.1.3), which is also the maximum misalignment between probe and surface (Figure 2.9 C). The resulting distance measurement error is linearly dependent to this local slope, as shown in Figure 2.10 (right). This error can be substantial for large local slopes and large tangential errors. A sub-micrometer out-of-plane error is therefore desirable.

One may argue that the probe therefore is to be kept perpendicular to the local surface slope to avoid these errors. This would require the probe to be rotated around its tip while measuring a track, preferably with a virtual pivot at the probe tip. This would add two new stages to the system that have to be actuated and measured. Moreover, the motion system currently is a 2D system, which allows for direct 2D metrology to the probe as will be shown in Chapter 4. Adding the virtual pivot would turn the metrology system back to fully 3D, significantly increasing the complexity and the measurement uncertainty of the system. Local surface slope is expected to be below a few tenths of a degree for most surfaces. A 2D system is therefore designed, and the higher measurement uncertainty for a minority of highly complex freeform surfaces is accepted.

When the sensitivity of 0.087 is compared to the sensitivity of 1 for errors in normal direction, over an order of magnitude reduced sensitivity to tangential errors is seen. For surfaces with less local slope, this reduction is even better. A clear distinction between normal and tangential errors can thus be concluded.

With the metrology frame as a reference, 13 degrees of freedom can be distinguished. These are the 6 DOFs of the product, plus the 6 DOFs of the probe, plus the distance measured by the probe. For each of these, the resulting error (normal and/or tangential) between probe and product can be calculated as a function of position measurement error and surface geometry. Further, the measurement position has to be taken into account. When measuring a flat surface for instance, a radial error has no influence, and tilting of the product linearly influences the measurement error as a function of the radial measurement position. The resulting measurement error will thus be measurement-task specific.

As explained in Figure 2.10, the errors resulting from tangential errors on a curved surface are negligible. For aspheres, the measurement uncertainty is therefore predominantly determined by errors in normal direction. Only six degrees of freedom cause errors in normal direction, as shown in Figure 2.11. These degrees of freedom determine the basic measurement uncertainty for aspheres and mild freeforms, and are called the '*sensitive directions*'. The other seven directions are referred to as the '*less-sensitive*' directions.

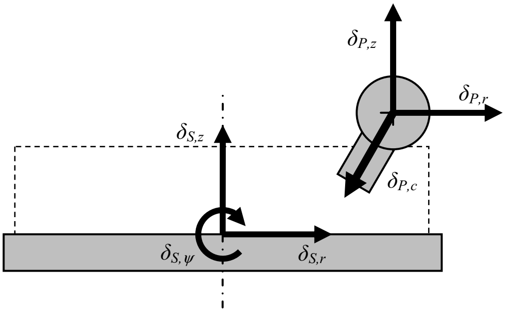

Figure 2.11: Degrees of freedom that result in a displacement between probe and surface in normal direction, i.e. the sensitive directions.

2.3.3 Error budget

When the error sources of the 13 individual degrees of freedom are assumed uncorrelated and normally distributed, the resulting uncertainty in *a*, *b* and *c* direction can be calculated with (2.1). Here, $\sigma_{i,j}$ is the rms error of part *i* in direction *j*, where the part is the spindle *(S)* or the probe *(P)*. The probe angle is ψ, *R* and *Z* are the probe tip position and L_P is the length of the probe.

$$\begin{aligned}
\sigma_a &= \sqrt{\left(\sigma_{S,r}\cos(\psi)\right)^2 + \left(\sigma_{S,z}\sin(\psi)\right)^2 + \left(\sigma_{S,\psi}R\sin(\psi)\right)^2 + \left(\sigma_{P,r}\cos(\psi)\right)^2 + \left(\sigma_{P,z}\sin(\psi)\right)^2 + \left(\sigma_{P,\psi}L_P\right)^2} \\
\sigma_b &= \sqrt{\left(\sigma_{S,y}\right)^2 + \left(\sigma_{S,\varphi}Z\right)^2 + \left(\sigma_{S,\theta}R\right)^2 + \left(\sigma_{P,y}\right)^2 + \left(\sigma_{P,\varphi}L_P\cos(\psi)\right)^2 + \left(\sigma_{P,\theta}L_P\sin(\psi)\right)^2} \\
\sigma_c &= \sqrt{\left(\sigma_{S,r}\sin(\psi)\right)^2 + \left(\sigma_{S,z}\cos(\psi)\right)^2 + \left(\sigma_{S,\psi}R\cos(\psi)\right)^2 + \left(\sigma_{P,r}\sin(\psi)\right)^2 + \left(\sigma_{P,z}\cos(\psi)\right)^2 + \left(\sigma_{P,c}\right)^2}
\end{aligned} \qquad (2.1)$$

The uncertainty in normal direction is equal to the uncertainty in *c*-direction, while the uncertainty in tangential direction is the resulting vector of the *a* and *b*-direction:

$$\begin{aligned}
\sigma_n &= \sigma_c \\
\sigma_t &= \sqrt{\sigma_a^2 + \sigma_b^2}
\end{aligned} \qquad (2.2)$$

If we assume that the normal and tangential uncertainties are uncorrelated for the sake of simplicity, this makes the total uncertainty equal to quadratic sum of the normal uncertainty plus the tangential uncertainty times the local resulting slope η:

$$\sigma_{tot} = \sqrt{\sigma_n^2 + \left(\sigma_t \eta\right)^2} \tag{2.3}$$

The error budget was iteratively divided over the individual components, with the somewhat arbitrary resulting maximum budgeted error (3σ) per DOF, relative to the metrology frame, as shown in Table 2.1. The spindle error budget is based on vendor specifications and error motion measurement literature, as further discussed in sections 3.3.5 and 4.4. The error budget for the probe position is based on design and calibration literature, as explained throughout Chapter 3 and Chapter 4. The error budget for the probe is based on a literature study as shown in Chapter 5 and Appendix I.

The six critical error directions are marked in gray; the other seven directions determine the magnitude of the less sensitive tangential error. Due to their reduced sensitivity, these can be allowed to be an order of magnitude larger than the errors in normal direction.

DOF	***Budget (3σ)***
$\delta_{S,r}$	15 nm
$\delta_{S,y}$	100 nm
$\delta_{S,z}$	15 nm
$\delta_{S,\varphi}$	2 µrad
$\delta_{S,\psi}$	0.1 µrad
$\delta_{S,\theta}$	2 µrad
$\delta_{P,r}$	30 nm
$\delta_{P,y}$	300 nm
$\delta_{P,z}$	20 nm
$\delta_{P,\varphi}$	2 µrad
$\delta_{P,\psi}$	5 µrad
$\delta_{P,\theta}$	2 µrad
$\delta_{P,c}$	25 nm

Table 2.1: Error budget

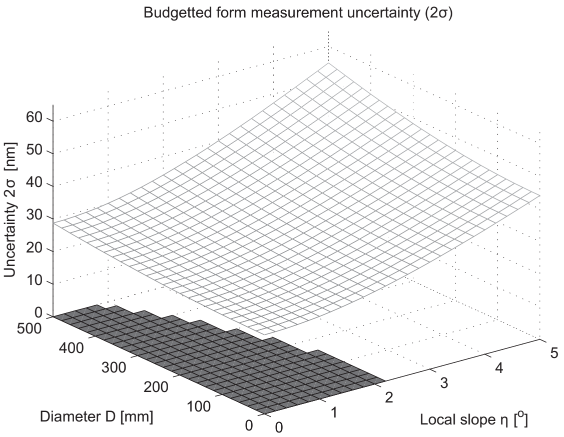

Figure 2.12: Budgeted expanded measurement uncertainty (2σ)

With the maximum error values chosen as shown in Table 2.1, the resulting form measurement uncertainty is shown in Figure 2.12. The uncertainty is task-specific, but is mainly dependent on the diameter of the part and the local slope. Figure 2.12 was calculated with $\psi = 22.5°$, $Z = 50$ mm and a probe length L_P of 100 mm. The gray area at the base plane shows the surfaces for which the 30 nm expanded uncertainty objective is met. The uncertainty increases to 55 nm for heavily freeform surfaces.

The values of Table 2.1 are the allowed maximum errors relative to the metrology frame, after calibration. The sensitive directions (in gray) are certainly challenging, and will be measured by the metrology loop. The other seven less-sensitive directions are also challenging, but are thought to be possible with the structural loop alone. The machine concept can thus be split into two parts: a 2D metrology loop that measures the position of the probe relative to the product within the measurement plane at nanometer level, and a structural loop that mechanically provides a sub-micrometer accuracy plane of motion for the probe relative to the product after calibration.

2.4 Machine design overview

2.4.1 Main design aspects

An overview of the main concepts that have been applied in the machine design is given in the following section, to aid better understanding of the detailed subsystem designs in the coming chapters.

Structural loop

The structural loop should provide a high accuracy plane of motion to the probe. To achieve this, the Z-stage is directly aligned to a vertical plane of the base using three air bearings. This provides higher out-of-plane accuracy, stiffness and stability compared to a stacked design.

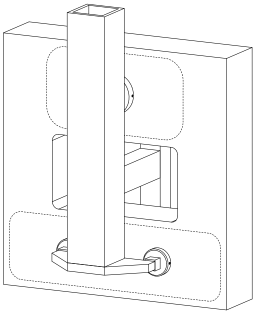

Figure 2.13: Z-stage with 3 bearings to a vertical plane

To minimize distortions and hysteresis, separate preload and position frames will be applied in both the R and Z-stage. Due to the cylindrical setup and the long range probe, the stages can be stationary while measuring a circular track. To increase the stiffness and stability of the stages in the actuated directions, mechanical brakes will be applied that clamp the stages. This prevents stage motion from encoder, amplifier and EMC noise, and may provide higher stiffness compared to the achievable servo stiffness. Only the degree of freedom in the motion direction of the stage will be clamped to prevent stage deformation.

Metrology loop

To satisfy the Abbe principle, the measurement systems should be aligned to the probe focal point. When measuring concave optics, however, the edge of the optic is blocking the horizontal line of sight between the outside reference and the probe focal point. Moreover, the vertical and horizontal position of the probe focal point changes with ψ-rotation, whilst the stages remain stationary. This would require a metrology system that tracks the probe-tip position independently of the stage position.
The setup is less-sensitive to tangential errors of the probe focal point relative to the product. As shown in the error budget calculations, this also includes the ψ-rotation of the probe. The Abbe point can therefore be shifted from the probe focal point to the Ψ-axis centre. The measurement systems can now be aligned with the Ψ-axis centre, and move along with the R and Z-stages. Due to the reduced tangential sensitivity, the Abbe principle is still satisfied.

To measure the displacement of the Ψ-axis rotor (1 in Figure 2.14) relative to the metrology frame (2), an interferometry system is applied. Hereto the Ψ-axis rotor has been made reflective such that the measurement beam (3) can be focused onto it by a lens (4). The beam layout is such that the measurement beam also reflects on a reference mirror (5), directly measuring the displacement between the Ψ-axis rotor and the reference mirror. A similar setup is employed in horizontal direction (6). Reaction forces of the probe servo system (7) on the Ψ-axis bearing, or pressure variations in the stage bearings will cause displacement of the probe. With this setup, the position errors of the whole motion system in r- and z-direction are measured at the Ψ-axis rotor, and can be compensated for in the data-processing.

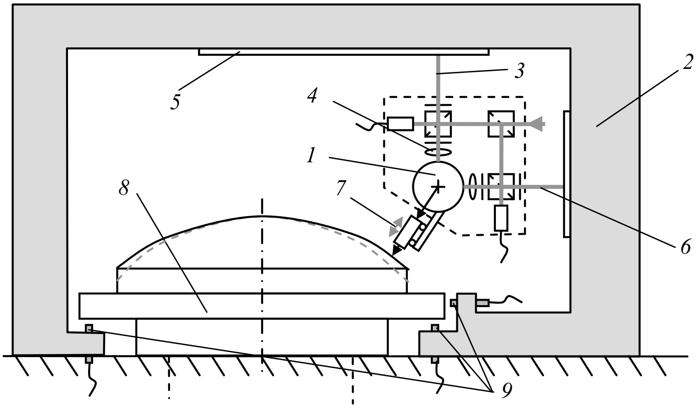

Figure 2.14: Metrology loop concept with interferometers measuring the probe displacement and capacitive probes measuring the spindle error motion

Although the acquired spindle (8) is specified to have an error motion of only 25 nm and 0.1 μrad, the position of the rotor needs to be determined to 15 nm and 0.1 μrad. To determine the position of the spindle rotor relative to the metrology frame, capacitive probes (9) are therefore added. Principally, three capacitive probes are sufficient to measure the three sensitive directions r, z and ψ. Seven probes are however applied, to separate the roundness error from the error motion with the multi-probe method.

The displacement of the probe and spindle are measured relative to the metrology frame. This frame is constructed out of Silicon Carbide. The high specific stiffness results in high eigenfrequencies, and the high thermal diffusivity combined with low expansion coefficient minimize the sensitivity to thermal gradients. Further, the material is hard enough to polish the reference mirrors directly onto the beams, avoiding separate strip mirrors of limited stiffness and stability and connection elements.

With this metrology loop concept, all six sensitive directions of Figure 2.11 are measured directly. When measuring a freeform surface, only the probe focusing mechanism is moving dynamically while measuring a circular track. The static and dynamic displacements that occur during this measurement are recorded by the metrology system and can be compensated for in the (off-line) data-processing.

Non contact probe

A two stage probe has been designed (Figure 2.15). The short stroke differential confocal principle measures the absolute distance to the surface, with a range of a few micrometers. This short stroke system is mounted on a linear guidance that is servo-controlled to keep the surface in range. The required displacement of the short stroke system is measured with the long stroke system. Incremental systems, such as an interferometer or optical encoder, can provide the required dynamic range here since this measurement no longer has to be absolute. The distance measured by the probe is the sum of the short and long stroke outputs.

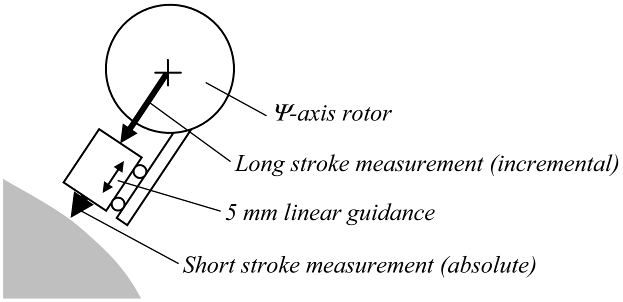

Figure 2.15: Two stage probe concept

2.4.2 Machine design overview

The final machine design is shown in Figure 2.16. It measures 2.1 m wide, 1.85 m deep and 1.8 m high. The total mass is approximately 3500 kg.

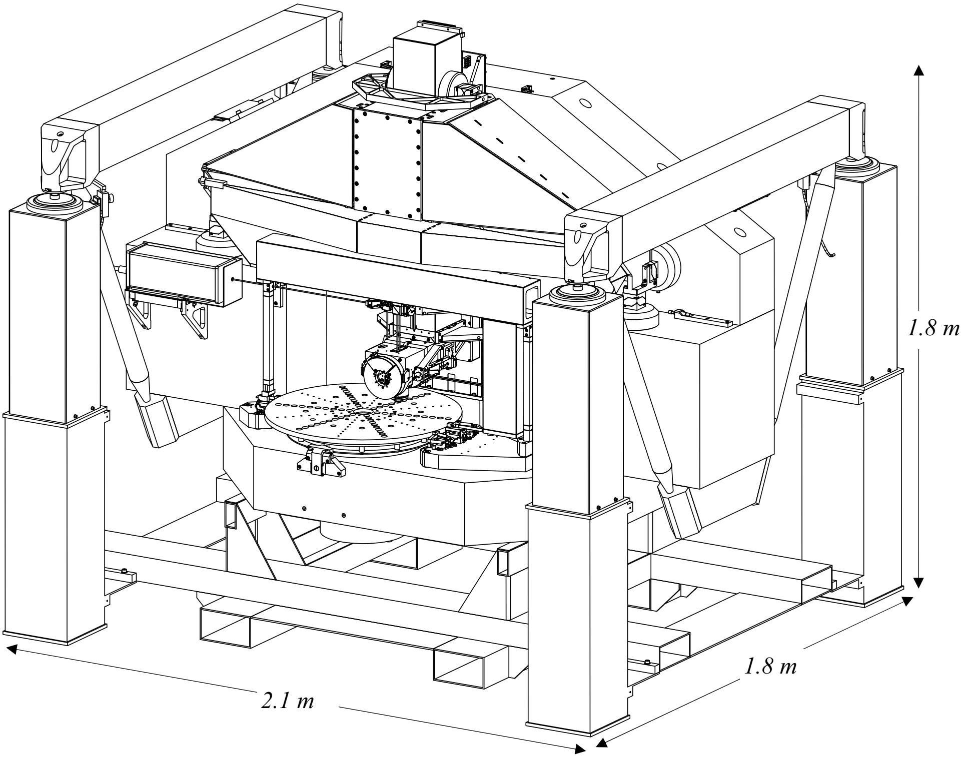

Figure 2.16: Machine design overview

The machine design consists of three main systems: the motion system, the metrology system, and the non-contact probe (Figure 2.17). These will be discussed in detail in Chapters 3 to 5. The fourth subsystem is the electronics and software, which will be discussed in Chapter 6. The complete machine assembly and validation experiments are discussed in Chapter 7.

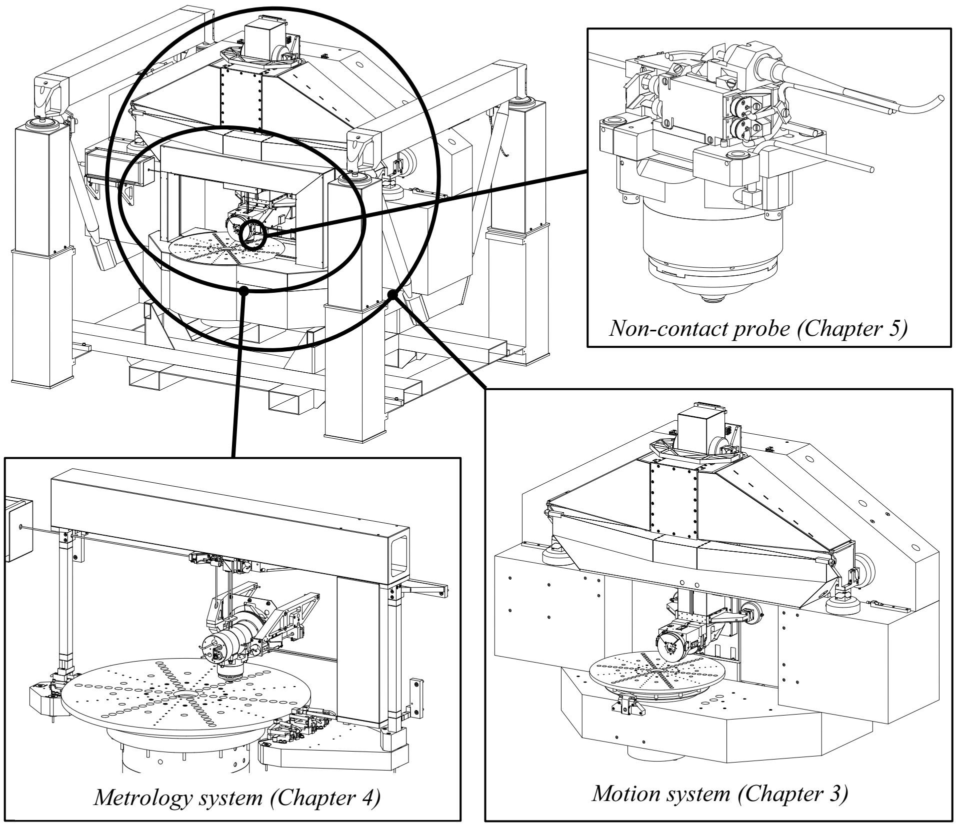

Figure 2.17: Main subsystems

Chapter 3

Motion system

The motion system positions the probe relative to the product in 4 degrees of freedom. The product is mounted on an air bearing spindle (θ), and the probe is positioned over it in radial (r), vertical (z) and inclination (ψ) direction by the R-stage, Z-stage and Ψ-axis, respectively. The motion system should provide a sub-µm repeatable plane of motion to the probe. The Z-stage is hereto aligned to a vertical plane of the granite base using three air bearings, to obtain a parallel bearing stage configuration. To minimize distortions and hysteresis, the stages have separate position and preload frames. Direct drive motors and high resolution optical scales and encoders are used for positioning. Mechanical brakes are applied while measuring a track. Measurements have been performed on the noise level, eigenfrequencies and stage tilt. Frequency responses have been measured to design robust motion controllers.

3.1 Concept

3.1.1 Requirements

The motion system positions the probe relative to the product by moving the probe in r, z and ψ-direction, and rotating the product in θ-direction. The required stroke is 400 mm, 150 mm and 165° in r, z and ψ-direction, respectively (see section 2.2). It should provide a high-accuracy plane of motion to the probe, preferably with sub-µm repeatability in the out-of-plane directions (y, φ and θ). In principle, repeatable behaviour in *r* and *z*-direction is not required due to the separate metrology system. The interferometers measure the probe position at the Ψ-axis centre, so the probe length causes an Abbe error for ψ-rotation. Besides the out-of-plane directions, the ψ-rotation of the probe should thus also be highly repeatable.

The machine will mostly be operated in circular measurement mode, during which the probe is positioned on a circular track and all stages are clamped using mechanical brakes. The stages thus move step-wise in this mode. In some cases, however, the probe may also be scanned over the surface, with or without a rotating product. This would give a spiral and radial scan respectively. A radial scan is for instance applied for drift compensation in section 7.2.3. For convex and concave surfaces, these scans require smooth and continuous motion of all stages. For this scanning mode, friction should thus be minimized for repeatability in the *r* and *z*-direction.

Since the measurement spot of the probe is only a few micrometers, high resolution scans on a small area may deliver valuable information on the surface mid-spatial frequencies. High-resolution positioning capabilities are hereto desired of the stages.

3.1.2 Basic components and principles used

Several basic components and principles are applied throughout the machine and are therefore explained first. These mainly concern the air bearings and their preloading, the actuators, the optical scales and encoders and the brakes.

Air bearings and cardanic hinges

The Z-stage is to be directly aligned to a vertical base plane, resulting in 2 DOF (*r,z*) relative motion. Air bearings are particularly suitable for this. They provide high stiffness and long range of motion. Due to the buffer effect they also have relatively high damping. The absence of Coulomb friction allows for infinite positioning resolution. The accuracy of the guiding surfaces can be (sub-)micrometer level. Gap height stability is only as good as its air supply, so care must be taken to avoid pressure variations, for instance by applying a pressure vessel. Gap height stability can be in the order of nanometers this way, with good straightness of motion and repeatability. Clean, dry air generally is available in metrology laboratories and workshops. Considering the above, air bearings are very suitable for application in this instrument.

Several air bearing types have been developed in the past, such as parallel gap, conical gap, and infinite stiffness membrane compensated bearings (Holster, 1967; Vermeulen, J., 1999; Vermeulen, M., 1999; Van Beek, 2006). Porous graphite air bearings are increasingly applied for their high load capacity, robustness to dry running and their commercial availability. Figure 3.1 (left) shows a photograph of a porous graphite air bearing.

Bearings of ∅150 mm, ∅125 mm and ∅100 mm are applied in the machine. Load capacity and stiffness were tested before installing the bearings in the machine. The load was applied by varying the pressure inside an air piston, while measuring the gap height using three LVDT gauges around the bearing (Figure 3.1, right).

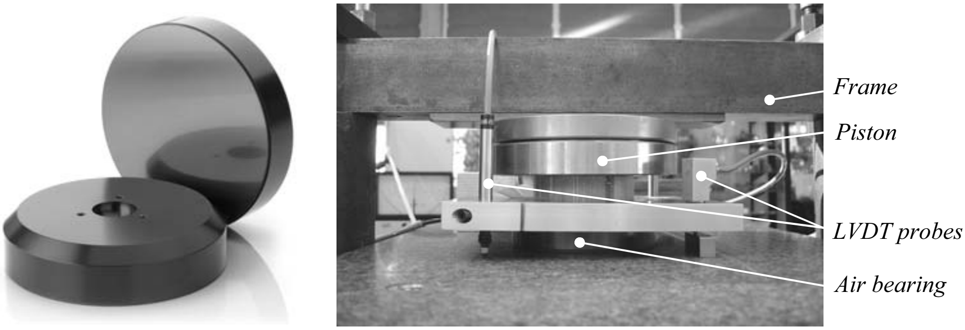

Figure 3.1: Porous graphite air bearings (www13) and bearing test setup

Figure 3.2 shows the test results as well as the load characteristic from the supplier, both at 5.5 bar supply pressure. The bearings do achieve their specified load capacity, but at a smaller air gap than specified. For robustness to dust and scratches, the bearings are chosen to operate at a minimum gap height of 10 µm. This provides a stiffness of about $2.8 \cdot 10^8$ N/m at 2000 N preload for the ∅150 mm bearings, $2 \cdot 10^8$ N/m at 1500 N preload for the ∅125 mm bearings and $1.4 \cdot 10^8$ N/m at 1000 N preload for the ∅100 mm bearings.

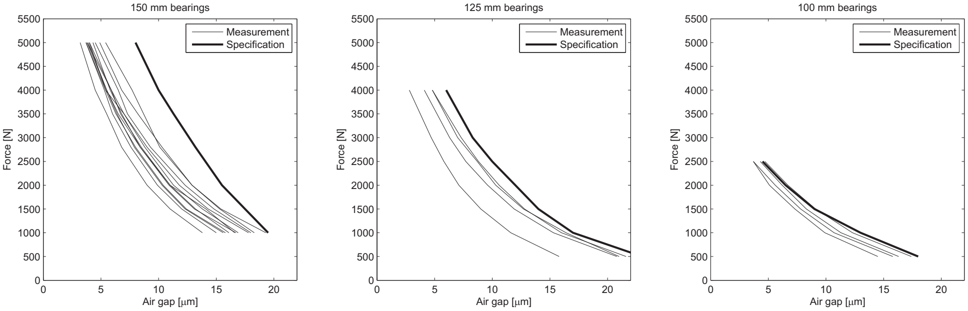

Figure 3.2: Air bearing test results at 5.5 bar

To enable the bearings to adjust themselves parallel to the guiding surfaces, elastic cardanic hinges are applied (Figure 3.3), similar to (Vermeulen, J., 1999 and Vermeulen, M., 1999). These provide 2 rotational degrees of freedom with intersecting axes of rotation, high axial stiffness and no friction and hysteresis.

Figure 3.3: Cardanic hinge for bearing self-alignment

The cardanic elements are manufactured from 34CrNiMo6 steel with a yield strength of 900 N/mm^2. The hinges have a hinge thickness h of 0.5 mm, width t of 2x30 mm and diameter D of 3 mm, giving a rotational stiffness of 114 Nm/rad (3.1) and an axial stiffness of $2.4{\cdot}10^9$ N/m (3.2). FEM calculations show an axial stiffness of $5.3{\cdot}10^8$ N/m for the middle body including the stiffening strips, giving a total axial stiffness of $3.7{\cdot}10^8$ N/m for the cardanic element.

$$c_{ax} = 0.48 \cdot \sqrt{\frac{h}{D}} \cdot E \cdot t \tag{3.1}$$

$$k_{tilt} = 0.093 \cdot \sqrt{\frac{h}{D}} \cdot E \cdot t \cdot h^2 \tag{3.2}$$

Bearing and cardanic hinge assemblies as shown in Figure 3.3 are used throughout the machine for the position determining bearings. The combined stiffness of these elements is $1.6{\cdot}10^8$ N/m for ∅150 mm, $1.3{\cdot}10^8$ N/m for ∅125 mm and $1{\cdot}10^8$ N/m for the ∅100 mm bearings. These values will be used for calculating the rigid body modes of the stages in this chapter.

Force closed preload

The preload forces are 2000 N, 1500 N and 1000 N for the ∅150 mm, ∅125 mm and ∅100 mm bearings, respectively. This force can be applied by mass, vacuum or an opposing bearing. In some cases, the attraction force of an iron core linear motor is utilized for the preload (Slocum et al., 2003). Preloading by mass may lead to pneumatic hammering (Holster, 1967; Vermeulen, M., 1999) and deteriorates dynamic behaviour. At 5.5 bar supply pressure, preloading by vacuum requires at least 5.5 times more vacuum area as bearing area, and is vulnerable to fluctuations in vacuum pressure. Preloading with an opposing bearing is therefore preferred. Force closed preloading with an air piston is applied, which is less sensitive to guidance parallelism and temperature fluctuations compared to form closed preloading. This therefore has better repeatability.

Figure 3.4 shows a preload piston as applied for all preload bearings in the machine. It consists of a cup and a disc, separated by an O-ring. The diameter has been chosen such that the desired preload force is obtained at 5.5 bar, such that all bearings and pistons operate on the same supply pressure.

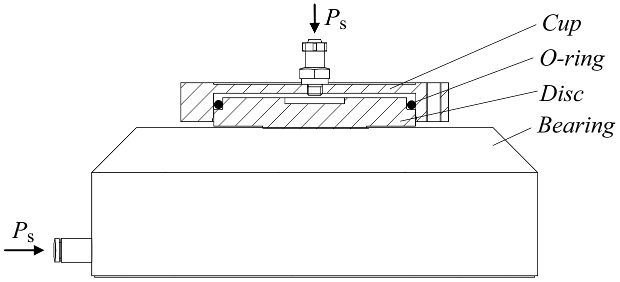

Figure 3.4: Air bearing with preload piston

The opposing bearing can generally be applied in three configurations, as shown in Figure 3.5. A strip-on-edge C-yoke can be applied around the guiding surface (Figure 3.5A). Each bearing thus has an individual yoke, and the preload bearings become individual mass-spring systems attached to the main stage structure. Especially when motion in two directions is intended, the yoke must leave space for this, requiring a relatively long horizontal part (1).

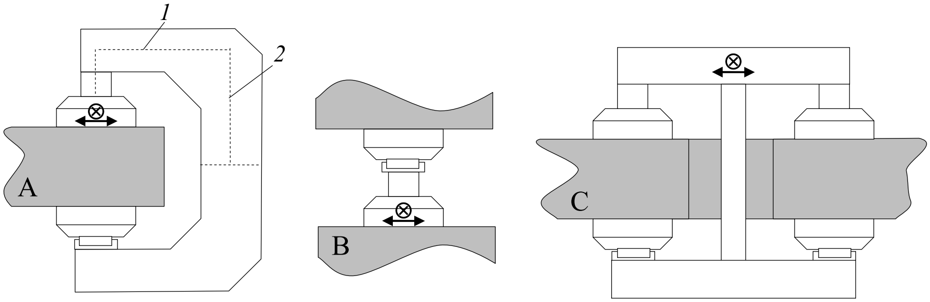

Figure 3.5: Opposing preload bearing configurations

The total deflection δ for a C-yoke consists of deflection of the horizontal part (δ_1) and the rotation φ_2 at the end of the vertical part times the length of the horizontal part (l_1), and can be approximated by (3.3). This means that when $I_1 \approx I_2$ and $l_1 \approx l_2$, 75% of the deflection is caused by bending of the vertical part.

$$\delta = \delta_1 + \varphi_2 l_1 = \frac{F l_1^3}{3EI_1} + \frac{M l_2}{EI_2} l_1 = \frac{F l_1^2}{E}\left(\frac{l_1}{3I_1} + \frac{l_2}{I_2}\right) \quad (with \quad M = F l_1) \qquad (3.3)$$

Applying two bearings between two guiding surfaces (Figure 3.5B), does not require the yoke, but the base structure is now loaded with bending and tension instead of compression.
By pairing 2 or 3 bearings, pure tension is obtained in the centre pull rod and symmetrical bending in the connecting beams (Figure 3.5C), similar to (Van Seggelen, 2007). The deflection is now a function of the 3rd power of the length of the horizontal beam. More height is generally available here to create more bending stiffness. Since the bearings are spaced some distance apart to obtain tilting stiffness, the space in between can be used for the pull rod. This avoids large c-yokes extending from the machine to enable 2D motion. For 2D motion, this paired setup is therefore preferred.

Separate position and preload frames

The large preload forces required for high-stiffness air bearings also give rise to large stresses and deformation in the stage structure. To minimize hysteresis due to varying preload forces, for instance when turning the supply pressure on and off, the function of position and preload frame can be separated. Figure 3.6 shows this for the paired bearing setup. The c-yoke configuration of Figure 3.5A is also a separate preload frame.

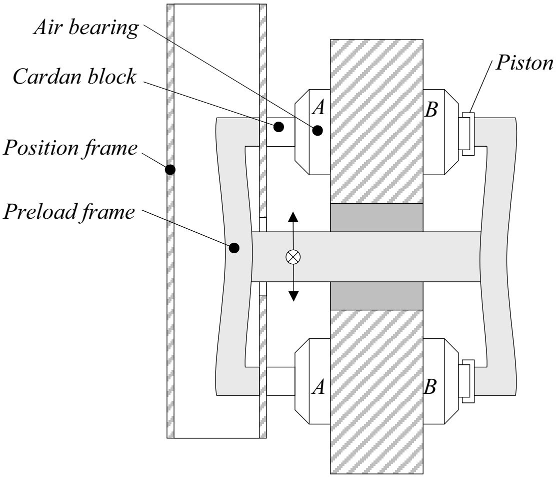

Figure 3.6: Separate position and preload frames

These frames take the preload force, to minimize stress in the position frames. Hysteresis will thus occur in the preload frame, but with the critical components attached to the position frame this will hardly affect the measurement uncertainty.

Principally, the preload frame only has to take the force required to preload the position determining bearings (A) and can thus be designed for strength rather than stiffness. The preload frame and preload bearings (B) are, however, also part of the dynamic behaviour of the stage, and resonances in this frame do influence the position accuracy of the critical components on the position frame. The preload frame thus has to achieve similarly high eigenfrequencies in order not to interfere with the position frame. This basically means that two full stage structures have to be integrated into one.

Direct drive brushless motors

For actuating the linear and rotary stages, brushless direct drive motors are applied. These motors are frameless and can thus directly be mounted to the stages. Since there are no brushes and bearings, there is no wear, friction or play, allowing for high resolution positioning and high bandwidth.

For the stages, Tecnotion UL series ironless linear motors (www21) have been selected (Figure 3.7, left). This motor has the highest motor constant (k_m) that fits within the available design volume, to minimize heat generation. The motors consist of a U-shaped steel magnet carrier and an epoxy coil carrier. The absence of iron in the windings eliminates attraction forces and cogging, but also reduces the efficiency compared to iron core motors. The U-shaped magnet setup limits the amount of leak flux. Commutation of the three motor phases is done electronically by the amplifier. This specific motor type has no Hall sensors for commutation. The magnet orientation is detected at amplifier power up by an automated ‘wake-and-shake’ procedure, after which a linear scale signal is required for high resolution commutation interpolation.

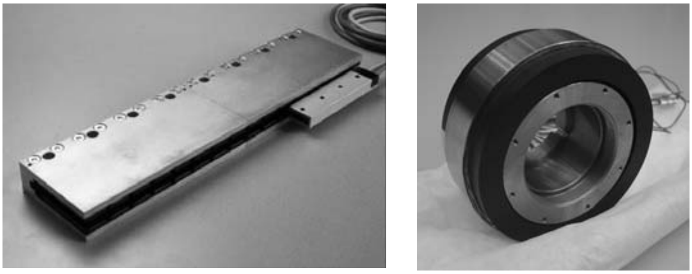

Figure 3.7: Linear ironless motor (www21) and DC brushless motor (www2)

For the Ψ-axis and spindle, rotating frameless brushless direct drive motors are applied (Figure 3.7, right). These motors have the same advantages as the linear motors. This specific motor has Hall sensors so commutation is detected instantly at amplifier power up. The commutation is interpolated by the amplifiers using the available encoder.

Optical linear scales and encoders

For the R- and Z-stages, interferometers are already available to measure the stage position. These are incremental, so they do not provide an absolute ‘home’ position.

This signal may easily be interrupted if the beam is accidentally blocked. Further, the interferometry system is one of the last modules to be assembled to the machine. To have a robust position feedback for the stages and motor commutation, high resolution optical scales and encoders are added. Heidenhain LIP481R scales have been selected (Figure 3.8, left), which have a 4 μm line pitch, outputting a 1 V_{PP}/2 μm. This allows for 5 nm resolution after 400-fold interpolation. One reference mark is present in the middle of the range.

Figure 3.8: Linear scale and angular encoders (www8)

For the spindle, the highest accuracy angular encoder with a central hole available, the Heidenhain ERP880 (Figure 3.8, middle), was selected. This encoder operates with the interferential scanning principle and has 90.000 lines (180.000 signal periods) and one reference mark, giving 0.17 μrad resolution after 200-fold interpolation. The data acquisition electronics can sample up to 500 kHz, allowing for 2.7 rev/s.
The Ψ-axis requires a large central hole. An Heidenhain ERA4280 ring encoder is applied here (Figure 3.8, right). This encoder has 20.000 lines and has distance coded reference marks. The angular resolution is 1.6 μrad resolution after 200-fold interpolation.

Brakes

The stages will be mechanically clamped after positioning the probe on a circular track. Better stability is obtained compared to servo-controlling the stages, especially for high frequency disturbances which are more difficult to measure and compensate for. This is partially because the mechanical clamp can have higher stiffness than the controller, and partially because scale, encoder and amplifier noise are not fed back into the motors. On the other hand, dominant frequencies may be notched by a controller, which is not possible with a mechanical brake.

The design[1] of the R and Z-stage and spindle brake is more or less similar, consisting of a monolithic elastic clamp which is normally closed by a preloaded spring and opened by an air piston (Figure 3.9). Two cylindrical Tungsten Carbide contacts clamp a strip that is attached to the stages. The two hinges (hinge 1) allow the clamp to adjust to sideways misalignment of the brake strip, while the hinges behind the contact points (hinge 2) allow the line contact to adjust to the orientation of the brake strip.

---

[1] *The brakes are designed by C.A.L. Aerts (Aerts, 2007).*

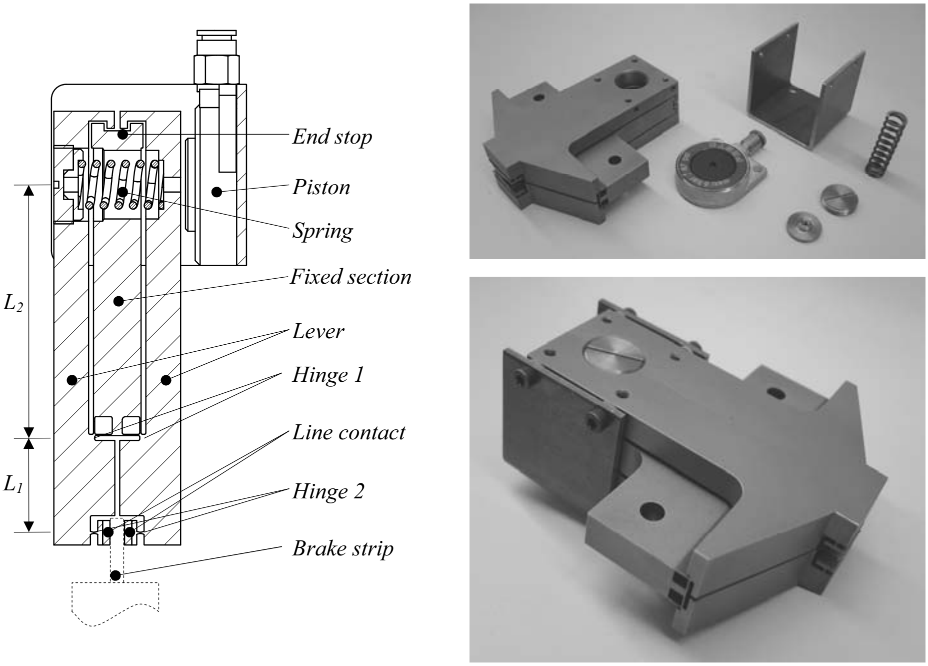

Figure 3.9: Brake design and realization

The brake stiffness and hysteresis calculations and test results are shown in Appendix C. The calculated stiffness of the brake is $2.4 \cdot 10^8$ N/m. Tests however showed a much lower stiffness, mainly due to limited stiffness of the supposedly ‘rigid’ world. Since this is difficult to improve, the measured stiffness of $5 \cdot 10^7$ N/m (Aerts, 2007) will be used for further calculations in the coming sections.

3.1.3 Motion system concept

The concept was shown schematically in Figure 2.6. The product is placed on a spindle since it is more or less rotationally symmetric. Together with the long range optical probe, this allows for high scanning speeds with minimal system dynamics. Since the products may weigh up to 50 kg, a vertical spindle setup provides the best accessibility for mounting and aligning products. An axially loaded spindle further provides the best error motion properties. A vertical spindle, however, also requires the r, z and ψ motion to take place in a vertical plane, which requires extra measures to overcome gravity. The advantages for the operator are considered more important.

A plane of motion is to be provided to the probe with sub-micrometer uncertainty. Initially, it was considered to align the probe directly to a vertical plane using a single air bearing, since this allows for 3 degrees of freedom: the r and z-translation and the ψ-rotation. This was found not to be practical due to the large required range of motion in ψ-direction (-45° to +90°). Next best is to perform the ψ-rotation with a separate bearing stacked on top of the Z-stage, such that the Z-stage only has to perform the r and z-translations. The Z-stage can be aligned to a vertical base plane using three air-bearings. This is expected to improve the stiffness (especially in θ-direction) and guidance accuracy compared to a stacked pinole stage design. The vertical moving mass however also increases. The following section briefly describes the evolution of the stage design.

Z-stage bearing layout

From a dynamics point of view, the Z-stage main tube should be directly above the probe and Ψ-axis, to have the probe reaction forces in the same plane as the bearings that guide the sides of the Z-tube. The probe and Ψ-axis are, however, moving underneath the horizontal beam of the metrology frame. The main tube of the Z-stage is therefore positioned directly behind this beam. This means that reaction forces of the probe servo system cause a moment around the length direction of the tube. This is an extra argument to align the Z-stage with 3 bearings to a vertical plane since this provides better rotational stiffness. The vertical base plane is positioned directly behind the edge of the mounting table, at 320 mm from the spindle centre line.
The main tube of the Z-stage is aligned with two bearings at the bottom and one at the top. In section 3.1.2 it was shown that force closed preloading with opposing bearings is preferred. These preload bearings of the vertical stage can basically be configured in three ways: with individual c-yokes, with a common c-yoke and with a central pull rod through a gap in the base plate.

Figure 3.10 shows the preload configuration with three c-yokes (1), dimensioned for the required range of motion. This requires the lower two ∅100 mm bearings (2) to be spaced 1040 mm apart to allow for 400 mm range of motion in r-direction for the top bearing. This is relatively far, requiring a high bending stiffness of the bridge (3) between the lower bearings. Further, the yokes must provide sufficient z-range which results in large deflections and low stiffness for constraining the in-plane degrees of freedom of the preload bearings (4).

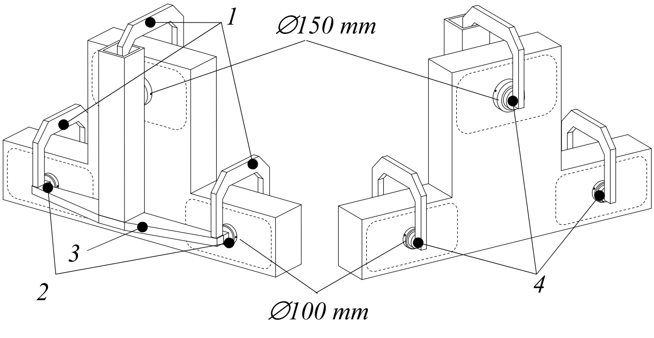

Figure 3.10: Z-stage preload with c-yokes

Figure 3.11 shows a preload configuration using one large central preload bearing (1). This bearing can be better constrained, for instance by using a tubular preload frame with large cross-section (2). Using a ∅150 mm bearing at the top and two ∅100 mm bearings at the bottom, results in the centre of force at half height between the bearings. A single ∅200 mm bearing provides enough load capacity to preload the three front bearings. The lower bearings can now be spaced closer together (~350 mm), which still provides plenty of rotation stiffness in θ-direction. The separate tubular preload frame (2) can be inside the Z-tube and built around the base in a big C-yoke to close the force loop. The required preload force is 4000 N, which results in millimeter order deflection in the tubular frame. Further, a bending moment is introduced in the vertical base plate (3) which decreases the flatness of the plane of motion.

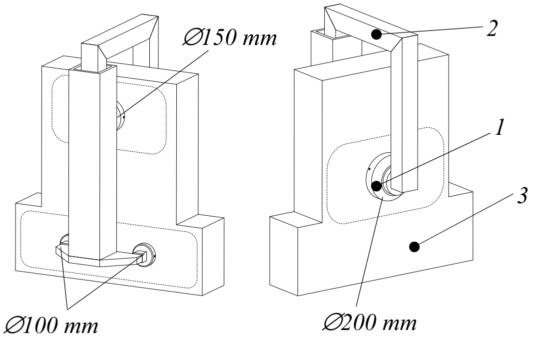

Figure 3.11: Z-stage preload using one central bearing

Using a central gap (1 in Figure 3.12) in the base with a pull tube (2) allows for a stiffer preload body that connects all the bearings. Since the forces are balanced, only tension is present in the pull tube which significantly reduces the total deflection. By using three preload bearings (3), the bending moment on the base is also removed. The attainable eigenfrequency for this preload frame is probably also higher than for the tubular C-frame of Figure 3.11.

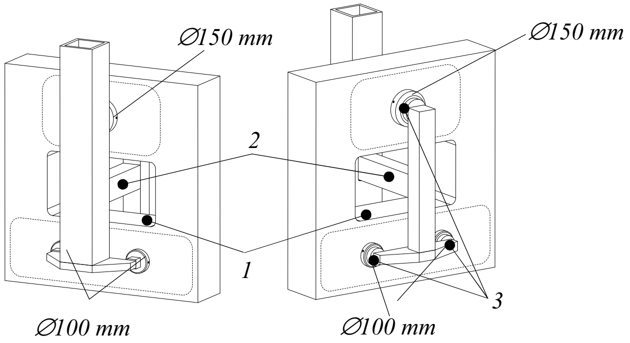

Figure 3.12: Z-stage preload with paired bearings through a central gap

The required range of motion in r is relatively large compared to z: 400 and 150 mm, respectively. The properties of Figure 3.10 are limited by the bending stiffness of the bridge. For smaller, squarer ranges of motion the configuration with the three C-yokes of Figure 3.10 may result in less moving mass and higher eigenfrequencies compared to Figure 3.11 and Figure 3.12.

Two main concepts have evolved, one in which a single preload bearing is applied (based on Figure 3.11) and one in which a central gap is applied (based on Figure 3.12). This choice has consequences for the R-stage design and preload, the base shape and the metrology frame connection.

Concept 1

The first concept (Figure 3.13 and Figure 3.14) has a single preload bearing for the Z-stage, as shown in Figure 3.11, and is adapted from the concept developed in (Henselmans, 2003). In this concept, the base is built from two flat plates (1 and 2) that make the vertical and horizontal guidance plane. The horizontal plate contains a hole in which the spindle (3) is mounted via a flange.

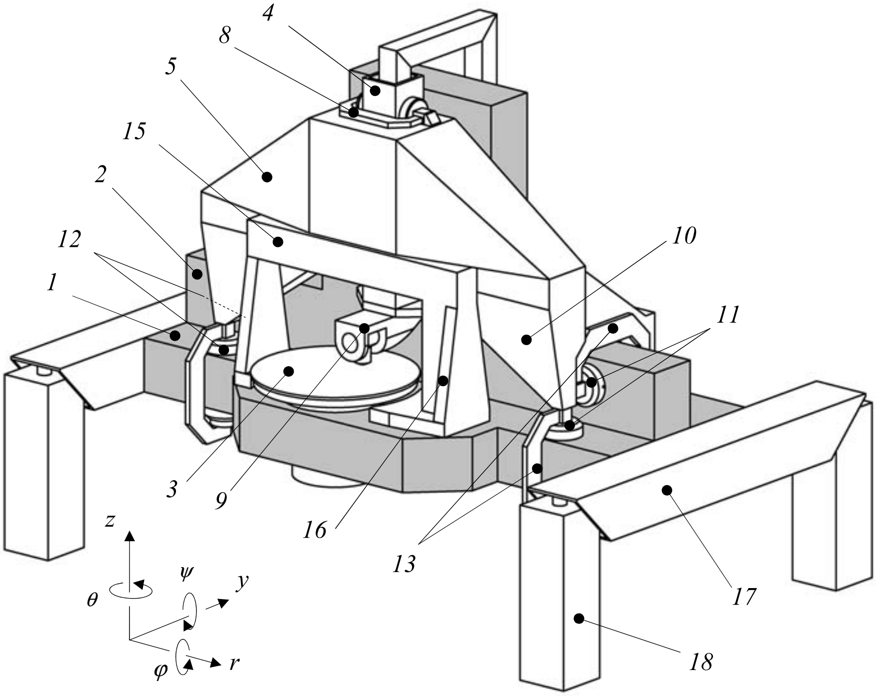

Figure 3.13: Machine concept 1, based on Z-stage with one central preload bearing

The r and ψ-direction of the Z-stage (4) are constrained relative to the R-stage (5) by two fixed (6 in Figure 3.14) and two preload bearings (7 in Figure 3.14) on the sides of the Z-stage main tube. Separate yokes (8 in Figure 3.13) keep the preload forces separated from the R-stage position frame. The dimensions of the probe and Ψ-axis (9) determine the minimal vertical position of the Z-stage, to maintain enough clearance from the measurement volume. The top position of the Z-stage determines the position of the bearings (6 and 7) that guide its tube and with that the vertical dimension of the R-stage is set. These bearings are to be supported towards the horizontal guidance plane. The box structure of the R-stage hereto has two legs (10) extending towards two pairs of horizontal and vertical bearings (11 and 12) that are preloaded by c-yokes (13).

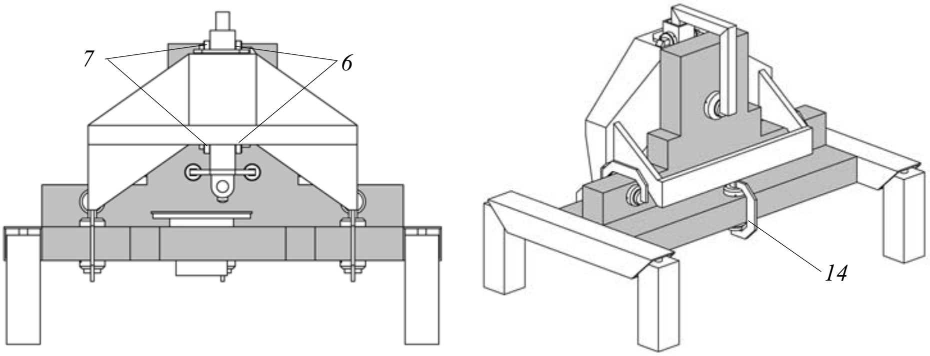

Figure 3.14: Machine concept 1, front and back view

With the y, z, ψ and θ-direction of the R-stage constrained, only the φ-direction remains. This can be constrained with a 3rd bearing high on the vertical plane, or with a 3rd bearing on the horizontal plane at the backside of the base. Since vertical stiffness is more important, the last option is chosen here (14).

The volume of the metrology frame (15) is also shown. Since the R-stage moves behind this frame, a direct support towards the vertical base plane to provide out-of-plane stiffness can not be made. Two flanges (16) are therefore added.

To support the base, two beams (17) are bolted to the sides of the horizontal base plate. These beams extend to the front and backside of the machine to the vibration isolators (18).

Some concerns remain with this concept. Since the probe and Ψ-axis require the Z-stage to be positioned quite high above the product, the R-stage is also high. This causes its centre of gravity to be far away from the bearings, in horizontal as well as vertical direction. The front c-yokes and preload bearings prevent the base frame beams from being closer together, which causes the large rectangular footprint of the machine of 2.6 x 1.7 m. The centre of gravity of the machine is also high above the isolators, which may cause tilting stability issues in the φ-direction. All c-yokes form individual mass-spring systems, giving a large number of eigenmodes at a relatively low frequency. The bearing configuration in this concept prevents out-of-plane stiffness to be provided from the vertical base plane to the metrology frame. Consequently, the metrology frame mounting stiffness is limited.

Concept 2

The second machine concept (Figure 3.15 and Figure 3.16) is based on the central gap in the vertical base plate of Figure 3.12 for preloading the Z-stage (1). The base now consists of three pieces (2, 3 and 4). The spindle (5) is mounted in a hole in the bottom block, again via a flange.
The Z-stage is guided relative to the R-stage (6), again by two fixed (7) and two preload bearings (8), shown in Figure 3.16. The dimensions of the Ψ-axis and probe (9) have not changed, so the position of the Z-stage relative to the product has also remained the same as in concept 1.

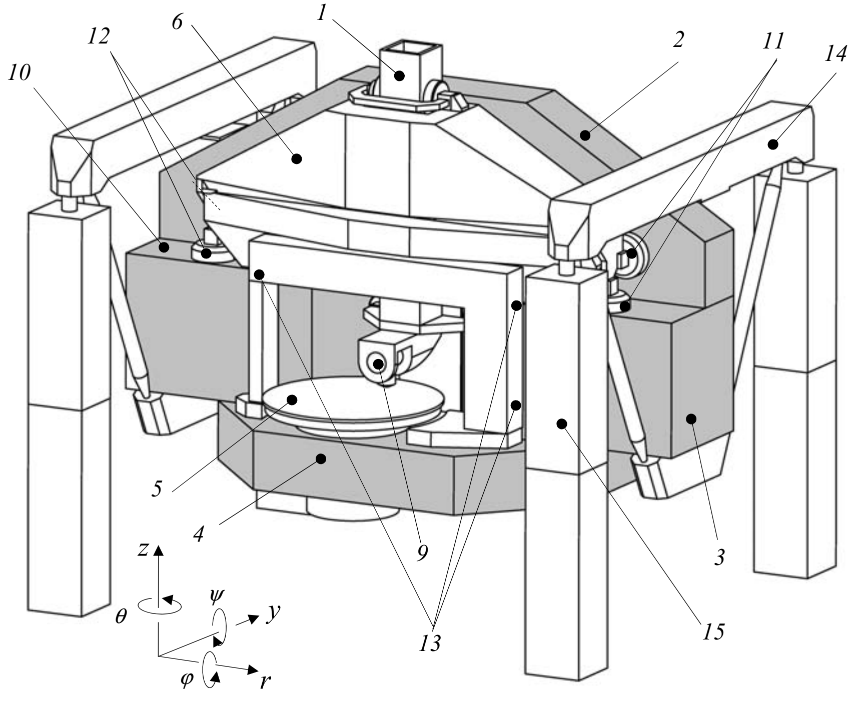

Figure 3.15: Machine concept 2, based on Z-stage with paired bearings through a central gap in the base

The horizontal guidance plane (10) has been raised to the same level as the gap in the vertical plane. This also raises the horizontal and vertical bearing pairs (11 and 12) of the R-stage, and thus lowers the centre of gravity of the R-stage relative to its bearings. Raising the horizontal guidance plane level further creates support points (13) for the metrology frame in out-of-plane direction. It also requires the vertical guidance plane to consist of two pieces (2 and 3), which reduces the achievable flatness (see section 3.2.1). The preloading of the R and Z-stage is further explained with Figure 3.17.

To support the base block, it is mounted onto two triangular frames (14). With the two struts intersecting below the centre of gravity of the machine, almost pure tension and compression is present in the beams. With the isolators (15) raised towards the end points of the triangles, the centre of gravity of the machine is now below the mounting points. This assures tilting stability when the mass of the stages moves from side to side, and reduces the footprint compared to concept 1 to a more square 2.1 x 1.85 m. It may however also amplify lateral vibrations of the floor if the isolators are not sufficiently compliant in lateral direction.

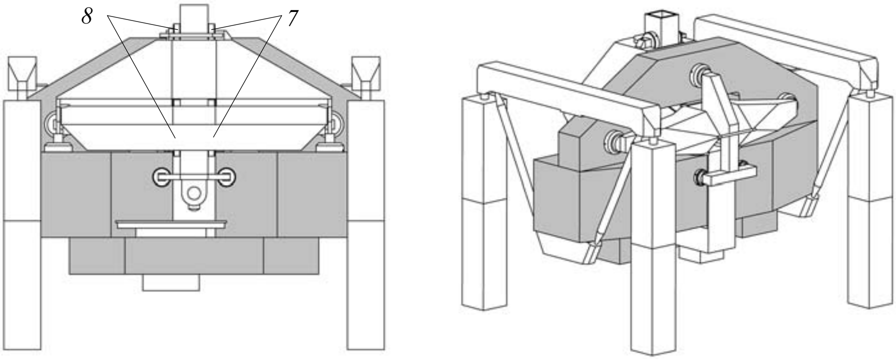

Figure 3.16: Machine concept 2, front and back view

Figure 3.17 shows a close up of the backside of the machine with a section of the base cut out, and the R-stage preload frame coloured gray for clarity. Just as the first concept, the R-stage has two horizontal (1) and two vertical (2) bearings at the front. The R-stage extends backwards through the gap in the base. To constrain this stage in φ-direction, one central horizontal bearing at the backside would be sufficient. The pull tube (3) of the Z-stage preload frame, however, drops to the level of the horizontal plane (4), to keep the overall dimensions minimal. This leaves no space for a single bearing. Two horizontal bearings (5) are therefore positioned left and right of the preload tube. To avoid over-constraining the R-stage, the stage structure has been given a torsional degree of freedom.

Preloading the two horizontal bearings (1) at the front of the R-stage with c-yokes would require very high yokes now. Preloading the vertical bearings with yokes around the vertical base plate has also become difficult because base material is required left and right of the central gap. An R-stage preload frame (gray) has therefore been designed that also makes use of the same central gap. A horizontal beam (6) is connected at the front side of the R-stage position frame (at 7), directly above the two bearing pairs. A tube (8) extends backwards from this beam. From this tube, two arms (9, left one blanked) extend to the two vertical preload bearings (10). This forms an H-shape in the horizontal plane that connects the vertical position determining and preload bearings. Because there is plenty of room to create a large box structure, the deflection of this large frame can be kept below a few tenths of a millimeter.

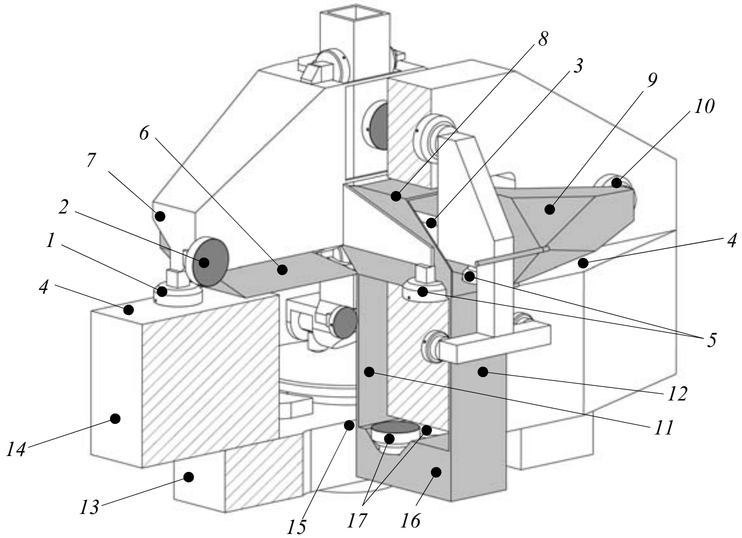

Figure 3.17: Concept 2 cross-section showing preload frame structure

To preload the four horizontal bearings (2 and 5), two plates (11 and 12) extend downwards from the central preload frame tube (8). The bottom base block (13) is connected to the middle block (14) such that it leaves a slit (15), through which the front plate (11) extends. Between the front and back plate, a box (16) is attached that carries two horizontal preload bearings (17). Together with the stage mass, these bearings provide the required preload force in the centre of force between the four horizontal bearings. The large height of the middle base block should provide enough bending stiffness against the bending moment that is introduced this way. To constrain the parallelogram motion of this part of the preload frame, a small extra support bearing has been added, as will be further explained in section 3.5.2.

Comparison

The vertically moving mass is approximately similar in both concepts. The mass of the R-stage will probably also not be very different, be it that most of the mass is concentrated in the position frame in concept 1, and spread over position and preload frame in concept 2. The total moving mass is thus very similar. All bearings have similar dimensions, so the static stiffness is also similar. The fourth horizontal bearing gives concept 2 slightly higher vertical stiffness. Since most moving mass is high above the R-stage bearings in concept 1, the dynamic behaviour and eigenfrequencies are expected to be better for concept 2. Furthermore concept 2 has a lower centre of gravity relative to the isolator mounting points, and therefore has better tilting stability when the stages are moving in the *r*-direction. The bearing preload frame of concept 2 allows for three mounting points from the base to the metrology frame in the out-of-plane direction. Concept 1 has bending in the vertical base plate, directly influencing the flatness of the plane of motion, but this will be repeatable. Concept 2 has no bending in the vertical plane, giving a better plane of motion. It does have some bending in the stiff horizontal base plate, causing (repeatable) tilting of the R-stage in ψ-direction. The footprint of concept 1 is 2.6 x 1.7, where the footprint of concept two is smaller and squarer with 2.1 x 1.85 m.

Considering the above, concept 2 is chosen. This comes at the cost of a more intricate and complex design, but the identified improvements in performance justify the added level of complexity.

3.1.4 Dynamic analysis

To estimate the dynamic behaviour of concept 1, a multi-body dynamic analysis was done. Hereto a model was made using Matlab SimMechanics (Figure 3.18), with which spindle unbalance, floor vibrations, excitation of the probe objective and moving of the stages were simulated. The resulting relative motion between probe tip and spindle is calculated this way. Some of this motion is compensated for by the metrology system, giving an estimate of the remaining measurement error due to machine dynamics. Although the final stage mass and stiffness of concept 1 and 2 are somewhat different from this model, it can still be used for an estimate of the errors to be expected from machine rigid body dynamics.

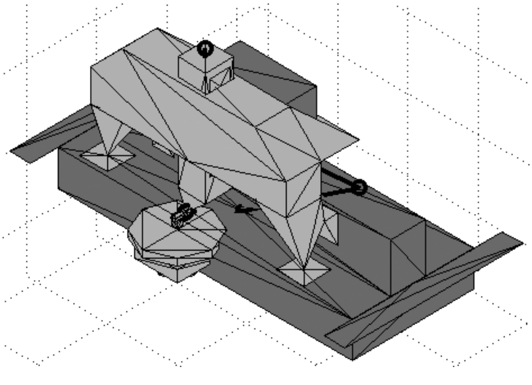

Figure 3.18: Multi-body dynamical simulation model of concept 1

From these simulations, it was concluded that spindle unbalance for typical eccentricities (smaller than 0.1 mm) does not result in significant relative motion, and thus also negligible measurement errors. Floor vibrations may result in several tens of nanometers of relative motion, but most of this is corrected for by the metrology system. No significant errors are thus expected from floor vibrations.

In the above model, a single sided Ψ-axis bearing was applied, as further discussed in section 3.6.1. Probe objective motion caused quite large tilts of the Ψ-axis rotor, and thus a considerable second order errors for this setup. A symmetric bearing should therefore be applied for the Ψ-axis.

Estimates of the dynamic behaviour will be made throughout the next sections with the mass and stiffness of the actual design. Where possible, the flexible body behaviour of the stages will also be taken into account.

3.1.5 Design overview

The following sections treat the design details of the main sub-systems of the motion system (Figure 3.19). The base will be explained first in section 3.2, followed by the spindle in section 3.3. Next, the Z-stage (section 3.4) and R-stage (section 3.5) will be shown, and the Ψ-axis will be explained last in section 3.6. The motion system assembly and experimental results will be discussed in section 3.7 and 3.8. The motion control will be discussed in section 3.9.

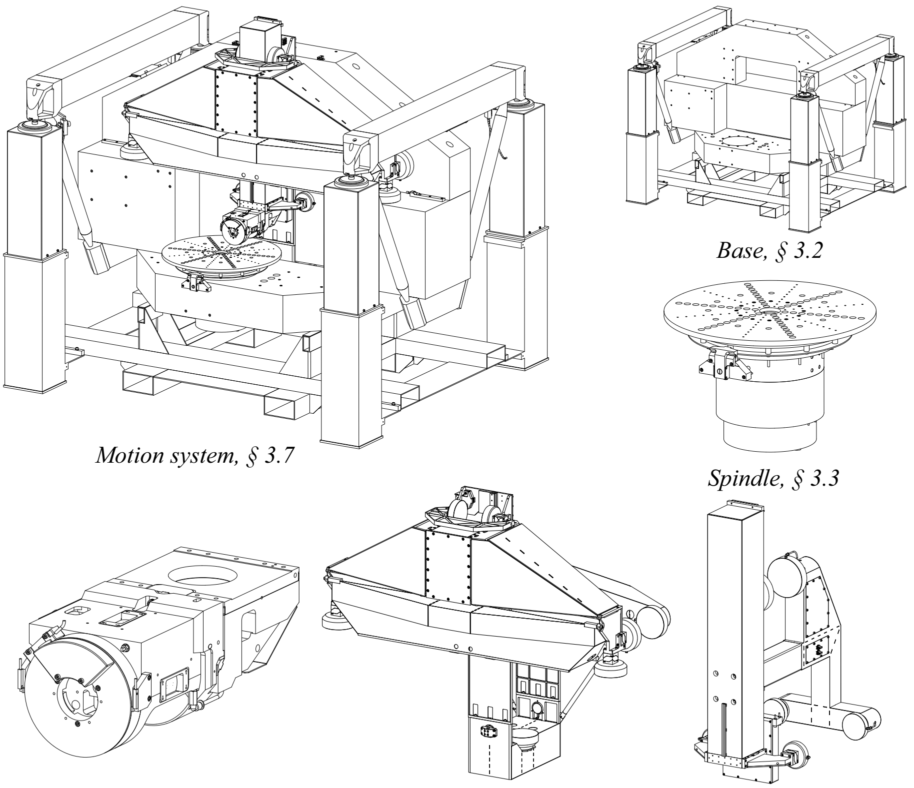

Motion system, § 3.7

Base, § 3.2

Spindle, § 3.3

Ψ-axis, § 3.6

R-stage, § 3.5

Z-stage, § 3.4

Figure 3.19: Motion system main sub-systems

3.2 Base

The base assembly consists of a granite block assembly, to which the spindle and metrology frame are mounted and that provides the guidance surfaces for the air bearings of the R- and Z-stage. This block is suspended on vibration isolators via two triangular frames. Transportation of the machine is possible by a forklift frame underneath the base block.

3.2.1 Base block

The granite base block (Figure 3.20) is built from three pieces: the bottom (1), middle (2) and top (3) block. It was designed in close collaboration with manufacturer Botech BV (www6). The bearing surfaces are shown dotted.

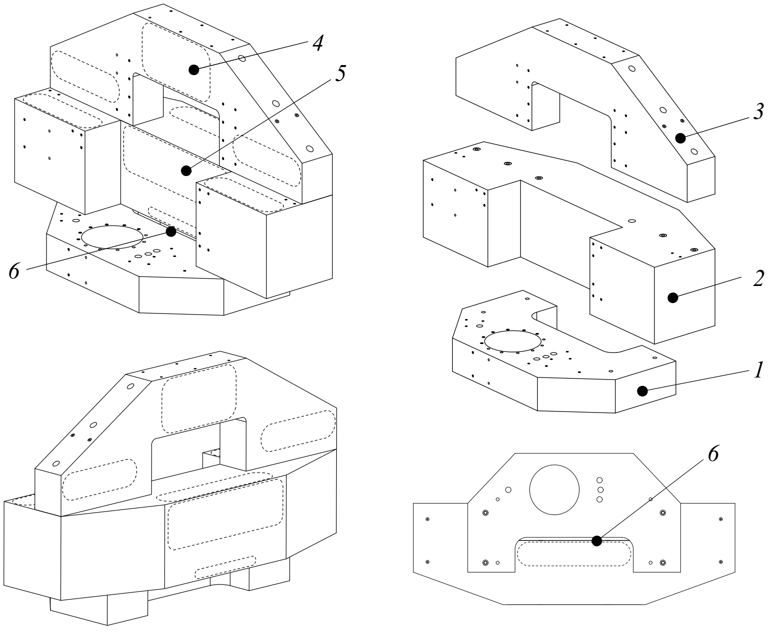

Figure 3.20: Base block assembly

The top and bottom block are bolted to inserts in the middle block using M20 bolts. After alignment was approved, capillary adhesive was applied around the seams to permanently fix the blocks. The bearing surfaces visible in the front view are all for fixed bearings, the surfaces visible in the back and bottom view are preload surfaces. The surfaces for the fixed bearings were ground and lapped flat to within 2 μm and the preload faces to 5 µm. The bearing surfaces for the Z-stage (4 and 5) were measured to be parallel within 1 µm. Steel inserts are applied for attaching various components. The slit for the R-stage preload frame is also shown (6).

The total mass of the assembly is 2150 kg and the first resonance is a bending mode at 336 Hz (Figure 3.21). The second resonance is a torsional mode at 342 Hz. The base block assembly is modelled as a single body, and the mass of the spindle and mounting table (215 kg) has been taken into account in this calculation.

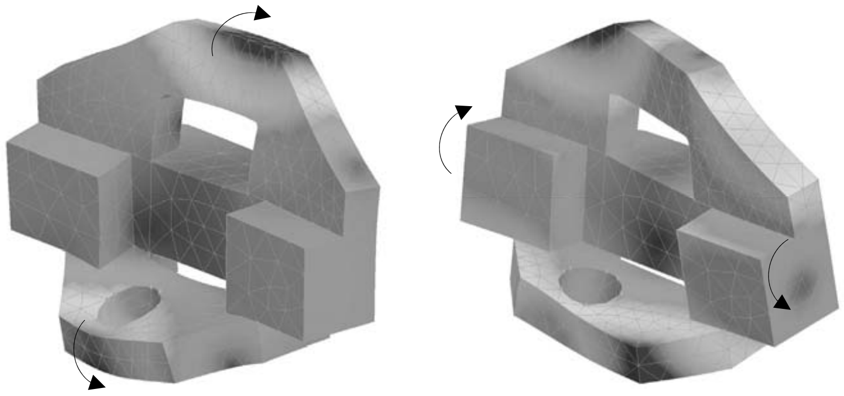

Mode 1 = 336 Hz *Mode 2 = 342 Hz*

Figure 3.21: Base block eigenmodes

The maximum deflection due to gravity is approximately 4.6 µm at the front of the bottom base block (Figure 3.22, left). The maximum deflection of the horizontal guiding surfaces of the R-stage is 1.5 µm, giving 1.8 µrad of tilt per side. During lapping, the middle block is supported on its final mounting points so most of this deflection is lapped out during manufacturing. The added mass of the bottom and top block still cause some deflection.

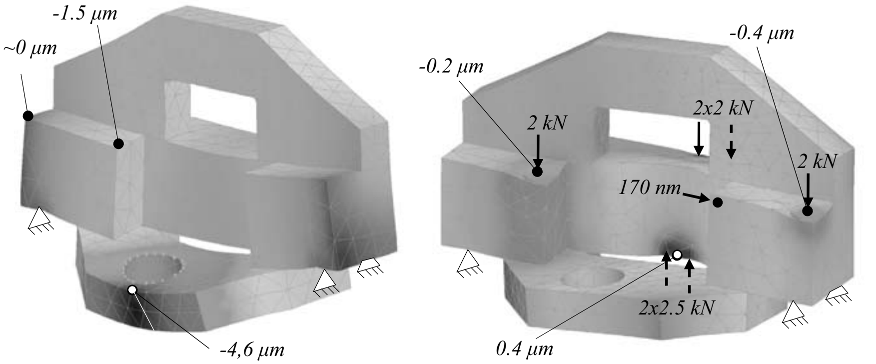

Figure 3.22: Base deformation from gravity (left) and R-stage bearing preload (right)

The R-stage bearing layout causes a 3 point bending moment on the base. When the stages move from left to right, the load also shifts, causing the R- and Z-stage to tilt in mainly the ψ-direction. The deflection for 2 kN on the fixed bearings and 2.5 kN on the preload bearings is shown in Figure 3.22, right. The difference between the left and right bearing is 0.2 μm over 1.4 m bearing spacing, or a tilt of 0.14 μrad in ψ-direction. This is well within the requirements for the interferometry system alignment, and probably even also highly repeatable. Having a central preload bearing is thus not a problem in this case, due to the large height of the middle block.

A plate will constrain the upper metrology frame in r-direction relative to the base (see section 4.3.4). The mounting point of this plate shifts about 170 nm when the R-stage moves from left to right. This shift will be eliminated from the metrology loop by a compensation mechanism.

Figure 3.23 shows the base block under construction at Botech BV, and the completed block just after delivery to the TU/e GTD workshop.

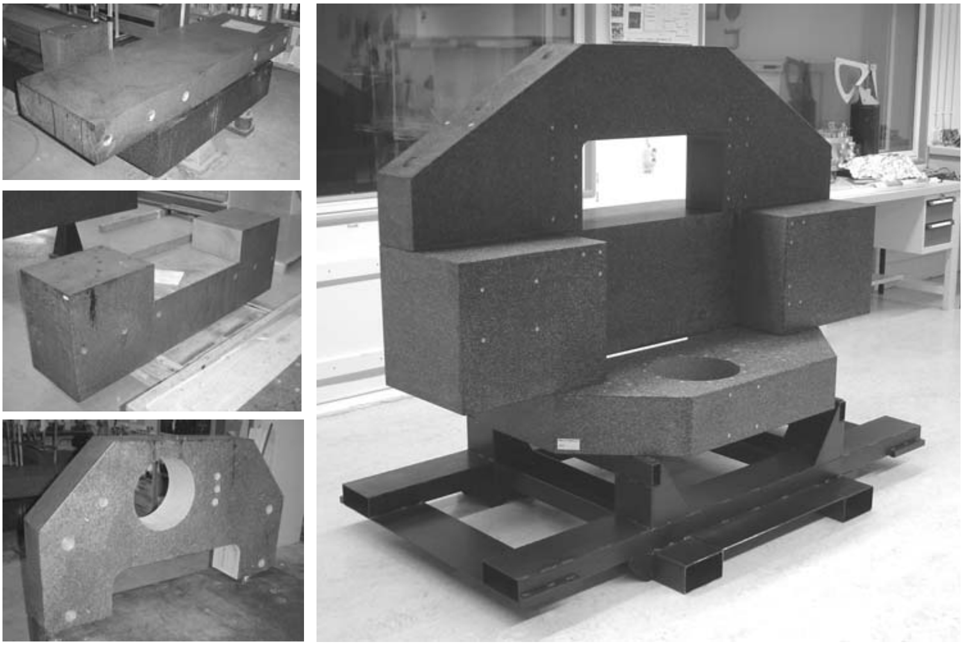

Figure 3.23: Base block

3.2.2 Vibration isolation

The base block is suspended onto four Newport I-2000S passive vibration isolators (1 in Figure 3.24). These isolators consist of a vertical air-spring with damping via a porous restriction, and horizontal isolation via an oil-damped pendulum. Mechanical levelling valves increase or decrease the pressure inside the air volume to adapt to shifting of the load due to moving of the stages. Each isolator is rated up to 900 kg, so with a total suspended mass of around 3000 kg, four are required. This also gives more tilting stability compared to three. The block is hanging in two triangular frames (2), with two plates (3) attaching the block to the top beams of these frames to constrain the sideways swinging degree of freedom. A rubber layer (4) is applied in this connection to provide damping between the steel beams and the block. This prevents acoustic vibrations in the low-damped steel triangles to propagate into the base block.

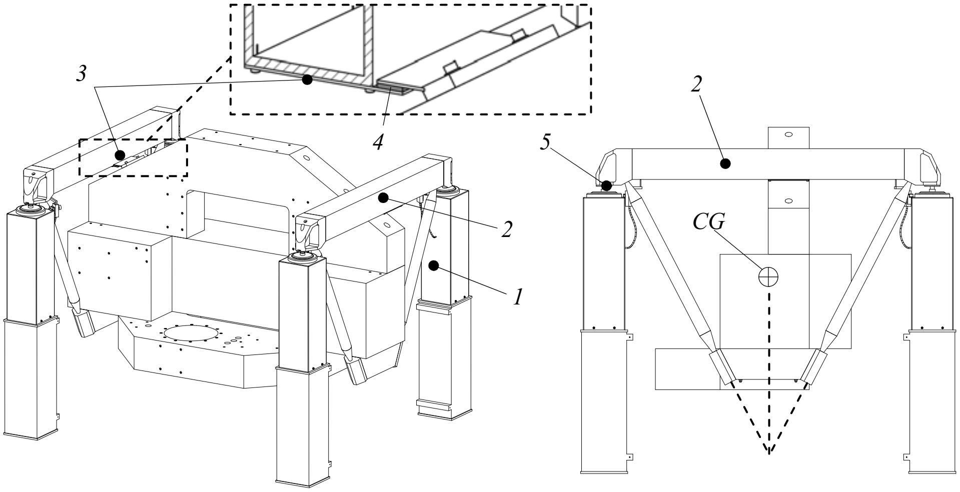

Figure 3.24: Base vibration isolation

The two struts cross below the centre of gravity of the machine (CG), resulting in almost pure tension and compression in the beams. This setup results in a centre of gravity that is about 450 mm below the mounting points (5), which gives inherent tilting stability and lowers the tilting frequency of the base. It also allows for an almost square footprint that is no wider than the base block itself. The final footprint size is 2.1 m x 1.85 m.

Isolation quality

When the machine is simplified to a dual mass-spring system (Figure 3.25), the isolation quality is given by (3.4), similar to (Vermeulen, M., 1999), and is equal to the ratio between the amplitude δ at the probe tip and the floor amplitude z_g. The Newport I-2000S isolators have a mass independent resonance frequency f_{isol} of around 1 Hz in vertical and 1.5 Hz in horizontal direction. The first (measured) eigenfrequency f_{eq} at the probe tip is about 75 Hz in vertical and 50 Hz in horizontal direction (see section 3.8.2).

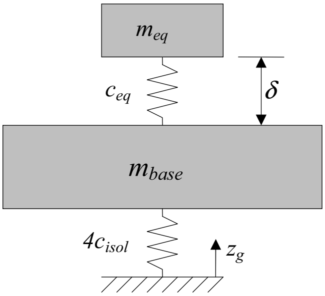

Figure 3.25: Base dual mass model and tilt model

$$\frac{\delta}{z_g} = \left(\frac{f_{isol}^2}{f_{eq} \cdot f_g} \right)^2 \tag{3.4}$$

Metrology laboratories typically have independent foundations providing floor frequencies f_g of around 5 Hz (Figure 3.30), which gives an isolation quality of $7 \cdot 10^{-6}$ in vertical and $8 \cdot 10^{-5}$ in horizontal direction. Translated to floor amplitude this gives a typical z_g of 3 μm, resulting in a displacement δ at the probe tip of 0.02 and 0.25 nm in vertical and horizontal direction, respectively. These values are only an indication of the actual displacements. In practice, these values will be higher due to parasitic stiffness of cables and non-ideal behaviour of the isolators. To calculate the remaining vibration amplitude spectrum at the probe tip more accurately, one may also use the Power Spectral Density of the actual laboratory in combination with the isolator and machine frequency response.

Levelling

When the stages move from left to right, the base will tilt in ψ-direction (Figure 3.26).

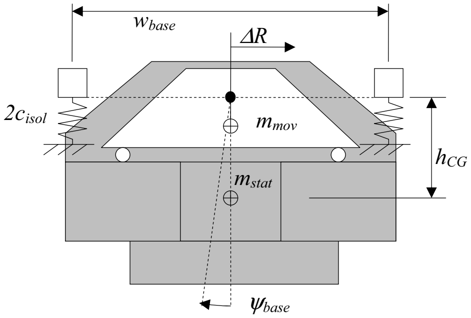

Figure 3.26: Machine levelling model

In case of a tilt, the equation of moments consists of a moment of the static mass (*stat*), the moved mass (*mov*) and the isolator springs (*isol*):

$$\begin{aligned}
&M_{stat} + M_{isol} - M_{mov} = 0 \\
&M_{stat} = m_{stat} \cdot g \cdot \sin(\psi_{base}) \cdot h_{CG} \\
&M_{isol} = k_{\psi} \cdot \psi_{base} \\
&M_{mov} = m_{mov} \cdot g \cdot \Delta R
\end{aligned} \tag{3.5}$$

Using the small angle approximation, the base tilt can herewith be expressed as:

$$\psi_{base} = \frac{m_{mov} \cdot g \cdot \Delta R}{m_{stat} \cdot g \cdot h_{CG} + k_{\psi}} \tag{3.6}$$

The total moving mass m_{mov} (stages, probe and interferometry system) is approximately 275 kg and the stationary mass m_{stat} (base, spindle and metrology frame) is approximately 2600 kg. This brings the total mass m_{tot} to 2875 kg that is suspended at 1 Hz. Using (3.7), this gives a vertical isolator stiffness of $2.8 \cdot 10^4$ N/m.

$$c_{isol} = \frac{\left(2\pi f_{isol}\right)^2 \cdot m_{tot}}{4} \tag{3.7}$$

The isolators are spaced 1860 mm apart, resulting in a tilting stiffness k_{ψ} of the base of $1 \cdot 10^5$ Nm/rad (3.8).

$$k_{\psi} = \frac{1}{2}\left(2c_{isol}\right) w_{base}^2 \tag{3.8}$$

When the R-stage moves from the centre position to the outer right position, it displaces 200 mm. The centre of gravity of the stationary mass is approximately 450 mm below the mounting points on the isolators. When no active levelling is applied, this results in a base tilt of 4.8 mrad. This is equivalent to 4.5 mm displacement at the isolators. Since there is no friction and a direct drive motor is applied, the R-stage motor would have to counter this tilt with about 13 N.

The afore-mentioned only happens when the R-stage moves swiftly (tens of mm/s) from left to right. The valves of the levelling system respond to approximately 0.1 mm displacement at the valve. The tuning of the levelling system restriction is a compromise between settling time and levelling speed. Since the primary mode of operation will be circular scanning, low settling time (high damping) is preferred above levelling speed. In practice, base tilt is negligible when scanning circular tracks, as is thus also the case for the required R-stage motor force.

3.2.3 Transportation

A forklift frame is present under the base block (Figure 3.27, gray). When the isolators are pressurized, the base is lifted 5 mm above this frame. Four bolts in inserts in the bottom of the base, extend into oversized holes in the forklift frame. The isolator columns are also attached to this frame. The bolts limit the range of motion of the base relative to the isolators to prevent the whole assembly from falling over.

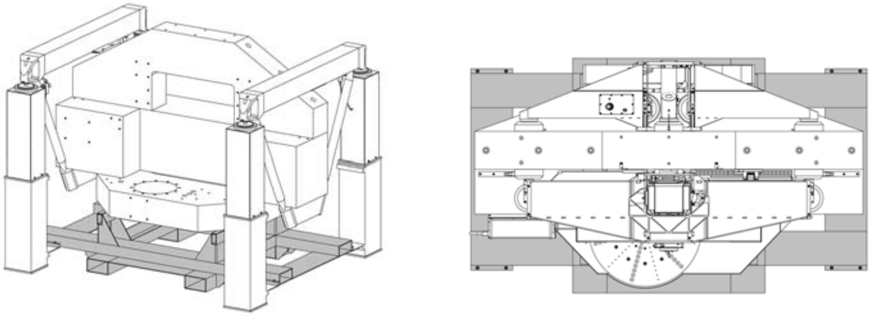

Figure 3.27: Transportation frame

When the isolators are depressurized, the block lands on the frame. After removing the triangular frames and the isolator columns, a footprint of 2.1 x 1.25 m remains. This is narrow enough to fit through a double door. In the top view (Figure 3.27, right), the transportation frame (gray) extends from under the machine in all directions, which protects the sensitive parts of the machine for instance from hitting a doorpost during transport.

During development of the machine, the TU/e GTD workshop moved to a new building which forced the transportability of the machine to be tested in practice (Figure 3.28). To prevent air bearing damage due to vibrations, air supply was maintained using a pack of compressed air cylinders. Small jacks were used to lift the machine and mount rollers underneath. It was then pushed towards to loading dock and into a truck by hand. At the new location, a forklift then lifted the machine out of the truck and onto the loading dock, after which it was rolled towards its new position.

Figure 3.28: Machine transportation during GTD move

3.2.4 Base assembly

Figure 3.29 shows the base assembly. Due to late delivery of the isolators, the spindle is already installed in this photograph. Warnings are placed on the bearing surfaces, to prevent damaging the surfaces. The total mass of the assembly is 2850 kg (spindle not included), of which 2350 kg is suspended on the vibration isolators. The footprint is 2.1 x 1.85 m, and the height is about 1.7 m.

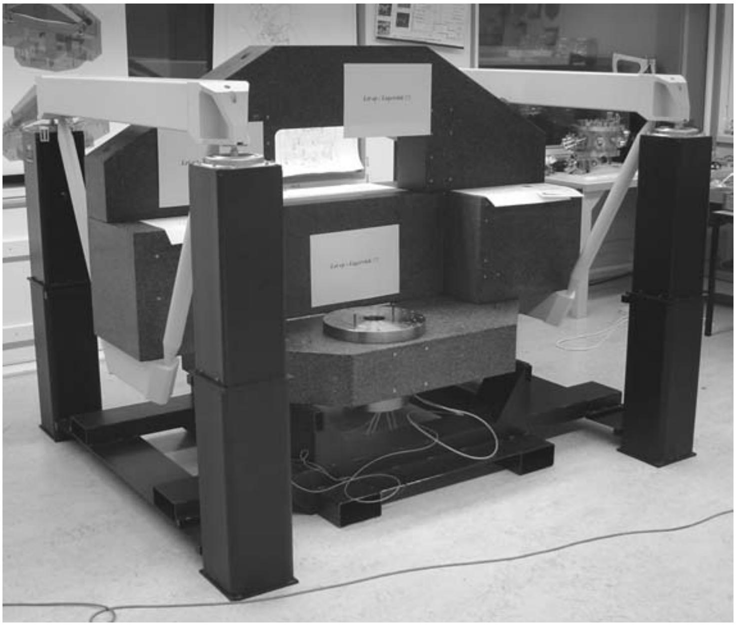

Figure 3.29: Base assembly

3.2.5 Vibration measurement

To measure the quality of the vibration isolation system, measurements were taken with an acceleration sensor (B&K 8318C). The vertical vibration levels were measured on the base and on the floor. Since only one sensor was available, no frequency response could be derived. It should further be noted that the measured vibration levels on the base are around the minimum specified sensitivity of 10^{-5} m/s^2 of this sensor. The achieved reduction can still clearly be seen in Figure 3.30. Around 2-3 Hertz, the vibration level on the base is slightly higher than on the floor. This is due to the amplification around the isolator resonance frequency. A sharp 50 Hz peak can also be seen from EMC interference of the mains. The source of the other peaks in the base measurement has not been investigated.

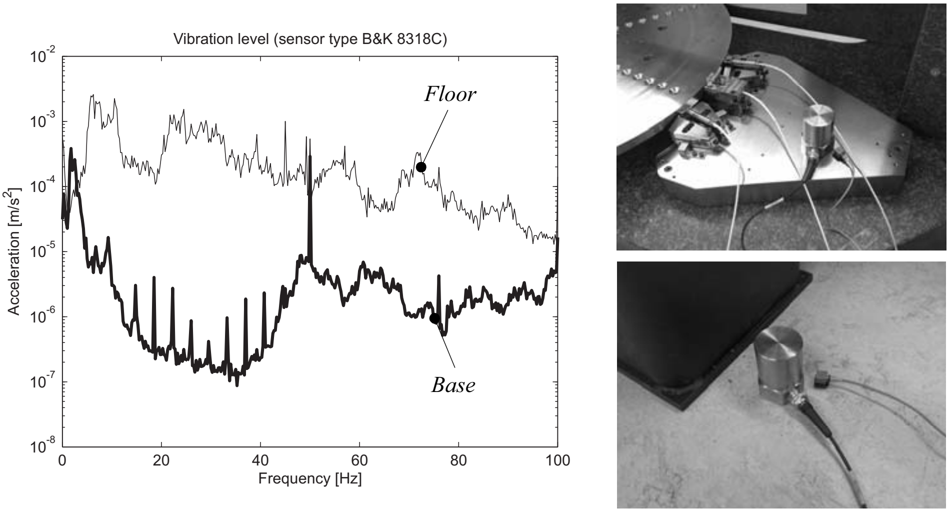

Figure 3.30: Measured vertical vibration levels on floor and base

The above measurements were taken at the former TU/e GTD workshop. The final machine validation measurements are performed at the new location at the TNO Eindhoven facility. No accelerometer measurements were performed here. The actual influence of the remaining vibration between probe tip and spindle is measured in section 3.8.2. The measured vibrations originate from floor vibrations, acoustic excitation and internal sources. The measured vibration levels are sufficiently low, so it can be concluded that the vibration isolation performs as required.

3.3 Spindle

The spindle assembly consists of an air bearing spindle that is mounted to the base via a flange. A steel mounting table is bolted to its rotor, on which the reference edge for the error motion measurement is machined. Some first ideas for a universal intermediate body are explained. A brake disc and calliper allow for locking the spindle when measuring a radial track or when mounting a product.

3.3.1 Air bearing spindle

After a survey of commercially available large air bearing spindles, the Professional Instruments BlockHead 10R spindle was selected (Figure 3.31). This spindle has the best stiffness, load capacity and error motion specifications compared to other vendors products at the time. The spindle bearing, mounting flange, motor and encoder were delivered as a complete assembly by the manufacturer.

Figure 3.31: BlockHead 10R air bearings spindle (www3)

The bearing consists of a double thrust bearing on the top and bottom with a central radial bearing in between. This makes it very suitable for a vertical setup with heavy products. At 8 bar supply pressure, the axial stiffness ($c_{S,ax}$), radial stiffness ($c_{S,rad}$) and tilt stiffness ($k_{S,tilt}$) amount to $1.4 \cdot 10^9$ N/m, $2.8 \cdot 10^8$ N/m and $9 \cdot 10^6$ Nm/rad, respectively. The axial working load capacity is 430 kg. The axial and radial error motion is specified as smaller than 25 nm and the tilt error motion as smaller than 0.1 µrad. The total mass of the bearing is 68 kg, of which 32 kg is the rotor with an inertia of 0.254 kgm^2. The normalized air consumption is about 85 l/min.

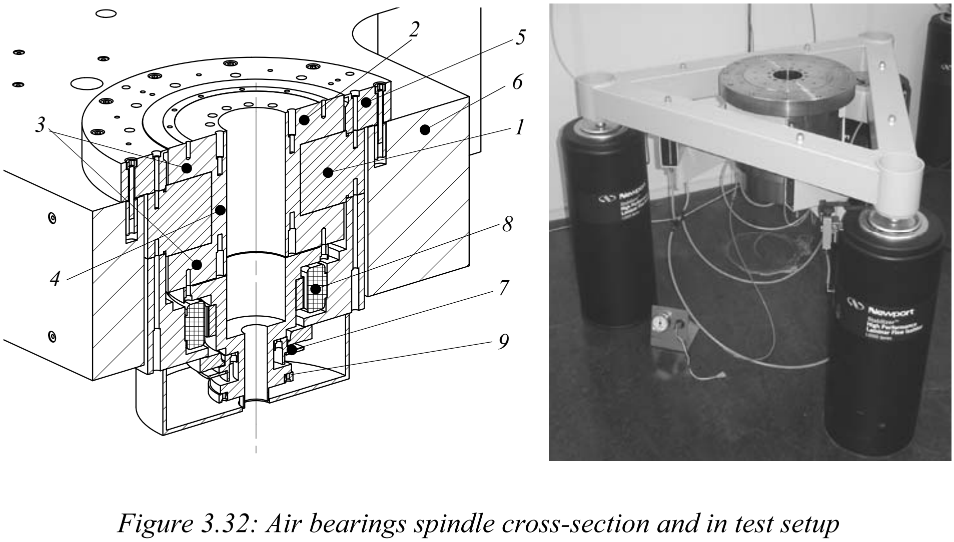

Figure 3.32: Air bearings spindle cross-section and in test setup

The spindle assembly shown in Figure 3.32 consists of a ring shaped stator (1) and a rotor (2) built from two thrust bearing discs (3) connected by a tube that functions as a radial bearing (4). A flange (5) was added to mount the bearing into a hole in the base

(6). The base and flange faces were manufactured to high flatness tolerances, allowing them to be bolted together face to face with minimal distortion of the spindle. To measure the rotation angle of the spindle, a Heidenhain ERP880 optical encoder (7) was installed. At the time, this was the best encoder available with a central hole. This central hole was to remain open for calibration purposes, as will be further discussed in sections 4.3.5 and 7.3. The encoder has 90.000 lines, resulting in 180.000 signal periods of 1 V_{pp} per revolution. According to Heidenhain, 200-fold interpolation may be reliably applied, resulting in 0.17 μrad resolution, or 44 nm in tangential direction at the outer edge of the measurement volume. The encoder has one reference mark, and system accuracy is specified at 1 arcsec, or 4.8 μrad.

To drive the spindle, an MCS B20-13 brushless DC motor (8) was installed by the manufacturer. This motor has a high motor constant of 0.65 $\mathrm{Nm}/\sqrt{\mathrm{W}}$, to limit the heat produced during operation. At startup, Hall sensors provide the rotor orientation for commutation. To assure smooth commutation, the amplifier uses the encoder signal to interpolate between the Hall sensors. Regular amplifiers can not cope with the high line count of the ERP880 encoder. A second encoder, a Renishaw RESR ring encoder with 20.000 lines (9), was therefore installed to aid commutation. The total inertia of the rotor assembly is 0.3 kgm^2. The assembly was obtained from the spindle manufacturer to prevent distortions from affecting the bearings air gaps.

3.3.2 Product mounting table and intermediate body

Stress-free mounting of optics is a science in itself and not included in the scope of this thesis. The stiffness required during machining is generally much higher than the stiffness required during operation. Statically determined mounting, for instance using three hinged leaf-springs generally is not sufficient (Van Venrooy and Ploeg, 2005). Another complication is that machining and measurement is usually done in vertical and/or horizontal setup, while the product may have any orientation relative to gravity in the final application. In space applications, gravity is not even present.

In polishing, it is common to attach the optic to a counter formed intermediate body using pitch or wax. By pushing the product into the molten wax, it is attached stress-free and with even support stiffness over its entire surface. In diamond turning, surfaces with a flat backside are generally clamped onto a vacuum chuck. Provided that the backside and the chuck are (diamond turned) flat, this provides relatively low mounting stresses and high stiffness. In some cases, for instance in open back structures, this is not possible and bolting the product to the chuck is necessary. Much care must be taken not to deform the product in this case.

Ideally, a universal intermediate body is applied in single-piece production, to which the product is waxed or bolted. This body serves as a quick and repeatable interface between manufacturing and measuring machine. Some first ideas are explained in Appendix D.

Mounting table

The mounting table is a solid steel disc, 600 mm in diameter and 40 mm thick. A solid disc provides highest stiffness within the available dimensions, and mass is no issue since the higher inertia only aids in keeping a constant speed. Steel was chosen to match the thermal expansion coefficient of the spindle, and to provide a hard, damage resistant mounting face. The total mass is 75 kg and the inertia is 2.9 kgm^2. The table has twelve rows of M5 holes for bolting or clamping a product or intermediate body to the table (Figure 3.33).

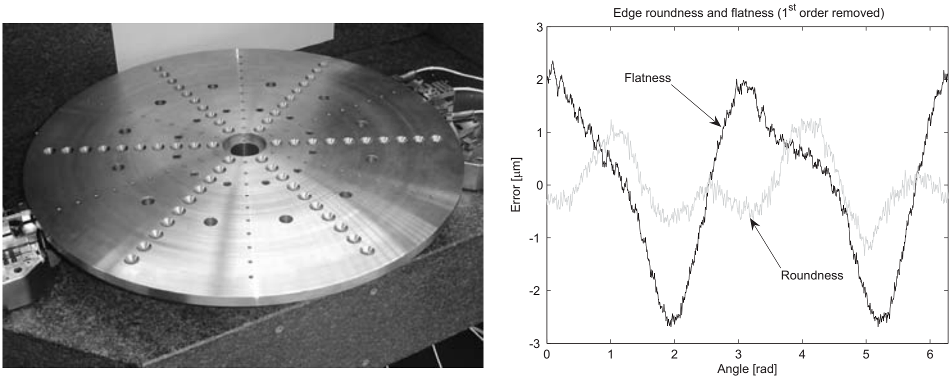

Figure 3.33: Mounting table and edge profile

As will be explained in section 4.4, the error motion of the spindle is measured by capacitive probes measuring to the edge of the table. This reference edge is machined onto the side and bottom of this table using a conventional 1960s carousel lathe. The steel disc was taken from a rod of bulk material instead of plate to have an axial symmetric stress distribution that allows for better flatness. After warming up the machine overnight, the edge was machined to a PV roundness of 2.3 µm and a PV flatness of 5.1 µm (Figure 3.33, right). The table was Nickel plated to protect it from corrosion. The profiles shown are actual capacitive probe signals with their first order (eccentricity and tilt) removed. Axially, the profile is mainly a 2nd order profile, indicating warp. Radially, the profile is less clear, but some elliptical form can be distinguished.

3.3.3 Spindle brake

When performing a radial scan or when installing a product, the spindle is clamped. A ring (1 in Figure 3.34) has hereto been lasercut from a stainless steel plate. This ring is bolted to the bottom of the table via 12 spacers (2). The brake clamp (3) is similar to the clamp mechanism described in section 3.1.2, but has a 90° bend in it. This way it can be bolted to inserts on the front of the bottom base block (4) via a spacer (5).

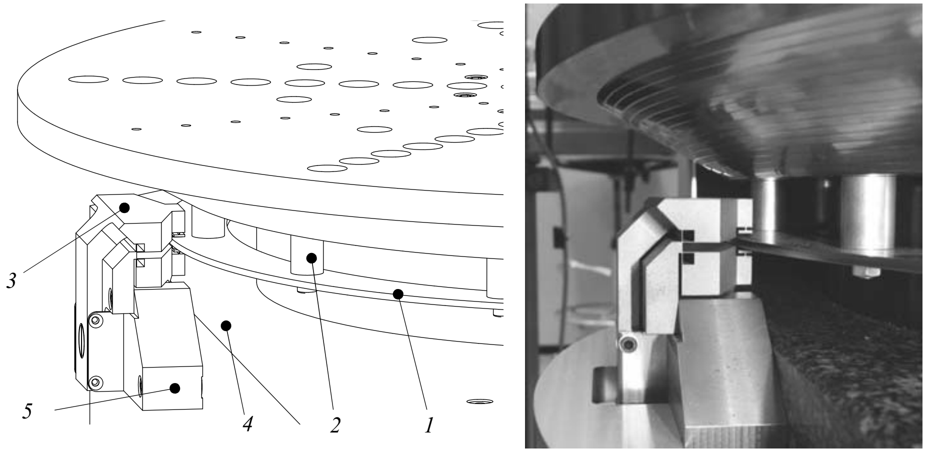

Figure 3.34: Spindle brake

As explained in section 3.1.2, the brake clamp has a stiffness of $5 \cdot 10^7$ N/m between the contact points and the base. The contact is at a radius of 230 mm, giving a rotation stiffness of $2.6 \cdot 10^6$ Nm/rad. The total inertia of the rotor, motor, encoders and table is 3.3 kgm^2, giving a resonance around the centre line of 141 Hz.

3.3.4 Spindle assembly

The spindle assembly with mounting table and brake is shown in Figure 3.35. The lower metrology system is already installed around the spindle in this photograph.

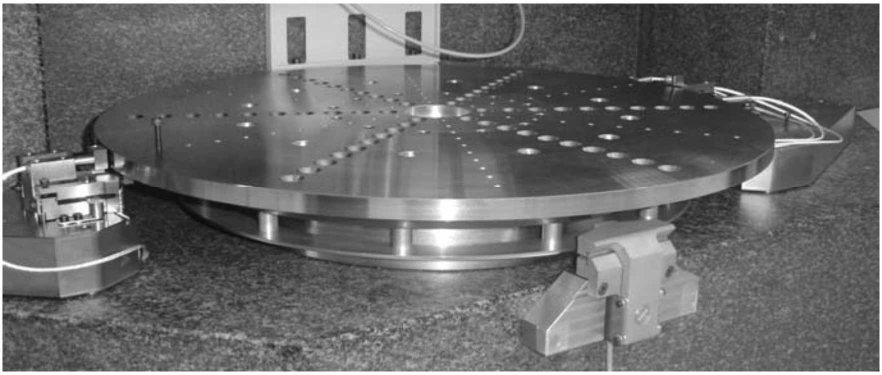

Figure 3.35: Realized spindle assembly

The total mass of the spindle assembly is about 215 kg. The rotor, motor, encoder and mounting table mass is 120 kg. Table 3.1 summarizes the theoretical spindle properties. Experimental validation will be done in section 3.8.2.

i	$c_{S,i}$ *[N/m]*	$m_{S,i}$ *[kg]*	$f_{S,i}$ *[Hz]*
z	$1.4 \cdot 10^9$	120	544
r, y	$2.8 \cdot 10^8$		243

i	$k_{S,i}$ *[Nm/rad]*	$J_{S,i}$ *[kgm²]*	$f_{S,i}$ *[Hz]*
φ, ψ	$9 \cdot 10^6$	2.4	308
θ *(brake)*	$2.6 \cdot 10^6$	3.3	141

Table 3.1: Spindle assembly theoretical rigid body properties

3.3.5 Error motion measurement

Several experiments were conducted to check the spindle after delivery. First of all, the air gap, stiffness and load capacity were verified. Using three LVDT probes, one central and two on the edge of the rotor, an air gap of only 3.5 µm was measured. This is relatively small for an air bearing and probably explains the high stiffness of this particular bearing.

After installing the spindle into the base, and bolting on the product mounting table, the error motion was measured to verify that no distortion was introduced during mounting, and to provide comparable results for testing the multi-probe method (section 4.4.2). The roundness of a steel reference sphere was first calibrated at NMi VSL. The minimum zone roundness profile is shown in Figure 3.36 (left). A contact stylus with a tip radius of 1.8 mm was used for this measurement. Capacitive probes with a spot diameter of 2.5 mm will be used in the experiment, which have different filtering properties. The roundness profile is hereto filtered by a flat averaging filter with 2.5 mm width, to approximate this effect.

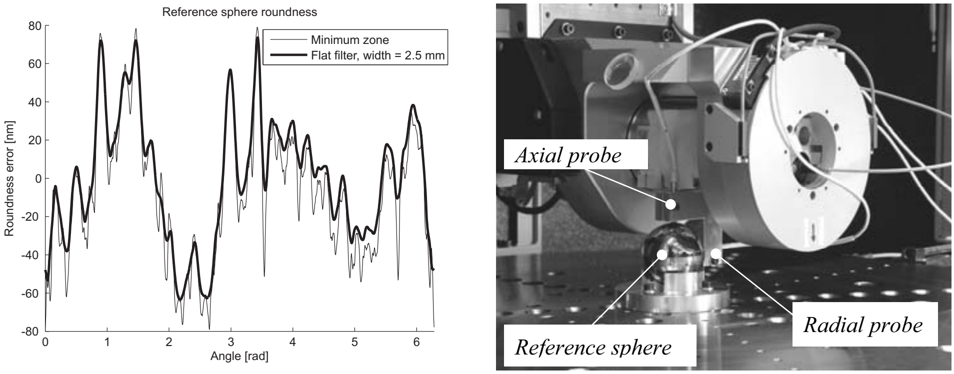

Figure 3.36: Reference sphere roundness (by NMi) and spindle error motion setup

The reference sphere was centred on the spindle, and an axial and radial capacitive probe were attached to the Ψ-axis rotor (Figure 3.36, right). The probes were aligned with the centre of the sphere by moving the stages towards the maximum readout of the capacitive probes. The Z-stage was landed for optimal stability. Tests were performed at 0.1, 0.5 and 1 rev/s with a sample rate of 1 kHz. At each speed, 20 revolutions were recorded.

Figure 3.37 (left) shows the axial measurement, which is by definition equal to the synchronous axial error motion (ASME, 1985). It can be seen that the synchronous axial error motion is 9 nm PV with a clear first order component.

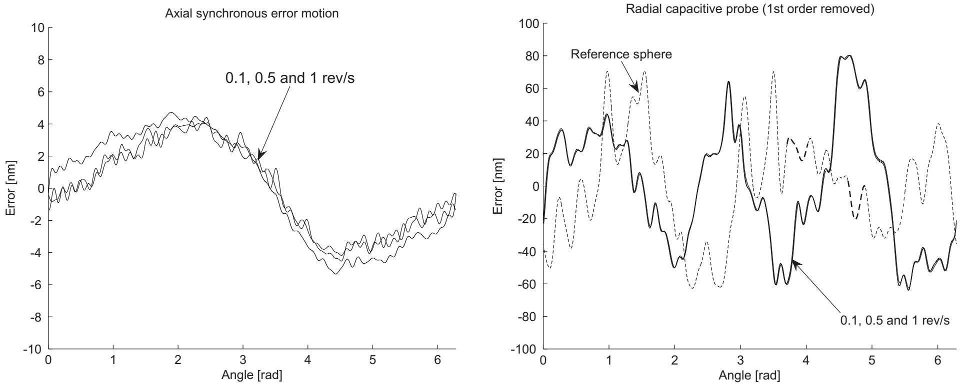

Figure 3.37: Axial synchronous error motion and radial capacitive probe signal

In Figure 3.37 (right) the radial measurement is shown. The reference sphere profile is also shown, from which a large radial error motion could be concluded. A multi-step measurement (ASME, 1985; Whitehouse, 1976; Grejda, 2002), however, indicates the contrary, as will be explained in the next paragraph.

The deviation from the average at 1 rev/s is shown for 20 revolutions in Figure 3.38, with a mean rms of 2.9 nm and 3.2 nm respectively. The noise level of the probes used is about 0.2 nm rms. At standstill, the noise level originating in air fluctuations and external vibrations is similar to Figure 3.38. The part of the asynchronous error motion coming from the rotation of the spindle is therefore only a small part of this signal.

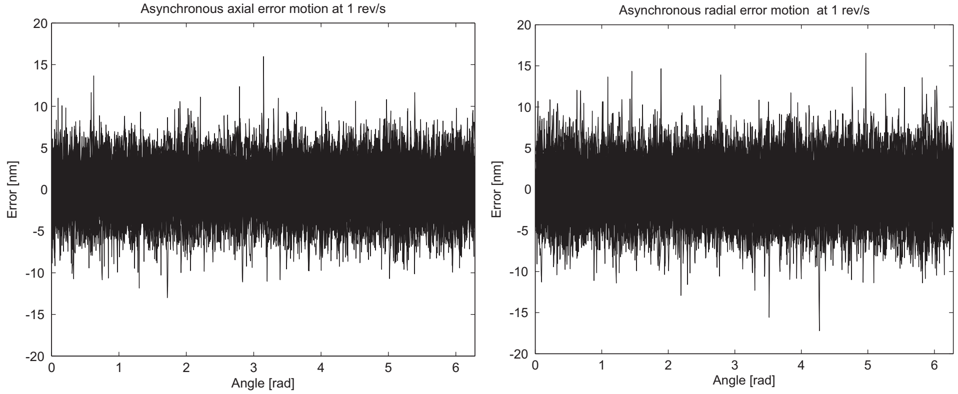

Figure 3.38: Axial and radial asynchronous error motion

To double check the radial error motion results of Figure 3.37, a multi-step measurement was performed. The reference sphere was measured again at the three speeds for 20 revolutions, but now also at three orientations spaced 120° apart. It should be noted that these steps are not exact, since no exact means of indexing was available at that time. As can be seen from the measurement results in the coming paragraphs, the resulting errors are probably smaller than what Figure 3.37 (right) suggests. Figure 3.39 (top left) shows the averages of the 9 measurements. Subtracting the shifted sphere profile from these measurements does not give a repeatable radial error motion result, again indicating that the radial error motion results shown in Figure 3.37 (right) are unreliable.

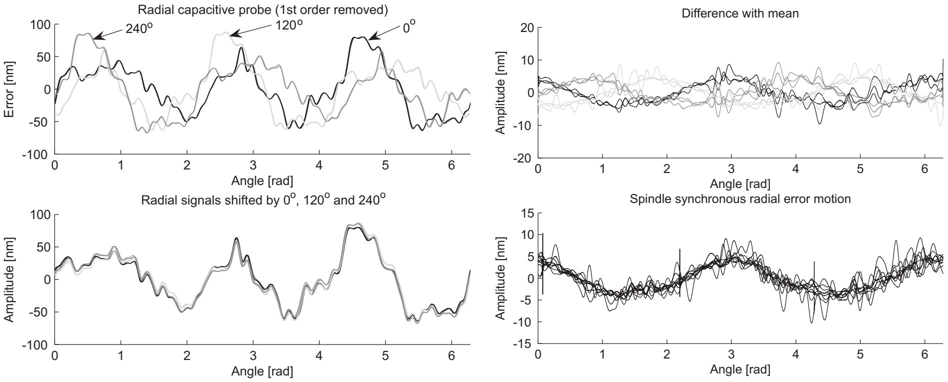

Figure 3.39: Spindle radial synchronous error motion from multi-step method

In the multi-step measurement signals (Figure 3.39, top left), the sphere roundness profile component is shifted by 0°, 120° and 240° while the synchronous error motion component has a fixed orientation. As can be seen, the profiles look very much alike, indicating that the error motion component is small. Figure 3.39 (bottom left) shows the measurements shifted back by 0°, 120° and 240° degrees respectively. Figure 3.39 (top right) shows the difference of these measurements with their collective average. This difference is equal to the synchronous error motion shifted by 0°, 120° and 240°. Again, much similarity can be seen, and shifting these signals back results in the radial synchronous error motion. The 2nd order component in this profile has a PV value of about 12 nm.

The large discrepancy between the NMi calibration and the multi-step method is probably due to the different filtering properties of the contact stylus that was used for the reference sphere calibration and the capacitive probe that was used in the multi-step. It is concluded that the axial and radial error motion results shown in Figure 3.37 and Figure 3.39 are the most reliable. After installation to the base and bolting on the product mounting table, the spindle still shows excellent error motion properties.

3.4 Z-stage

The Z-stages provides 6 degrees of freedom to the Ψ-axis. It should constrain these such that sub-µm uncertainty is achieved at the probe tip. This especially concerns its y, φ, ψ and θ-direction; the r and z-direction are measured by the interferometry system on the Ψ-axis rotor. The Z-stage is aligned with three bearings to a vertical plane, constraining it in y, φ and θ-direction. The other three degrees of freedom are constrained by the R-stage. Two bearings along the side of the main tube constrain the r and ψ-direction, and the z-direction is constrained by the Z-motor or Z-brake.
The Z-stage front and back view are shown in Figure 3.40. The Z-stage consists of a position frame (1), a preload frame (2) and a motor (3), brake (4) and linear scale (5). Further, a weight compensation (6), connected to the R-stage (7), and an emergency brake (not shown) are applied. The main components of the Z-stage will be explained in the coming sections.

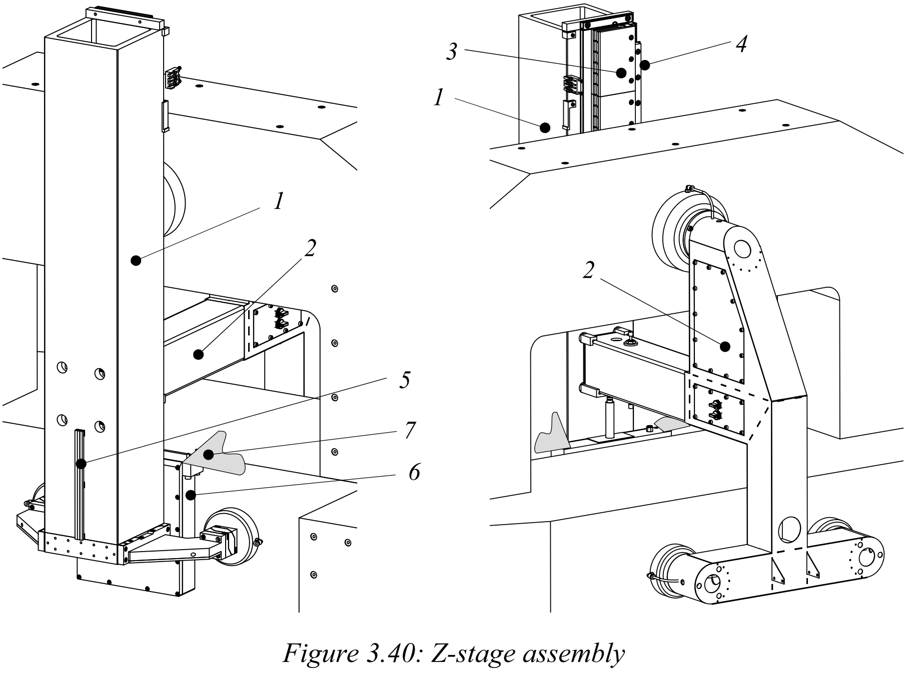

Figure 3.40: Z-stage assembly

3.4.1 Position frame

The basis of the Z-stage position frame is the vertical tube that is straight guided on its sides by two air bearing pairs on the R-stage. Main characteristic for the material selection is a high specific stiffness, to obtain high eigenfrequencies but also because every kilogram has to be weight compensated. Further, a high hardness is desired to enable grinding and lapping of the air bearing faces. As can be seen in Table 4.1, Silicon Carbide is the best material here again, but Alumina is a good second. This is more common and therefore is available in more cross-sections, has a shorter lead time and has a lower cost.

The Al_2O_3 tube (1) has outer dimensions of 150.5 x 155 mm, a wall thickness of 15 mm and a mass of 29 kg. The guidance face (2) and preload face (3) are lapped to a straightness of less than 2 μm. Holes are provided in the front and backside for connecting the preload frame and the top air bearing (Figure 3.41).

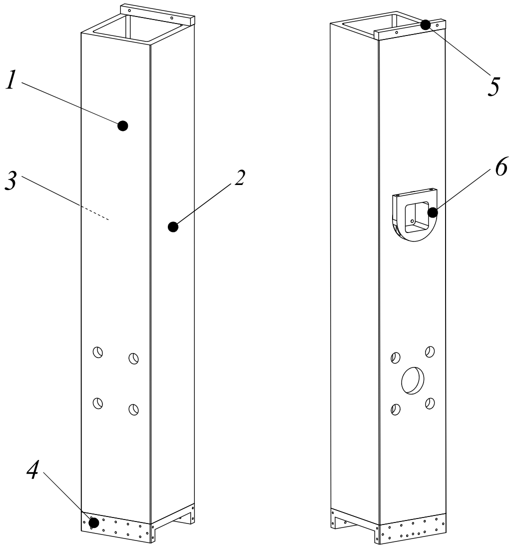

Figure 3.41: Z-stage Alumina tube with bonded interfaces

Three metal interfaces (4-6) are bonded to the ceramic tube. Due to the large difference in thermal expansion coefficient, special alloys such as Vacon^{TM}, Kovar^{TM} or Nilo^{TM} (www11) that also have an α of almost 6 μm/m/K are sometimes used. These metals are hard to obtain and have high cost, and are only required when large temperature differences are expected.

The difference in expansion between steel and Al_2O_3 is 6 μm/m/K, or 0.45 μm/K at the corners of the 150 mm tube. Araldite 2020 adhesive has an E-modulus of $2 \cdot 10^9$ N/m^2, a shear modulus G of ~$6 \cdot 10^8$ N/m^2 and a shear strength of approximately 25 N/mm^2. When the Al_2O_3 and steel parts are supposed to be rigidly expanding (Figure 3.42, left), a temperature change of 2.2 K would break a 0.025 mm thick layer of adhesive. Larger temperature shifts must however be expected, for instance during transport.

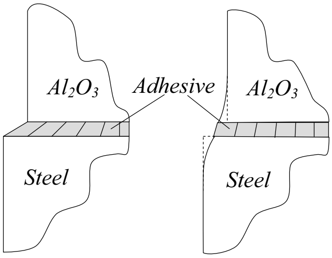

Figure 3.42: Deformation of the adhesive layer under thermal expansion

The steel and Al_2O_3, however, are not rigid (Figure 3.42, right). For the bottom interface, the shear stress of 25 N/mm^2 causes deformations in the steel and Al_2O_3 of about 7 and 5 μm, respectively. Together with the allowable deformation of the adhesive of 1 μm, the total expansion difference can be 13 μm. This occurs at a (homogeneous) temperature shift of 29 K, which is a safe margin.

To mount the ∅150 mm top bearing (1 in Figure 3.43), a steel cup (2) is bonded into the ceramic tube. A ring (3) is bonded on the inside to create a symmetrical connection. The cardanic hinge (4) of the bearing is bolted into this cup. The cup has a conical socket at the backside to connect the force frame (5) via a sphere (6), and the topside of the cup is flattened to mount the Z-stage motor and brake strip (7) as will be further explained in section 3.4.4. This way, the bearing has a stiff connection to the ceramic tube, while the preload force can be applied directly behind the bearing without distorting the position frame.

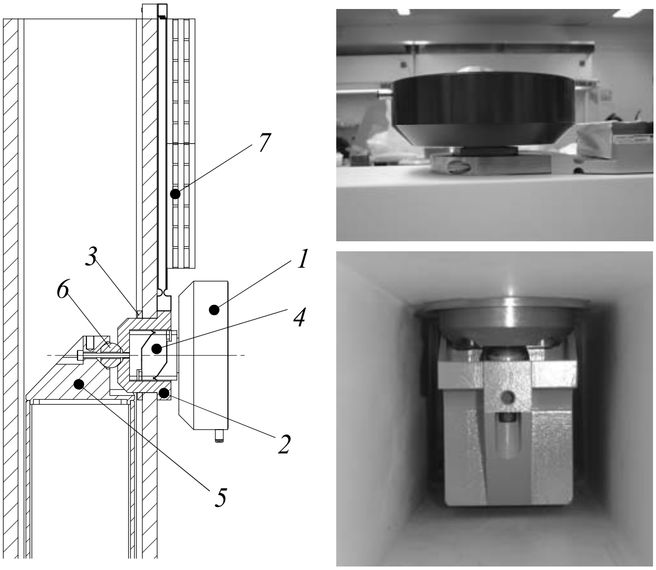

Figure 3.43: Connection of the top bearing

At the steel interface on the bottom of the ceramic tube (1 in Figure 3.44), the two lower ∅100 mm bearings are to be attached, together with the mount for the Ψ-axis and the Z-stage optics assembly. The two bearings and their cardanic hinges are mounted to an aluminium hollow bridge. This bridge consists of 4 parts: a centre part (2), two arms (3, 4) and a bottom cover plate (5). The two arms are bolted to the centre part and form a closed box together with the cover plate. The preload frame (6) will be mounted inside (but separated from) this box, as is further explained in section 3.4.2.

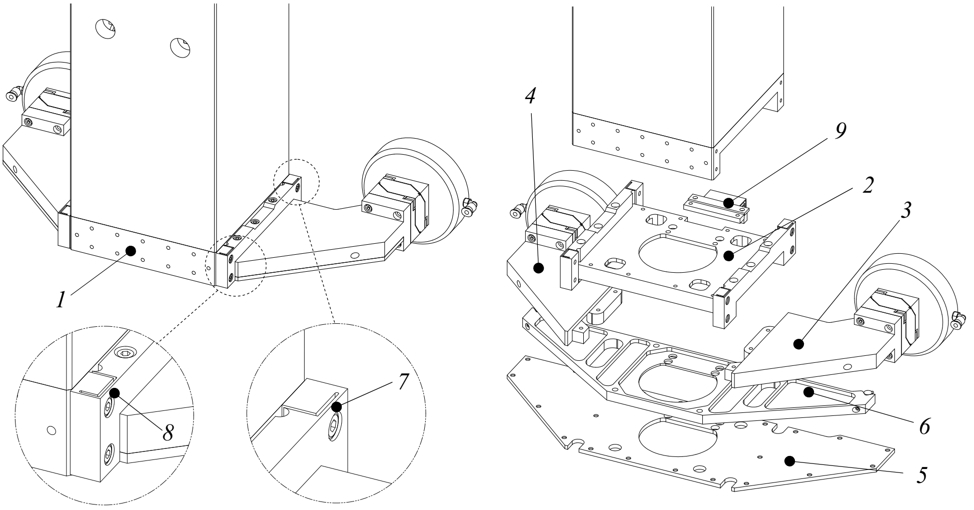

Figure 3.44: Bridge carrying the lower bearings

The *y*-position of the Ψ-axis and thus of the probe tip is determined by the *y*-position of the bottom of the ceramic tube, which gets its *y*-position from the two bearings. To avoid hysteresis between the bridge and the interface, the aluminium centre part of the bridge is attached to the steel interface using two leaf springs (7) and two folded leaf springs (8), manufactured into the centre part by wire EDM. A folded leaf spring (9) constrains the remaining sideways degree of freedom. This way thermal snapping due to the difference in thermal expansion coefficient is avoided, and the route from the ceramic tube to the two bearings in *y*-direction is shortest.

The 2 ∅100 mm bearings are spaced 350 mm apart, and the distance between these bearings and the top ∅150 mm bearing is 595 mm. The ∅100 mm bearings with the cardanic hinges each have a stiffness of $1 \cdot 10^8$ N/m, and the ∅150 mm bearing has a stiffness of $1.6 \cdot 10^8$ N/m. Supposing the Z-stage as rigid, this gives a stiffness $c_{Z,y}$ of $3.6 \cdot 10^8$ N/m, $k_{Z,\varphi}$ of $3.2 \cdot 10^7$ Nm/rad, and $k_{Z,\theta}$ of $6.1 \cdot 10^6$ Nm/rad. The 2 ∅125 mm bearings on the side of the ceramic tube have a stiffness of $1.3 \cdot 10^8$ N/m and are spaced 595 mm apart. This gives a stiffness between the R-stage and Z-stage in *r* and ψ-direction of $c_{Z,r} = 2.6 \cdot 10^8$ N/m and $k_{Z,\psi} = 2.3 \cdot 10^7$ Nm/rad.

The total mass of the Z-stage position frame is 35 kg, including the position determining bearings. These bearings also have to support the preload frame, the Ψ-axis and the probe. The total mass, inertia and resulting rigid body modes of the Z-stage assembly will be explained in section 3.4.6.

The Z-stage preload frame will be mounted directly onto the bearings, as will be explained in the next section. This mainly lowers the rigid-body mode frequencies of the Z-stage, but does not influence the flexural body modes of the position frame. The 1st and 2nd flexural eigenfrequencies of the Z-stage are bending modes of the bridge in phase and counter phase at 367 Hz and 381 Hz (Figure 3.45). The 3rd eigenfrequency is in-plane bending of the bridge at 600 Hz, where the 15 kg of Ψ-axis mass is taken into account.

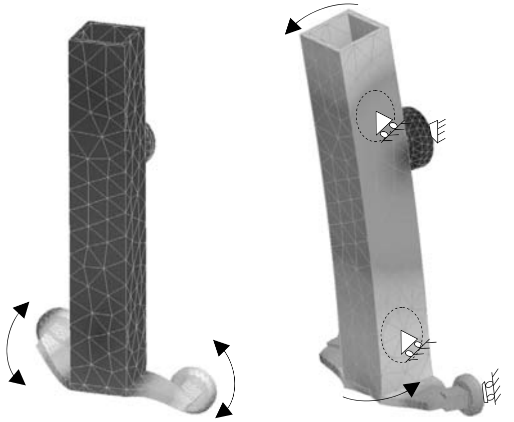

Figure 3.45: Z-stage position frame eigenmodes

Figure 3.46 shows the partially realized Z-stage position frame with the cup and the motor mount on the left. The assembled bridge, with the two ∅100 mm bearings, is shown on the right.

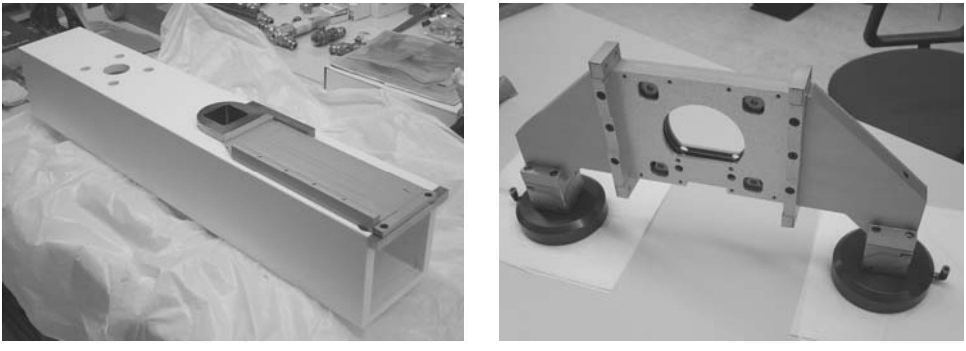

Figure 3.46: Alumina Z-stage tube and lower bearings bridge

3.4.2 Preload frame

The ∅150 mm bearing requires 2000 N and the ∅100 mm bearings require 1000 N. The Z-stage preload frame applies the preload forces while preventing distortion of the Z-stage position frame. The frame consists of a steel tube (1) inside the ceramic tube (2), as shown in Figure 3.47. The central pull tube (3) is bolted to this vertical tube with four spacers (4) extending through holes in the ceramic tube. A box structure (5) at the end of the pull tube carries the preload bearings. The vertical tube is a welded fabrication. The top part (6) contains a conical socket that is aligned with the conical socket in the cup (8), shown in Figure 3.43. A 25 mm hardened steel sphere (9) in between constrains the 3 translations of the preload frame, relative to the position frame. As will be shown later, the motor and brake are also connected to the cup (8), constraining the vertical position of the position and preload frame in a short and direct route.

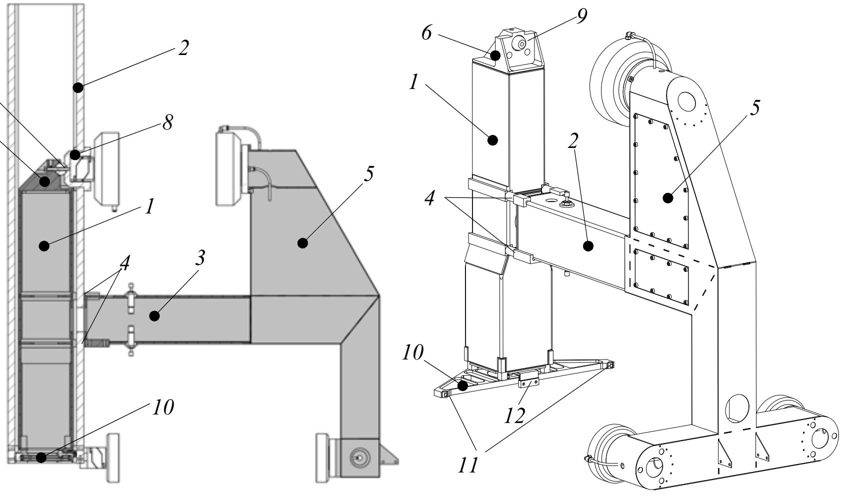

Figure 3.47: Z-stage preload frame

At the bottom, a plate (10) that preloads the bottom bearings via 2 contact cylinders (11) is bolted to the vertical tube. This plate is mounted inside the hollow bridge of Figure 3.44 and constrains the φ and θ-direction of the preload frame. A folded leaf spring (12), attached to the lower interface on the ceramic tube, constrains the remaining ψ-direction.

To mount the Z-stage into the R-stage, the ceramic tube with the vertical preload frame tube are lowered in from the top. Next, the bridge with the preload plate inside, together with the two bearings, is installed. Then, the backside part of the preload frame is assembled from the backside of the machine, and bolted to the vertical preload tube through holes in the front and the backside of the ceramic tube. Besides the sphere, two cylinders and the folded leaf spring that constrain the six degrees of freedom, the preload frame does not contact the position frame.

The wall thickness of the vertical and horizontal tubes is 4 mm and the box thickness is 1 mm. As can also be seen in Figure 3.47, all plates extend into the opposite plate at sharp corners, to increase the torsional stiffness of the box. The box is welded from lasercut sheets using plug welding. The maximum stress is 60 N/mm^2 and the maximum deflection is 0.38 mm, as shown in Figure 3.48.

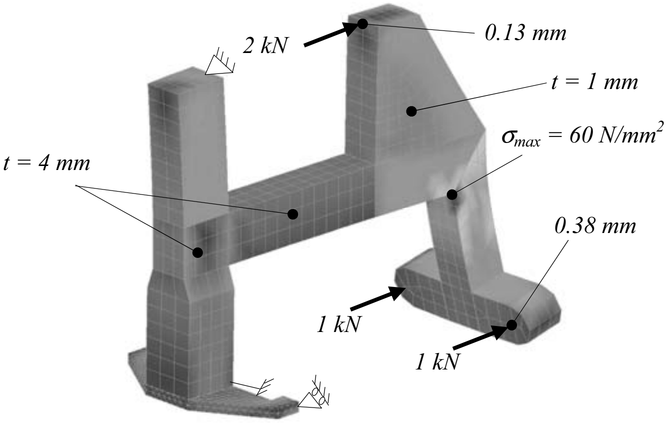

Figure 3.48: Z-stage force frame deformation due to preload forces

The combined mass of the preload bearings and pistons is 4 kg, which has to be constrained by torsion and bending of the vertical and horizontal tube. The relatively large thickness of 4 mm is required to constrain this mass that is far away from the mounting points. The first mode (Figure 3.49) is torsion in the vertical tube, causing the backside to swing from left to right at 84 Hz. The second mode is bending in the pull tube, causing the backside to swing up and down at 105 Hz. The total preload frame mass is 22.6 kg, including the preload bearings and pistons.

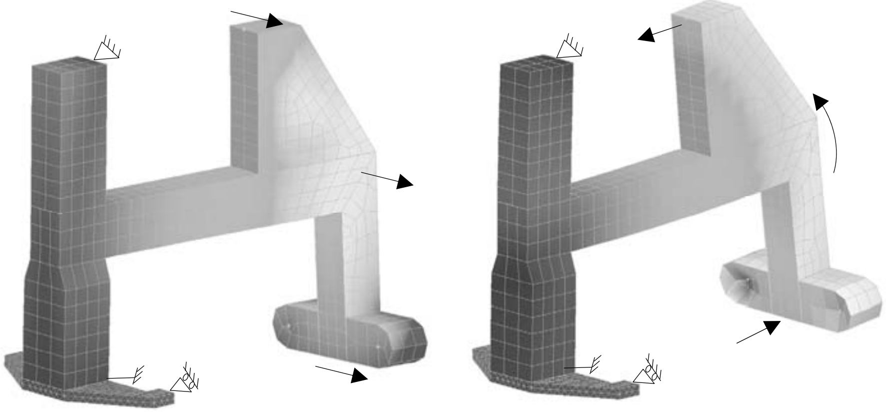

Mode 1 = 84 Hz *Mode 1 = 105 Hz*

Figure 3.49: Z-stage preload frame eigenmodes

Figure 3.50 shows the preload frame and the lower plate with the contact cylinders inside the hollow aluminium bridge (bottom cover plate removed).

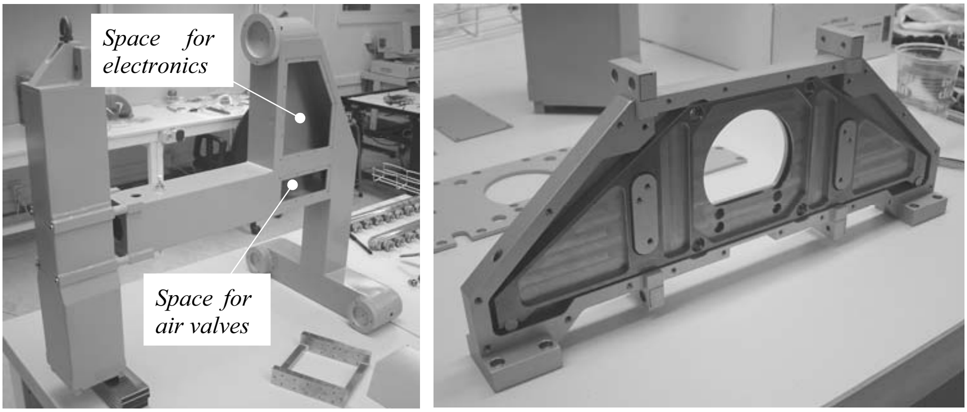

Figure 3.50: Z-stage preload frame

As will be explained in Chapter 5, the probe electronics should be close to the probe to minimize capacity of the cables. They are therefore mounted into the backside box of the Z-stage. From there BNC cables transport the ±10 V signals to the data acquisition system. Inside the horizontal tube of the preload frame, air valves and the solenoid valve for the Ψ-axis brake are mounted. This limits the number of air hoses that have to move along with the Z-stage.

With the two valves, the air of the Ψ-axis and the air to the fixed front bearings of the Z-stage can be closed. The air pressure on the preload bearings and pistons remains, clamping the Z-stage to the vertical base plate. This is useful for testing of the machine since it eliminates the R- and Z-bearings and brakes from the structural loop.

3.4.3 Weight compensation

The total vertically moving mass is about 85 kg. To avoid the motor having to continuously lift this weight and thereby forming a disturbing heat load, the weight is compensated. Also, the brake can be much lighter if no weight is to be held up. Friction must be minimal to avoid virtual play that limits the positioning resolution. Several methods can be applied for generating a constant upward force over a large stroke (Frank et al., 2005).

Most common is balancing with a mass via a pulley, using a wire or strip (Figure 3.51A). This doubles the moving mass and introduces an extra body of which five degrees of freedom have to be constrained relative to the R-stage. The friction introduced by the pulley may be acceptable, but introducing another 85 kg of moving mass to the machine is not preferred.

A Tensator® spring (www18) generates a constant force over a considerable stroke (Figure 3.51B). It is, however, not capable of providing 850 N over 150 mm. The rolling of the windings further also is not frictionless. It is also difficult to adjust to the increasing weight during assembly and to finetune when assembly of the machine is completed.

An air piston (Figure 3.51C) has a much higher force density. A ∅52 mm piston at 4 bar delivers the required force. Sealing the gap between cylinder wall and piston usually introduces unacceptable amounts of friction. Using air bearings for guidance and a narrow gap as a seal eliminates the friction, but has very tight manufacturing tolerances.

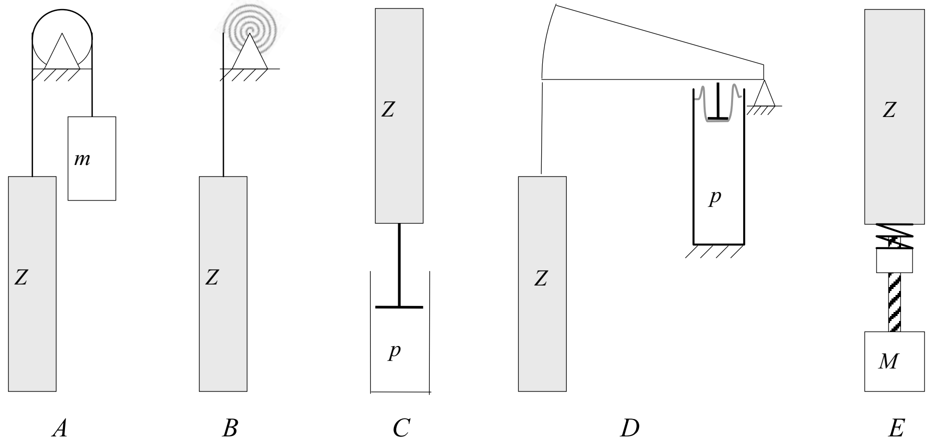

Figure 3.51: Weight compensation concepts

To avoid the air bearing, one may also use a pressurized volume with a rolling membrane and a lever (Figure 3.51D). If the pressurized volume is large enough, the force is almost constant over the range. The stroke of the membrane is generally limited to a few tens of millimeters, requiring a lever ratio in the order of 1:10. The piston area or air pressure thus have to be increased by one order of magnitude to compensate 85 kg over 150 mm this way, which is not practical.

A more mechatronic solution would be to drive a lead screw with a motor (Figure 3.51E). With a spring between the nut and the Z-stage, it can still move frictionless. A control system should maintain a constant force in the spring. Lifting 85 kg over 150 mm requires 125 J to be inserted in for instance 1 second. Quite a powerful motor is thus required, and a new heat source would be introduced into the machine.

An air bearing piston is chosen to be applied. Since a single round bore could not provide enough surface area within the available volume, a rectangular piston (70 x 30 mm) was chosen (Figure 3.52). The piston (1) has 12 porous air bearing plugs (2) similar to those used in the Ψ-axis (see section 3.6.1). The individual air bearing pads (3) are separated by atmospheric grooves (4). The air bearings are fed from the pressurized volume (5) through holes (6) in the bottom of the piston. The normalized air consumption of the air bearing is approximately 0.8 l/min.

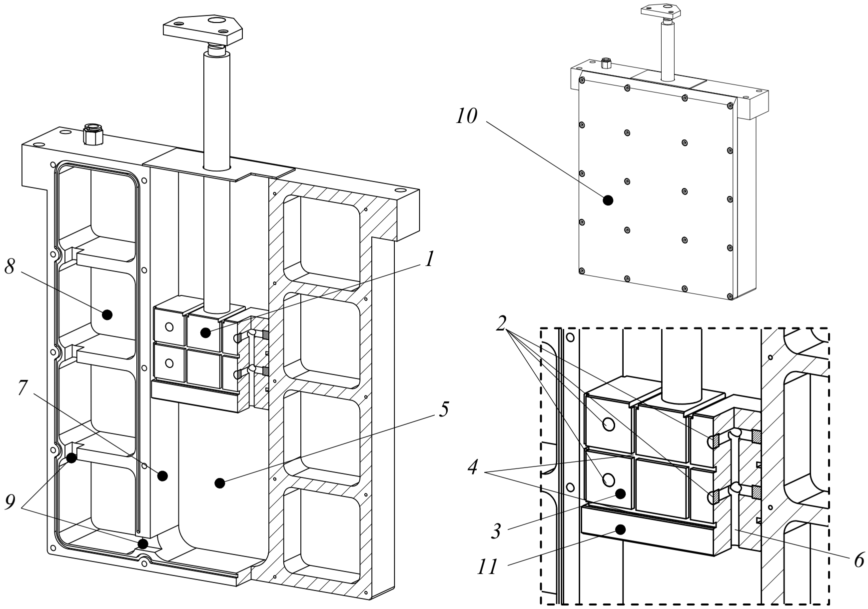

Figure 3.52: Z-stage weight compensation

The entire available volume is used as an air chamber to minimize the relative volume reduction when the piston is moving. This is done by machining the bore (7) and chambers (8), interconnected by holes (9) from a solid block of aluminium and covering it with a lid (10). The piston was then made to fit the bore. A passive precision pressure regulator is used to finetune the pressure to the actual mass of the Z-stage and to (passively) keep this pressure constant. Some hysteresis will be present in this valve. In combination with the tuning error this will give a remaining force that is to be countered by the motor.

The pressure chamber is sealed with a parallel gap resistance (11). The resistance *R* of a parallel gap with width *w*, gap height *h* and length *l*, and dynamic viscosity η is given by:

$$R = \frac{12\eta l}{b h^3} \tag{3.9}$$

The volume flow *Q* through the gap with a differential pressure *ΔP* is:

$$Q = \frac{\Delta P}{R} \tag{3.10}$$

The air bearing gap h is 7 μm. The 10 mm long parallel gap seals the pressure chamber with a circumference of 200 mm. The dynamic viscosity $\eta = 17\cdot10^{-6}$ Pa.s. This results in a resistance R of $3.0\cdot10^{10}$ Pa.s/m^3. With a pressure inside the cylinder of 4 bar, the normalized leakage is equal to 3.2 l/min. The leakage is a function of the 3rd power of the gap height, so small manufacturing tolerances or for instance scratches cause a large increase in the leakage. The total normalized air consumption of the weight compensation is 4 l/min.

The combined centre of gravity of the Z-stage, Ψ-axis, probe and Z-stage optics is located at the backside of the ceramic tube, as shown in Figure 3.53. The weight compensation system is nearly aligned with this centre of gravity. The piston rod is connected to the Z-stage preload frame and the pressure chamber is connected to the R-stage preload frame as shown later in section 3.5.2. Connecting the weight compensation to the preload frames minimizes varying deflection in the position frames due to varying compensation forces.

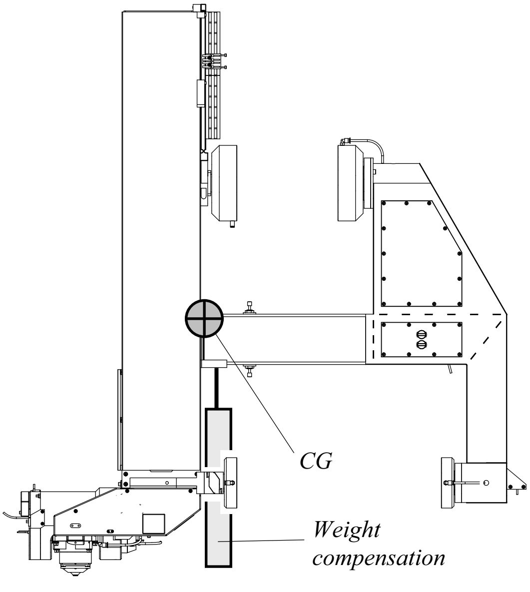

Figure 3.53: Z-stage centre of gravity and weight compensation location

Figure 3.54 shows five measured hysteresis loops after careful alignment, obtained by applying a triangular force as a disturbance to a pure gain controller. The controller stiffness has been subtracted from this graph. The discontinuity in the force in combination with the absence of damping causes the oscillations. Around the centre of the stroke (z = 40 mm), the residual friction is about 1 N and at the ends of the stroke (z = -20 mm and z = 120 mm) this is 4 N and 5.5 N, respectively.

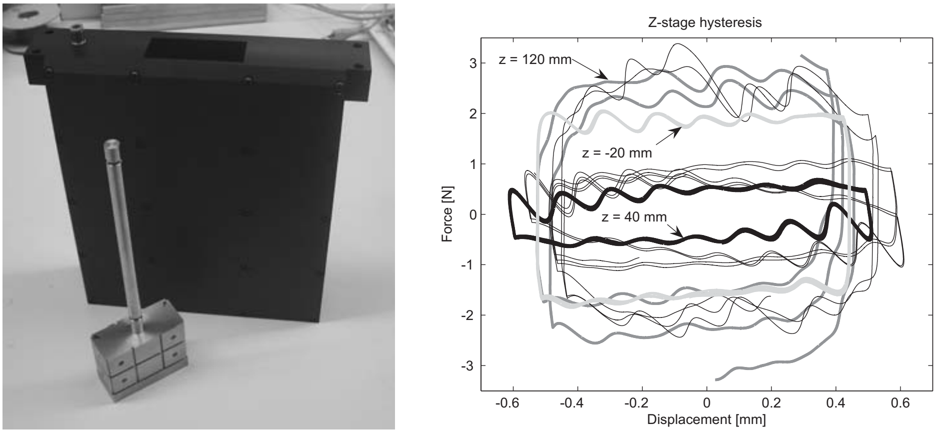

Figure 3.54: Weight compensation of Figure 3.52 and its hysteresis loop

3.4.4 Motor, brake and linear scale

For optimal dynamic behaviour, the motor should be aligned with the centre of gravity. The centre of gravity of the combined Z-stage, Ψ-axis and probe is situated approximately on the back face of the ceramic tube as shown in Figure 3.53. An aluminium plate (1) is hereto bolted to the cup and the interface block on top of the ceramic tube (Figure 3.55). Hinges (2, 3) are machined into the plate to cope with the difference in expansion coefficient. The magnet yokes (4) of the motor are bolted to this plate, and the coils (5) are mounted to the R-stage position frame (6). Placing the motor this high, keeps the heat source away from the metrology loop. Next to the motor magnets, the brake strip (7) is mounted. The motor plate is bolted directly to the interface cup, which provides a stiff coupling between the motor and brake and the Z-stage position and preload frame. The brake clamp (8), as discussed in section 3.1.2, is mounted to the R-stage position frame, next to the motor coils.

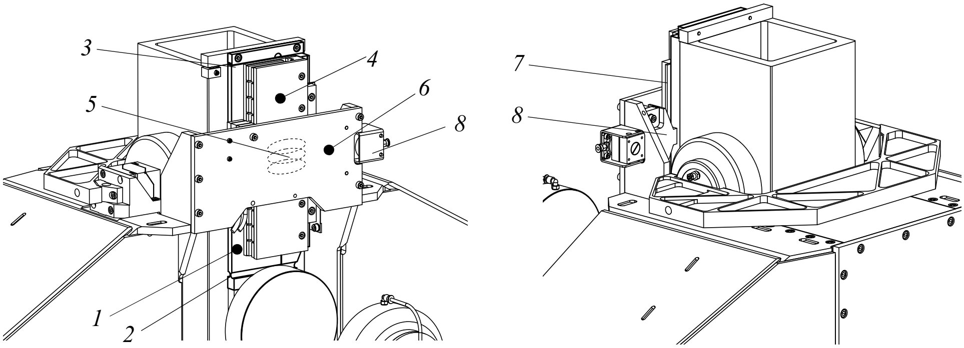

Figure 3.55: Z-stage motor and brake

The remaining friction and tuning error of the weight compensation was measured to vary between 1 and 5.5 N along the stroke. The selected Tecnotion UL3 ironless linear motor has a motor constant of 97 N^2/W, a peak force of 240 N and a continuous force of 35 N. This particular motor has the highest motor constant and thus the least power dissipation to fit the available volume.
When measuring circular tracks, the amount of Z-stage work depends on the height variation of the product. Making a 1 mm step in 1 s with a 3rd order profile requires a peak acceleration of 6.3 mm/s^2, which is equal to a peak force of 0.5 N on 85 kg. When opening the brake, the residual weight compensation error thus determines the required force. Generating 5 N during 1 s requires 0.25 J, and for 250 steps during 15 minutes 62 J. When assuming ideal operation of the amplifier, this is a negligible average heat dissipation of 69 mW.

An optical linear scale is used for position feedback (Figure 3.56). The Heidenhain LIP481R Zerodur scale is bonded to the front of the Al_2O_3 tube via small flexure blocks to allow differences in thermal expansion. The bottom block, which is closest to the probe, has no flexure and determines the vertical position of the scale. The mounting and alignment mechanism of the read head on the R-stage position frame will be discussed in section 3.5.4.

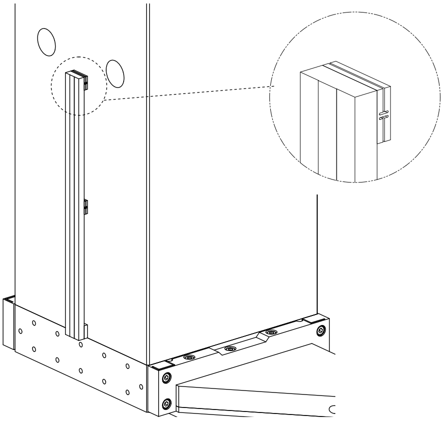

Figure 3.56: Z-stage linear scale

The linear scale is positioned relatively far from the motor, which may cause control instabilities. The loop between motor and linear scale is stiff, consisting of only the motor plate and the Alumina tube. The motor drives the Z-stage through its centre of gravity, so parasitic rotations will be small. This non-collocated setup is preferred to have the Z-position measurement close to the probe.

The brake, motor and scale are shown in Figure 3.57. Two pairs of limit switches are also shown, for detecting the ends of the Z-stage stroke. These will be further discussed in Chapter 6.

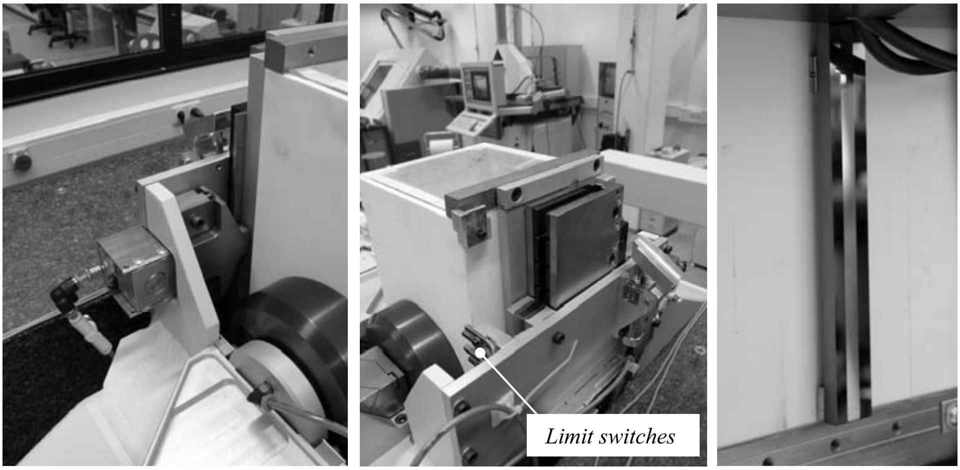

Figure 3.57: Z-stage brake (left), motor (centre) and linear scale (right)

3.4.5 Emergency brake

When air pressure fails, the weight compensation pressure will also drop. Since the brake is not able to hold the 85 kg mass, the Z-stage will plummet down. Shock absorbers are present to dampen this, but when the probe is oriented vertically, it will crash into the table or into a product that is rotating underneath. To prevent this, an emergency brake system is included. A pressure vessel is present, giving a few minutes of spare pressure supply.

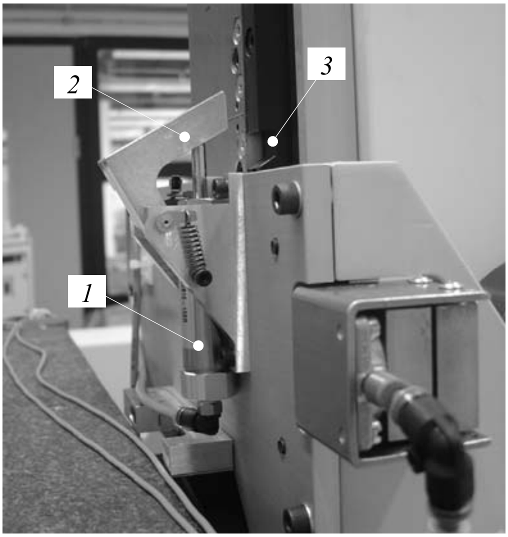

Figure 3.58: Z-stage emergency brake

If an electronic or passive sensor detects an air pressure failure, a series of valves diverts a slightly higher pressure to the weight compensation, which causes the Z-stage to be swiftly lifted. In the mean time, the pressure also drops from the spring preloaded piston (1) shown in Figure 3.58. This causes the lever (2) to lock into the slot (3) in the Z-stage motor mount, locking it at the top position. Tests have shown that this takes less than a second, which is probably fast enough to save the probe. This procedure is executed when the air pressure fails, when the control software stops responding, when the emergency stop is pressed or when electric power fails.

3.4.6 Z-stage assembly

The Z-stage is shown in Figure 3.59 as it is mounted in the R-stage. The ceramic tube with the preload tube inside was lowered into the R-stage from the top, after which the lower bearing bridge was bolted on. Next, the central pull tube and the backside box were bolted on. The alignment of the Z-stage will be discussed in section 3.7, along with the assembly of the rest of the motion system.

Figure 3.59: Z-stage assembly

Table 3.2 summarizes the (theoretical) properties of the Z-stage. The Ψ-axis, probe and Z-stage optics assembly have been taken into account in the mass and inertia calculations. The total mass is 80 kg, and about 5 kg is added for cables and the probe electronics. The vertical stiffness $c_{Z,z}$ is the brake stiffness only, so the stiffness of the Z-stage relative to the R-stage. This is also the case for $c_{Z,y}$ and $k_{Z,\psi}$. The complete structural loop stiffness from probe tip to base will also be explained in section 3.7. Experimental validation will be done in section 3.8.2.

i	$c_{Z,i}$ [N/m]	$m_{Z,i}$ [kg]	$f_{Z,i}$ [Hz]
r	$2.6 \cdot 10^8$	85	278
y	$3.6 \cdot 10^8$		327
z (brake)	$5 \cdot 10^7$		122

i	$k_{Z,i}$ [Nm/rad]	$J_{Z,i}$ [kgm^2]	$f_{Z,i}$ [Hz]
φ	$3.2 \cdot 10^7$	12.1	259
ψ	$2.3 \cdot 10^7$	9.1	253
θ	$6.1 \cdot 10^6$	3.6	207

Table 3.2: Z-stage assembly theoretical rigid body property summary

3.5 R-stage

The R-stage constrains the r, ψ and z degrees of freedom of the Z-stage, so it must provide high stiffness in these directions. Since the r and z-position are measured directly at the Ψ-axis rotor, especially the ψ-direction must be provided with high repeatability. Since the Z-stage is directly aligned to the base in y, φ and θ-direction, errors of the R-stage in these directions do not influence the position of the probe tip. The R-stage, however, also carries the scale read heads and R-stage optics assembly, of which the alignment is critical. The other three degrees of freedom of the R-stage should thus be constrained with high stiffness and repeatability as well.

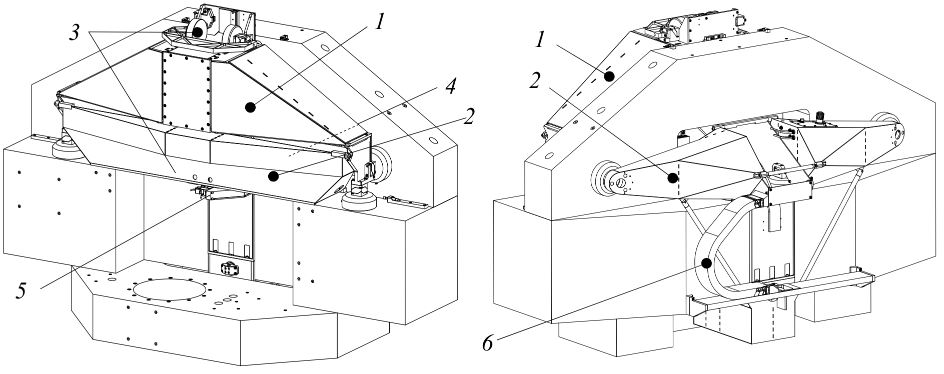

Figure 3.60: R-stage assembly

Figure 3.60 shows the front and back view of the R-stage assembly. In the coming sections the main components will be explained, starting with the position frame (1), the preload frame (2) and the Z-stage r and ψ constraining bearings (3). Next, the R-stage motor and brake (4) and linear scale (5) will be explained, followed by the cable guidance (6).

3.5.1 Position frame

The R-stage position frame (Figure 3.61) has two horizontal bearings (1 and 2) at the front constraining the z and ψ-direction, in the same plane as the ceramic tube axis of the Z-stage. Two plates extend backwards to two horizontal bearings (3 and 4) at the backside that constrain the φ-direction. The position frame has a torsional degree of freedom to prevent overconstraining. It is hereto built from two box structures (5 and 6) on the left and right, which are connected by a U-shaped bridge (7). The plate (8) and strut (9) were added to increase the bending stiffness in the horizontal plane, and also to provide a mounting point for the Z-stage motor and brake. Two horizontal bearings (10 and 11) against the vertical base plane constrain the y and θ-direction to the same plane as to which the Z-stage is aligned.

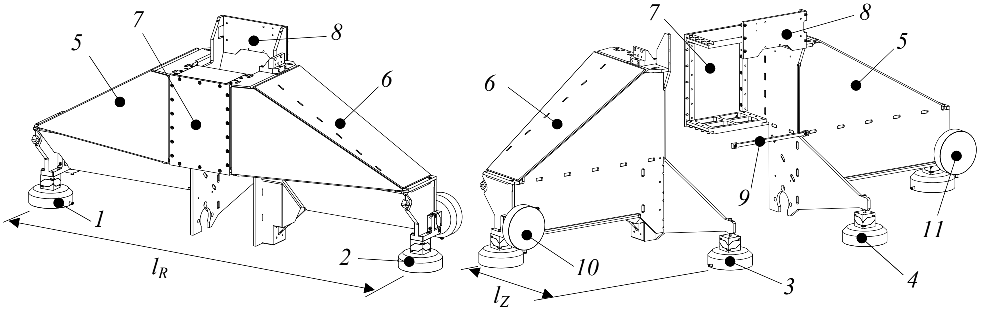

Figure 3.61: R-stage position frame

The ∅150 mm bearings and cardanic hinges have an in series stiffness of $1.6 \cdot 10^8$ N/m. The distance l_R between bearing pairs (1) and (2), and (10) and (11) is 1.4 m. The distance l_Z between these bearing pairs and bearings (3) and (4) is 470 mm. This gives a stiffness in y-direction of $c_{R,y} = 3.2 \cdot 10^8$ N/m, in z-direction of $c_{R,z} = 6.4 \cdot 10^8$ N/m, a tilting stiffness in ψ and θ-direction of $k_{R,\psi} = k_{R,\theta} = 1.6 \cdot 10^8$ Nm/rad and a tilting stiffness in φ-direction of $k_{R,\varphi} = 3.5 \cdot 10^7$ Nm/rad.

The R-stage position frame is constructed from 10 mm thick aluminium plate, mainly for its high thermal conductivity and good machinability. These plates can be connected by bolting, bonding or welding. Bolting requires tight tolerances and many threaded holes in the (inclined) side faces of the plates. The limited contact area between the plates forms a high heat flow resistance, which increases thermal gradients over the structure. Main advantage is, however, that the stage can be disassembled in case of damage or a design change. Bonding requires narrow bond gaps to create high stiffness. This requires high dimensional tolerances, adhesive forms a resistance to heat flux and disassembly is not possible. Welding requires less tight dimensional tolerances since small gaps can be closed with filler material when welding. Welds have high stiffness and good conductivity, but disassembly is not possible. Due to the high conductivity, the structure has to be pre-heated to create good welds. During welding, much heat is further brought in very locally. This may lead to distortions and internal stresses during cooling. Annealing is applied to reduce these, but this may further increase distortion. Machining the interfaces to other parts after welding and annealing solves this problem.

The left and right boxes (Figure 3.62) consist of a vertical back plate (1) to which the vertical plate (2) containing the support to the backside bearing is joined. A horizontal plate (3) is mounted in between these boxes. The inclined top plate (4) and front plate (5) form a triangular box. Another plate (6) is added at 45° on the bottom to form a horizontal triangular tube. A stiffening plate (7) is added inside the top box to stiffen the horizontal plate where the 45° plate is attached. After the box structure has been welded, the interface faces were machined and the end plate (8) was bolted to it to connect the bearings.

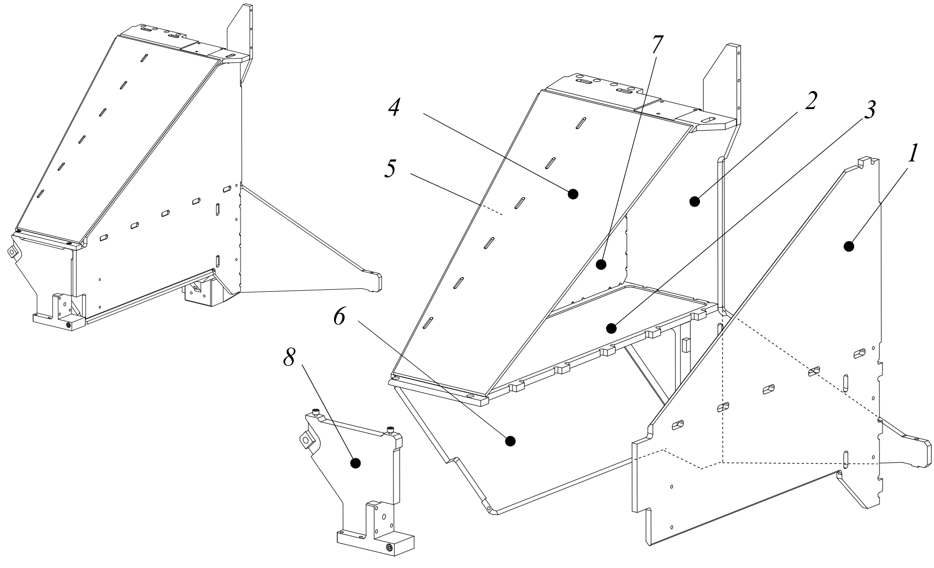

Figure 3.62: R-stage position frame box structure

The outside corners (L-connections) of the box are made by adding a chamfer, such that the weld is at the intersection of the plate centre lines (A in Figure 3.63). At the end plate of the triangular tube, plate 3 and 4 are welded and the end plate is bolted such that the plate mid-planes intersect (B). All T-joints are made by plug welding (C), where the plug is slightly recessed to have the weld at the mid-plane and reduce the weld bulging out of the slot. At the intersection of plate 3, 6 and 7 an alternate combination of joint A and C has been made (D).

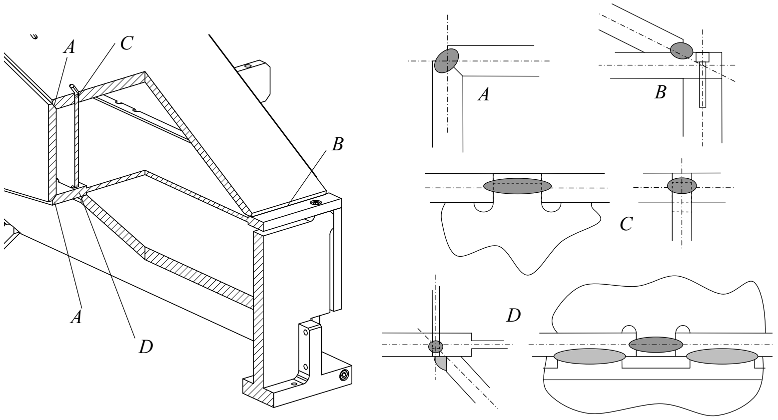

Figure 3.63: R-stage position frame weld connections

The total mass of the R-stage position frame is about 68 kg. Figure 3.64 shows the first and second eigenfrequency, at 139 Hz and 227 Hz respectively. In the first mode, the stage is mainly rotating in φ-direction, which does not influence the Z-stage position since this makes the bearings that guide the Z-stage, slide over the sides of the ceramic tube. The second mode is bending of the stage, which causes a ψ-rotation of the Z-stage since the two bearings that guide it move in r-direction in counter phase. The calculated stiffness in z-direction at the Z-stage brake clamp mounting position is $7.1\cdot10^{7}$ N/m. The tilting stiffness in ψ-direction at the Z-stage bearing points is $1.15\cdot10^{7}$ Nm/rad.

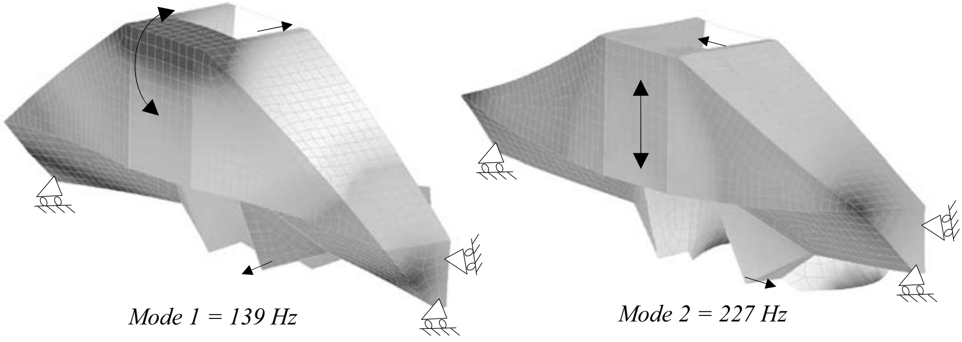
Mode 1 = 139 Hz

Mode 2 = 227 Hz

Figure 3.64: R-stage position frame eigenmodes

The structure is designed such that it can be completely assembled jig less before being welded, to minimize distortions. Figure 3.65 shows the assembly and welding of an R-stage position frame box structure. The assembled position frame is shown before painting.

Figure 3.65: R-stage position frame welding

3.5.2 Preload frame

Each ∅150 mm bearing must be preloaded with 2 kN, with minimal distortion of the R-stage position frame. The combined mass of all stages, which is about 275 kg, partially preloads the horizontal bearings (1-4) as shown in Figure 3.66. In this figure, the end plates (5 and 6) of the R-stage position frame are also shown. The centre of mass is located in the front half of the stage, resulting in a higher preload of the two front bearings (1 and 2). The four horizontal bearings (1 – 4) combined require 8 kN, of which 2750 N is provided by the stage mass, and the remaining 5250 N should be provided by the horizontal preload bearings. This is done by two ∅150 mm bearings (7), each with a piston that generates 2625 N, at the cost of a slightly smaller air gap.

The two bearings with the highest load capacity as measured in Figure 3.2 are used here. These bearings are positioned such that the resulting force vector of the mass and the preload bearings results in 2 kN at each position determining horizontal bearing.

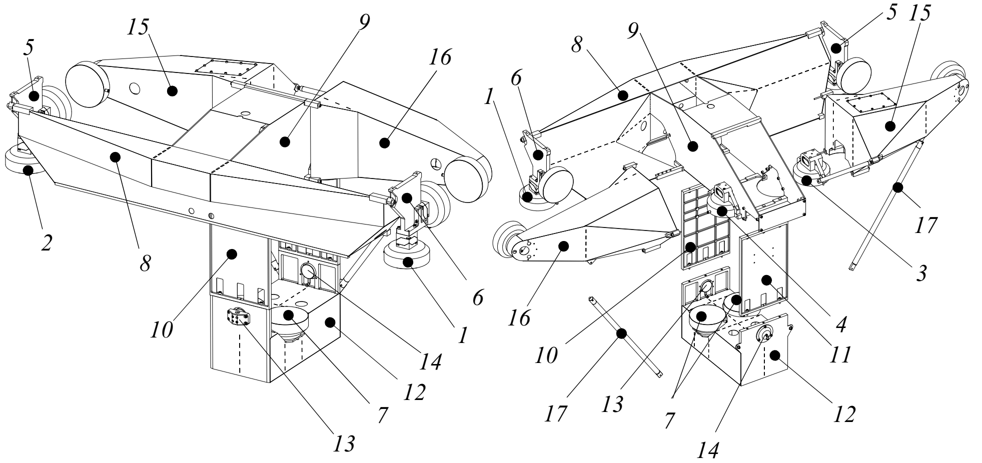

Figure 3.66: R-stage preload frame assembly

The preload frame has to connect these bearings to the R-stage position frame and deliver the forces directly onto the bearings to minimize distortion. It hereto consists of a horizontal front beam (8), which is connected to the endplates of the position frame with two shoulder bolts. A flexure at these two points constrains the y, z, ψ and θ-degrees of freedom. From this beam, a tube (9) extends backwards through the gap in the base, which has its side faces aligned with the two fixed bearings (3 and 4) at the backside. This constrains the φ-degree of freedom. The r-direction will be constrained by the motor and brake, as shown in section 3.5.4. Several cut-outs have been made to allow space for the Z-stage and its bearings, and to introduce a torsional degree of freedom just as with the position frame.

From the central tube (9), two plates (10 and 11) extend downwards to a box structure (12) that carries the two preload bearings (7) and pistons. The front plate runs through the slit between the bottom and middle base block. To prevent parallelogram motion, two ∅50 mm bearings (13 and 14) are added, the front one fixed, the backside one with a piston.

From the central tube, two arms (15 and 16) extend to the left and right, carrying the horizontal preload bearings and pistons. Two support struts (17) provide stiffness in vertical direction to the arms.

The preload frame is mainly constructed of 1 mm thick steel sheets. Only the vertical sides of the central tube are 4 mm thick. Steel is chosen here because of the high load the frame has to withstand, and for the better weldability of thin sheets compared to

Aluminium. The total mass of this frame is 55 kg. Figure 3.67 shows the 1st and 2nd eigenfrequency at 68 Hz and 73 Hz respectively. In practice, the pistons will provide some stiffness and damping, increasing the eigenfrequencies. The preload forces cause a maximum deflection of 0.56 mm at the ends of the arms on the backside, and a stress of 240 N/mm^2.

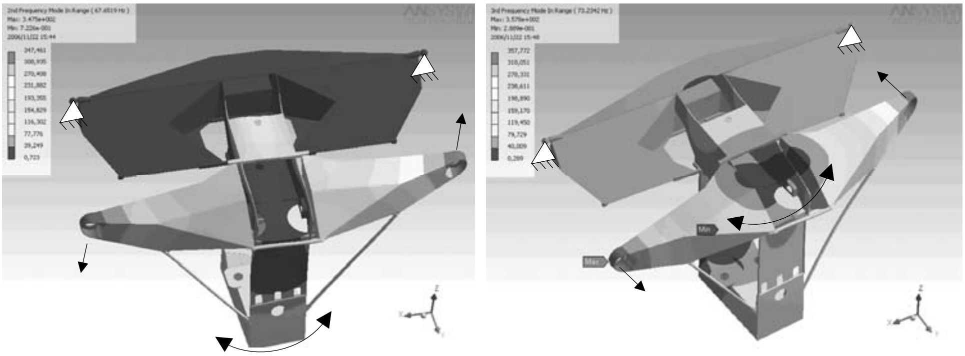

Mode 1 = 68 Hz *Mode 2 = 73 Hz*

Figure 3.67: R-stage preload frame eigenmodes

The preload frame is constructed of 1 and 4 mm thick lasercut steel sheets. T-joints are made using plug welding, and L-joints are simply welded together. Figure 3.68 shows the bottom box assembled just before welding and the completed preload frame before paint.

Figure 3.68: R-stage preload frame realization

3.5.3 Z-stage tube bearings

The fixed ∅125 mm bearings that guide the Z-stage tube are attached to the right half of the R-stage position frame (Figure 3.69). A stiff arm (1) hereto extends from the R-stage position frame towards the lower position determining bearing (2). A bracket (3) is used to bolt the upper position determining bearing (4) to.
These bearings require a preload of 1500 N. The opposing preload bearing and piston are hereto mounted to a plate (5) that is bolted to the R-stage position frame, constraining only the in-plane degrees of freedom. At the upper bearings, the force loop is closed with a C-yoke (6). The lower bearings are bonded to two cups (7 and 8) which are connected with two pull rods (9) due to space constraints. In both cases the force loop is separated from the position frame this way.

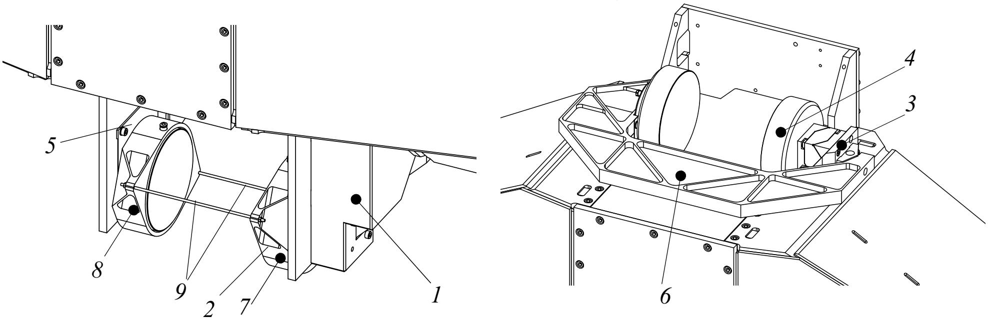

Figure 3.69: Z-stage tube bearings

The lower Z-stage tube bearing assembly is hidden behind the R-stage preload frame. The visible preload bearing cup is shown in Figure 3.70 (left). The upper Z-stage tube bearing assembly with the C-yoke is shown in Figure 3.70 (right).

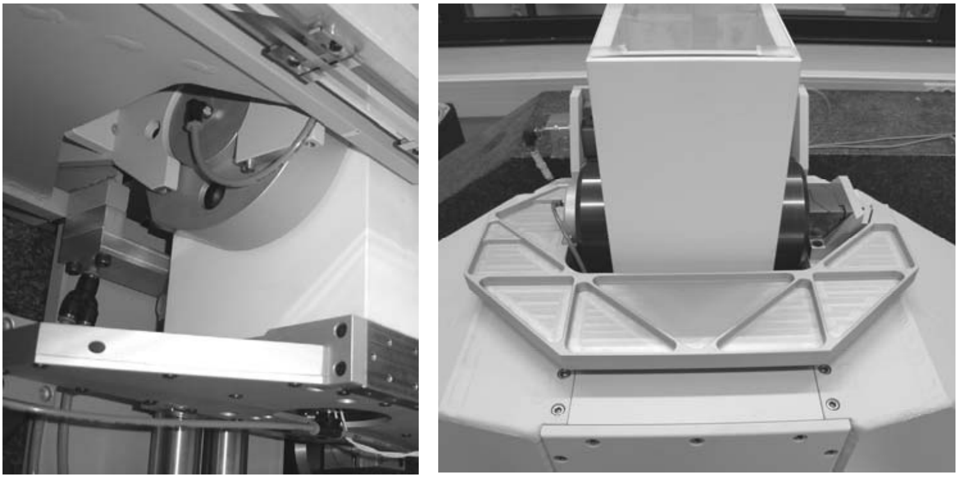

Figure 3.70: Z stage lower (left) and upper (right) tube bearings

3.5.4 Motor, brake and linear scale

The location of the centre of gravity of the stages, with the Z-stage in its middle position, is shown in Figure 3.71. The R-stage motor and brake are aligned with this point. Just as with the Z-stage, an aluminium plate (1) is bolted to the backside of the position frame. The magnet yoke (2) and the brake strip (3) are mounted to this plate. A folded leaf spring (4) constrains the *r* degree of freedom of the R-stage preload frame (5) to create a short route from motor and brake to this frame. The motor coils (6) and brake clamp (7) are mounted to a plate (8) that is bolted onto inserts in the top base block.

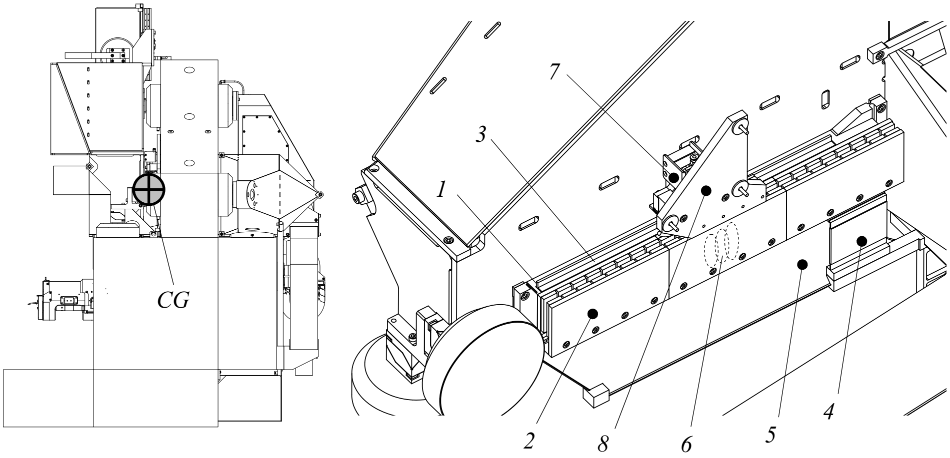

Figure 3.71: Stage assembly centre of gravity and R-stage motor and brake assembly

As explained in section 3.2.2, a maximum base tilt of 4.8 mrad is expected when the R-stage moves from left to right, requiring a counterforce from the R-stage motor of 13 N. Similar to the Z-stage, the R-stage makes 1 mm steps in 1 s between measurements. This requires a peak acceleration of 6 mm/s^2, or 1.6 N. During these small steps, base tilt is negligible so only acceleration and deceleration forces are required from the motor. The mean force during this 3rd order profile is 1.4 N, requiring 0.02 J for a single step. For 250 steps in 15 minutes, this is equal to 5 J. Assuming ideal operation of the amplifier, the mean power dissipation is only 6 mW.

As with the Z-stage, a Heidenhain LIP481R linear scale is applied for feedback (Figure 3.72). This scale (1) is mounted onto the metrology frame (not shown) using flexure blocks similar to those used for the Z-stage. The R- and Z-stage read heads (2 and 3) are mounted to an aluminium arm (4) that extends from the R-stage position frame (5) via two alignment mechanisms (6 and 7). These monolithic mechanisms consist of a plate spring (8) that constrains three degrees of freedom, and three spring preloaded adjustment screws (9) to adjust tip, tilt and focus. Rotating the read head in its mounting hole provides the fourth degree of freedom required for proper alignment.

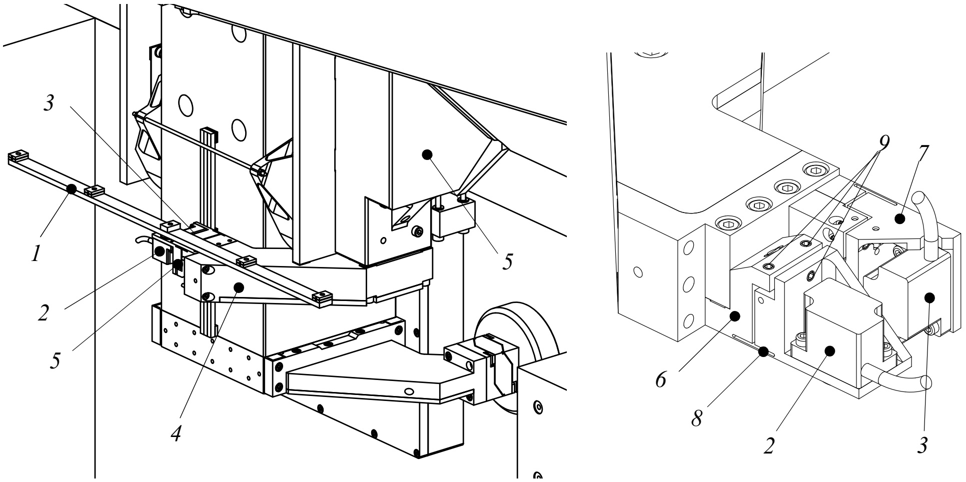

Figure 3.72: R-stage linear scale and read head alignment mechanisms (upside down)

Figure 3.73 shows the motor and brake as assembled on the machine. It also shows the R and Z scales with their read heads and alignment mechanisms. The R-stage optics assembly can also be seen in this figure, which is attached to the read-head arm on one side.

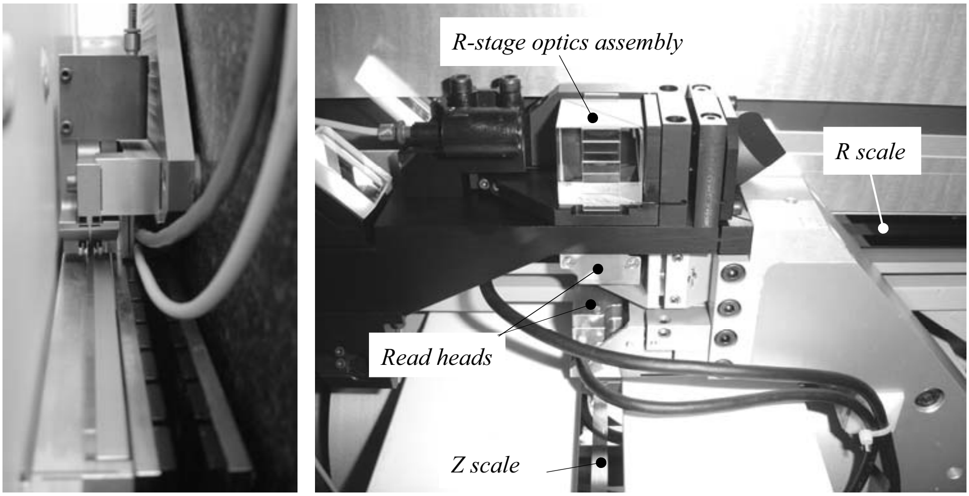

Figure 3.73: R-stage motor and brake, and linear scale read head assembly

3.5.5 Cable guidance

Measuring many parameters inside the machine has many cables, fibres and connectors as a consequence. The cables and air supply hoses mostly run inside the machine. 3 cables come from the probe and 5 from the Ψ-axis. They run through the Z-stage preload frame, together with the air supply hoses for the Z-stage and Ψ-axis bearings. The 2 probe signal cables are connected to the probe electronics in the backside of the Z-stage, and changed into 7 BNC cables and 2 power supply cables for the electronics. All 17 cables then come out at the bottom of the Z-stage preload frame and are guided through a cable chain onto the R-stage. From here, they are joined by about 10 more cables and air hoses from the R-stage and go into the R-stage cable chain to be transferred to a bar on the base. From here, the cables go to the electronics cabinet, together with the about 20 cables from the spindle, the lower metrology frame and the R-stage motor. This makes a total of 47 cables coming off the machine.

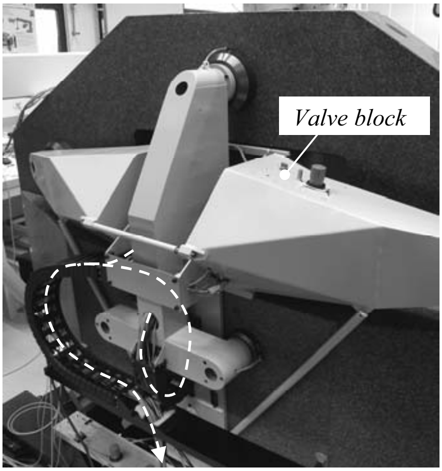

Figure 3.74: Cable chain assembly

The applied cable chains have rubber flexures instead of links, which reduces friction. In practice, the friction was found to be small enough to not influence the positioning resolution. The chains are connected to the preload frames. The R-stage cable chain has a minimum in its gravitational energy content when most of it is resting on the horizontal bar. This causes a small disturbing force on the R-stage. Mounting the cable chain horizontally would have kept the gravitational energy constant, but this was difficult due to space constraints.

Air hoses are thick and quite rigid. To minimise their disturbing forces, a single air line passes from the base to the R-stage and is split in a valve block (Figure 3.74) inside a backside arm of the preload frame. With this valve block, the R-stage bearings can be turned off to land the stage, the Z-brake can be operated manually and the air pressure of the weight compensation can be adjusted. One air hose passes from the R-stage to the Z-stage and is split there as explained earlier. The Z-stage also has a valve block from which the air to the Ψ-axis and to the Z-stage front bearings can be closed for testing.

3.5.6 R-stage assembly

Figure 3.75 shows the R-stage with the Z-stage already installed. The backside was already shown in Figure 3.74. The position frame was mounted on the base first, after which the central T-section of the preload frame was installed from the front. Next the backside arms and other preload components and bearings were installed. A beam was used for mounting the R-scale temporarily, to allow for testing.

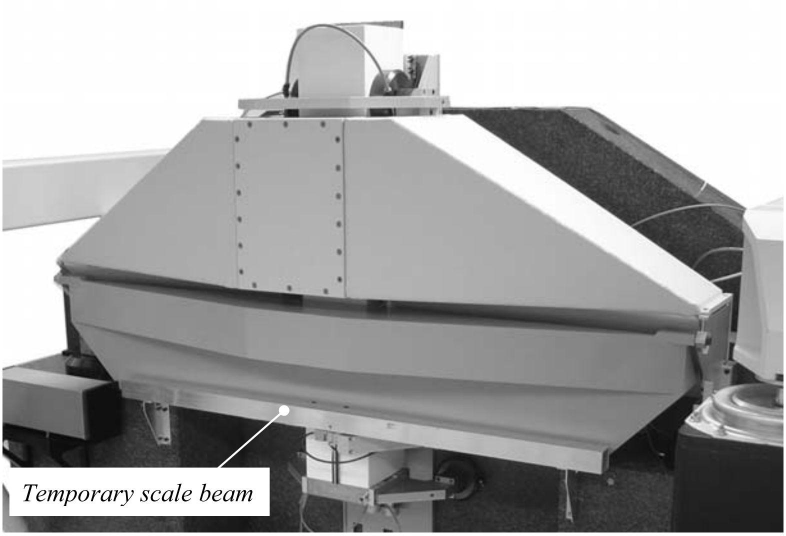

Figure 3.75: R-stage assembly

Table 3.3 summarizes the (theoretical) properties of the R-stage. The total mass of the R-stage is 174 kg. Since the Z-stage has its own bearings in y-direction, the mass to be calculated with in this direction is 174 kg. In the other directions, the combined R and Z-stage and Ψ-axis mass of 275 kg is used. For rotations, the Z-stage has its own bearings in φ and θ-direction, thus only the R-stage inertia is used here. In ψ-direction the R and Z-stage inertia are summed. Experimental validation will be done in section 3.8.2.

i	$c_{R,i}$ [N/m]	$m_{R,i}$ [kg]	$f_{R,i}$ [Hz]
r (brake)	$5\cdot10^7$	275	68
y	$3.2\cdot10^8$	174	216
z	$6.4\cdot10^8$	275	243

i	$k_{R,i}$ [Nm/rad]	$J_{R,i}$ [kgm^2]	$f_{R,i}$ [Hz]
φ	$3.5\cdot10^7$	21.3	204
ψ	$1.6\cdot10^8$	50.7	283
θ	$1.6\cdot10^8$	35.3	339

Table 3.3: R-stage assembly theoretical rigid body property summary

3.6 Ψ-axis[1]

The Ψ-axis orients the probe perpendicular to the best-fit asphere. Part of the rotor is a cylindrical mirror on which the R- and Z-interferometer measure its radial rotor displacement relative to the metrology frame. An angle encoder measures the ψ-rotation of the rotor. Axial and tilt error motion cause a second order error, and are not measured in the metrology loop. Since sub-micrometer accuracy is desired for the axial and tilt error motion, a rotary air bearing has been designed. For measuring convex to concave optics, a range of motion from +45° to -45° is sufficient. To also enable the measurement of cylinders and to calibrate the vertical reference mirror, the range is increased to +90°. A nulling mirror has been added to home the probe, for which the range has been further increased to +120°. This brings the total range to +120° to -45°.

The Ψ-axis design consists of a housing (1) in which the bearing rings and rotor (2) are mounted, as shown in Figure 3.76. The rotor has a chamber (3) in which the probe is mounted. It further has a brushless DC motor (4), an encoder (5) and a brake (6). In the bearing housing, the cylinder lenses (7) are mounted for focussing the R and Z-interferometer beams onto the cylindrical mirror (8) centre line. A nulling target (9) is present for nulling the probe. The Ψ-axis is mounted on a thermally compensated mount (10). The Z-stage optics assembly is also attached to this mount. Each of these components will be further explained in the coming sections.

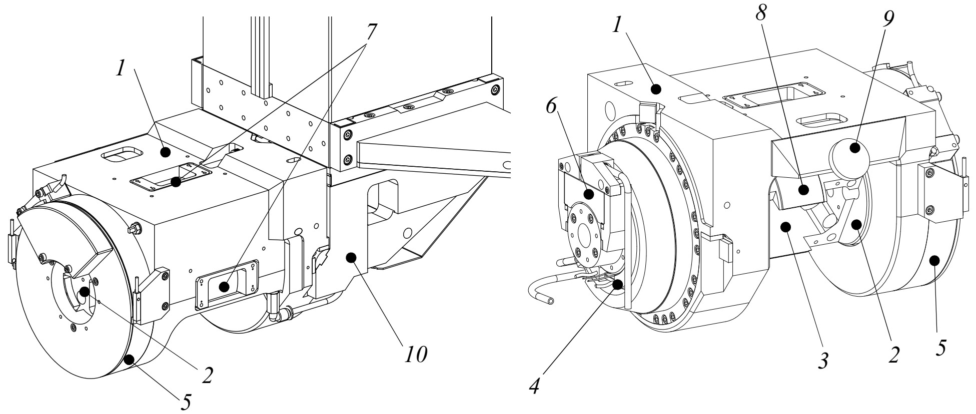

Figure 3.76: Ψ-axis assembly

---

[1] *The Ψ-axis design is largely based on the MSc thesis of C.A.L. Aerts (Aerts, 2007)*

3.6.1 Air bearing

The main dynamic force acting on the rotor is the reaction force of the acceleration of the probe objective. A single sided bearing (Figure 3.77, left) is preferred for the large stroke, but dynamic simulations (section 3.1.4) show that this would result in large tilts of the rotor, with large out-of-plane errors at the probe tip as a consequence. A symmetrical radial bearing layout converts these forces into radial error motion, which is measured by the metrology loop. The large range of ψ-motion of -45° – +120° requires a substantial part of the connecting housing between the two radial bearings to be open. The housing outer diameter is limited for measuring deeply concave optics (dotted line in Figure 3.77), which thus also limits the thrust bearing dimension and location.

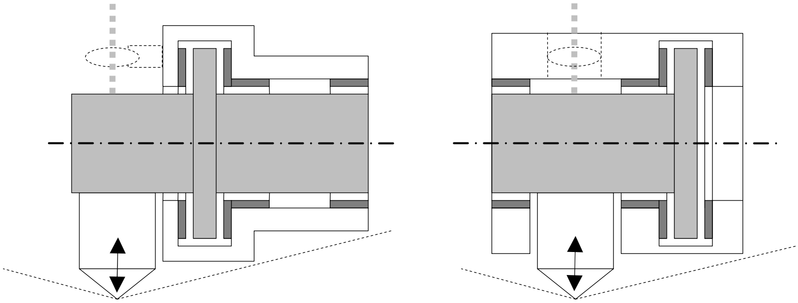

Figure 3.77: Ψ-axis bearing configurations

Porous plug air bearings

For a radial bearing to have stiffness, it must be composed of at least three individual bearing segments. This is generally done by supplying pressure to restrictions around the bearing. These restrictions can be small holes, in the order of tenths of millimeters (Figure 3.78A), in orifice or inherent compensated form (Holster, 1967; Van Beek, 2006). A chamber is sometimes added for extra load capacity and stiffness, but with the risk of pneumatic hammering. Small hole restrictions tend to get easily clogged with dirt particles. A porous graphite ring (Figure 3.78B) essentially has an infinite amount of restrictions. Machining this ring to the roundness tolerances required is very difficult, since graphite is a difficult material to work with. An intermediate solution is to use porous plugs as restrictions (Figure 3.78C). These may have the same flow resistance as the small holes, but have a much larger surface area which makes them much less vulnerable to dirt. The carrier ring in which they are mounted can be machined to the required roundness.

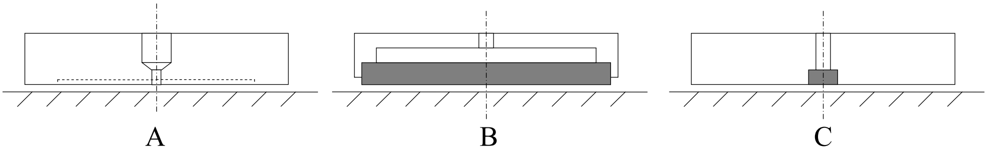

Figure 3.78: Air bearings with hole (A), porous (B) and porous plug (C) restrictions

A porous plug bearing unit can be characterized as shown in Figure 3.79, with the supply pressure P_S, the pressure after the restriction P_R, and the atmospheric pressure P_a. The porous plug has radius r_1 and thickness s, and the bearing surface has radius r_0. The bearing gap has height h.

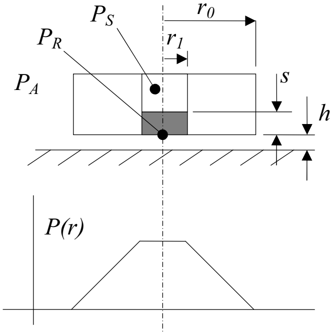

Figure 3.79: Porous plug bearing and pressure distribution

The mass flow $\dot{M}_{plug}$ through the porous plug can be calculated with the permeability k_p, the surface area A_p, the viscosity η, the gas constant R and temperature T (Van Beek, 2006):

$$\dot{M}_{plug} = \frac{k_p A_p}{2s} \frac{P_S^2 - P_R^2}{\eta RT} \tag{3.11}$$

The mass flow $\dot{M}_{gap}$ through the air gap can be calculated with:

$$\dot{M}_{gap} = \frac{\pi h^3}{12 \ln(\frac{r_0}{r_1})} \frac{P_R^2 - P_a^2}{\eta RT} \tag{3.12}$$

Equalling the two mass flows results in:

$$\frac{P_S^2 - P_R^2}{P_R^2 - P_a^2} = \frac{\pi h^3}{12 \ln(\frac{r_0}{r_1})} \frac{2s}{k_p A_p} = gh^3 \tag{3.13}$$

Where the geometry factor *g* is:

$$g = \frac{\pi}{6 \ln(\frac{r_0}{r_1})} \frac{s}{k_p A_p} \tag{3.14}$$

This results in the pressure after the restriction P_R and the exact solution for the pressure distribution *P(r)*:

$$P_R = \sqrt{\frac{P_S^2 + gh^3 P_a^2}{1 + gh^3}} \quad and \quad \left(\frac{P(r)}{P_a}\right)^2 = \left(\frac{P_R}{P_a}\right)^2 - \frac{\ln(r/r_1)}{\ln(r_0/r_1)}\left(\left(\frac{P_R}{P_a}\right)^2 - 1\right) \tag{3.15}$$

The pressure distribution may also be approximated by a cone:

$$\begin{aligned} &P(r) = P_R \quad for \quad r \le r_1 \\ &and \\ &P(r) = P_R - \frac{P_R - P_a}{(r_0 - r_1)}(r - r_1) \quad for \quad r_1 \le r \le r_0 \end{aligned} \tag{3.16}$$

Integrating the pressure over the area gives the load capacity F_{unit} of a single bearing unit:

$$\begin{aligned} &F_{unit} = \frac{1}{3}\pi\left(P_R - P_a\right)\left(r_0^2 - r_1^2 + r_0 r_1\right) \\ &and \\ &F_{unit} = \frac{1}{3}\pi\left(P_R - P_a\right)r_0^2 \quad when \quad r_1 \ll r_0 \end{aligned} \tag{3.17}$$

The stiffness c_{unit} of a single bearing unit can now be calculated with

$$c_{unit} = -\frac{dF_{unit}}{dh} \tag{3.18}$$

The permeability of the batch of carbon to be used was experimentally determined to be $5.5 \cdot 10^{-15}$ m^2 (Aerts, 2007). For a bearing unit radius of 10 mm, a plug diameter of 5 mm and a thickness 3 mm, the load capacity, stiffness and airflow are shown in Figure 3.80. Here, r_1 is not supposed to be much smaller than r_0.

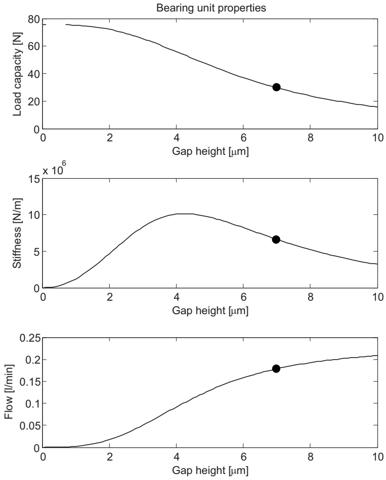

Figure 3.80: Bearing unit load capacity, stiffness and flow rate
(r_0 = 10 mm; r_1 = 2.5 mm; s = 3 mm)

An air gap of 7 µm is considered a good compromise between manufacturability, robustness to contamination and bearing properties. Figure 3.81 and Figure 3.82 show the influence of the porous plug dimensions on load capacity, stiffness and airflow for this gap height. A plug diameter of 5 mm and a thickness of 3 mm was selected for the Ψ-axis bearings, giving a load capacity of 29.6 N, a stiffness of $6.5 \cdot 10^6$ N/m and a normalized air consumption of 0.18 l/min per bearing unit.

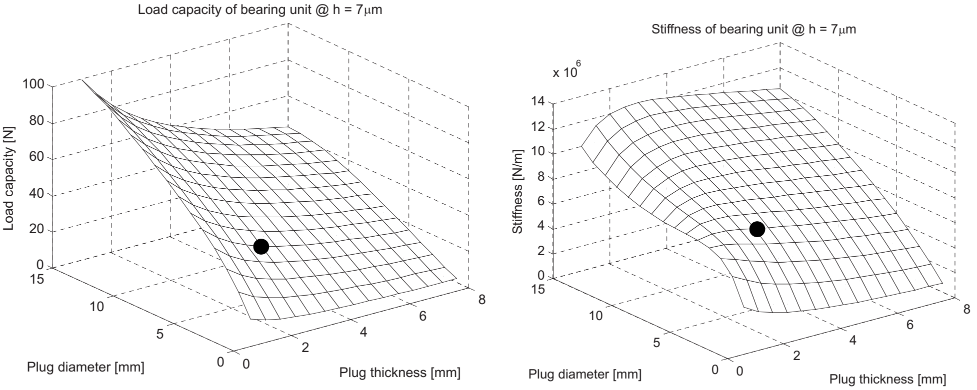

Figure 3.81: Load capacity and stiffness as a function of the plug dimensions at 7 µm gap height

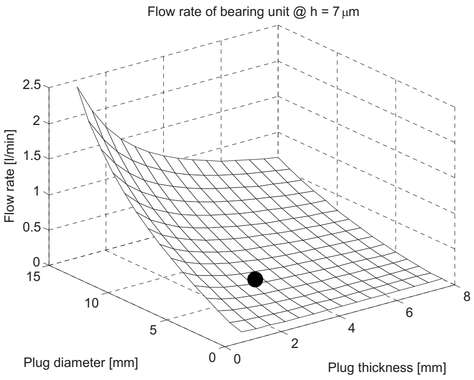

Figure 3.82: Flow rate as function of plug dimensions at 7 μm gap height

Axial bearing properties

The designed radial and thrust bearings consist of 18 bearing units. For the axial bearings this has 18 times the properties of an individual unit, or $c_{ax} = 1.2 \cdot 10^8$ N/m, $F_{ax} = 533$ N and $Q_{ax} = 3.2$ l/min (normalized). Since the thrust bearing will be form closed, stiffness is doubled to $c_{\Psi,ax} = 2.4 \cdot 10^8$ N/m.

To verify the bearing properties, an axial bearing was made as shown in Figure 3.83, left. The flow rate of each plug was verified first after gluing in, as shown in the photo. The bearing stiffness was tested using the same setup as used for the porous air bearing (Figure 3.1). The measured and theoretical results are shown in Figure 3.83, right. The parameters were somewhat different from the final design, so this graph is not equal to the final Ψ-axis thrust bearing stiffness. The theoretical curve agrees quite well with the experimental values.

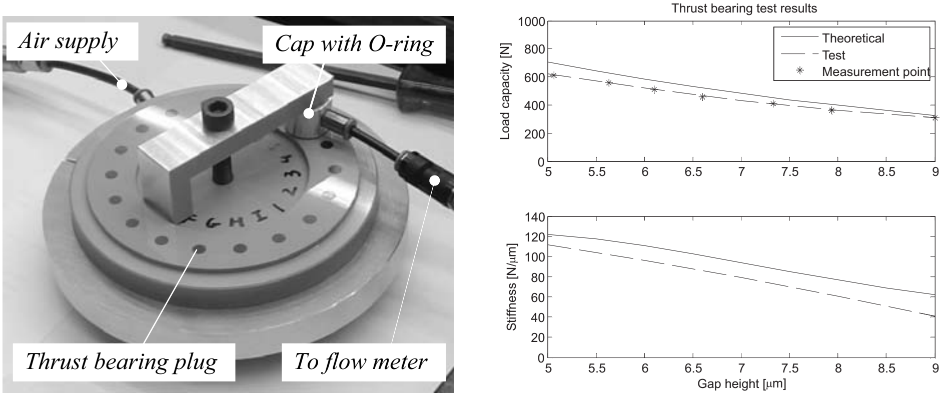

Figure 3.83: Test thrust bearing and test results

Radial bearing properties

For a radial bearing with relative eccentricity e, the bearing gap around the circumference is calculated with:

$$h(\psi) = h_0\left(1 - e\cos(\psi)\right) \tag{3.19}$$

With this gap height, the properties of each bearing unit along the circumference can be calculated. The resulting force as a function of the eccentricity can herewith be calculated along with the stiffness and air flow. For a radial bearing with 18 bearing units, a diameter of 70 mm and an initial gap height h_0 of 7 µm, the force, stiffness and airflow as a function of the eccentricity are shown in Figure 3.84.

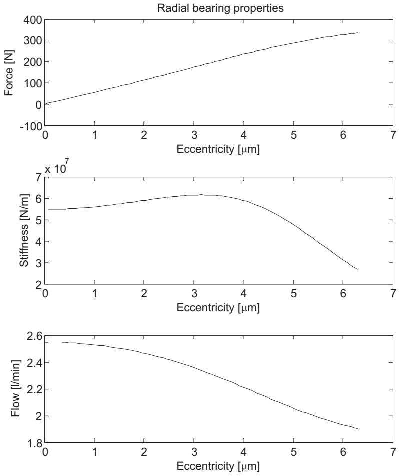

Figure 3.84: Radial bearing force, stiffness and flow rate

The rotating mass (rotor, motor, encoder, probe and counterbalance) is about 5.6 kg. At this load, the eccentricity for the two radial bearings is 0.5 µm. The stiffness per bearing is $5.5 \cdot 10^7$ N/m, giving a total radial stiffness of $c_{\Psi,rad} = 1.1 \cdot 10^8$ N/m. The bearings are spaced 123 mm apart, giving a tilting stiffness of $k_{\Psi,\varphi} = k_{\Psi,\theta} = 4.2 \cdot 10^5$ Nm/rad. The normalized air consumption per radial bearing is 2.5 l/min.

Bearing design

The bearing housing (1 in Figure 3.85) is machined from a solid block of aluminium, as is the rotor (2). The front radial bearing (3) is a separate ring that is bolted onto a seat in the housing. The second ring (4) is a combined radial and thrust bearing. On a spacer (5), the second thrust bearing (6) is bolted. Three holes (7) in the housing, together with three further holes in the rotor (8), function as an exhaust for the radial and thrust bearing.

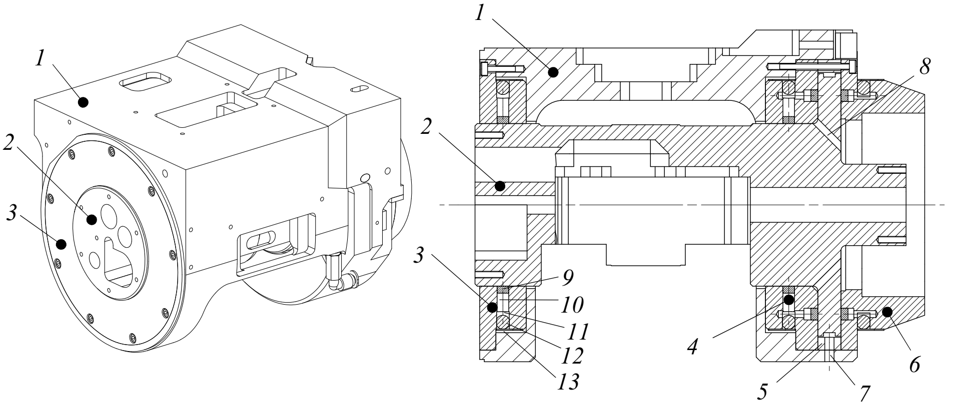

Figure 3.85: Ψ-axis bearing design

For the radial bearings, the porous plugs (9) are bonded into radial holes (10). The bearing rings have a wide supply groove (11) around them which is sealed with an O-ring (12) and a thin metal band (13). This way air pressure inside the groove does not distort the housing and thus the bearing alignment. Further, the flange is close to the groove, limiting distortion of the ring to about 0.2 µm. The air supply to the two radial bearing rings is provided through the housing via a series of holes.

The aluminium bearing rings are opalized to create a hard and dense bearing surface. The rotor has been coated with electroless nickel. This provides a hard layer which can be diamond turned and does not oxidize. This way, the cylindrical mirror and all bearing surfaces have been machined by SPDT in a single setup at the TNO Optical Workshop (Figure 3.86). This provides optimal perpendicularity and colinearity of the bearing surfaces and the mirror.

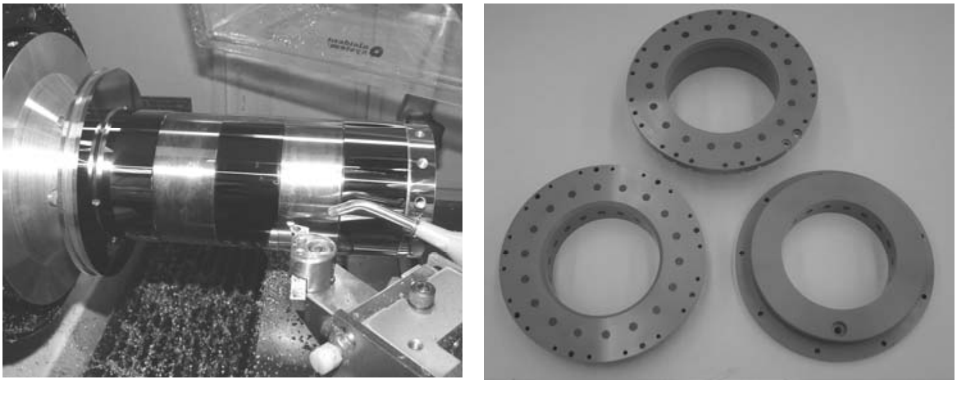

Figure 3.86: Ψ-axis rotor, bearing rings and bearing assembly

Figure 3.86 (right) shows the assembled bearing. It was found that using a stethoscope works well for detecting small contact during rotation. One can also detect an increase or decrease in this contact noise to aid alignment. Small dust particles, maybe breaking loose from the porous plugs, have caused quite some assembly difficulties but eventually frictionless operation was achieved.

Since calibration of the Ψ-axis mirror roundness is not possible in the assembled bearing, this was measured at NMi VSL before installation (Figure 3.87, left). The probe interface plate was installed to include the possible resulting deflection. The mirror roundness was measured to be 351 nm MZC, averaged over 20 revolutions and with a 50 upr Gaussian filter applied. The unfiltered data is shown in (Figure 3.87, right).

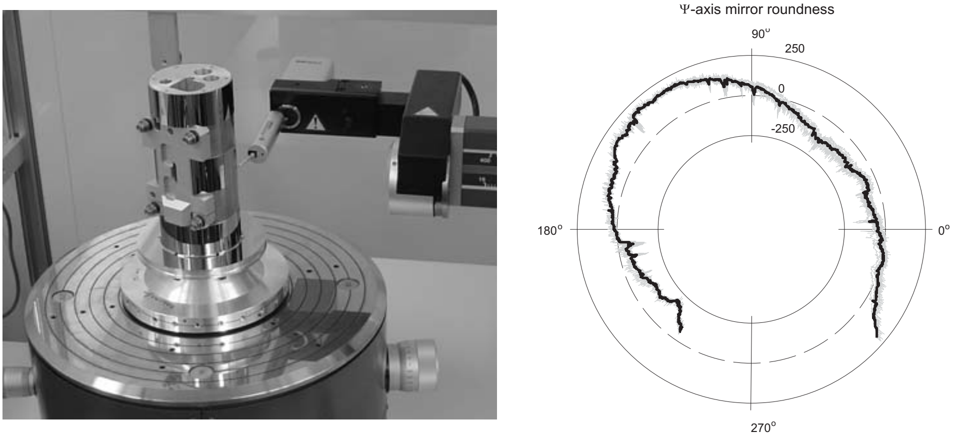

Figure 3.87: Ψ-axis mirror roundness measurement and result

3.6.2 Motor, brake and encoder

An Aerotech S-76-35B brushless motor is mounted at the rear of the Ψ-axis (Figure 3.88, left). This motor has a motor constant of 0.083 Nm/√W. The coils are mounted to the thrust bearing ring. The rotor is held in place by the brake drum. A counterbalance is applied to minimize the required motor torque. The accelerations required during measurement of a product with large slope variations require a negligible amount of power. Moreover, the motor is cooled by the exhaust air from the rear thrust bearing.

A smaller version of the brake clamp described in section 3.1.2 clamps the rotor drum. With a contact force of 100 N, a stiffness of about $5 \cdot 10^4$ Nm/rad is obtained. The inertia of the rotor assembly and the probe is approximately 0.01 kgm^2, giving a first resonance in the order of 350 Hz.

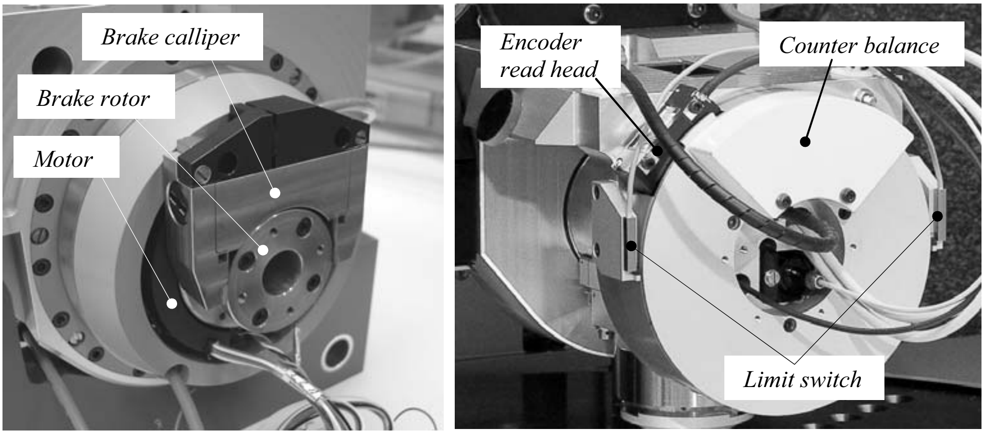

Figure 3.88: Ψ-axis motor, brake and encoder

For the encoder, as many lines as possible are desired. Further, a central hole is required for the probe cables exiting the Ψ-axis rotor from the front. A Heidenhain ERA4280 encoder with 20.000 lines was the best fit available to this geometry. An interpolation factor of 200 gives an angular resolution of 1.57 µrad or a tangential resolution at the probe tip of 157 nm, which is only just sufficient.

The encoder is protected by a ring that is bonded to the bearing housing. The front side is covered by a disc that has a cam. This cam limits the stroke of the Ψ-axis by running into two rubber stops. Limit switches detect this to notify the control system.

3.6.3 Probe nulling target

To null the probe interferometer, a nulling target is mounted to the Ψ-axis housing. Figure 3.89 shows the probe oriented at 120°, measuring to this target. This target determines the zero-length of the probe. It is made of an uncoated λ/20 optical flat with very low roughness.

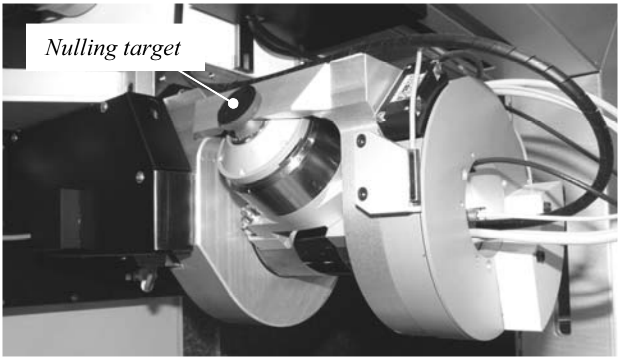

Figure 3.89: Probe nulling target

3.6.4 Ψ-axis mount

The Ψ-axis mount connects the Ψ-bearing to the Z-stage. The Ψ-axis may be removed for servicing or be replaced by another unit with an alternative measurement method. The mount should therefore be reproducible. It should further also provide thermal stability, mainly in y-direction.

Kinematic mount

The Ψ-axis has to be aligned such that when rotated, the path of the probe-tip coincides with the measurement plane. When removed for servicing, the alignment should be maintained. The Ψ-axis is therefore connected via a kinematic mount to a steel yoke that is bolted to the Z-stage bottom interface (Figure 3.90). The Z-stage optics assembly is also connected to this yoke, to be able to remove the Ψ-axis without removing the interferometry system. Since the cylinder lenses are removed along with the Ψ-axis, a flat mirror can now be inserted for separate testing of the sub-systems.

The front of the yoke (1 in Figure 3.90) has three hardened steel barrel shaped contacts (2), and the backside of the Ψ-axis bearing housing has three pairs of Tungsten-Carbide contact shims (3) that form 3 V-grooves. The thermal centre (TC) of this mount coincides with the Ψ-axis centre line. By adjusting the thickness of two axial shims (4 and 5), the Ψ-axis can be aligned in φ and θ.

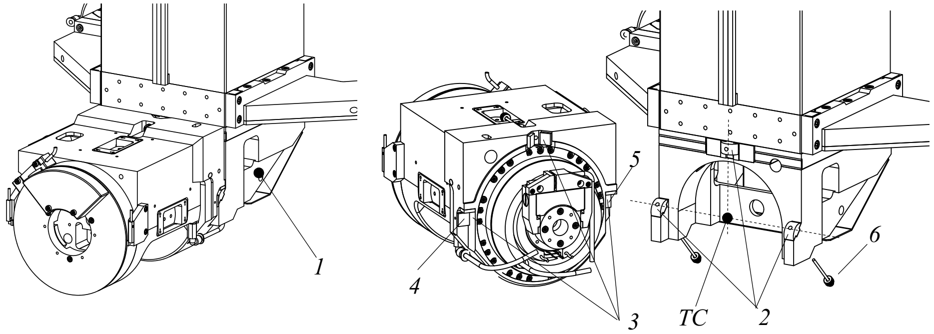

Figure 3.90: Ψ-axis kinematic mount

A preload force of around 500 N is applied over the contacts by 3 bolts with disc springs (6). With a minor and major contact radius of 20 mm and 1 m, this gives a stiffness of $1.2 \cdot 10^8$ N/m per contact point (see formulas in Appendix C). This approximately gives a stiffness of the kinematic mount of $1.7 \cdot 10^8$ N/m in r-direction, $4.1 \cdot 10^8$ N/m in y-direction and $2.8 \cdot 10^8$ N/m in z-direction. For tilting, the stiffness is about $3.2 \cdot 10^5$ Nm/rad in φ-direction, $2 \cdot 10^6$ Nm/rad in ψ-direction and $1.4 \cdot 10^6$ Nm/rad in θ-direction.

The probe tip also has to be centred on the spindle, preferably also at sub-micrometer level. The mounting of the probe to the Ψ-axis rotor provides means for coarse adjustment in y-direction (Chapter 5), and the Ψ-mount provides the fine-adjustment as further explained later in this section.

Thermal stability

The r- and z-position of the Ψ-axis rotor centre are measured with the interferometry system, and the ψ-rotation with the encoder. The y-position and φ and θ-rotations should be provided mechanically with sub-micrometer uncertainty at the probe tip, since these are less-critical out-of-plane directions. The repeatability of the Ψ-axis air bearing in these directions is expected to be of nanometer order. The main expected error source are thermal deformations that cause shifting of the Ψ-axis as a whole. Here, the inequality between the thermal loop between probe and product in y-direction is the main error source. Tilting due to gradients is not expected to cause significant errors.

In y-direction, the (uncompensated) thermal loop between product and Ψ-axis consists of the steel spindle and granite base at the bottom, and the aluminium bearings, steel cardanic hinges, steel Ψ-axis mount and the aluminium Ψ-axis bearing at the top (Figure 3.91). With the thermal properties and dimensions as shown in this figure, the stability of this loop is 3.3 μm/K for a uniform temperature change. Here, it is assumed that the spindle is constrained symmetrically in the granite, such that its centre line position is determined by the granite alone.

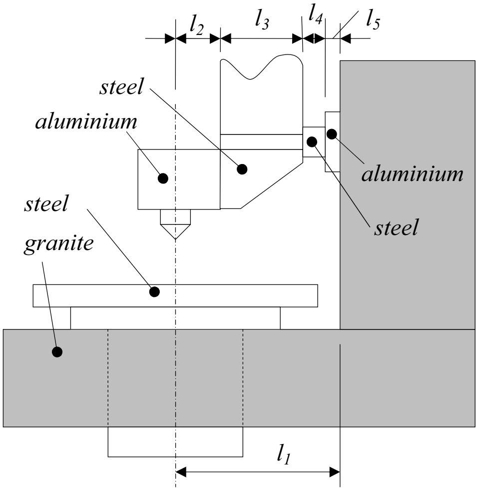

$\alpha_{alu} = 24\ \mu m/m/K$
$\alpha_{steel} = 12\ \mu m/m/K$
$\alpha_{granite} = 6\ \mu m/m/K$

l_1 = 320 mm granite
l_2 = 90 mm aluminium
l_3 = 155 mm steel
l_4 = 50 mm steel
l_5 = 25 mm aluminium

Figure 3.91: Thermal loop between probe tip and product

The time constants of the top and bottom part of the loop are quite different. With formula (4.15) it can be calculated that the time constant of the lower base block and

the spindle are both approximately 6.5 hours. The time constants of the aluminium Ψ-axis bearing, mount, cardanic hinge and ∅100 mm bearing are about 1 hour. During a measurement, the relative displacement in *y*-direction between probe tip and spindle is thus mainly determined by the top half of the loop, with a thermal sensitivity of 5.2 μm/K. Between measurements, the sensitivity from day to day is 3.3 μm/K.
Since the measurement time is in the same order of magnitude as the time constant of the top half, the measurement may be significantly influenced by environmental temperature changes. Internal heat sources are the Ψ-encoder read head, the Ψ-motor and the probe actuator. The encoder read head produces about 1 W, but this is a constant heat flux which will have a transient response. The Ψ-motor produces a negligible amount of heat due to the counterbalance, brake and intermittent motion in small steps. The probe actuator power dissipation strongly depends on the surface being measured, but will generally be less than 50 mW (section 5.3.3). Environmental temperature variations are thus the main error source. With the sensitivity of 5.2 μm/K, a short term temperature fluctuation of 0.2 K will thus result in 1 μm displacement in *y*-direction, causing 100 nm measurement error when measuring on a 5° slope.

To decrease the thermal sensitivity, one can choose to make the sensitivity of the top and bottom half equal by thermal compensation, or to make the sensitivity of the top half as small as possible. The first option will cause the probe tip to remain coincident with the measurement plane for very slow temperature changes, but shifting for fast changes due to the large difference in time constants. The second option makes the probe tip *y*-position constant during measurement, but shifting relative to the measurement plane by several micrometers from day to day. To remain centred on the measurement plane, the *y*-position may thus have to be adjusted from day to day. The second option is preferred, and is combined with the fine adjustment in *y*-direction that was already required for initial alignment.

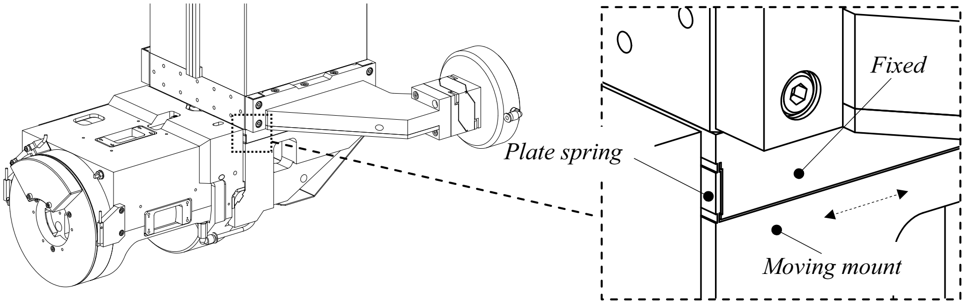

Figure 3.92: Parallelogram in Ψ-axis mount

The kinematic mount constrains six degrees of freedom of the Ψ-axis bearing. A parallelogram has been machined into this mount by wire-EDM, to release the *y*-degree of freedom of the Ψ-axis (Figure 3.92).

A Super-Invar strut (1) is added (Figure 3.93), which is connected to the Ψ-axis bearing housing at the measurement plane (2), and the backside of the Ψ-axis mount (3). This strut now constrains the *y*-direction, and excludes the steel mount and aluminium Ψ-bearing from the thermal loop. This loop now consists of 25 mm aluminium for the ∅100 mm bearing, 50 mm steel for the cardanic hinge and 245 mm SuperInvar strut ($\alpha = 0.6$ µm/m/K). This results in a thermal sensitivity of 1.3 µm/K. This a reduction of a factor four compared to the uncompensated sensitivity of 5.2 µm/K.

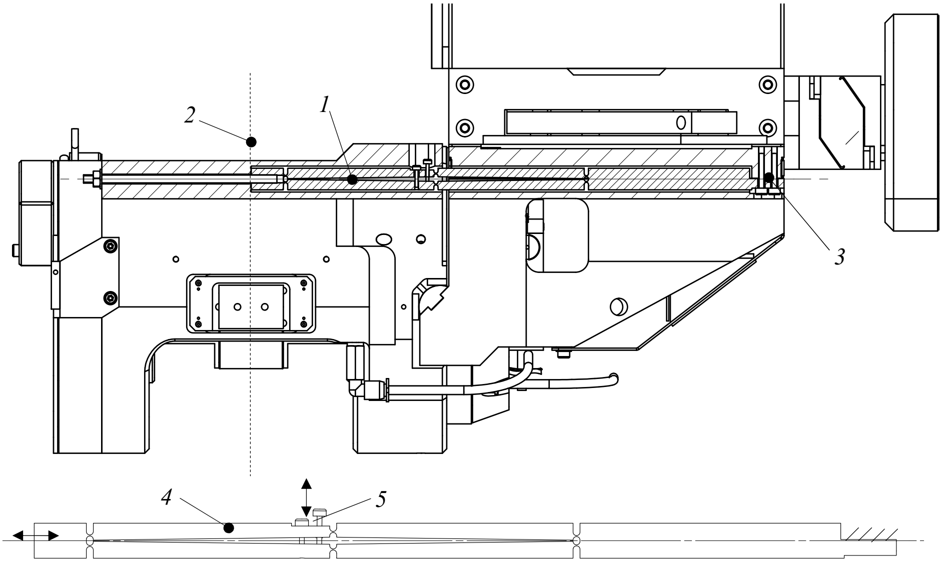

Figure 3.93: SuperInvar strut (1) for thermal stability and alignment adjustment

To align the probe tip to the measurement plane, the Super-Invar strut has two two-bar-linkages machined into it (4), which are connected by a pair of push-pull screws (5). The linkages are slightly opened, such that the strut lengthens when they are closed, and the strut shortens when they are opened. With the length of the links being 70 mm, the stroke is 15 µm. The axial stiffness hardly changes with this adjustment. The adjustment screws are reachable at the top of the Ψ-axis, since realignment may be necessary every few days due to the very long time constant of the base.

The hinges of the strut have a hole diameter of 2 mm and a thickness of 0.3 mm and a width of 8 mm, giving an axial stiffness of $2.2 \cdot 10^8$ N/m per hinge. Combined with the axial stiffness of the strut, this gives a total axial stiffness of the strut of $3.2 \cdot 10^7$ N/m. The plate springs of the mount are 10 mm long, 150 mm wide, have a centre thickness of 1 mm and a hinge thickness of 0.4 mm. This gives a stiffness in *y*-direction of $8.7 \cdot 10^5$ N/m. The combined mass of the Ψ-axis and the bottom part of the mount is 12 kg, giving 263 Hz eigenfrequency in *y*-direction.

In case of a temperature change in the Super-Invar strut, the stiffness ratio between strut and parallelogram is 1:0.027. Suppose the strut heats up with 1 K, causing a thermal expansion of 147 nm. Ideally this would push the Ψ-axis mount backwards by this amount, but the limited stiffness of the strut causes a remaining error of 4 nm .

In the other directions, the next two calculated eigenfrequencies are shown in Figure 3.94. The stiffness of the kinematic mount is not taken into account here. The second resonance occurs in ψ-direction at 727 Hz and the third in φ-direction at 905 Hz.

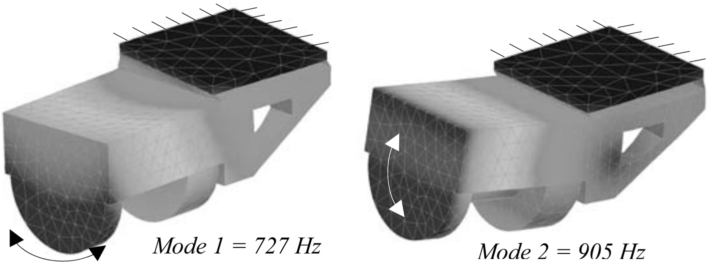

Figure 3.94: Ψ-axis mount eigenmodes

The Ψ-axis mount is shown in Figure 3.95. The steel mount has been Nickel-plated to prevent corrosion. The top right figure shows one of the plate springs of the parallelogram in the mount. The bottom right figure shows two pairs of Tungsten-Carbide shims and a barrel shaped contact of the Ψ-axis.

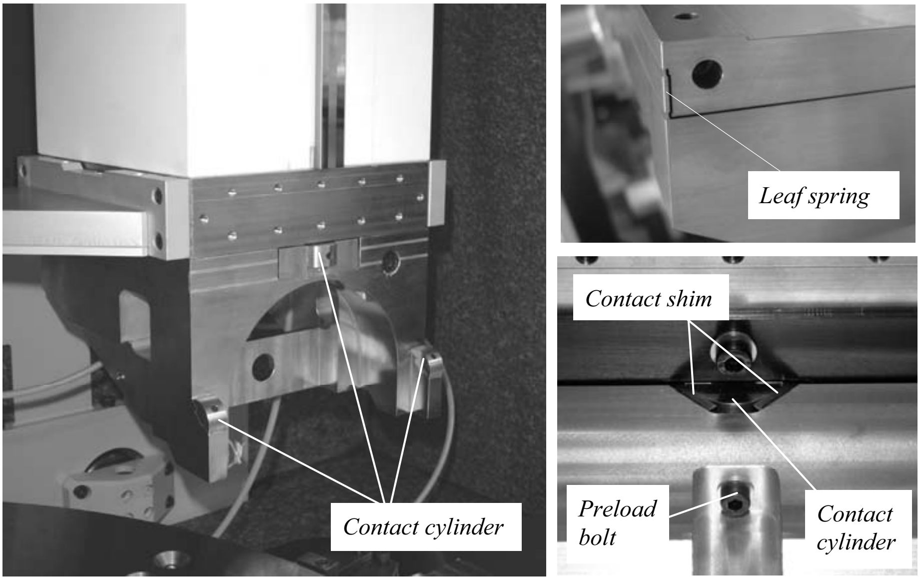

Figure 3.95: Ψ-axis mount (left), leaf spring (top right) and shim adjustable V-groove contact (lower right)

3.6.5 Ψ-axis assembly

Figure 3.96 shows the Ψ-axis assembly mounted on the Z-stage. The probe and Z-stage optics are already installed in this photograph. The alignment procedure and accuracy are discussed in section 3.7.

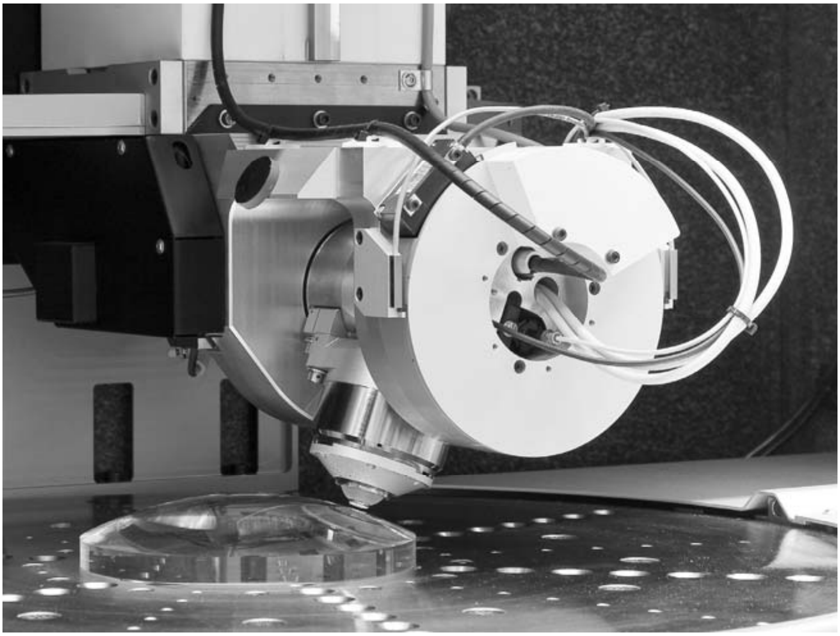

Figure 3.96: Ψ-axis assembly (probe already installed)

Table 3.4 summarizes the properties of the Ψ-axis bearing. The non-contact probe mass of 1 kg and its inertia relative to the Ψ-axis centre line have been included in the rotor mass and inertia. Experimental validation is shown in section 3.8.2.

i	$c_{\Psi,i}$ *[N/m]*	$m_{\Psi,i}$ *[kg]*	$f_{\Psi,i}$ *[Hz]*
y	$1.2 \cdot 10^8$	5.6	736
r, z	$1.1 \cdot 10^8$		705

i	$k_{\Psi,i}$ *[Nm/rad]*	$J_{\Psi,i}$ *[kgm²]*	$f_{\Psi,i}$ *[Hz]*
φ, θ	$4.2 \cdot 10^5$	~0.03	~595
ψ *(brake)*	$5.0 \cdot 10^4$	0.01	356

Table 3.4: Ψ-axis rigid body bearing properties

The mount is much stiffer than the kinematic connection. The properties of the connection are shown in Table 3.5. The removable part of the Ψ-axis assembly (including the probe) has a mass of 8.6 kg. The inertia shown in Table 3.5 is the inertia of this removable part relative to the centre point of the kinematic mount.

i	$c_{\Psi mount,i}$ [N/m]	$m_{\Psi mount,i}$ [kg]	$f_{\Psi mount,i}$ [Hz]
r	$1.7\cdot10^8$	8.6	708
y	$4.1\cdot10^8$		1100
z	$2.8\cdot10^8$		908

i	$k_{\Psi mount,i}$ [Nm/rad]	$J_{\Psi mount,i}$ [kgm^2]	$f_{\Psi mount,i}$ [Hz]
φ	$3.2\cdot10^5$	0.14	240
ψ	$2\cdot10^6$	0.025	1424
θ	$1.4\cdot10^6$	0.14	503

Table 3.5: Ψ-axis mount rigid body theoretical properties

3.7 Motion system assembly and alignment

The spindle is bolted directly to the base and therefore does not possess any alignment possibilities. Where possible, the spindle centre line is used as the vertical reference, for instance for aligning the Z-stage and the metrology frame. The R-stage bearings run on the base and therefore determine the direction of motion of the R-stage. Due to the force closed preload and statically determined construction, no alignment or fine-tuning is required. The Z-stage has to be aligned parallel to the spindle axis in ψ-direction, as will be described in the coming paragraphs. Next the Ψ-axis is to be aligned parallel to the measurement plane, as will be explained after. This section closes with the estimated stiffness and resonances at the probe tip.

3.7.1 Z-stage alignment

To align the Z-stage parallel to the spindle centre line, a straightedge reversal is applied (Evans et al., 1996). A straightedge, a precision cylinder in this case, is hereto mounted vertically to the spindle (Figure 3.97, left). A capacitive probe is attached to the Z-stage. Moving the Z-stage up and down gives the angle between the straightedge and the Z-stage. The straightedge is now reversed with the spindle, where the tilt errors of the spindle are very small. The probe is reversed, and the angle between the straightedge is measured again. The sum of the measurements now gives the alignment error of the Z-stage, and the difference of the measurements gives the angle of the straightedge relative to the spindle centre line. By adjusting the bracket of the top ∅125 mm bearing, the ψ-orientation of the Z-stage can be adjusted. After careful adjusting, a misalignment of 0.3 μm over 150 mm range was finally achieved, which is equal to 2.1 μrad.

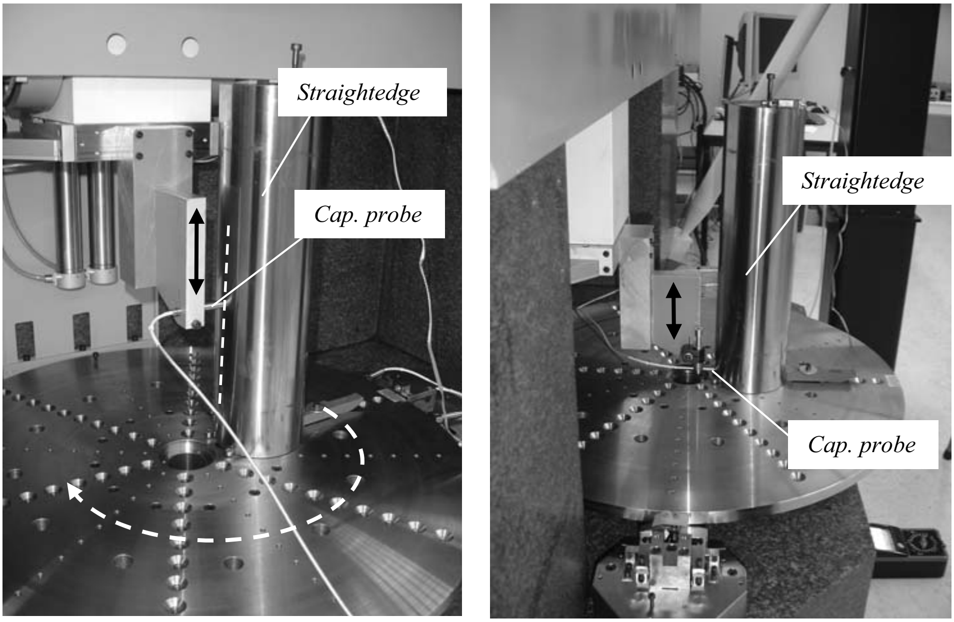

Figure 3.97: Z-stage alignment with straightedge reversal

Since the alignment of the straightedge relative to the spindle centre line directly follows from this measurement, it also offered the opportunity to measure the parallelism between the spindle centre line and the vertical base plane. The straightedge and probe were hereto rotated by 90° (Figure 3.97, right), and the Z-stage was moved up and down again. This error was about 3.7 μm over 150 mm, which is equal to 7.5 μrad.

3.7.2 Ψ-axis alignment

The Ψ-axis mount was bolted to the Z-stage first. Next, the Ψ-axis was mounted to the kinematic mount with temporary shims. To measure the alignment, a steel plate was ground flat, and mounted to the spindle (Figure 3.98). An LVDT probe was attached to the Ψ-axis rotor. The R-stage was then moved from left to right to align the plate parallel to the measurement plane. When the Ψ-axis is rotated, the sensor follows a circular trace over the plate.

The plate flatness and alignment are unknown. To eliminate these from this procedure, the Ψ-axis is locked at 0°, and the R and Z-stage are moved such that the probe follows the same circular trace. Over this small range, the base plane flatness is much better than the plate flatness. The probe reading is thus equal to the flatness and alignment of the plate. The R and Z-stage are now locked again. When the Ψ-axis is rotated, the probe readings should be equal to the readings recorded when moving the R and Z-stage.

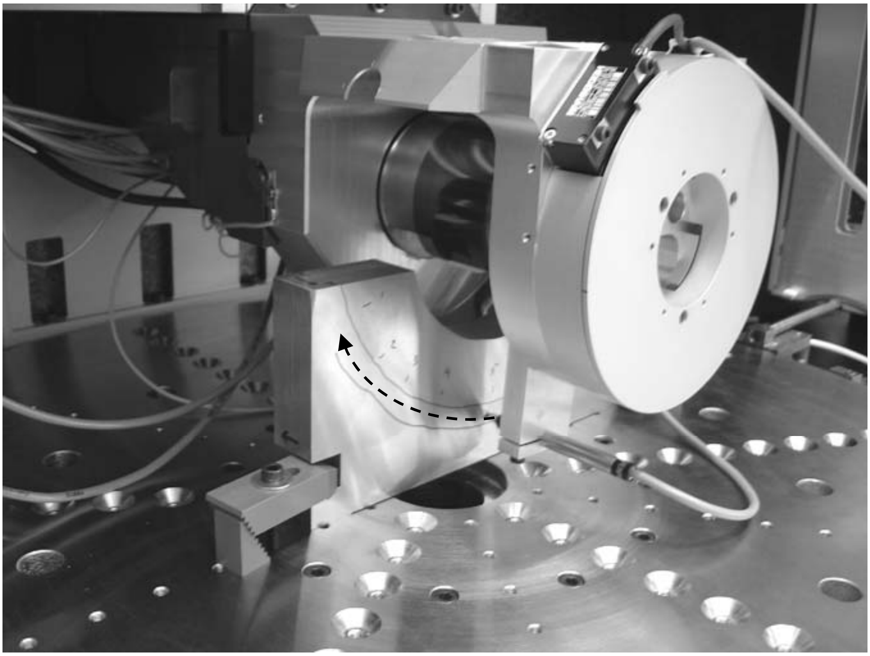

Figure 3.98: Ψ-axis alignment setup

Next, the R and Z-stage are locked such that when the Ψ-axis is rotated it describes the same trace as measured when moving the R and Z-stage. By rotating the Ψ-axis back and forth and adjusting the two shims, the alignment of the Ψ-axis is adjusted until the readout of the probe is equal to the readout when moving the stages. Eventually, the Ψ-axis rotor has been mounted perpendicular to the measurement plane with $d\varphi < 156$ μrad and $d\theta < 10$ μrad. Especially the adjustment of $d\varphi$ is very sensitive due to the short distance between the shims in this direction. With these alignment values, the probe tip will follow the measurement plane within about 4.5 μm. Further calibration is thus required, but the behaviour is highly repeatable, and the resulting error is of the less-sensitive type.

3.7.3 Motion system assembly

The front and backside view of the motion system are shown in Figure 3.99. Due to the assembly order, the metrology system and probe are already installed in these photographs.

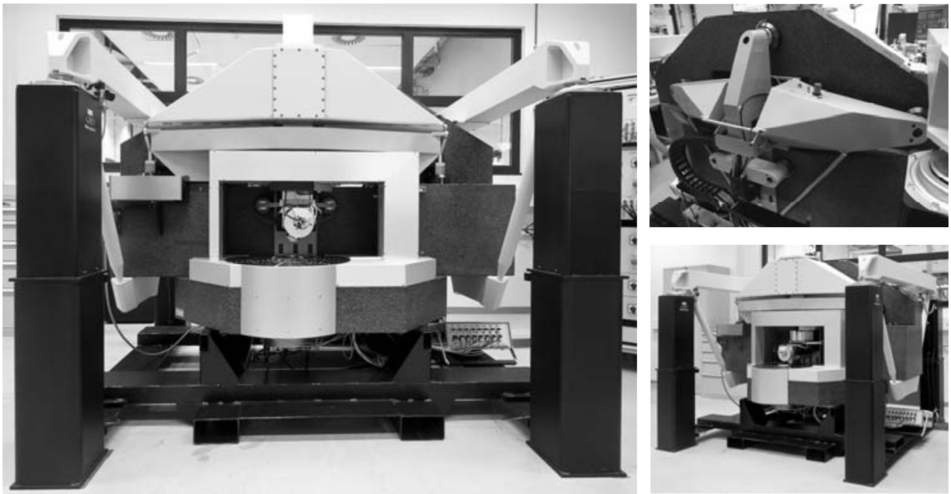

Figure 3.99: Motion system assembly (metrology system and probe already installed)

3.7.4 Motion system assembly property summary

In the previous sections, the mass, theoretical stiffness, and rigid and flexural body eigenfrequencies have been calculated for the individual sub-systems. The calculated properties of the total motion system assembly are summarized here. The measured properties are explained in the next section.

The total mass of the motion system is 3340 kg, of which 2840 is supported on the vibration isolators. The total spindle assembly mass is 215 kg, the rotor mass is 120 kg (without the product) and the total rotor inertia is 3.3 kgm^2. The R-stage assembly mass is 174 kg, the Z-stage assembly is 70 kg and the Ψ-axis is 13.8 kg. This brings the total horizontal moving mass, including the cables, to 275 kg, and the total vertical moving mass to 85 kg.

The eigenfrequencies of the individual sub-systems have been shown in the previous sections. The first eigenfrequencies in r, y and z-direction at the probe tip can be approximated from these results. For more accurate results, a full multi-body model should be made. The first eigenfrequency in r-direction is determined by the R-stage brake stiffness. The 275 kg stage mass on $5 \cdot 10^7$ N/m gives an eigenfrequency of 68 Hz. The first rigid body eigenmode in y-direction is caused by φ-rotation of the Z-stage at 259 Hz. The Z-stage preload frame, however, has a first resonance in φ-direction at 105 Hz, which will probably propagate to the probe. In z-direction, the structural loop stiffness mainly consists of the R-stage bearings ($c_{R,z} = 6.4 \cdot 10^8$ N/m), the R-stage position frame stiffness ($7.1 \cdot 10^7$ N/m) and the Z-stage brake stiffness ($5 \cdot 10^7$ N/m). The resulting stiffness is $2.8 \cdot 10^7$ N/m, giving a resonance at 91 Hz in z-direction. Eigenfrequency measurements are shown in section 3.8.2 and Appendix E.2.

3.8 Experiments and calibration

Tests that have been done to validate the mechanical properties of the motion system assembly are summarized in this section. The measured noise level and eigenfrequencies are shown first, followed by the stage tilt calibration. Stiffness measurements and a detailed explanation of the eigenfrequencies can be found in Appendix E.

3.8.1 Noise level

In section 4.6, tests will be described that measure the positioning stability of the motion system and show the residual error after correction with the metrology system data. In these tests, a dummy probe was built onto the Ψ-axis (Figure 3.100). This dummy has 3 orthogonal faces at 100 mm from the Ψ-axis centre line, at the location where the probe tip will be. Capacitive probes were bolted to the spindle, to measure the relative displacement between spindle and probe tip. The noise level of these probes is 0.2 nm rms and about 1.7 nm PV.

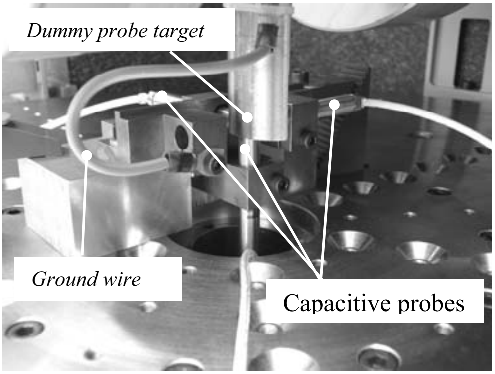

Figure 3.100: Stability test setup

Figure 3.101 (left) shows the measured displacement. The probe tip was located at r = 0 mm, z = 40 mm and ψ = 0°, and all brakes were clamped. During this 10 s measurement, the noise level in r-direction is 6.8 nm rms and 58 nm PV. The noise level in y-direction is 4.8 nm rms and 45 nm PV. The noise level in z-direction is 4.4 nm rms and 35 nm PV. This is the most sensitive direction in this case since it would be perpendicular to the surface under test. Note that these values are the physical displacement between probe tip and spindle, most of which is also measured and compensated for by the metrology system. The accuracy of this correction will be shown in 4.6.

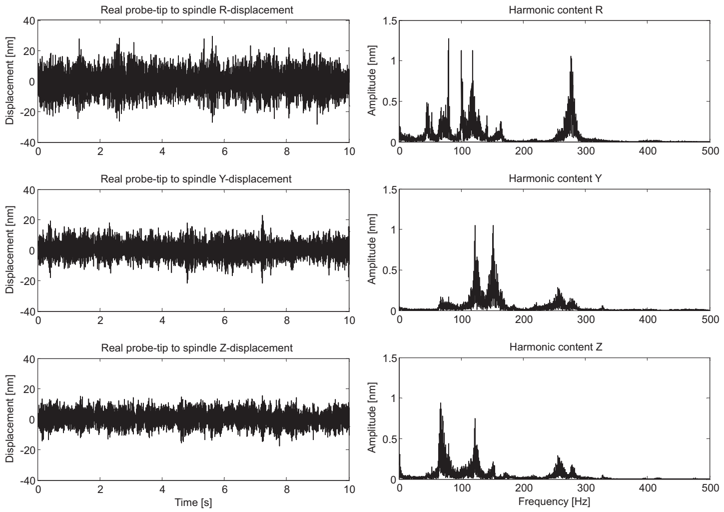

Figure 3.101: Relative probe tip to spindle stability of motion system assembly

3.8.2 Eigenfrequencies

The harmonic content of the signal (Figure 3.101, right) reveals the eigenfrequencies as measured at the probe tip location. By opening and closing the brakes and by landing the R and Z-stage, the source of each frequency was identified. The first resonance in r-direction is vibration of the stage assembly on the R-stage brake stiffness, but at 46 Hz instead of the calculated 68 Hz. The first resonance in y-direction is at 122 Hz instead of the calculated 107 Hz. This resonance is also present in z-direction, indicating that it is indeed caused by φ-rotation of the Z-stage preload frame. In z-direction, the first resonance is vibration of the Z-stage on the Z-brake at 67 Hz, instead of the calculated 91 Hz. In both the r- and z-direction, the true stiffness is about half of the calculated stiffness. This is probably due to the high stiffness of the bearings and the brakes, which is in the same order as the stiffness of the stage structure. The stiffness of the structure was, however, not taken into account in the calculations. Further analysis of the eigenfrequencies can be found in Appendix E.

3.8.3 Stage tilt calibration[1]

To measure the tilt of the stages, an autocollimator (Möller-Wedel Elcomat, 0.025 µrad resolution) was bolted to the base (Figure 3.102), at the location where the interferometer laser will be installed later. Experiments have been designed such that the φ, ψ and θ tilts of the R as well as the Z-stage can be measured with the autocollimator at this position.

---

[1] *These measurements were performed together with NMi VSL*

Figure 3.102: Test setup for measurement of Z-stage ψ and θ-rotation

A mirror was first fixed to the R-stage as schematically shown in Figure 3.103 (left). By moving the R-stage through its range, the tilt in ψ and θ-direction is measured. The φ-rotation of the R-stage is around the optical axis of the autocollimator and can not be measured directly. To measure this φ-rotation, a pentaprism is mounted to the R-stage (Figure 3.103, right), which deflects the beam down at an angle of exactly 90°, towards a $\lambda/20$ flat reference mirror that is placed on the mounting table. Rotation of the prism around the φ-direction misaligns the beam relative to the mirror, and is therefore measureable with the autocollimator. Rotation of the prism around the ψ-direction has no effect. Rotation around the θ-direction has the same effect in first order (for small rotations) as φ-rotation. Since the θ-rotation of the R-stage was already known from the first experiment, the φ-rotation of the R-stage can be calculated. Ideally, a 400 mm reference flat should be used, but this is not available. A ∅100 mm $\lambda/20$ reference flat is therefore used, that is moved when the R-stage reaches the edge. By overlapping the start and end points, the measurements are stitched together. The flatness of the mirror is part of the result, but is very small compared to the measured tilt.

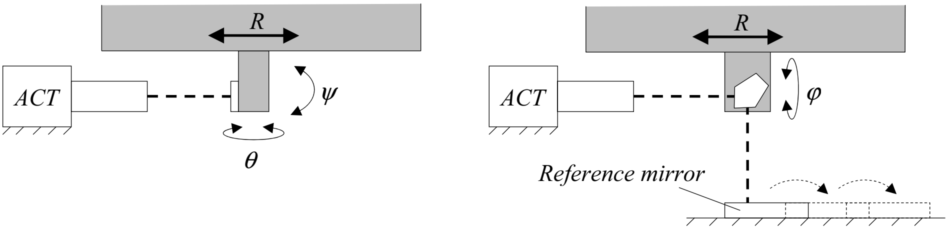

Figure 3.103: Schematic test setups for R-stage ψ and θ (left) and φ (right)

The above two measurement have both been performed twice. The results are averaged and the tilt is set to zero at R = 0 (Figure 3.104). In ψ and θ-direction the repeatability was 0.2 and 0.3 μrad, respectively. The total tilt in ψ and θ-direction is 4.3 and 3.1 μrad. The repeatability in φ-direction is somewhat worse with 2.2 μrad, probably due to the stitching. The total tilt in φ-direction is 18.5 μrad. This is higher than the tilt in the other directions. This is probably due to the smaller spacing between the bearings, compared to the other directions.

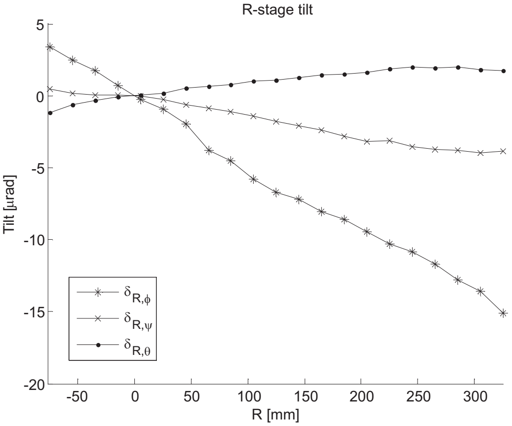

Figure 3.104: R-stage tilt measurement results

To measure the tilts of the Z-stage, the ∅100 mm optical flat is attached to the Z-stage (Figure 3.105 (left) and Figure 3.102). The R-stage and Z-stage are now moved through their range to measure the ψ and θ-rotation of the Z-stage. Since the mirror is not large enough to cover to whole Z-range it is repositioned once, with overlap to stitch the data together.

To measure the φ-rotation of the Z-stage, the pentagon prism is attached to the R-stage again (Figure 3.105, right). A horizontal mirror is now attached to the Z-stage, and the stages are moved through their range again. The measured φ-rotation is the φ-rotation of the Z-stage minus the φ-rotation of the R-stage plus the θ-rotation of the R-stage. Since the φ and θ-rotation of the R-stage were already known from the previous experiment, the φ-rotation of the Z-stage can now be calculated. The ψ-rotation of the Z-stage is also measured by this experiment, since ψ-rotation of the pentagon prism has no influence on the measured angle.

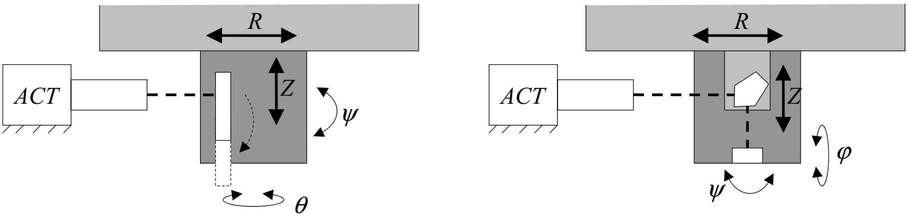

Figure 3.105: Schematic test setups for Z-stage ψ and θ (left) and φ (right)

Figure 3.106 shows the tilt of the Z-stage in ψ and θ-direction. These measurements were also performed twice, with a repeatability of 0.2 and 0.3 µrad, respectively. The total tilt in ψ-direction is 8.6 µrad and the total tilt in θ-direction is 34.2 µrad. The large tilt in this direction is again probably caused by the relatively small bearing spacing of the lower ∅100 mm bearings.

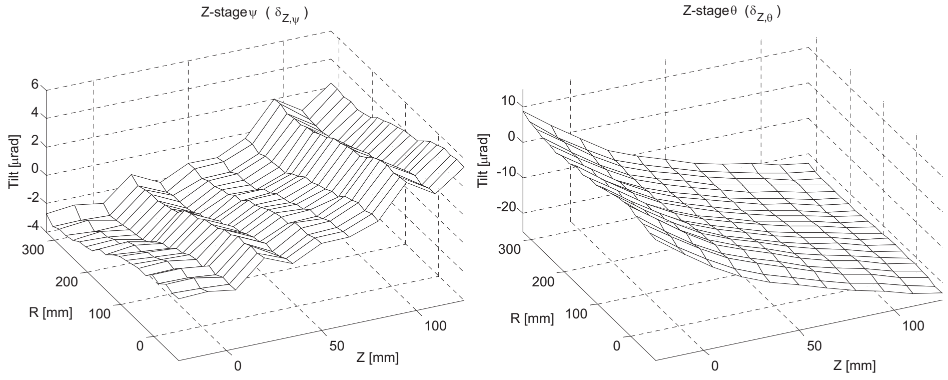

Figure 3.106: Z-stage tilt measurement results in ψ and θ-direction

The measurement results of the φ-rotation calibration are shown in Figure 3.107 (left). By subtracting the rotation in φ and θ-direction of the R-stage (Figure 3.104), the φ-rotation of the Z-stage relative to the base is obtained (Figure 3.107, right). This measurement has also been done twice, with a repeatability of 1.2 µrad. The total tilt is 7.5 µrad.

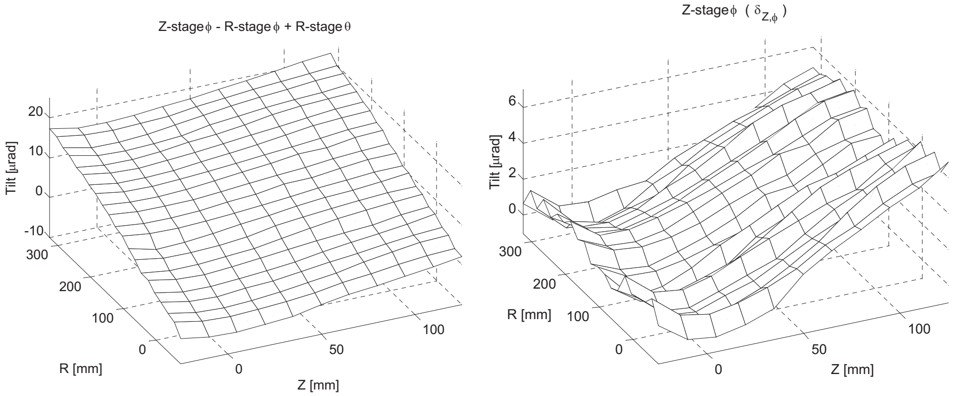

Figure 3.107: Z-stage tilt measurement results in φ-direction

The Z-stage was aligned directly to the vertical base plane to provide a high accuracy plane of motion to the probe. Regarding the tilt it can be concluded that although the

R-stage tilts up to 21.5 μrad in φ-direction, the Z-stage only tilts 7.5 μrad. The rotation in θ-direction appears to be relatively large at first sight. In conventional stacked pinole designs the bearing spacing is much smaller, which would probably lead to higher tilts. In ψ-direction the stages are stacked, but the large bearing spacing results in relatively small tilts of up to 8.6 μrad.

Since the probe position will be measured at the Ψ-axis centre, tilts will cause tangential (less-critical) position errors at the probe tip. The obtained tilt values can be used to compensate this. This will especially reduce the measurement uncertainty for surfaces with high local surface slope. The repeatability of the measurements varies from 0.2 – 2.2 μrad rms. The expanded measurement uncertainty is 5.5 μrad in φ-direction, and 1.0 μrad in ψ and θ-direction, or 2.25 μrad and 0.5 μrad rms respectively.

Stage tilt causes a tangential measurement error, due to the Abbe offset between Ψ-axis centre and the probe tip. With the probe length of 100 mm, the (largest) uncertainty in φ-direction causes a tangential error of 225 nm rms, which translates to 19 nm rms on a freeform surface with 5° local surface slope.

3.9 Motion control[1]

The stages are locked during measurement of the circular tracks, and the position of the Ψ-axis rotor is measured directly with the interferometry system. The positioning accuracy of the stages therefore does not influence the measurement uncertainty. Emphasis has been on the overall machine control software to enable safe operation. To design robust stage controller to be used during motion, as well as to obtain insight in the dynamics of the stages, frequency response measurements have been done by inserting noise as a disturbance to the system. Based on these measurements stabilizing motion controllers have been designed. In this section, the plant frequency response functions will be shown. In this case the plant is defined as the system consisting of the DAC, the motor amplifier, the actuator, the stage, the scale or encoder, and the ADC.

Spindle

Figure 3.108 (left) shows the plant frequency response of the spindle. Pure frictionless mass behaviour is shown up to a significant mass decoupling at 270 Hz. This is probably caused by decoupling of the mounting table and upper thrust bearing, relative to the lower thrust bearing to which motor and encoder are attached. The thrust bearing plates are coupled by a thick-walled tube that forms the radial bearing.

---

[1] *The motion control design and experiments are the work of G.F.IJ. Kramer of TNO.*

Calculations show a torsional mode at 286 Hz, so this seems to be the cause of the anti-resonance. The next resonance occurs at 1460 Hz. The departure from the model approximation (using a fit) around this resonance may be due to the lowered bandwidth of the amplifier. The implemented controller has a bandwidth of 40 Hz.

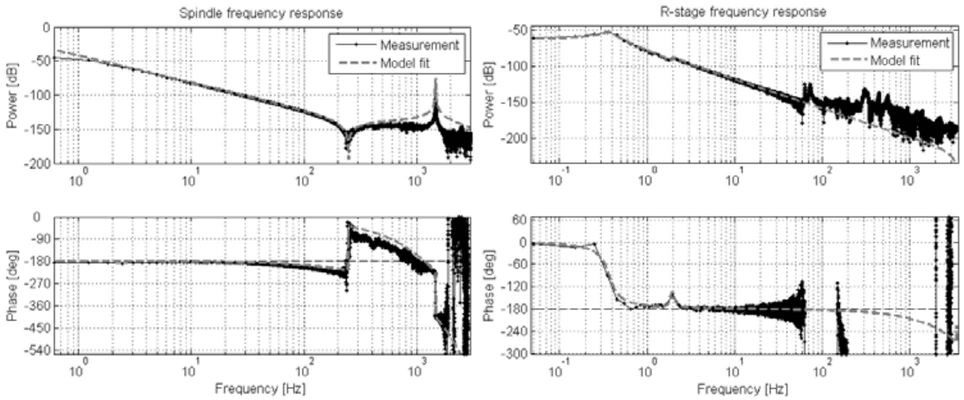

Figure 3.108: Spindle and R-stage plant frequency response

R-stage

Figure 3.108 (right) shows the plant frequency response of the R-stage. This measurement does include the Z-stage, but not the Ψ-axis and the probe. The first rigid body resonance occurs at 0.35 Hz, and is probably caused by the cable guidance. The second occurs at 2 Hz, which is the isolation frequency of the base. The base mass decouples above this frequency, which also corresponds well with the model. Above this frequency pure frictionless mass behaviour is shown until resonances start around 60 Hz. Due to the applied measurement method, measurement data becomes noisier at higher frequencies. The increased noise on the phase before this resonance is a measurement artefact. The implemented controller has a bandwidth of 10 Hz.

Z-stage

Figure 3.109 (left) shows the plant frequency response of the Z-stage, and does not yet include the Ψ-axis and the probe. Similar to the R-stage, pure frictionless mass behaviour is shown up until about 45 Hz. The deviation from this behaviour at very low frequencies may be due to the cable guidance or friction in the weight compensation. No sharp resonances occur. This may indicate damping in the system (for instance from the weight compensation), but the phase measurement is too noisy to confirm this. Similar to the R-stage, the measurement data becomes less reliable for higher frequencies and the increasing noise on the phase is a measurement artefact. The bandwidth of the applied controller is 8 Hz.

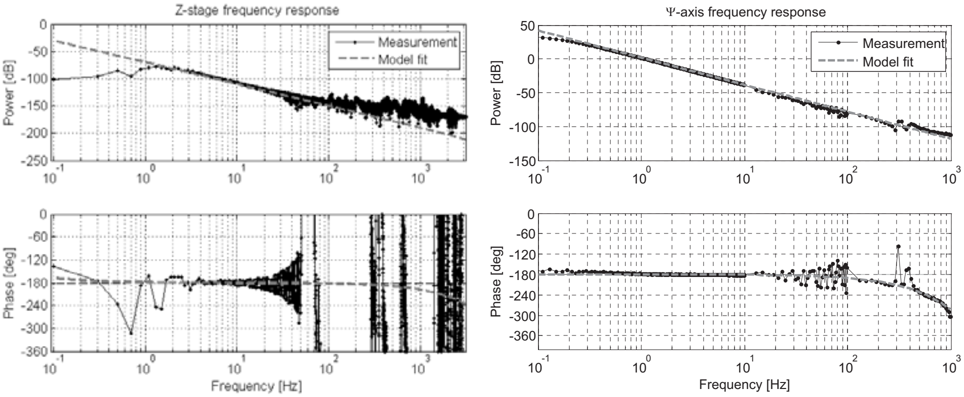

Figure 3.109: Z-stage and Ψ-axis plant frequency response

Ψ-axis

Figure 3.109 (right) shows the plant frequency response of the Ψ-axis, with the probe and counterbalance not yet installed. A first small resonance occurs at around 300 Hz. The phase lag due to the electronics delay is limiting now, but probably the added dynamics of the probe and counterbalance will eventually determine the achievable bandwidth. The controller bandwidth of the Ψ-axis with the probe installed is 20 Hz. No new experiment has yet been performed after installation of the probe.

3.10 Conclusion

The motion system positions the probe relative to the product. The product is mounted on an air bearing spindle, and the probe is positioned over it in r, z and ψ-direction. The Z-stage is aligned directly to the vertical base plane using three air bearings. Separate preload frames are applied for the R and Z-stage, to minimize distortions and hysteresis, and the motors and brakes are aligned with the centres of gravity of the stages.

The stages are locked mechanically when measuring circular tracks, resulting in a noise level of 6.8, 4.8 and 4.4 nm rms in r, y and z-direction respectively. When locked, the first eigenmodes occur at 46 Hz, 122 Hz and 67 Hz in r, y and z-direction. The tilt error of the Z-stage over the entire range is 7.5 μrad, 8.6 μrad and 34.2 μrad in φ, ψ and θ-direction.

The low noise level and high eigenfrequency in y-direction, and the low tilt error in φ and θ-direction are contributed to the parallel bearing setup. Compared to a stacked design, the higher stiffness comes at the cost of higher moving mass and a more intricate design. This especially holds for the separate preload frames, which are to achieve similarly high eigenfrequencies as the position frames. As will be shown in section 4.6, much of the displacement in r and z-direction will be compensated for by the metrology system.

For the Z-stage, the tilt calibration repeatability is 1.2 µrad in φ-direction and 0.3 µrad in θ-direction. Taking the probe length of 100 mm into account, this translates to up to 120 and 30 nm out-of-plane displacement at the probe tip, respectively. With the Ψ-axis being an air bearing, similar repeatability is expected here. Although the y-displacement at the probe tip is still to be calibrated, the repeatability of the tilt measurements indicate that the required sub-micrometer uncertainty plane of motion of the probe is achievable.

Chapter 4

Metrology system

The metrology system measures the position of the probe relative to the product in the six critical directions in the plane of motion of the probe (the measurement plane). By focussing a vertical and horizontal interferometer onto the Ψ-axis rotor, the displacement of the probe is measured relative to the reference mirrors on the upper metrology frame. Due to the reduced sensitivity in tangential direction at the probe tip, the Abbe criterion is still satisfied. Silicon Carbide is the material of choice for the upper metrology frame, due to its excellent thermal and mechanical properties. Mechanical and thermal analysis of this frame shows nanometer-level stabilities under the expected thermal loads. The multi-probe method allows for in-process separation of the spindle reference edge profile and the error motion. Tests demonstrate the stability of the metrology system.

4.1 Concept

In this section, the metrology loop concept will be explained. After a short discussion of the expected error sources, several methods of determining the relative position between probe and product are discussed.

Error sources

The probe and product position will deviate from the nominal position. Errors are generally separated in systematic and random errors. Systematic errors are repeatable and can thus be calibrated. They include guidance straightness, mirror flatness and roundness, position dependent gravity deflection etc. By planning the calibration during the design (section 7.3), it is assured that each of these errors can be calibrated and hence be compensated for in the data-processing.

Random errors do not repeat, and can thus not be compensated for. The term random is disputable, since every error has a cause that can be physically explained. In this deterministic approach *'non-repeatability primarily depends on time, money and skill (culture) of the user'* (Bryan, 1984). This group of errors includes system dynamics due to for instance to acceleration forces of the probe objective, unbalance of the spindle and floor vibrations. Acoustics may also be a source of dynamic excitation. Further, variations in the supply pressure to the air bearings will cause variations in gap height and thus in variation of the position of the stages. Thermal disturbances from inside the machine (e.g. actuators, read heads, etc) as well as from the environment, cause departures from the nominal position. According to (Bryan, 1990), thermal disturbances can be split in the effects of uniform temperatures other than 20°C and the effects of non-uniform temperatures, acting on a three part system made up of product, machine frame and the reference. By measuring as directly to the point of interest as possible (i.e. probe-tip and product), the above 'random' errors are measured and thus cancel from the measurement result.

Measuring the probe tip position

To satisfy the Abbe principle (Abbe, 1890), the measurement systems should be aligned to the point of interest: the probe tip. Intuitively, one aligns the measurement systems with the horizontal and vertical direction. For concave optics, this would require them to be placed outside the measurement volume, far away from the probe. Although the Abbe principle may be satisfied now, many elements have to be introduced that increase the length of the metrology loop. Tilting the measurement systems over 45° allows for measuring to the probe tip into concave optics. A further complication is the rotation of the probe. This requires the measurement systems to move separately from the R- and Z-stage, to maintain alignment with the probe tip in both cases.

One method that is applied to achieve direct measurement in orthogonal CMMs is the addition of laser trackers (Hughes et al., 2000). By measuring the distance and orientation to a target, or by using multi-lateration with several targets, the position and orientation of an object in space can be calculated. Usually the target is a retro-reflector or cat's eye. Pointing of the beam is done by auxiliary pointing mechanisms. These mechanisms tend to be complex and have an accuracy in the order of a micrometer. They are mainly applied in very large Coordinate Measuring tasks, such as used for airplane construction.

Measuring the Ψ-axis centre position

As explained in the error budget calculations, the setup is less-sensitive to tangential errors of the probe tip relative to the product. This also includes the ψ-rotation of the probe. This basically means that the Abbe point can be translated along the probe centre line (*c*-axis). The Abbe criterion can now be satisfied with measurement systems aligned with the Ψ-axis centre, and thus moving along with the R- and Z-stage. A further advantage is that for a practical probe length of 100 mm, the Ψ-axis centre never drops below the edge of concave optics. The position measurement system thus continuously have a clear 'line of sight' to the Abbe point.

Two measurement systems can provide the required range, resolution and accuracy: optical linear scales and laser interferometers. A good comparison of the two can be found in (Kunzmann et al., 1993). Optical linear scales provide robust measurement at a relatively low cost, but can only measure the displacement between two bodies translating in one direction relative to each other. To measure two orthogonal displacements in Abbe, intermediate bodies can be introduced (Vermeulen, M., 1999; Van Seggelen, 2007), or a capacitive sensor or vacuum preloaded air bearing can be added as suggested in (Hemschoote et al., 2004). A 2D encoder grid may also be applied, but these presently do not have the accuracy of a 1D scale.
Laser interferometers are directly traceable to the SI unit of length, but are more susceptible to environmental disturbances, since the wavelength of light depends on the refractive index of air. Therefore, to obtain high accuracy, the measurement has to be compensated for temperature, pressure and humidity (Estler, 1985). It can also be done in a vacuum environment or have a continuous conditioned air flow. The crucial advantage, however, is that laser interferometers are able to measure the displacement of an object in one direction, while allowing for displacement in other directions, for instance using a plane mirror interferometry setup (Zanoni, 1989). The mirror flatness and orientation can be calibrated. Further, focusing the laser beams onto the Ψ-axis allows for direct position measurement of the Ψ-axis rotor rotating over large angles.

Ideally, the Ψ-axis (1 in Figure 4.1) position is measured directly relative to the product (2) or spindle (3) with a differential beam layout, but this proved to be not practical. It was therefore chosen to only measure the Ψ-axis position interferometrically (4 and 5), relative to reference mirrors (6 and 7) on a metrology frame (8). The product position will be measured using capacitive probes (*9*), as will be explained later.
In the design, a split is made between the upper part of the metrology frame (8) that holds the mirrors, and the lower part of the metrology frame (10) that holds the capacitive probes. As shown later, the capacitive probes are calibrated in-process and do thus not required a frame with extreme long term stability. In contrast, the upper part should remain straight and square at nanometer level at all times. The base is supposed to be the stable reference here to which the spindle and both metrology frame parts are mounted. A patent has been granted on this metrology system concept

(Henselmans and Rosielle, 2004), the main novelty being the application of the focused interferometers to enable the high accuracy position measurement of an optical probe, which has to be rotated over large angles to be kept perpendicular to inclined surfaces.

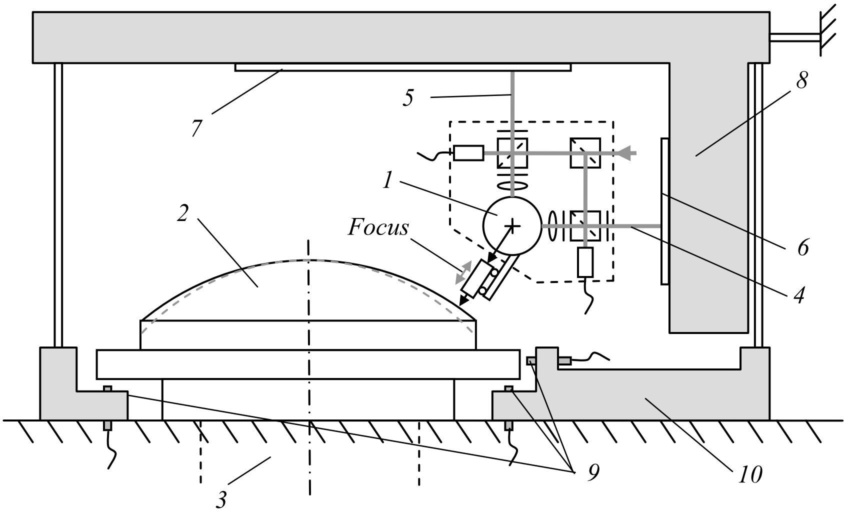

Figure 4.1: Metrology loop concept with interferometers measuring the probe displacement and capacitive probes measuring the spindle error motion

The components within the dashed area can be translated in *r* and *z*-direction, causing the laser beams to move over the reference mirror while maintaining orthogonal alignment to the Ψ-axis centre. The Ψ-rotor can be rotated relative to the dashed area. This way, the displacement of the rotor of the Ψ-axis, and thus of the probe, is measured relative to the reference mirrors on the metrology frame, directly and without Abbe offset. This cancels the non-repeatable *r*- and *z*-errors of the probe from the metrology loop.

Measuring the product position

Ideally, the position of the product is measured on the product itself. Since this can be any shape, this is not practical. Next best would be measuring to the intermediate body it may be mounted on. Especially mirrors will have their mounting points incorporated in their structure and thus be mounted directly on the mounting table. Measuring to the edge of the mounting table therefore is the most practical option. Care must be taken to ensure that the product is fixed rigidly to the table, since relative motion between product and table is not measured by the metrology system. This should be done with minimal distortion of the product, for instance with pitch or wax. The fixation of the product is not shown in Figure 4.1.

Although the acquired spindle is specified to have an error motion around 25 nm and 0.1 µrad, the position of the rotor needs to be determined with higher accuracy. To determine the position of the spindle rotor relative to the metrology frame, capacitive probes are added. As shown in Figure 4.1, the sensitive directions are r, z and ψ, which are measured by three capacitive probes (9); two vertical and one radial. In principle, this should be enough to measure three degrees of freedom. To separate the edge shape from the error motion, the multi-probe method will be applied, using 7 probes.

Design overview

With this metrology system concept, all six sensitive directions of Figure 2.11 are measured. When measuring a freeform surface, only the probe focusing mechanism is moving dynamically while measuring a circular track. The dynamical displacements that occur during this measurement are recorded by the metrology system and can be corrected for afterwards (off-line).

Figure 4.2 shows the final design of the metrology system. The interferometry system, consisting of the laser and the R and Z-stage optics assemblies will be explained in detail in section 4.2. Next, the upper metrology frame, which holds the reference mirrors, will be described in section 4.3. The lower metrology frame, holding the capacitive probes for the spindle error motion measurement is explained in section 4.4. This chapter will close with the final assembly (section 4.5) and verification of the performance (section 4.6).

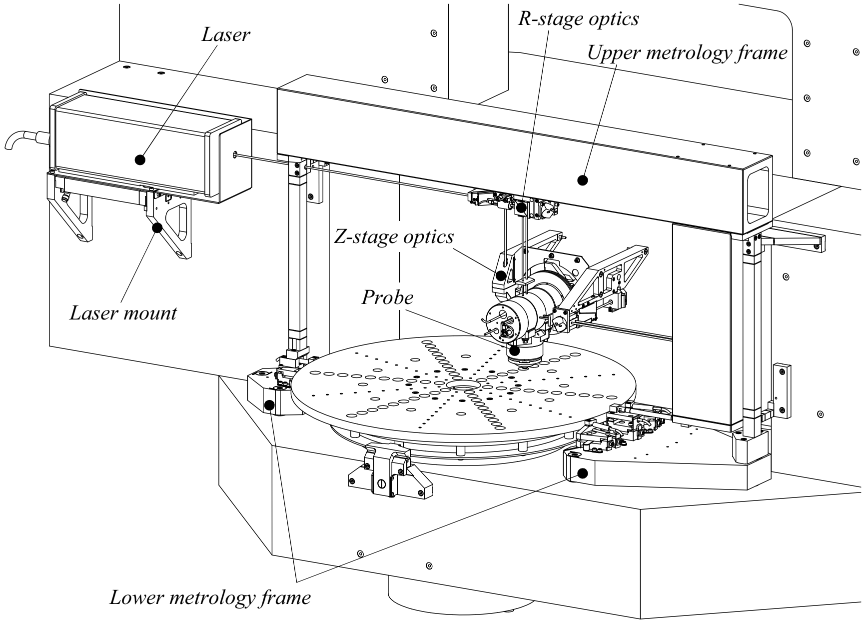

Figure 4.2: Metrology system overview

4.2 Interferometry system

The interferometry system measures the displacement of the Ψ-axis centre relative to the reference mirrors in on the metrology frame. The setup measuring the *r* and *z*-displacement of the Ψ-axis will be explained first. The third axis of the interferometry system measures the displacement of the probe focusing objective. The beam supply to the probe will be explained in section 4.2.2. Next, the influence of environmental disturbances is discussed. After explaining the beam layout and alignment tolerances, the design and realization will be shown. The main components here are the laser mount, the R-stage optics assembly and the Z-stage optics assembly. Test results are included in the metrology system testing (section 4.6). Since interferometers are incremental, they have to be nulled before a measurement. Nulling of the R and Z interferometer and the probe interferometer will be discussed in sections 7.3 and 5.7, respectively.

4.2.1 R and Z interferometer concept

The Ψ-axis translates 400 mm in *r*, and 150 mm in *z*-direction, and rotates from -45° to +120° in ψ-direction. Similar to wafer stage metrology (Zanoni, 1989), one may mount a flat mirror or corner cube on the Ψ-axis bearing housing to measure its displacement. Due to various error sources, such as probe short stroke reaction forces, air pressure fluctuations and thermal effects, the Ψ-axis rotor position will not be equal to the Ψ-axis bearing housing position. Therefore focussing the beams onto the Ψ-axis rotor is applied. This allows for direct measurement of the displacement of the Ψ-axis rotor, and thus of the probe, in the sensitive *r* and *z*-direction.

Heterodyne and homodyne interferometry

Two types of laser interferometry systems are commercially available: homodyne and heterodyne. In homodyne interferometry a single frequency laser is applied, which is split in intensity. After recombination, multiple photodetectors are applied to obtain quadrature detection. This makes the system sensitive to intensity variations, for instance from reflectivity changes while translating laterally over the mirrors, from beam intensity profile changes during displacement (e.g. from ambient light) and from beam overlap variation. Since a single frequency laser is used, the beam can be supplied via a fibre. After interference, polarization must be maintained such that the receiving fibre should be kept free of stresses and thermal changes, making fibre reception difficult. It is therefore best to have the detectors at the recombination point. In heterodyne interferometry, a dual wavelength laser is applied that emits two orthogonally linearly polarized frequencies that differ by a few MHz. The recombined beam passes through a polarizer and is measured with a single photodetector. The beat signal of the two frequencies is compared to a reference beat signal from the laser, to directly determine the relative phase of the reference and measurement beam. The Doppler shift caused by moving one of the mirrors causes a phase change that is converted into displacement. Measuring phase makes this system insensitive to reflectivity variations of the mirrors and overlap changes. Further, quadrature detection is not necessary, so the recombined light can be transported to the detectors using fibres. Since the polarization of the supply beam must be maintained, this cannot be transported to the system by a fibre, and should be done with mirrors if the fibre is subject to varying stress (Knarren, 2003). Generally, a heterodyne system is less difficult to align and is less sensitive to noise (air turbulence, electrical noise and light noise).

The acquired Agilent heterodyne system is the only system that is commercially available in a 3-axis PCI PC-card version, which is convenient to integrate with the other system electronics (see Chapter 6). It consists of a stabilized HeNe Laser (type 5517C-003) with a 3 mm beam diameter output, high-performance fibre coupled remote receivers (E1709A) and the PCI processing electronics board (N1231B). The update frequency of the 36 bits output is 20 MHz. In dual pass, the resolution is 0.15 nm (4096x interpolation) and the maximum target speed is 0.35 m/s. Custom designed optics and alignment mechanisms can be applied, which allows for design and beam layout flexibility.

Focus on Ψ-axis

In the setup of Figure 4.3, the interferometer beam comes in from the top. This beam consists of 2 orthogonally polarized components with a slightly different frequency. At the polarizing beamsplitter (PBS), the out-of-plane polarization component passes straight into the pickup (PU) and the in-plane component is reflected towards the reference mirror (RM). After passing through quarter wave plate 1 (QWP 1), oriented at 45°, the beam becomes circularly polarized. After reflection at the reference mirror, the beam passes through the quarter wave plate again to become out-of-plane polarized. This beam now passes through the polarizing beamsplitter and quarter wave plate 2, and becomes circularly polarized again. The beam is now focused onto the Ψ-axis centre by a cylindrical lens. The Ψ-axis surface has been provided with a mirror by diamond turning, on which the beam reflects. After passing through quarter wave plate 2 again, the beam becomes in-plane polarized and is reflected towards the pickup by the polarizing beamsplitter, to join the first out-of-plane polarized beam. In short, one part of the beam travels straight through into the pickup, and the other part travels an extra distance between the reference mirror and the Ψ-axis. The resulting optical path difference (OPD) is detected by the interferometer electronics and converted into displacement. A similar setup is applied in vertical (z) direction, as already schematically depicted in Figure 4.1.

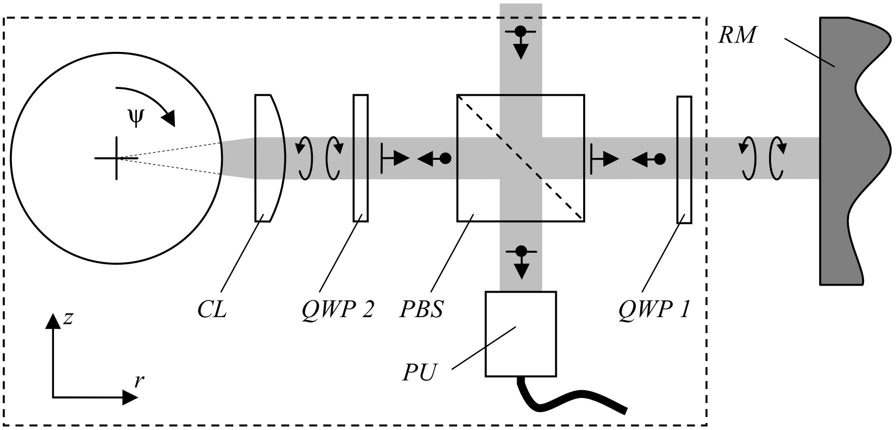

Figure 4.3: Interferometer setup for direct displacement measurement of Ψ-axis rotor

Focus on Ψ-axis surface or centre

In Figure 4.3, the beam is focussed onto the Ψ-axis centre. Focussing the beam onto the Ψ-axis surface is also possible. The main advantage here is that the alignment requirements for the cylinder lens are less critical, especially for rotation around the optical axis. According to Gaussian beam theory (O'Shea, 1985), the wavefront in the waist is flat. For cylindrical optics, the spot width is equal to the waist diameter D_0 of spherical optics, and is given by (4.1).

$$D_0 = \frac{4\lambda}{\pi\theta} \tag{4.1}$$

With a wavelength λ of 633 nm and a divergence θ of 0.15 rad (d = 3 mm and f = 20 mm), this gives a spot width of 5.4 µm. The small spot size makes it very vulnerable to scratches and dust on the mirror surface, which may well be equal to or larger than the spot. This would result in a total loss of modulation depth. The flat wavefront further reflects on the curved mirror surface, which will introduce curvature to the reflected wavefront that again reduces the modulation depth.

When the beam is focussed onto the Ψ-axis centre, alignment of the cylinder lens relative to the Ψ-axis rotor is critical (µm and µrad level). By fixing the lenses in the Ψ-axis bearing housing, this alignment will only have to be done once and will be sufficiently stable over time. The spot size on the mirror surface is now approximately 2 mm, making it robust to surface imperfections. Further, the cylindrical wavefront matches the mirror, making each ray perpendicular incident on the surface. Apart from aberrations of the lens, no curvature is thus introduced in the reflected wavefront. Although alignment is to be done with care, focussing the beam onto the Ψ-axis centre is more robust and is thus preferred.

Dual pass concept

When the cylinder lens is properly aligned to the Ψ-axis, this assembly basically acts as a flat mirror. The single pass layout as shown in Figure 4.3 is very susceptible to alignment errors of these two mirrors, as illustrated in Figure 4.4, left. Generally, the alignment between reference and measurement wavefront must be better than λ/8, or 50 μrad, to have sufficient modulation depth (Agilent, 2002). Changing this layout to a dual pass configuration resolves this sensitivity, as shown in Figure 4.4, right. Only an overlap error (walk-off) remains, of which a minimum of 10% is required. The doubled measurement path length doubles the resolution, but also doubles the sensitivity to environmental disturbances. Nevertheless, the reduced alignment sensitivity is considered to weigh well up to this.

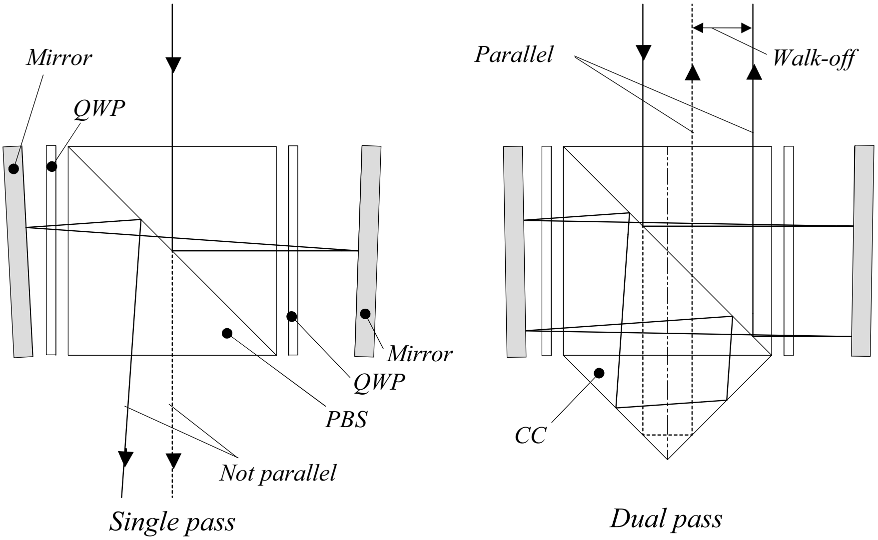

Figure 4.4: Sensitivity to mirror tilt of single and dual pass plane mirror interferometry (exaggerated for illustrational purposes)

4.2.2 Probe interferometer polarization rotation

Besides the R and Z-interferometer, a third interferometer is applied for measuring the displacement of the probe short stroke mechanism. As explained, a heterodyne beam cannot be supplied by a fibre and should thus be supplied by mirrors. It is therefore directed into a hole in the backside of the Ψ-axis rotor (Figure 4.7), aligned with its centre line. The polarizing beamsplitter inside the Ψ-axis rotates, but the polarization direction of the supply beam is constant; one horizontal and one vertical. The polarization direction of the supply beam must hence be rotated to match the orientation of the beamsplitter.

To achieve this, a quarter wave plate on the Z-stage gives the beam circular polarization. A second quarter wave plate on the rotated probe gives the beam a linear polarization again, but now aligned to the also rotated polarizing beam splitter. In Figure 4.5, this schematically depicted for a general case, with the initial polarization directions $\vec{E}_r$ and $\vec{E}_z$, and the orientation between the components ψ_1, ψ_2 and ψ_3.

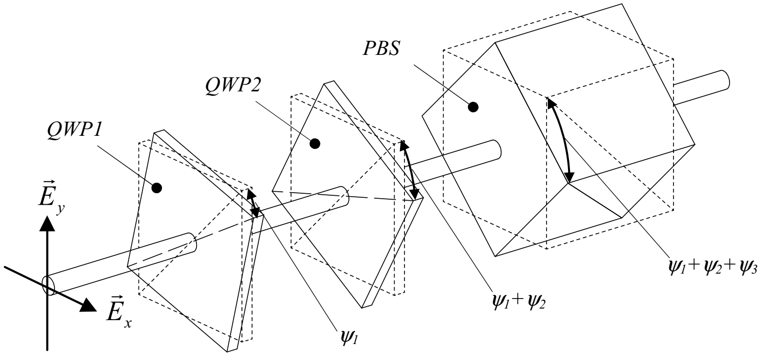

Figure 4.5: Polarization rotation with two quarter wave plates

To prove this, the supply beam can be described by the electric vector in Jones form (Hecht, 1998), where z is along the optical axis:

$$\vec{E} = \begin{bmatrix} E_x(z,t) \\ E_y(z,t) \end{bmatrix} = \begin{bmatrix} E_{0,x}e^{j\sigma_x} \\ E_{0,y}e^{j\sigma_y} \end{bmatrix} \quad with \quad \sigma = kz - \omega t \tag{4.2}$$

For plane polarized light, $\sigma_x = \sigma_y \pm m\pi$ with $m = 0, 1, 2, \ldots$. When $\sigma_x = \sigma_y \pm m\frac{1}{2}\pi$ with $m = 1, 3, 5, \ldots$, and $E_{0,x} = E_{0,y} = E_0$, the light is circularly polarized. For right polarized light (the y-component leads the x-component by 90° or $\pi/2$), the Jones representation is:

$$\vec{E}_{\Re} = \begin{bmatrix} E_0 e^{j\sigma_x} \\ E_0 e^{j(\sigma_x - \pi/2)} \end{bmatrix} = \begin{bmatrix} E_0 e^{j\sigma_x} \\ E_0 e^{j\sigma_x} e^{-j\pi/2} \end{bmatrix} = E_0 e^{j\sigma_x} \begin{bmatrix} 1 \\ e^{-j\pi/2} \end{bmatrix} = E_0 e^{j\sigma_x} \begin{bmatrix} 1 \\ -j \end{bmatrix} \tag{4.3}$$

When an incident polarized beam represented by its Jones vector $\vec{E}_i$ passes through an optical element, it is transformed to the transmitted wave $\vec{E}_t$. This transformation can be described by the Jones matrix A:

$$\vec{E}_t = A\vec{E}_i \tag{4.4}$$

A quarter wave plate with its fast axis in vertical direction can be described by:

$$A_{QWP} = \begin{bmatrix} 1 & 0 \\ 0 & -j \end{bmatrix} \tag{4.5}$$

To decompose the incident beam to the orientation of the quarter wave plate, it is multiplied by rotation matrix R_i:

$$R_i = \begin{bmatrix} \cos(\psi_i) & \sin(\psi_i) \\ -\sin(\psi_i) & \cos(\psi_i) \end{bmatrix} \quad with \quad i = 1,2\,or\,3 \tag{4.6}$$

The beam emerging after the second quarter wave plate, relative to the orientation of the polarizing beamsplitter, is now according to (4.7). In the final step, *cos*(ψ_1) and *sin*(ψ_3) have been replaced by c_1 and s_3 etc, for shortness.

$$\vec{E}_t = R_3\, A_{QWP}\, R_2\, A_{QWP}\, R_1\, \vec{E}_i =$$

$$= \begin{bmatrix} \cos(\psi_3) & \sin(\psi_3) \\ -\sin(\psi_3) & \cos(\psi_3) \end{bmatrix} \begin{bmatrix} 1 & 0 \\ 0 & -j \end{bmatrix} \begin{bmatrix} \cos(\psi_2) & \sin(\psi_2) \\ -\sin(\psi_2) & \cos(\psi_2) \end{bmatrix} \begin{bmatrix} 1 & 0 \\ 0 & -j \end{bmatrix} \begin{bmatrix} \cos(\psi_1) & \sin(\psi_1) \\ -\sin(\psi_1) & \cos(\psi_1) \end{bmatrix} \begin{bmatrix} E_x \\ E_y \end{bmatrix} \tag{4.7}$$

$$= \begin{bmatrix} E_x\left(\left(c_1c_2c_3 + s_1c_2s_3\right) + j\left(s_1s_2c_3 + c_1s_2s_3\right)\right) + E_y\left(\left(s_1c_2c_3 - c_1c_2s_3\right) + j\left(s_1s_2s_3 - \mathrm{c_1s_2c_3}\right)\right) \\ E_x\left(\left(s_1c_2c_3 - c_1c_2s_3\right) + j\left(\mathrm{c_1s_2c_3} - s_1s_2s_3\right)\right) - E_y\left(\left(c_1c_2c_3 + s_1c_2s_3\right) - j\left(s_1s_2c_3 + c_1s_2s_3\right)\right) \end{bmatrix}$$

When the first quarter wave plate is oriented at 45° relative to the supply beam, and the second quarter wave plate at 45° relative to the polarizing beamsplitter, $\psi_1 = \pi/4$ and $\psi_3 = -\pi/4$. Now, $c_1 = c_3 = ½\sqrt{2}$ and $s_1 = s_3 = -½\sqrt{2}$ and (4.7) simplifies to:

$$\vec{E}_t = \begin{bmatrix} E_y\left(\cos(\psi_2) - j\sin(\psi_2)\right) \\ E_x\left(\cos(\psi_2) + j\sin(\psi_2)\right) \end{bmatrix} = \begin{bmatrix} E_y\left(\cos(-\psi_2) + j\sin(-\psi_2)\right) \\ E_x\left(\cos(\psi_2) + j\sin(\psi_2)\right) \end{bmatrix} = \begin{bmatrix} E_y e^{-j\psi_2} \\ E_x e^{j\psi_2} \end{bmatrix} \tag{4.8}$$

The angle ψ_2 is equal to the global angle ψ of the Ψ-axis. Further, if the two plane polarized components f_1 and f_2 are assumed to be in phase and have equal amplitude E, their incident and transmitted Jones vectors are:

$$\begin{aligned} \vec{E}_{i,f_1} &= \begin{bmatrix} E \\ 0 \end{bmatrix} \Rightarrow \vec{E}_{t,f_1} = \begin{bmatrix} 0 \\ Ee^{j\psi} \end{bmatrix} \\ \vec{E}_{i,f_2} &= \begin{bmatrix} 0 \\ E \end{bmatrix} \Rightarrow \vec{E}_{t,f_2} = \begin{bmatrix} Ee^{-j\psi} \\ 0 \end{bmatrix} \end{aligned} \tag{4.9}$$

From this result it can be seen that the two quarter wave plates act together as a half wave plate since both $\vec{E}_{i,f_1}$ and $\vec{E}_{i,f_2}$ are rotated 90°, respectively counter clockwise and clockwise. Further, no mixing occurs and both components are exactly aligned to the splitting directions of the polarizing beam splitter. The horizontal and vertical components get a phase change that is linearly dependent of ψ, resulting in a total phase difference of 2ψ. When the probe objective mirror is fixed, and the Ψ-axis is rotated, an apparent displacement is thus measured equal to 2ψ times the laser wavelength of 633 nm. To compensate for this to an error below 1 nm, the angle of the Ψ-axis needs to be known with an accuracy smaller than $2\pi/633 = 10$ mrad, which is no problem.
A different embodiment of this principle, utilizing a dual pass layout, a corner cube and a fixed detector can be found in (Bockman, 1996). Due to the dual pass layout, the laser beam moves over the optical surfaces when the assembly is rotated.

This method was tested during assembly of the interferometry system. The probe interferometer supply beam is collinear with the Ψ-axis rotor centre line, and with no probe mounted, exits the rotor through a hole in the front into a pickup. A fixed quarter wave plate is on the Z-stage optics assembly as will be explained in section 4.2.6. A temporary quarter wave plate was installed inside the Ψ-axis rotor. With no geometrical path difference between the measurement and reference beam, rotation of the Ψ-axis should result in only the apparent displacement. Figure 4.6 shows the interferometer reading, and the result when compensated for the rotation according to the result of (4.9). The curve in the error is probably due to the coarse alignment of the temporary quarter wave plate and the pickup.

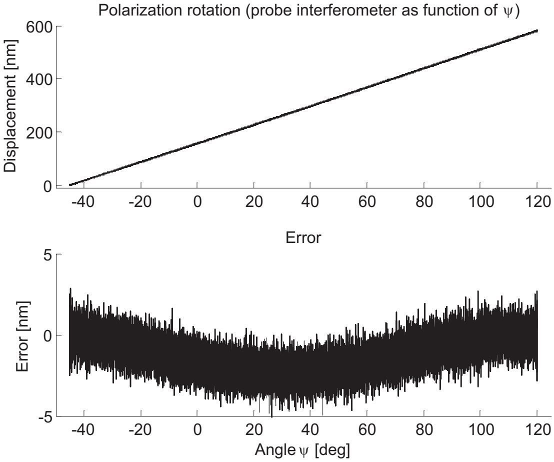

Figure 4.6: Polarization rotation test results

4.2.3 Environmental disturbances

One of the main disadvantages of interferometry compared to optical scales is the sensitivity to environmental disturbances. The optical path length is equal to the geometrical path length times the wavelength of the media in that path. Thermal expansion influences the geometrical path length of the optics, and the refractive index is a function of temperature and for gasses also of pressure and composition.

Thermal expansion

In the proposed dual pass layout, the measurement beam travels four times the combined thickness of the polarizing beamsplitter, two quarter wave plates and the lens more through glass than the reference beam. This is equal to 101.6 mm of BK7, 8 mm crystal quartz and 20 mm Fused Silica, respectively. With $\alpha_{BK7} = 7.1 \cdot 10^{-6}$ m/m/K, $\alpha_{quartz} = 7.6 \cdot 10^{-6}$ m/m/K and $\alpha_{FS} = 0.56 \cdot 10^{-6}$ m/m/K, the geometrical path length changes 720 nm, 60 nm and 11 nm per Kelvin, respectively. With $n_{BK7} = 1.517$, $n_{quarz} = 1.458$ and $n_{FS} = 1.458$, the total optical path length change is 1196 nm per Kelvin. The expected temperature change of the (covered) optics during a measurement is expected to be around 10 mK, giving 12 nm OPD error. In the dual pass layout this is equal to 3 nm displacement error.

Refractive index of air

Variation of the refractive index of air is generally the main source of uncertainty with path lengths larger than a few millimetres. The refractive index of air is mainly influenced by temperature, pressure and humidity. Other factors, such as CO_2 content, have less influence. The wavelength in air can be calculated with Edlén's formula (Edlén, 1966), or by later adaptations as summarized in Appendix G of (Cosijns, 2004). The Birch and Downs equation (Birch and Downs, 1993) is most commonly used for precision measurements around 20°C. Here, the pressure (*P)* in Pa , the temperature (*T)* is in K and the partial water vapour pressure (*H*) in Pa:

$$\begin{aligned} n_{PTH} = {} & \frac{2.7653 \cdot 10^{-4} \cdot P}{96095.43} \cdot \frac{1 + 10^{-8} \cdot (0.601 - 0.00972 \cdot (T - 273.15)) \cdot P}{1 + 0.0036610 \cdot (T - 273.15)} \\ & - H \cdot 3.63442 \cdot 10^{-10} + 1 \end{aligned} \tag{4.10}$$

As can be calculated from (4.10), the sensitivity to pressure variations is $2.68 \cdot 10^{-9}$/Pa, the sensitivity to temperature variations is $-9.30 \cdot 10^{-7}$/K and the sensitivity to humidity variations is $-3.7 \cdot 10^{-10}$/Pa. (Cosijns, 2004) also gives the typical daily variation for these parameters: 20 hPa for P, 0.1 °C for T and 1 hPa for H, giving an effect of $5.36 \cdot 10^{-6}$, $-9.3 \cdot 10^{-8}$ and $-3.7 \cdot 10^{-8}$, respectively. This thus gives large errors, especially pressure. Refractive index compensation is therefore applied by measuring the environmental conditions (Estler, 1985).

The expanded uncertainty of the Vaisala PTU300 sensor that is used for measurement of room pressure, temperature and humidity is 30 Pa, 0.2 K and 1% or 24 Pa, respectively. The dead path error for the interferometer path design is 0.5 m for the R-interferometer and 0.2 m for the Z-interferometer. Assuming that pressure, temperature and humidity are uncorrelated, gives a worst case uncertainty (2σ) of 102 nm in R and 40 nm in Z.

This does not yet include other uncertainties such as the accuracy of the Birch and Downs model and the vacuum laser wavelength. It must be noted that this is the absolute uncertainty. During a measurement, the trend in the environmental fluctuations is expected to be measured with higher resolution, be it with an offset compared to the absolute values. This will appear as a scaling error in the form measurement, which is relatively acceptable for optics at this level.

To improve this absolute uncertainty, the interferometers can be operated in vacuum or in a gas of which the refractive index is better known. This adds greatly to the complexity of the machine. The uncertainty is therefore accepted for now.

Turbulence

With the above described procedure, global environmental condition variations can be compensated for. Local variations of the refractive index due to turbulence for instance, will cause higher frequency disturbances of the signal. Two main sources of turbulence are the air-conditioning and the releasing boundary layer of the rotating spindle.

An enclosure around the metrology system, telescopic tubes or bellows around the beams, and a box around the beams are discussed in Appendix F. Besides these atmospheric solutions, the air inside the telescopic tubes may also be replaced with Helium. This reduces the effect of turbulence by a factor of 10 (Bryan, 1979; Bryan and Carter, 1979). An even more rigorous approach would be to apply a (low) vacuum in these tubes, as done in (Donaldson and Patterson, 1983) and (Thompson, 1989). A pressure of only 10 mbar would improve the uncertainty by a factor of 100. The required enclosure and vacuum forces would have a large impact on the design.

An ‘air shower’ of turbulent, well-mixed and well-conditioned air may also be blown through the beams, such that the average index of refraction is constant over the path length (Bobroff, 1987).

Since little quantitative data is available on the effect of turbulence, tests were performed on the machine to determine what level of shielding was required. Appendix F shows typical results of these tests. The rms noise level clearly decreases when the volume around the metrology system is enclosed by a tent. Fluctuations with a typical wavelength of 10-30 s are further reduced by telescopic tubes or a box, but fluctuations with a wavelength of several minutes are amplified now. The best results were eventually obtained with the easiest solution: the enclosure around the metrology system.

4.2.4 Beam layout

In Figure 4.7 the beam layout is shown that supplies the interferometer laser to the 3 interferometer axes, around the structure of the R- and Z-stage and the Ψ-axis. Note that the assembly is viewed from the backside for clarity. The laser (1) is aligned to the R-stage, on which also the R-stage optics assembly (2) is mounted. When the R-stage is repositioned (and thus also the Z-stage and Ψ-axis), the R-stage optics assembly moves away from or towards the laser at a constant distance under the horizontal reference mirror (3). Since an air bearing guides are used, the motion perpendicular to the laser will be in the order of micrometers.
At the R-stage optics, the beam is split by a 66% non-polarizing beamsplitter (NPBS1), where 33% passes through towards the Z-interferometer and 66% is reflected in *y*-direction toward a fold mirror (FM1). The Z-interferometer consists of a polarizing beam splitter (PBSZ), two quarter wave plates (QWPZ), a corner cube (CCZ) and a pickup (PUZ).

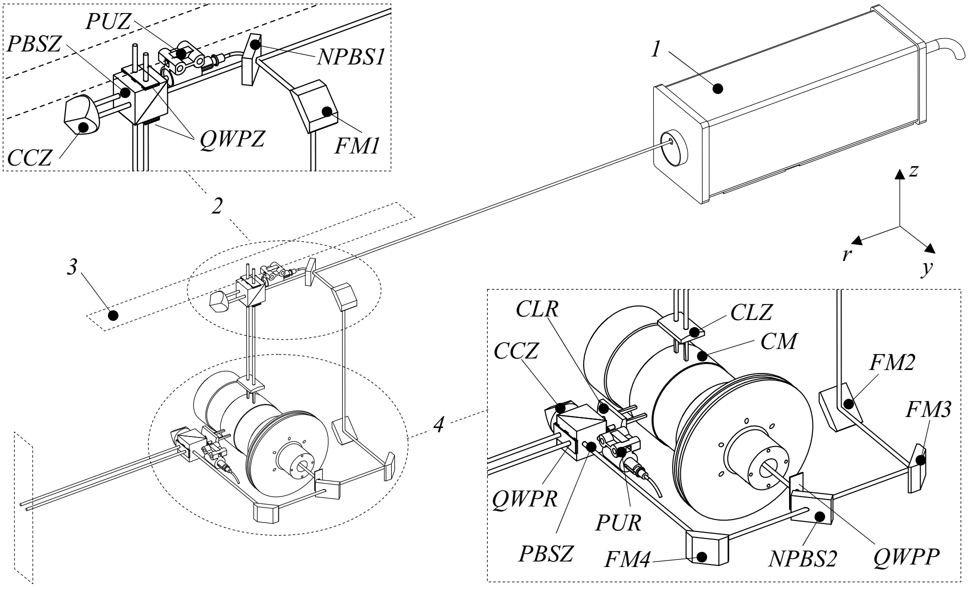

Figure 4.7: Interferometry system beam layout (backside view)

Fold mirror 1 and 2 (FM1 and FM2) together form a periscope between the R- and the Z-stage optics assembly (4). This allows the Z-stage optics assembly to move vertically relative to the R-stage optics assembly. After reflecting on fold mirror 3 (FM3), the beam arrives at a 50% non-polarizing beamsplitter (NPBS2). Here, 50% is reflected into the Ψ-axis rotor, aligned with its centre line. It passes through a quarter wave plate (QWPP), towards the probe interferometer.

The remaining 50% of the beam is directed towards the R-interferometer by fold mirror 4 (FM4). Just as the Z-interferometer, the R-interferometer consists of a polarizing beamsplitter (PBSR), two quarter wave plates (QWPR), a cube corner (CCR) and a pickup (PUR). Also shown here are the two cylinder lenses (CLR and CLZ), which are mounted into the Ψ-axis bearing housing. These lenses focus the interferometer beams onto the cylindrical mirror (CM) on the Ψ-axis.

4.2.5 Alignment tolerance analysis

Misalignment of the optical elements causes measurement errors, originating in wavefront tilt and curvature, cosine error and polarization mixing. A tolerance analysis was performed to investigate alignment requirements for the optical elements.

Wavefront tilt and curvature

Ideally, the measurement and reference wavefront are flat and perfectly overlapping. Due to alignment differences between the two wavefronts, they will be tilted and / or curved. When this is combined with relative displacement between the two, the average phase of the overlap area changes, which causes a measurement error. When w is the relative beam displacement (walk-off) over the stroke, ε is the total alignment difference, κ is curvature difference and λ is the wavelength, the phase error from tilt (ϕ_t) and curvature (ϕ_κ) is given by (Johnstone et al., 2004):

$$\phi_t = \frac{\pi w \varepsilon}{\lambda} \quad and \quad \phi_\kappa = \frac{\pi w^2 \kappa}{2\lambda} \tag{4.11}$$

With the phase written as an error part δ of the wavelength λ:

$$\phi = \frac{\delta}{\lambda} 2\pi \tag{4.12}$$

The resulting errors from tilt δ_t and curvature δ_κ are:

$$\delta_t = \frac{w\varepsilon}{2} \quad and \quad \delta_\kappa = \frac{w^2 \kappa}{4} \tag{4.13}$$

For a given error budget, one is free to choose the ratio between beam tilt and relative displacement, using equation (4.13). In the system described in this thesis, the relative beam displacement is expected to be small. In lithography systems for instance, the rotation of the stage is measured using two interferometers. A dual pass setup ensures the alignment of the wavefronts, but the relative beam displacement may amount up to several millimeters. The stages only translate in this application, giving minimal walk-off.

The alignment error between the measurement and reference wavefront should not be chosen larger than *λ/8* at the edge of the spot, to prevent fringes over the aperture (Agilent, 2002). Fringes will reduce the intensity of the spot, which decreases the modulation depth. The described system uses a beam diameter of 3 mm, which allows for a maximum misalignment of 50 μrad. With a maximum remaining relative beam displacement of 0.05 mm, this would result in an error of 1.25 nm. Similarly, a curvature difference of 2 m also results in 1.25 nm. Generally, these large curvature differences do not occur, making wavefront tilt the main alignment requirement.

Cosine error

When the measurement beams are not aligned with the global axes of the coordinate system, a cosine error will occur. This error is linear with the stroke and repeatable, and thus in principle calibratable. The R-stroke is 400 mm, but the geometrical path length travelled by the beam is 2 m. The maximum walk-off over this stroke is 0.05 mm, giving a measurement error of 0.6 nm. With the Z-path length of 0.7 m and similar walk-off values, the expected cosine error here is 1.8 nm.

Polarization mixing

The polarizing components (polarizing beamsplitters, quarter wave plates and polarisers) are not ideal. Their limited extinct ratio causes one polarization state to leak into the other (polarization mixing). Misalignment of these components relative to the chief polarization directions of the laser increases this mixing (Cosijns, 2004). Polarization mixing causes a periodic (non-cumulative) error, generally in the order of a few nanometers with proper alignment.

Alignment tolerances

The interferometer setup has been modelled in ZEMAX, to calculate the sensitivity to alignment and position errors of the individual components (Figure 4.8). This has been calculated for focussing onto the surface as well as the centre of the Ψ-axis, and for different path lengths. As already discussed before, focussing onto the centre of the Ψ-axis is more sensitive to alignment but more robust in practice. The alignment sensitivity is largest when the beam path is longest, which is 400 mm for the R-interferometer in the left-most position. These (worst-case) values have been used as alignment tolerances for the system.

Figure 4.8: ZEMAX model of Z-interferometer (focus on Ψ-axis surface case)

With this model, the sensitivity of each individual direction of each component has been determined. Next, the alignment budget has been divided over the components such that the system can be assembled and aligned piece by piece, and that the alignment directions are decoupled as much as possible. The most critical alignments are the laser parallelism to the R- and Z-stage and the 3 beamsplitters, for which alignment resolutions between 5 and 30 µrad are to be achieved. Hereto alignment mechanisms are designed as further explained in the next section.

The model also gives the nominal wavefront error due to aberrations. With a slightly different lens from the one eventually used, the rms error is 0.0016 waves (1.0 nm) and the peak-to-valley error is 0.015 waves (9.5 nm).

Alignment procedure

The interferometry system will be assembled in the same sequence at which the beam arrives at the components. To minimize the relative beam displacement, the beams will be aligned to the motion direction of the stages. This minimizes walk-off errors as described by equation (4.13), but may give rise to cosine errors in case of misalignment of the stages. These will have to be calibrated later.

Beams in r and z-direction will be aimed at a Position Sensitive Detector (PSD), with which the spot position can be measured to a few micrometer (after averaging). While moving the stages through their range, the components are manipulated until the spot displacement is minimal. This gives sufficient resolution to achieve the above mentioned alignment requirements.

A pentaprism will be inserted in beams in y-direction. This deflects the beam at an inherent square angle, allowing for alignment in one direction. By executing the procedure in horizontal and vertical direction, the beam can be aligned in φ and θ-direction.

The cylinder lenses in combination with the cylindrical Ψ-axis mirror act as a flat mirror. Alignment can therefore be done using a Fizeau interferometer, to minimize the fringes over the aperture. This is described in section 4.2.7.

4.2.6 Design and realization

The interferometry system consists of an adjustable laser mount and the R and Z-stage optics assemblies. This section describes the design of these assemblies in general and some of the components in detail.

Laser mount

The laser is to be aligned parallel to the R-stage in ψ and θ-direction within 5 μrad. In Figure 4.9, the laser mount assembly and exploded view are shown. The laser (1) is bolted to a rectangular tube (2) with three spacers (3) in between. The coarse alignment of the laser is done by sliding the laser while tightening this connection and adapting the spacers if necessary. The tube is mounted to the two plates (4 and 5), which are connected by a triangular plate (6), and bolted to inserts in the granite base (7). An aluminium shield (8) is also added to prevent heat from the laser reaching the base block or metrology frame by direct radiation or convection.

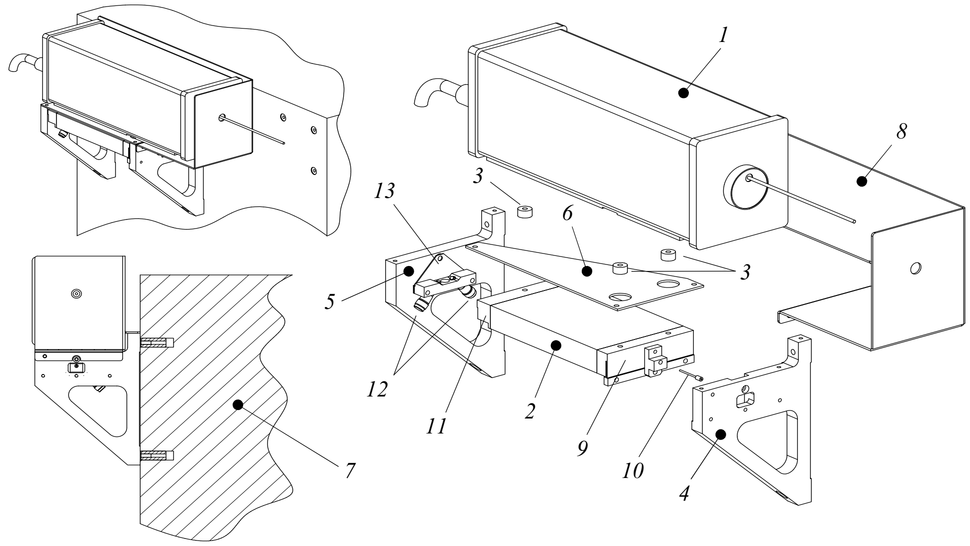

Figure 4.9: Laser mount design

The rectangular tube has two pieces glued to either end. The right one (9) has a plate spring machined into it by wire-EDM. A strut (10) is glued in to form a cross-spring that leaves the ψ and θ-rotations free. The fixed end of this cross spring is mounted to the fixed right plate (4).

At the left end-piece of the tube (11), two orthogonal micrometer screws (12) are positioned under 45°, in contact with two 45° faces that are machined in the left end-piece. This allows for independent actuation of both rotations, while the micrometer screws are reachable and the laser weight provides the preload on the contacts. Once the laser is aligned, the position is locked by an A-shaped locking plate (13), that constrains the ψ and θ-rotations to the fixed left plate (5). The micrometer screws can then be screwed back, leaving the laser constrained statically determined, with four degrees of freedom constrained at the front and two at the backside. The laser mount assembly is shown in Figure 4.10.

Figure 4.10: The laser mount

Adjustable optics mounts

Several of the previously discussed optical components have to be aligned to within several tens of microradians, for which dedicated alignment mechanisms have been designed. An alignment mechanism generally consists of a guidance, an actuator and a means of locking.

Due to the absence of friction, flexure hinges allow for infinite positioning resolution, and can well be machined into the mount by wire-EDM. The stroke limits are best machined into the mount as well, to prevent failure of the hinge. Several degrees of freedom can be incorporated into one mechanism this way, resulting in a compact and stable mechanism. These are therefore common practice in opto-mechanical instruments (Van der Lee et al., 2003).

To achieve microradian resolution for lever lengths in the order of 50 mm, micrometer resolution actuation is required. Micrometer screws or differential screws can be applied to achieve this, in combination with a separate locking mechanism to exclude the instability of these screws from the structural loop. These screws are relatively large compared to the optics to be adjusted, and it is difficult to prevent a shift during locking. The micrometer screws may be removed after locking to save space.

Two small screws, in push-pull setup, can also be applied. An M2 with a pitch of 0.4 mm allows for a coarse adjustment of approximately 0.01 mm, and the second screw is used for fine adjustment by deformation of the thread and contact points. Small screws are best used due to the lower stiffness of the threads and smaller contact surface. The adjustment is somewhat cumbersome, but the main advantage is that a separate locking mechanism is not required as long as the two screws preload each other. Further, the required space is much less compared to the micrometer or differential screws. Since tightening the two screws against each other introduces a moment, the two screws should be aligned perpendicular to the hinge to prevent parasitic rotations. Push-pull screws are applied throughout the alignment mechanisms of the interferometry system.

The optics are bonded to the mechanism. To minimize deformation, they are mounted onto three raised areas. In the centre of these a 0.1 mm deep recesses are machined in which a drop of adhesive is deposited. Shrinking of the adhesive during UV curing preloads the contacts, providing a stable connection.

The mounts of NPBS1 and FM1 must be adjustable for one rotation, and the mounts FM3, NPBS2 and FM4 for two rotations. These mounts are monolithically machined from aluminium and black anodised against stray light reflections. The M2 push-pull screws are aligned perpendicular to and at the centre of the hinge.

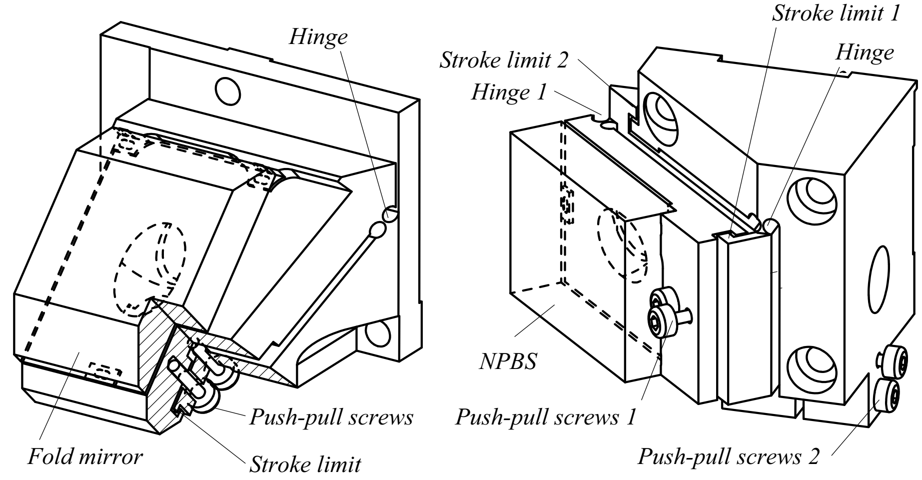

FM1 Mount *NPBS2 Mount*

Figure 4.11: Alignment mechanisms for 1 (left) and 2 (right) rotations

The polarizing beamsplitters are anti-reflection coated, just as both sides of the quarter wave plates. The quarter wave plates were therefore bonded to the beamsplitters with spacers in between to create an air-gap. The PBSR and PBSZ assemblies (Figure 4.12) are to be aligned in two rotations with higher resolution than the previously discussed mounts. Space unfortunately was limited, since the corner cube and pickup are close by and two beams pass through the beam-splitter on four sides.

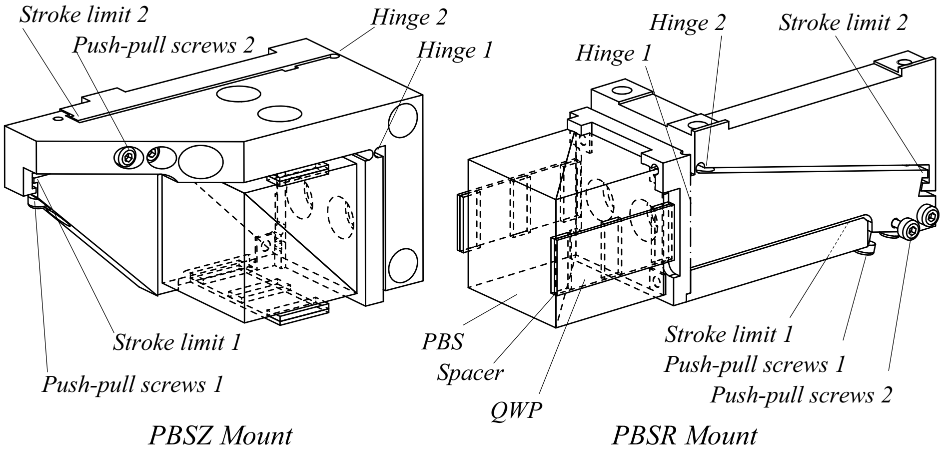

Figure 4.12: Beamsplitter mechanisms for 2 rotations

Both mechanisms are assembled from two parts. A lever is glued to the moving part of hinge one (Figure 4.12), with the other end interlocking with the monolith to form stroke limit 1. Due to the space constraints, these levers actuate the hinges on the side instead of in the centre, which will cause parasitic rotation. This can be compensated with the second available rotation, since two of the three rotations of a beam splitter have the same first order effect.

R-stage optics assembly

The R-stage optics assembly consists of a central aluminium beam (1 in Figure 4.13) to which the mounts of NPBS1 (2), PBSZ (3), CCZ (4), FM1 (5) and the pickup (6) are mounted. This beam is bolted to the read-head arm (7) that is connected to the R-stage position frame (8), as discussed in section 3.5.4. At the other end, the beam is bolted to a plate (9) which is also connected to the R-stage position frame (8). The R-stage position frame provides a stable base for the optics, as explained in Chapter 3. A dowel pin (10) in the read-head arm and shoulder bolts (11) in the plate connection provide some repeatability in case the R-stage optics assembly needs to be removed. Since the construction is statically determined, no tight position tolerances are required, the position only needs to be repeatable. Some realignment can probably not be avoided.

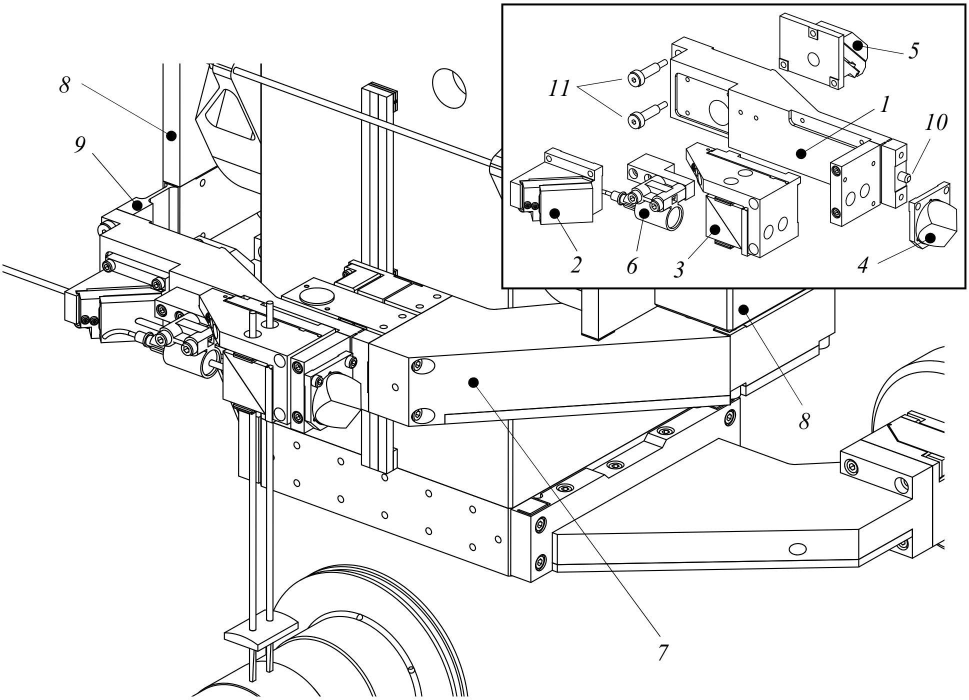

Figure 4.13: R-stage optics assembly

Figure 4.14 shows the R-stage optics components (left) and the assembly (right). The assembly is black anodized against stray light reflections. This assembly will be protected by a cover.

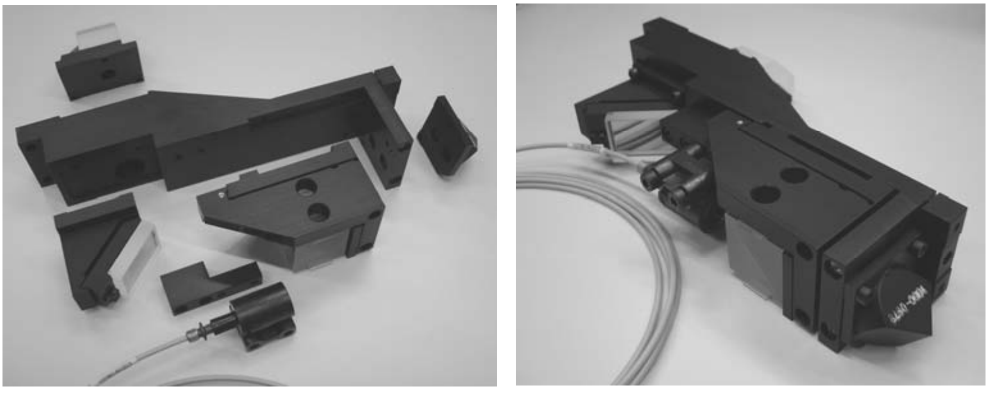

Figure 4.14: R-stage optics assembly

Z-stage optics assembly

The Z-stage optics assembly consists of two beams (1 and 2), which are mounted left and right of the Ψ-axis mount (3). A shoulder bolt (4) constrains three degrees of freedom at the backside. A plate (5) is connected to the Z-stage mounting interface (6), to which the two beams are connected via two shoulder bolts (7) that constrain the remaining three degrees of freedom. In between the two beams, a bridge (8) is connected, again with two shoulder bolts (9), to which the NPBS2 (10) and QWPP (11) mount are attached. This bridge has a flexure to relieve the distance between the beams which was already constrained by the shoulder bolts and the Ψ-axis mount. No tight position tolerances are required for the shoulder bolts since the structure is statically determined. They only provide some repeatability in case of disassembly.
The mounts for FM2 (12) and FM3 (13) are connected to the left beam (1), and the mounts for FM4 (14), PBSR (15), CCR (16) and the pickup (17) are connected to the right beam (2).

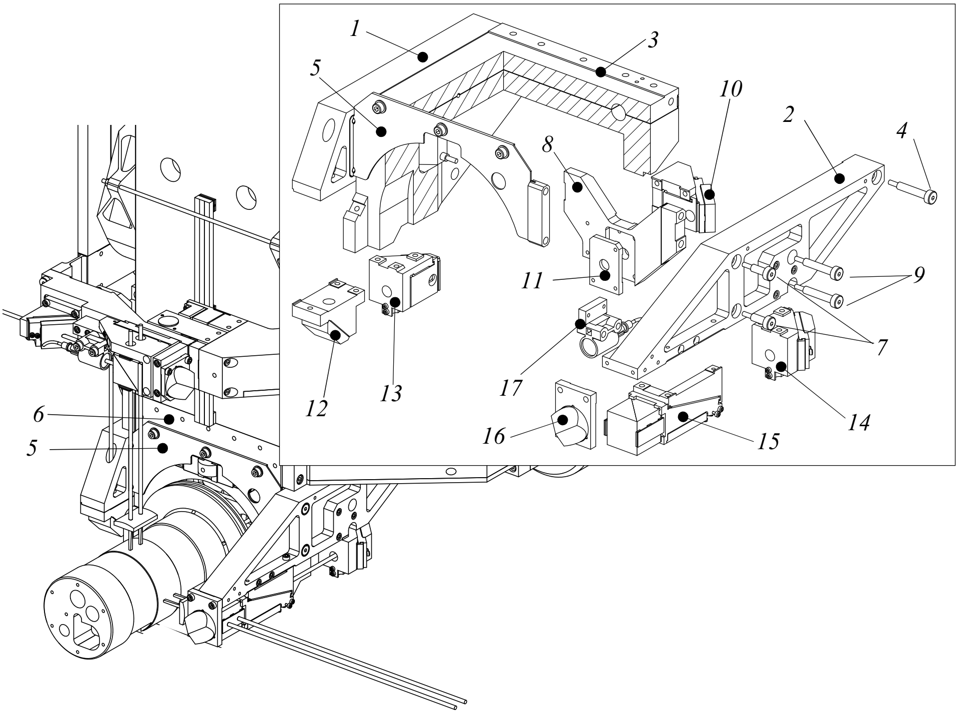

Figure 4.15: Z-stage optics assembly

Figure 4.16 shows the optics mounts (left) and the Z-stage optics assembly (right) as it is assembled apart from the Ψ-axis mount. After alignment, this assembly is also protected by covers.

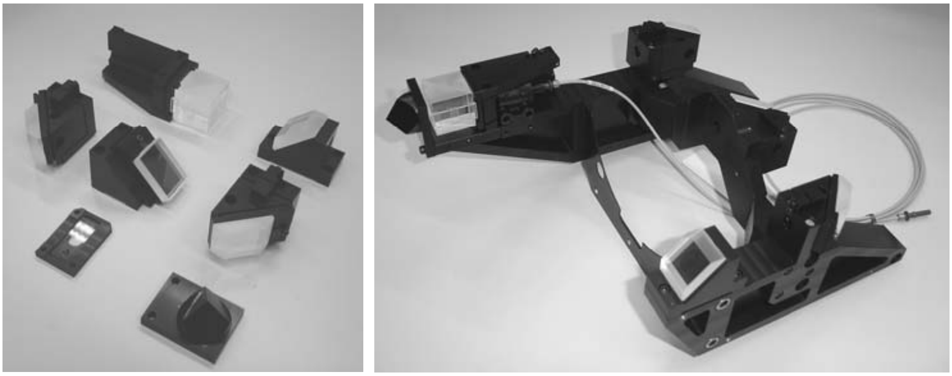

Figure 4.16: Realized Z-stage optics mounts and assembly (upside down)

4.2.7 Assembly and alignment

Figure 4.17 shows the interferometry system assembled to the machine. A general purpose mounting plate is attached to the Ψ-axis mount for testing. The laser was aligned by attaching a PSD to the R-stage. Over the 400 mm stroke, the displacement measured at the PSD was 5 µm in y-direction, and 1 µm in z-direction, which is equal to an alignment of 12.5 and 2.5 µrad. The periscope beam between the R and Z-stage was aligned parallel to the Z-stage to within 2.5 µm over 130 mm stroke. Together with the alignment of the interferometers, this has resulted in 10 µm over 130 mm for the Z-interferometer and 10 µm over 300 mm for the R-interferometer. This is within the cosine error and walk-off budget.

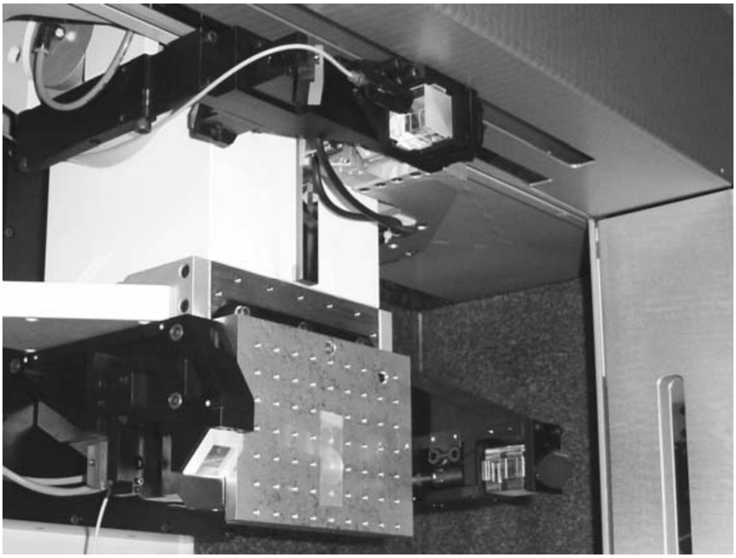

Figure 4.17: Interferometry system as assembled on the machine

To aid aligning the probe interferometer collinear to the Ψ-axis, a central through hole is present in the rotor through which the beam exits at the front. To align the beam parallel to the Ψ-axis centre line, a pentaprism is attached to the rotor that points the beam down in z-direction onto a fixed PSD. Moving the Z-stage up and down shows the misalignment. Rotating the Ψ-axis 90° allows for the same with the R-stage. Next the pentaprism is replaced with a PSD, such that rotating the rotor shows the eccentricity. The alignment and position were iteratively adjusted this way, until the beam was parallel to the Ψ-axis centre line within 100 µrad in φ and 12.5 µrad in θ-direction, and centred to 30 µm in r and 50 µm in z-direction.

Cylinder lens alignment

The cylinder lenses in the Ψ-axis housing are bonded into two cups, which are in turn bonded to the Ψ-axis housing. Shims are applied to adjust focus, and a removable 2DOF manipulator is used to adjust alignment while the adhesive is curing (Figure 4.18, left).

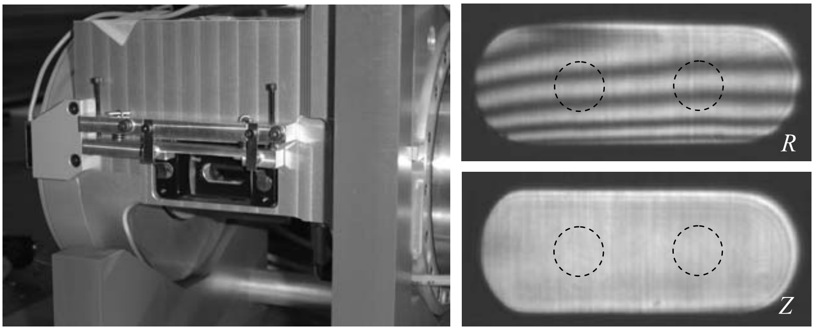

Figure 4.18: Cylinder lens alignment manipulator and measured interferogram

During alignment, a Phase-Shifting Interferometer is used to measure the reflected wavefront quality. The two final interferograms are shown in Figure 4.18, right. In R-direction some tilt is still present due to shifting during curing of the adhesive. The reflected wavefront error is 56 nm PV in R and 79 nm PV in Z over the ∅3 mm pupils, with tilt removed. This wavefront error mainly consists of the spherical aberration of the cylinder lens.

4.3 Upper metrology frame

The reference mirrors are to be supported by the upper metrology frame (Figure 4.1), either as separate mirrors or as an integral part. The flatness of the mirrors should be highly stable at all times, as well as their alignment relative to the lower metrology frame.

4.3.1 Concept

The main parameter in the design of the upper metrology frame is the choice of material, where the optimum trade-off between mechanical and thermal behaviour must be found. Availability and manufacturability play a role here since large pieces of (sometimes exotic) materials are involved. One has to take this into account in the design.

Disturbances

Thermal disturbances are the main error source, and originate in environmental temperature fluctuations, internal heat sources (actuators, read heads etc.) and operator body heat radiating onto the machine. Mechanical disturbances are vibrations and deflections of the granite machine base and acoustical excitation. The sensitivity of the metrology frame to these disturbances is minimized by optimizing the thermo-mechanical behaviour, the eigenfrequency, by statically determined mounting to the base and by enclosing it with a shield.

Material selection

The beams with the reference mirrors should stay as straight as possible under thermal gradients. The parameters that describe the transient thermal behaviour of a material are the expansion coefficient α, the thermal conductivity k and the specific heat c_p. The curvature of a beam due to a non-uniform heat flux (Figure 4.19) is proportional to the thermal sensitivity α/k and to the ratio of the wall thickness b and the beam width B, according to (4.14) (Breyer and Pressel, 1991).

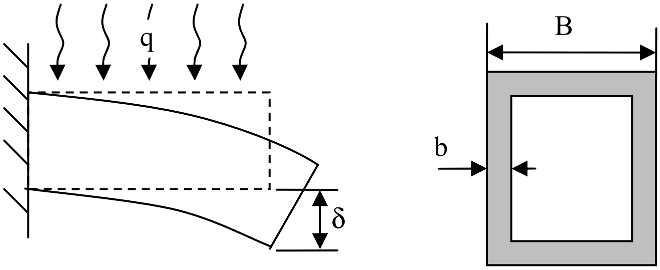

Figure 4.19: Deflection due to a temperature gradient from a single sided heat flux

$$\delta \sim \frac{\alpha}{k}\frac{B}{2b} \tag{4.14}$$

For a beam to stay straight under the influence of a heat flux, either temporary (operator) or continuous (read heads), the ratio of expansion coefficient and conductivity should thus be small, and the conductive area between top and bottom should be large.

The time dependent behaviour of a body is described by (4.15). For natural convection, the convection coefficient h is generally constant (5 W/m^2/K). The volume V and surface area A_s are determined by the geometry, and the density ρ and specific heat c_p are material properties.

$$\frac{dT}{dt} = -\frac{hA_s}{\rho c_p V}(T - T_\infty) \quad \Rightarrow \quad \frac{T - T_\infty}{T_1 - T_\infty} = e^{-\frac{hA_s}{\rho c_p V}(t - t_c)} \tag{4.15}$$

In this formula, the temperature T of the body is supposed to be uniform. To also include the temperature distribution, the volumetric thermal diffusivity is defined as $k/(\rho c_p)$, with conductivity k. This parameter describes how fast a body adapts to a new environmental temperature, and how long it takes for the distribution to be uniform again.

If the expansion coefficient is also included, the volumetric thermal stability is defined as $k/(\alpha\rho c_p)$. This also takes the amount of deformation into account that is caused by the non-uniform temperature distribution, which the thermal diffusivity does not.

One can go two ways now. Either one goes for a large thermal time constant, such that the frame is continuously but slowly changing temperature and curvature, but does not drift too much during a short measurement, or one goes for a small time constant that swiftly follows room temperature at a uniform distribution and thus continuously stays straight. The dimensions of the part determine whether one should go for a high or low thermal diffusivity.

From a mechanical point of view, high stiffness (Young's modulus E) is required against distortion due to internal and external loads. For dynamic loads a high first resonance and/or large material damping is required to minimize amplitude. Since material damping for most high stiffness materials is very small, the specific stiffness E/ρ is the parameter used. Formula (4.16) gives the relation between geometry, material and eigenfrequency. It can be seen that a high structural frequency is obtained by high E/ρ, and a large percentage of material on the outer perimeter of the beam cross-section (i.e. a large thin walled structure).

$$f_e \sim \sqrt{\frac{I}{A} \cdot \frac{E}{\rho}} \tag{4.16}$$

In Table 4.1, the above described properties are listed for some possible upper metrology frame candidate materials. Aluminium and Invar were for instance compared in (Ruijl, 2001), Zerodur is used in (Becker and Heynacher, 1987; Jäger et al., 2001) and granite was applied in (Takeuchi et al., 2004). Further, it has also been indicated whether a material can be polished or diamond turned, such that the reference mirrors can be applied directly onto the frame, perhaps with an extra reflective coating.

Property	***Unit***	Al Alloy 6061	Invar 36 (Carpenter)	Super Invar 32-5 (Carpenter)	Zerodur (Schott)	SSiC (CoorsTek)	Al_2O_3 [1] (CoorsTek)	Impala granite (Botech)
E	$\times 10^9$ N/m^2	69	141[2]	145	90	410	303	65-85
ρ	$\times 10^3$ kg/m^3	2.7	8.1	8.1	2.5	3.15	3.7	2.9
E/ρ	$\times 10^6$ Nm/kg	26	17.4	17.9	36	131	81	22-29
α	$\times 10^{-6}$ m/m/K	24	1.3	0.6	0.05[3]	2.1	6.1	5-6
k	W/m/K	180	10.5	10.5	1.46	175	24.7	3.2
c_p	J/kg/K	880	515	515	800	658	880	800
α/k	$\times 10^6$ m/W	0.13	0.12	0.06	0.03	0.012	0.25	1.7
$k/(\rho c_p)$	$\times 10^6$ m^2/s	76	2.5	2.5	0.73	84.4	7.6	1.4
$k/(\alpha \rho c_p)$	m^{2}K/s	3.2	1.9	4.2	14.6	40	1.24	0.25
Machinability		++	+	+/-	+/-	-	+/-	+/-
Mirror (polish / SPDT)		Yes	No	No	Yes	Yes	Yes	No

Table 4.1: Material properties (optima marked in gray)

Many types of Silicon Carbide exist (Van Veggel, 2007), but Sintered Silicon Carbide (SSIC) has the best properties. As can be seen from the table, it has twice the stiffness of steel and only slightly higher density than Aluminium. This material has thus a superior E/ρ. The expansion coefficient of Zerodur is by far the lowest. The thermal conductivity is also very low, especially compared to SSiC and Aluminium. Invar also has very low conductivity. Remarkably, the thermal sensitivity is better for SSiC than for Zerodur. The volumetric thermal diffusivity, describing the uniformity and magnitude of the temperature distribution, is slightly higher for SSiC than Aluminium. For Zerodur this is two orders of magnitude smaller. Zerodur will thus constantly have large temperature gradients with little deformation as a consequence due to the low α. This is also reflected by the volumetric thermal stability. SSiC is even better.

SSiC and Zerodur basically operate in two different ways to have good thermal stability: SSiC has a very uniform temperature with a small but present thermal expansion, while Zerodur always has thermal gradients but these have no effect due to

---

[1] *AD-96 (96% purity)*

[2] *Annealed*

[3] *Expansion class 1 (class 0 = $0.02 \cdot 10^{-6}$m/m/K and class 2 = $0.1 \cdot 10^{-6}$m/m/K)*

the extremely low α. All other materials perform much worse compared to SSiC and Zerodur.

Based on the thermal and mechanical properties, Silicon Carbide is the material of choice for the metrology frame. Care must be taken in the design, since it is very hard and brittle, and thus difficult to machine. It can only be ground with diamond and even then it is very time consuming. It is only recently becoming available in high-precision custom shapes. The fact that the material is polishable, is also a great advantage. Machining the mirrors directly onto the side of the beams avoids the need for assembly and alignment, and thus greatly improves mirror flatness stability. Polishing and coating beams of this size requires special tools and expertise. Manufacturer CoorsTek (www7) agreed on fabricating these parts, and was closely involved in the further design process of the upper metrology frame.

Layout

The length of the horizontal beam is approximately 950 mm and the cross-section is 100 mm wide and 120 mm high. The vertical beam is approximately 330 mm high and has the same cross-section as the horizontal beam. The base design allows for supporting the frame in vertical direction to the lower metrology frame, and backwards directly to the granite base. Providing support points on the granite base directly behind the frame has greatly affected the choice of motion system concept, which has already been commented in section 3.1.3.
To keep the horizontal mirror beam stationary relative to the lower metrology frame, it will be supported by two Super Invar struts, which are connected to the mirror surface of the beam on one side, and to the steel lower metrology frame on the other side (Figure 4.20). Here, a material with the smallest expansion coefficient is desired, which is Zerodur. For machinability and robustness, however, Super Invar was chosen. Since the spindle is made of steel that sits on the granite surface, the steel lower metrology frame has the same height as the mounting surface of the spindle.

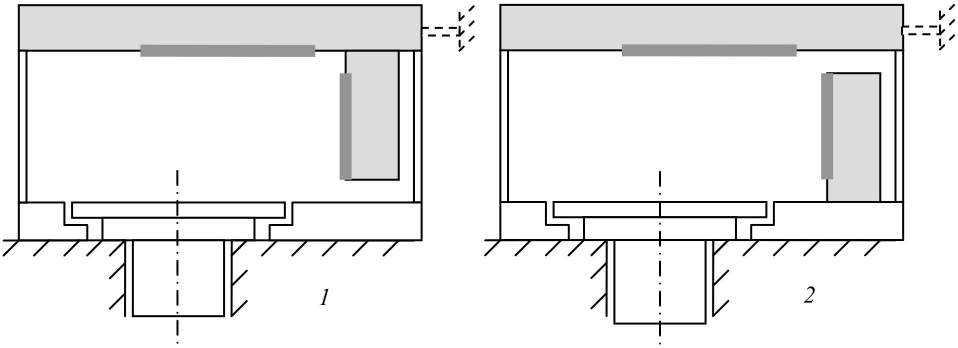

Figure 4.20: Metrology frame layout options (horizontal support discussed later)

The vertical mirror beam can now be mounted upwards to the horizontal beam (Figure 4.20, left), or downwards directly onto the lower metrology frame (Figure 4.20, right). In both cases there is a large thermal length between the spindle centre line and the vertical mirror face. In the second case, less mass is to be supported, but small deflections in the granite base are amplified in mirror displacements at the top of the vertical beam. Since keeping the mirror alignment constant is critical, the first option is preferred. The horizontal constraint (dashed), and the out of plane constraints will be further discussed later.

Silicon Carbide manufacturing

Extensive information on properties, manufacturing processes and design guidelines of different types of SiC can be found in (Van Veggel, 2007), on which this section is based. Sintered Silicon Carbide (SSiC) is manufactured by cold isostatic pressing α-SiC powder combined with organic binders and sintering aids, at about 2000 bar. The compacted powder exhibits chalk-like behaviour and is called the 'green' state. In the green state the substrate can be machined by conventional milling to make holes, pockets etc. The minimum wall thickness is generally about 2 mm, and all sharp edges must be rounded or chamfered. Further, shape limitations are similar to standard CNC machining. The green shape is pressureless sintered next, at approximately 2100°C in a non-oxidizing environment. Shrinkage during sintering is about 17%, which can be predicted to approximately 0.4%.

After sintering, the material becomes extremely hard but also brittle. This means that all machining (grinding or polishing) must be done with diamond abrasives. Machining is very time consuming and tool wear is high. The attainable roughness after grinding is $R_a \approx 0.3$ μm, and polishing can improve this to 1 nm. SSiC contains an open porosity of about 3%, so micro holes (excluded from the roughness figure) must be expected to cause stray light.

Frame structure

Several frame structures have been evaluated from thermal and mechanical point of view (Figure 4.21). For straightness of the beams, the solid version is best since it is least susceptible to thermal gradients. Mechanically however, this is not optimal since the inner core material contributes little to the bending stiffness (4.16), resulting in a first eigenfrequency of 494 Hz. Since the outer dimensions are fixed, removing the inner core to obtain a square tube significantly increases the eigenfrequency, typically to 617 Hz for 15 mm wall thickness.

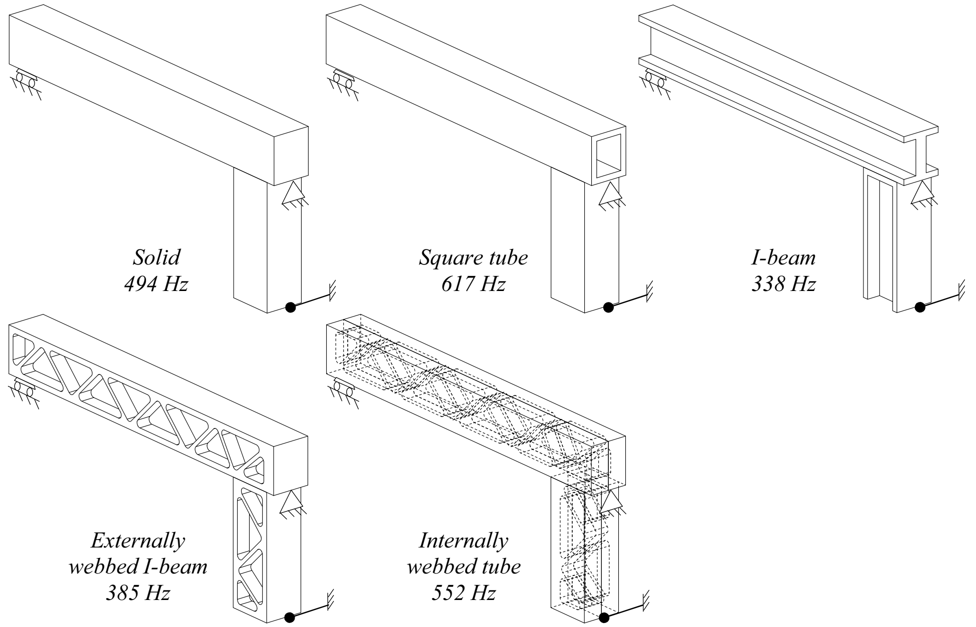

Figure 4.21: Possible frame structures and indicative 1^{st} eigenfrequencies

From a manufacturing point of view, pressing a solid and then machining it in the ‘green state’ from the outside is easier. The I-beam and I-beam with webbing are made this way and typically result in 338 Hz and 385 Hz eigenfrequency, respectively. To make a more torsionally stiff structure this way, one may machine two open back halves and bond or braze them together, obtaining an internally webbed tube. This would typically result in 552 Hz eigenfrequency, but production is relatively difficult.

Curvature due to thermal gradients in steady state conditions for instance occurs when a continuous heat flux is applied on the bottom of the beam, such as coming from the linear scale read heads. When this flux is transported upwards to the top of the beam, some of it is extracted from the beam by natural convection. The amount of convection is linearly dependent on the surface area in contact with outside air. This area is minimal for the solid beam. Next comes the I-beam, then the square tube and next the I-beam with webbing. The amount of convection on the inside of the closed box structure depends on the pocket size.

In close cooperation with the beam supplier, it was chosen to apply the square tube option since it is the best compromise between thermal and mechanical behaviour and manufacturability. The 900 mm long beam is made out of one piece, and the mirror is polished onto one side. No CVD coating is applied, since sufficiently low roughness is achievable without it.

Reducing thermal disturbances

Besides minimizing the sensitivity to thermal disturbances of the upper metrology frame, the magnitude of these heat loads can also be minimized. In (Ruijl, 2001) the metrology frame is enclosed in an aluminium box, which acts as a low-pass filter for dynamic thermal disturbances such as operators and environmental fluctuations. The high conductivity of aluminium creates a uniform temperature distribution over the shield, thereby also creating a uniform heat load on the metrology frame inside and thus reducing thermal gradients in the frame. Simulations in the next section will show that this simple solution is sufficient, and no active thermal stabilization is required.

Conclusion

Silicon Carbide is the material of choice for the upper metrology frame, since it is least susceptible to thermal gradients under steady state as well as dynamic heat loads. The frame is built out of 2 rectangular tubes forming a square that is supported by Super Invar struts. The mirrors are polished directly onto the sides of the tubes. Passive shielding is applied by an aluminium box. Thermal and mechanical simulations will be performed in the next sections to simulate the performance of this concept, and to optimize the dimensions.

4.3.2 Thermal analysis

To estimate the stability of the square tube Silicon Carbide metrology frame and to optimize the wall thickness, a thermal analysis has been conducted. After identifying the heat loads and heat conduction mechanisms that are present, the response is simulated.

Heat loads

Three main disturbances have been identified for which the response of the upper metrology frame is calculated.

1. The periodic fluctuation of the environmental temperature (air conditioning), which is assumed to be 20±0.2°C, typically with a period of about a half hour (Ruijl, 2001).
2. The heat load of an operator standing close to the machine, for instance while loading and aligning a product. The radiative heat loss of a human body is approximately 100 W (www1). The heat load on the shield can be calculated with (4.17). The Bolzmann constant $\sigma = 5.67 \cdot 10^{-8}$ W/m^{2}K^4. The outside temperature (T_1) of a clothed human is about 28°C and the temperature of the shield (T_2) is 20°C. The emissivity (ε_1) of a human is near unity and about 0.1 for the anodized aluminium shield (ε_2). The surface area of a human (A_1) is about 2 m^2 and 0.2 m^2 for the shield (A_2). The view factor F_{12} is estimated at 5% at 0.5 m distance. This gives a total heat load on the metrology frame shield of about 1 W.

$$q_{1-2} = \frac{\sigma\left(T_1^4 - T_2^4\right)}{\frac{1-\varepsilon_1}{\varepsilon_1 A_1} + \frac{1}{A_1 F_{12}} + \frac{1-\varepsilon_2}{\varepsilon_2 A_2}} \tag{4.17}$$

3. The read heads of the linear scales are situated directly underneath the horizontal beam, and dissipate about 1W each. Part of this will be transmitted to the R-stage by conduction, and part of it will be transmitted to the upper metrology frame by convection and radiation.

Required thermal stability

The position as well as the flatness of the mirrors should be constant over time, which is determined by rigid body motion of the frame and thermally induced deformation of the frame.

The temperature variation in the SuperInvar struts during a 15 minute measurement is estimated at 0.01K and their length is 380 mm. This results in small z-displacement of 2.3 nm. If this occurs in only one of the struts, the mirror tilts with a negligible 2.5 nrad. The three struts in y-direction may cause small drift in y, φ and θ, to which the interferometry system is insensitive. A horizontal Super Invar strut couples the vertical mirror plane to the horizontal capacitive sensor, as will be explained in later. This eliminates the sensitivity to rigid body motion in r-direction.

A vertical thermal gradient (*dT/dz*) causes curvature of the horizontal mirror (Figure 4.22), and out of squareness between the two mirrors. A horizontal gradient (*dT/dr*) causes bending of the vertical mirror. A gradient in y-direction (*dT/dy*) causes out of plane deflection of the frame, which has no first order effect on the mirrors. The elongation of the beams has negligible effect on the measurement due to the high flatness of the mirrors.

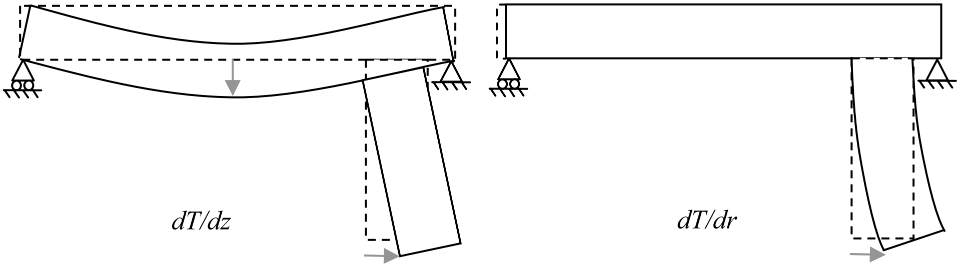

Figure 4.22: Metrology frame deflection due to thermal gradients

Slope ψ and deflection δ of a beam due to a temperature difference *dT* between top and bottom as shown in Figure 4.23, is given by (4.18) (Appendix G):

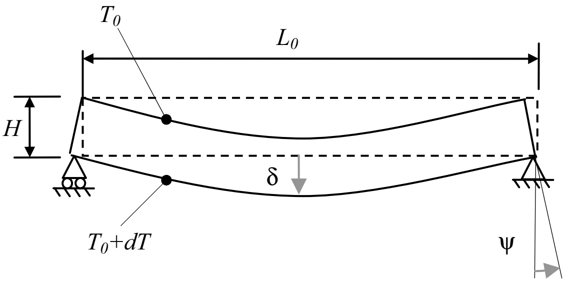

Figure 4.23: Beam deformation due to thermal gradient

$$\begin{aligned} dL &= \alpha \cdot L_0 \cdot dT \\ \psi &= \frac{dL}{2H} = \frac{L_0}{2H} \cdot \alpha \cdot dT \\ \delta &= \frac{dL\left(L_0 + dL\right)}{8H} \approx \frac{L_0^2}{8H} \cdot \alpha \cdot dT \end{aligned} \tag{4.18}$$

For *dT/dz*, the metrology frame is most sensitive to out of squareness of the vertical beam. To obtain 10 nm stability of the vertical mirror, the length difference between top and bottom of the horizontal beam must be smaller than 8 nm, which is equal to 3.4 mK. For *dT/dr*, the length difference for the vertical sides must be smaller than 16 nm, or 10.7 mK. Rocking of the vertical beam due to curvature of the horizontal beam is thus the most sensitive to thermal gradients, where the maximum vertical gradient should be in the order of a few mK over the height of the beam.

Convection

Natural convection will occur along the vertical walls. For the convection from the outside walls to the environment, a convection coefficient h_{air} of 5 W/m^{2}K will be used. To assess whether conduction or convection is the main heat transfer means in the air layer between the shield and the frame, their contributions are compared using (Bejan, 1993). For still air with a conduction coefficient k_{air} = 0.025 W/mK, an air layer thickness t_{air} = 5 mm and an estimated temperature difference dT = 0.01 K, the heat flux through conduction can be calculated with (4.19) to be 0.05 W/m^2.

$$q'' = \frac{k_{air}}{t_{air}} dT \tag{4.19}$$

With a gap height H of 120 mm, the Rayleigh number can be calculated with (4.20) to be $4.4 \cdot 10^4$. The flow is thus laminar.

$$Ra_H = \frac{g\beta}{\alpha\upsilon} \cdot \frac{q'' H^4}{k} \quad with \quad \frac{g\beta}{\alpha\upsilon} = 107\, cm^{-3} K^{-1} \tag{4.20}$$

The thickness of the air layer t_{air} is initially set to 5 mm. This gives a H/t_{air} ratio of 24. From (Bejan, 1993) it can be seen that the flow is in the tall enclosure regime, where the heat transfer rate is practically equal to the pure conduction estimate. This is the case down to $H/t_{air} = 14$, so the air pocket may be slightly enlarged (to 8.6 mm) to obtain a higher thermal resistance of the air layer before convection has to be taken into account.

For a vertical wall, the heat loss to the environment on one side, and the air pocket on the other, can be estimated with:

$$q'' = h_{air}\left(T - T_\infty\right) + \frac{k_{air}}{t_{air}}\left(T - T_\infty\right) \tag{4.21}$$

In this case h_{air} is 5 W/m^2K and k_{air}/t_{air} is also 5 W/m^2K. The heat loss to the environment and the air-pocket are thus equal.

Radiation

The radiation between for instance the shield wall and the frame can be calculated with (4.17). The emissivity is in the order of 0.1 for aluminium and 0.8 for SiC (estimation), the temperature difference is about 0.01 K, the area is 0.09 m^2 and the view factor is 1. This gives a radiation heat transfer of 0.5 mW, which is an order of magnitude smaller than the conductive heat transfer. Radiation will therefore not be taken into account in the further calculations.

Finite Element Model

To calculate the time-dependent and steady state behaviour of the horizontal beam, a finite element model was made in Matlab Simulink (Figure 4.24). The model consists of wall elements that are composed of a shield, air and SiC part, of which the equations used are explained in Appendix G. Since the model is symmetrical, only half has to be modelled. The shield is modelled with the opening at the bottom for the mirror, such that part of the heat input is into the shield and part of it is directly into the metrology frame beam.

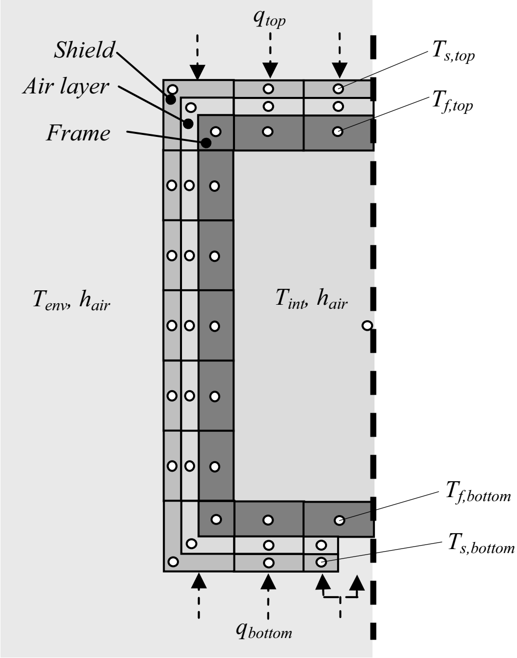

Figure 4.24: Thermal FEM model of the horizontal metrology frame beam

It should further be noted, that the vertical beam should be connected to the horizontal beam with high thermal resistance, otherwise it will start to function as a cooling fin for the bottom of the beam. This would increase the temperature difference between the top and bottom at the location of the connection. As long as this is done, the model is valid.

Simulations

The thermal behaviour of the system was simulated for shield thickness (t_s) of 1 to 10 mm and frame thickness (t_f) of 5 to 25 mm. These values are related to the available space in the design. With this geometry, the response to periodic fluctuations and temporary heat loads (e.g. operators) was simulated.
The typical response of a SiC frame with 15 mm wall thickness and 2 mm shield to periodic fluctuations of the environment temperature is shown in Figure 4.25. The low-pass behaviour of the shield is clearly visible. At 10^{-2} cycles per hour, or about 4 days, both shield and frame follow the environment almost one to one. At 2 cycles per hour, the shield response is 0.1 and the frame response is about 0.02, or a factor 50 reduction in amplitude compared to the environmental fluctuations.

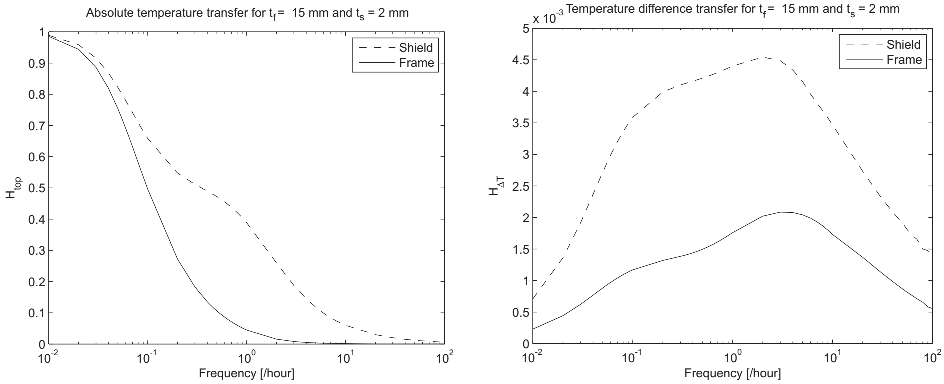

Figure 4.25: Frequency dependent transfer coefficient of temperature (left) and temperature difference (right)

Due to the opening in the shield, a phase and/or amplitude difference between top and bottom occurs. This gives rise to a temperature difference and thus to curvature of the beams. In Figure 4.25 (right), the maximum transfer coefficient for the temperature difference is shown to be $2 \cdot 10^{-3}$ at approximately 4 periods per hour (15 min.). In SiC the (small) temperature difference is mainly caused by an amplitude difference due to heat lost to convection in the side walls.

Simulating the frequency dependent transfer coefficient for variable frame and shield thickness for SiC and Zerodur, results in Figure 4.26. Since the thermal mass ($\rho V c_p$) is almost equal, the difference in response can only be caused by the large difference in conductivity. Due to this, the peak temperature difference of Zerodur is about 23 times higher and the peak frequency is about 10 times lower. For materials with high volumetric diffusivity, shield thickness is of less influence to the response than for materials with low volumetric diffusivity.

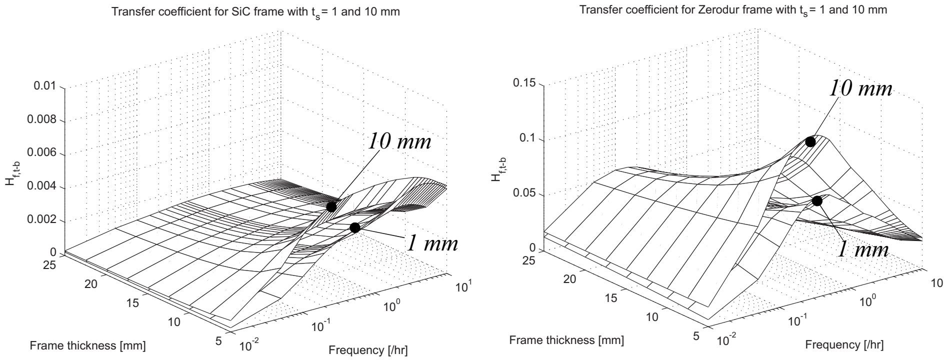

Figure 4.26: Transfer coefficient for temperature gradient for SiC and Zerodur

To translate the transfer coefficient to deflection, it is multiplied by the temperature amplitude, the expansion coefficient and the frame dimensions, according to (4.18). A frame thickness of 15 mm in combination with a shield thickness of 2 mm was chosen as a compromise between transfer coefficient, frame weight and shield robustness. The transfer coefficient and deflection of the vertical beam are shown in Figure 4.27 for several materials for comparison. The temperature amplitude is chosen 0.2°C and constant over the frequency spectrum. Due to the almost equal volumetric thermal diffusivity, the response of Invar and SuperInvar, and of Aluminium and SiC are equal.

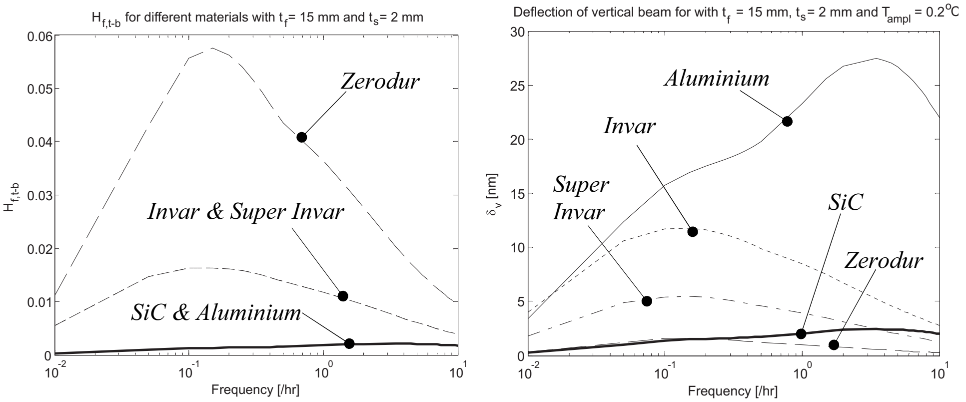

Figure 4.27: Transfer coefficient for temperature difference and deflection for various frame materials

The thermal deflection of the vertical beam is lowest for Zerodur over the entire spectrum, at about 1.6 nm at a cycle of about 6.5 hours. Up to this frequency, the response of SiC is approximately equal. Above this frequency, the deflection rises to 2.4 nm at a cycle of 17 minutes (which unfortunately is equal to the expected duration of a measurement). The low conductivity of Zerodur is starting to make the beam too slow to follow the input. The maximum response of SuperInvar, Invar and Aluminium is 5.4, 11.8 and 27.5 nm, respectively.

Next, the influence of an operator standing in front of the machine for 1 hour and then leaving again is simulated. Most of the radiative heat load will be applied to the front of the shield, causing a gradient in y-direction with negligible effect to the mirrors. At worst case, it is estimated that 10%, or 0.1 W, radiates onto the bottom of the shield and frame. For the frame thickness of 15 mm and shield thickness of 2 mm, the response of the bottom and top temperature is shown in Figure 4.28.

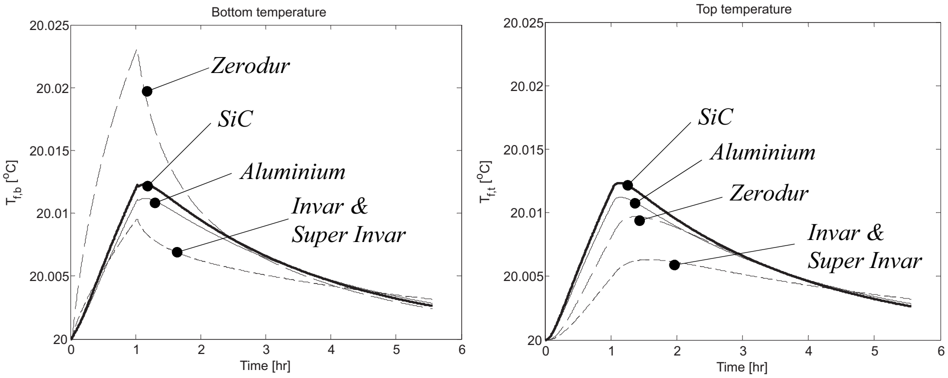

Figure 4.28: Top and bottom temperature of frame from operator heat load

As can be seen, the low conductivity of Zerodur gives a high temperature rise at the bottom, from where the heat load is applied. The top temperature clearly falls behind. For SiC and Aluminium, the bottom and top temperatures are almost equal. The low response of Invar is due to its large $\rho V c_p$.

The temperature difference and resulting deflection of the vertical beam are shown in Figure 4.29. SiC and Aluminium reach equilibrium swiftly, while the other materials are still drifting after 1 hour. When the operator leaves again, SiC and Aluminium are stable again after a few minutes, while the other materials require more than one hour. The actual temperature difference and deflection are 0.4 mK and 2,2 nm for SiC and 15 mK and 2.1 nm for Zerodur. Coincidentally, the performance is thus equal for this timescale, heat load and geometry. If steady state conditions were reached, the ratio in deflection would have been equal to the ratio of α/k.

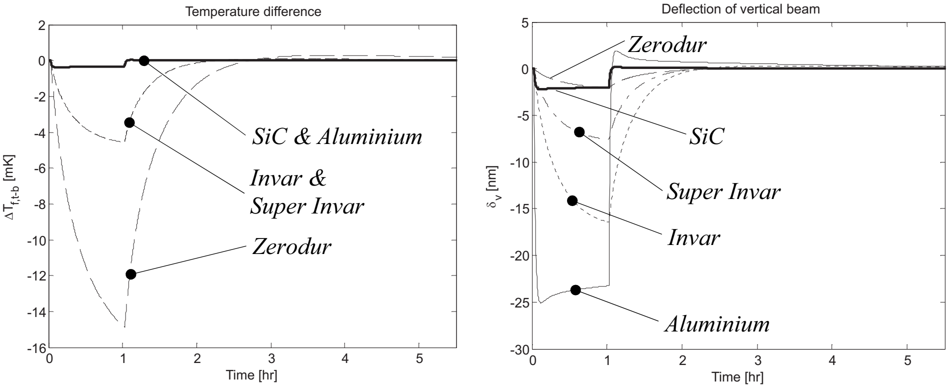

Figure 4.29: Temperature difference and deformation from operator heat load

Another source of continuous heat flux is the linear scale read-heads, situated directly underneath the horizontal beam. The read heads produce 1 W each, most of which will flow into the stages by conduction. The part that flows into the frame by radiation will be much less then the worst case flux of the operator calculated above, and be steady state as well. This is therefore estimated to have negligible effect.

Silicon Carbide and Zerodur are the two materials that are best used for the metrology frame. Their stability relies on either a very high, and very low volumetric thermal diffusivity, respectively. For the described geometry and thermal loads, Zerodur is more stable at higher frequencies while Silicon Carbide is better under continuous or slowly varying heat flux conditions. Both materials show stabilities in the order of a few nanometers, which is well below specification.

4.3.3 Mechanical analysis

For the dimensions chosen in the last section, the first three eigenmodes and frequencies are shown in Figure 4.30. The first mode only has second order influence on the mirror position. The second mode at 658 Hz does have first order influence. This frequency is expected to be sufficiently high.

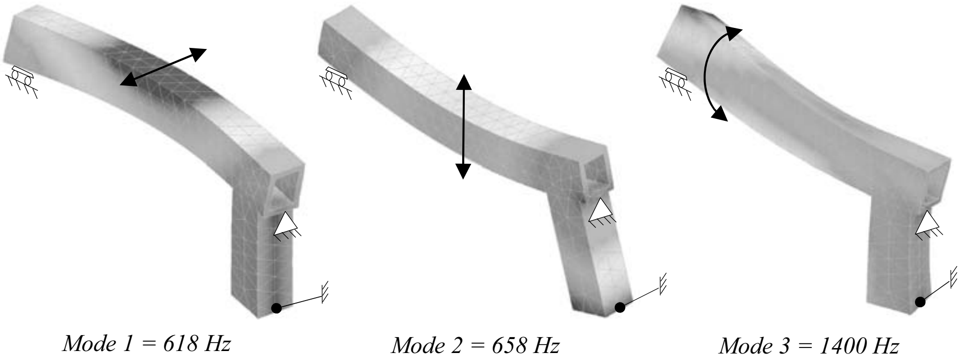
Mode 1 = 618 Hz *Mode 2 = 658 Hz* *Mode 3 = 1400 Hz*

Figure 4.30: First three eigenmodes of the upper metrology frame

The total gravity deflection is 520 nm at the centre of the horizontal beam and 550 nm at the bottom of the vertical mirror, as shown in Figure 4.31. This is a steady state deflection, but is has to be taken into account in the alignment budget of the interferometry system. The slope at the ends of the horizontal mirror is approximately 0.6 μrad, and the tilt of the vertical mirror is approximately 1.5 μrad. These tilts are small compared to the budget explained in interferometry alignment analysis.

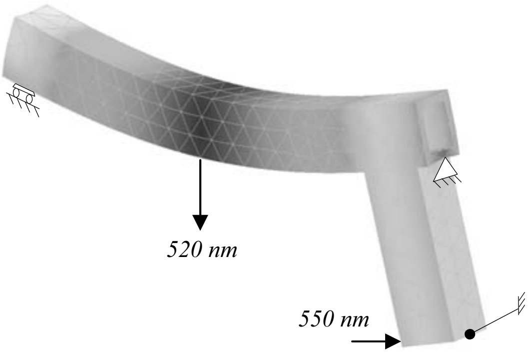

Figure 4.31: Gravity deflection

4.3.4 Design and realization

The two Silicon Carbide beams containing the mirrors are connected with high stability and aligned as square as possible. This assembly will then be mounted to the base and the lower metrology frame in a statically determined manner. The shielding is mounted separately from the metrology frame.

SiC beams with mirrors

The upper metrology frame beams have their mirrors directly polished onto the beams, and are manufactured by CoorsTek (Figure 4.32). Reflectivity is enhanced by a protected Aluminium coating. Polishing has taken much more effort than expected, but finally resulted in a flatness of about 1 μm PV over the entire mirror length and a R_a roughness of 5.7 nm, as shown in Figure 4.32 (right).

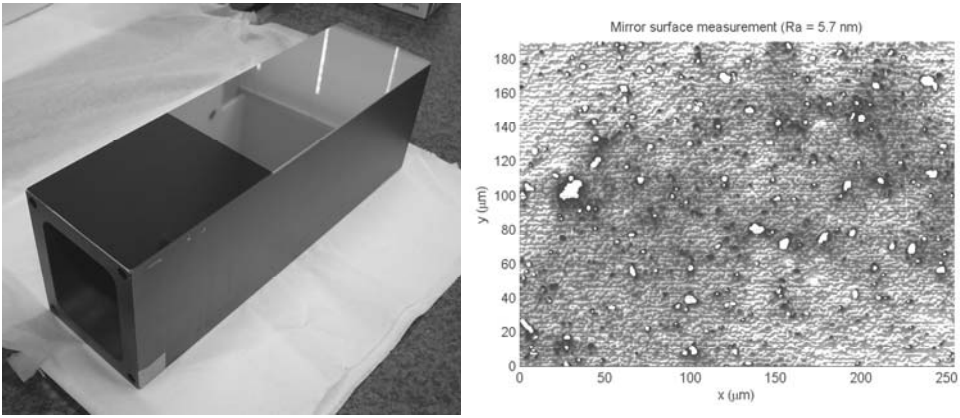

Figure 4.32: Metrology frame vertical beam with mirror, and confocal microscope measurement of mirror surface.

In the surface finish measurement the porosity of Sintered Silicon Carbide can clearly be distinguished. The remaining pores vary in size from 100 nm to a few of 10 µm and are up to 0.5 µm deep. The area covered by the pores is approximately 1.2 %. The pores will mainly cause scattering, which is not expected to influence the measurement as long as the area between the pores is flat enough to preserve the reflected wavefront flatness.

Beam connection

The horizontal and vertical beams are to be connected with high stability and aligned as square as possible. Since the top face of the vertical beam is not very square to the mirror, the beam connection should allow for alignment. As explained in the thermal analysis, the beam connection should further have high thermal resistance to prevent the vertical beam from acting as a cooling fin on the bottom of the horizontal beam. It should also be possible to disassemble the frame, in case of mirror damage for instance.

A pull rod through the beams or a bolted connection between two glued-in inserts can easily be disassembled. The forces required to obtain sufficient contact pressure will deform the beam and thus the mirrors. Further, alignment should be done by adjusting shims at the contact points, either by lapping or by elastic deformation.
A dowel pin connection is stressless and can be aligned while the adhesive is curing. Since a high thermal resistance is required, it was chosen to leave a 1 mm gap between the beams. This gap also allows for sawing the pins with a wire saw in case disassembly is required. The pins are further provided with M3 thread through the centre for extracting them after heating the adhesive. The stiffness transfer is through the pin's outer cylindrical surface.

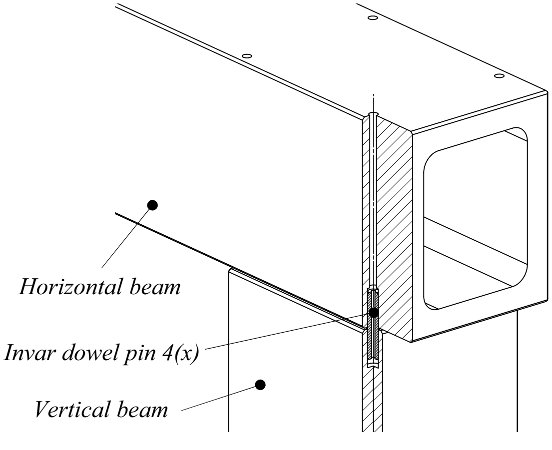

Figure 4.33: Dowel pin connection of metrology frame beams

Invar 36 was chosen since it is easier to machine and its expansion coefficient better matches that of SiC, compared to Super Invar. The maximum pin diameter in the 15 mm thickness of the beam walls is 8 mm. The pins were made to fit the holes to 0.02 mm after the beams were delivered. With the half pin length of 17 mm, the surface area of the glue layer is 855 mm^2. Araldite 2020 adhesive has a Young's modulus of approximately 2 GPa and a Poisson's ratio ν of 0.3, giving a shear stiffness of one glue layer of $3.3 \cdot 10^{10}$ N/m. For the total 4-pin connection, the axial stiffness is $6.6 \cdot 10^{10}$ N/m.

Upper metrology frame mounting

The upper metrology frame is mounted to the base kinematically, to prevent frame deformations due to thermally or mechanically induced deformation of the base. In z and ψ-direction this is done with two Super Invar struts. These struts have been heat treated after machining to regain the original low expansion coefficient. They further have hinges to reduce the sideways stiffness and are bolted to Invar blocks that are glued to the Silicon Carbide. The alignment of the horizontal mirror relative to the spindle is done by adjusting this connection. Since the two supports are almost 900 mm apart, sufficient angular resolution can be obtained here relatively easily.

In r-direction the frame has to be constrained such that the vertical mirror has a stable or known position relative to the capacitive probe measuring the error motion of the spindle in r-direction. The distance between this probe and the mirror surface is 155 mm, due to the space required by the Ψ-axis and Z-stage optics in the outer right position. This distance is bridged by a Super Invar strut.
In the first option of Figure 4.34, the probe is fixed and the Super Invar strut constrains the r-direction of the upper metrology frame. Deflections of the base will not cause relative motion between the upper and lower metrology frame, but the r-support is far below the centre of gravity of the upper metrology frame. This will lead to the first eigenmodes being bending of the vertical beam that is trying to constrain the r-direction of the (heavier) horizontal beam, typically at 260 Hz.

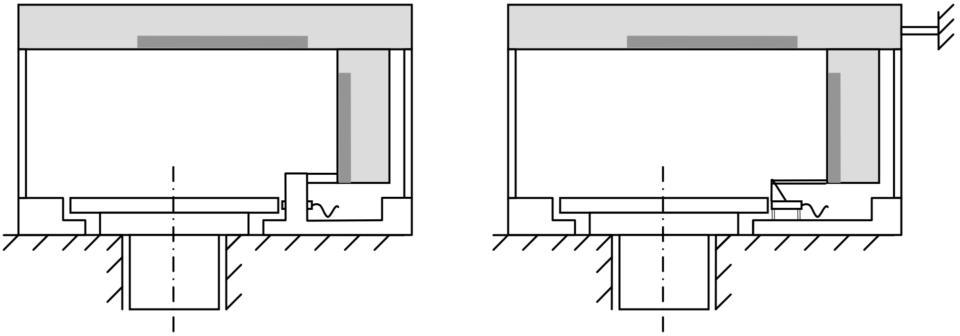

Figure 4.34: Constraining of horizontal degree of freedom of the metrology frame

In the second option, the *y*-support is aligned with the centre of gravity of the frame, Since it is connected to the base, the upper metrology frame will now shift sideways with bending of the base due to R-stage motion. By mounting the capacitive probe to an elastic parallelogram that is linked to the mirror face by the Super Invar strut, this probe will shift along with the frame. This will cause the R-interferometer and the capacitive probe to measure an equally larger or smaller distance and thus cancelling this shift from the metrology loop. This option is preferred since its first eigenmodes is typically at 620 Hz and thermally equal compared to the first option.

Invar pads are bonded to the SiC frame to interface with the mounting elements. The above described constraint in *r*-direction is combined with a constraint in *y*-direction into a steel A-plate (1), as shown in Figure 4.35. The φ and θ-directions are constrained by two steel struts (2 and 3). Steel is used here since no high thermal stability is required in these directions. Both the A-plate and the struts extend backwards to inserts in the granite base (4).

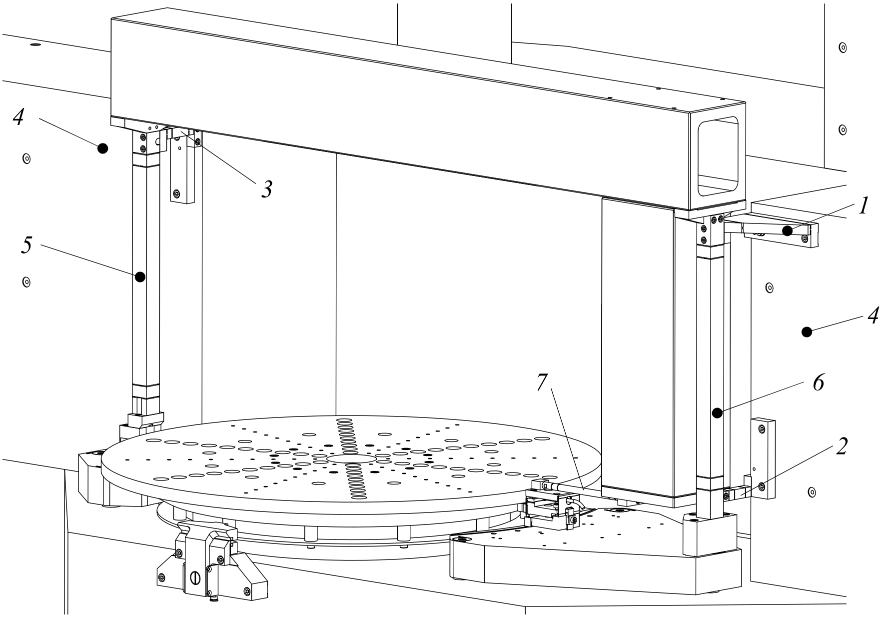

Figure 4.35: Upper metrology frame mounting

The two vertical Super Invar struts (5 and 6), the A-plate and the two steel struts now constrain the upper metrology frame in six degrees of freedom. The dimensions of the struts and hinges is chosen such that the first rigid body mode is around 600 Hz, which is similar to the first eigenfrequency of the SiC frame. The Super Invar strut (7) that connects the mirror face of the short beam to a parallelogram on which a capacitive probe is mounted will be further discussed in the design of the lower metrology frame (section 4.4.3).

Shielding

The thermal shielding consists of a 5 mm Aluminium back plate that is bolted to the base with rubber dampers in between, as shown in Figure 4.36. The covers (3 and 4) for the horizontal and vertical beam and the left support strut (5) are made from single pieces of folded 2 mm thick Aluminium plate, to maintain high conduction between the front and the top and bottom. The covers are bolted to the back plate using M3 screws that can be reached through the small holes in the front.
To reduce acoustically induced vibrations, a 1 mm rubber strip is applied between the back plate and the covers to increase the damping. This virtually eliminates thermal conduction between the cover and back plate, which is different compared to the model. For uniform environmental temperature changes this makes little difference since the shield is uniformly heated with negligible in-plane conduction. Operator induced heat is applied from the front and conducted to the top and bottom, which also makes little difference compared to the model. The shielding is connected to the base via rubber mounts, completely isolated from the upper metrology frame. The lower metrology frame is also enclosed with a cover.

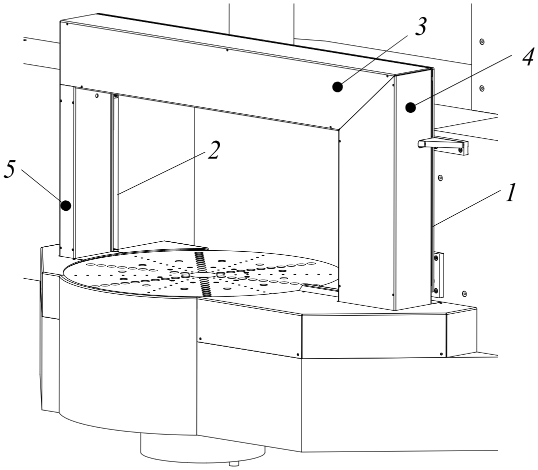

Figure 4.36: Metrology frame shielding

Realization

The two beams are assembled on a flat granite table. First, an autocollimator (Möller-Wedel Elcomat) was adjusted parallel to the table by pointing the beam downwards with a pentaprism to an optical flat on the table. This flat was rotated 180° to eliminate the non-parallelism between its front and back surface. Next, the beams were placed on their sides in front the autocollimator to verify the perpendicularity between the sides and the mirror face. The beams were mounted on spacers to match the height of the autocollimator. A calibrated pentaprism was then aligned in front of the autocollimator, to measure the alignment of the two mirrors (Figure 4.37, left).

The Araldite 2020 adhesive was then applied to the dowel pins and the parts are assembled. This adhesive requires 24 hours to cure, giving about 45 minutes to align the two mirrors.

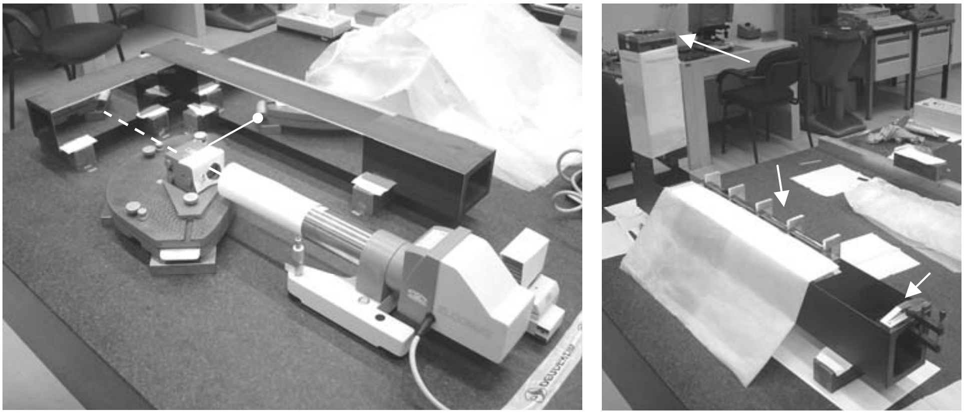

Figure 4.37: Metrology frame mirror alignment and bonding of the interfaces

The NMi VSL pentaprism used has a calibrated deviation of 1.18 arcsec with an uncertainty of 0.27 arcsec. FEM simulations show a gravity deflection of 0.4 arcsec, so the beams are to be aligned to 1.58 arcsec. With a noise level of about 0.1 arcsec, the averaged result was 1.6 arcsec. The alignment was checked after curing for several days, and had remained stable.

Next, the Invar interface blocks and the linear scale were mounted to the frame, again with Araldite 2020 adhesive. After curing, the frame was installed on the machine (Figure 4.38).

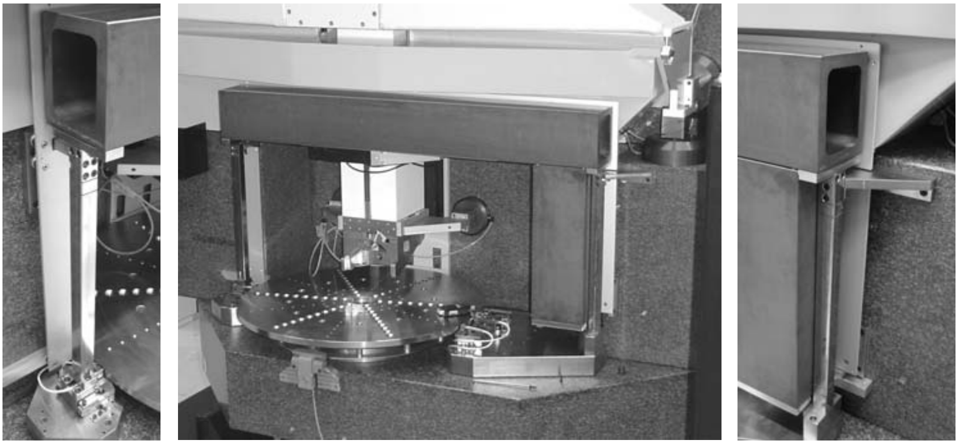

Figure 4.38: Upper metrology frame after installation

4.3.5 Alignment and calibration

The metrology frame mirrors must be aligned to the spindle axis of rotation and the measurement plane. To achieve this, an autocollimator is mounted to the granite base and a 45° mirror directs the beam upwards through the hole in the spindle (Figure 4.39A). A mirror is placed upside down on the spindle and adjusted perpendicular to the spindle axis by rotating the spindle (Figure 4.39B). The spindle tilt is specified to be 0.1 µrad, which is below the resolution of the autocollimator (0.05 arcsec or 0.24 µrad. The wobble of the mirror can therefore be adjusted to almost zero. Next, the autocollimator was aligned perpendicular to the mirror, after which it was collinear with the spindle axis of rotation to within ±0.05 arcsec, which is equal to the noise level of the autocollimator. The mirror on the spindle was removed, revealing the horizontal metrology frame mirror to the autocollimator. By adjusting the bolted connection of the struts, the horizontal mirror was set perpendicular to the autocollimator in φ and ψ-direction.

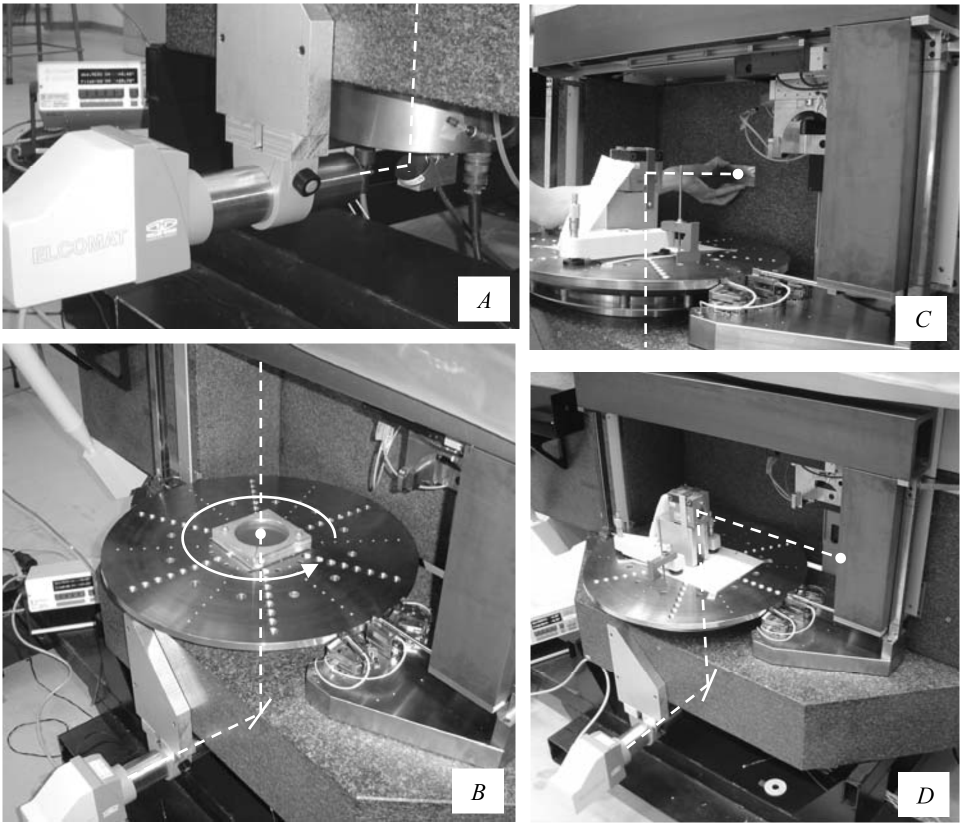

Figure 4.39: Upper metrology frame alignment

Next, a calibrated pentaprism of NMi VSL was positioned above the hole (Figure 4.39C), pointing the beam backwards towards the vertical granite base plane. This plane determines the orientation of the measurement plane. A 2-sided mirror with front and backside parallel to within 0.09 arcsec (calibrated) was then pressed to the granite face, after which the spindle was rotated to set the pentaprism perpendicular to this mirror.

The pentaprism was rotated exactly 90° by the spindle and its encoder, to point it towards the vertical mirror of the metrology frame (Figure 4.39D). The accuracy of the encoder is specified to be 1 arcsec, and the spindle controller positions the spindle well below this. The vertical mirror was now adjusted in θ-direction, such that it is square to the measurement plane.

The whole procedure was iterated several times. The horizontal mirror finally was aligned to +0.05 arcsec in the most critical ψ-direction, and to 0.1 arcsec in the less critical φ-direction. The vertical mirror was aligned to 0.75 arcsec in θ-direction. It must be noted that the flatness of the mirror is not taken into account here, and the alignment and perpendicularity measurements are done on a single point of the mirror. The actual flatness has not yet been calibrated, but is specified to be 200 nm/200 mm, which is equal to 1 μrad or 0.2 arcsec.

The perpendicularity was finally measured in a setup as shown in Figure 4.40, resulting in a perpendicularity error of $\psi = -3.53$ arcsec (17.1 μrad) after correction for the deviation of the NMi VSL pentaprism. This will only cause a measurement error for products with large height differences, and can of course be compensated for in the data processing.

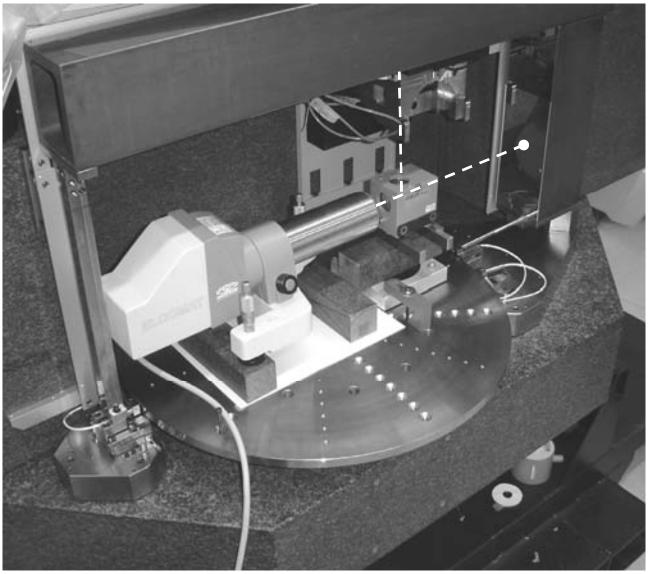

Figure 4.40: Mirror perpendicularity measurement

4.4 Lower metrology frame

The lower metrology frame measures the product position relative to the horizontal and vertical reference mirrors. The horizontal beam of the upper metrology frame is coupled to the lower metrology frame by the two vertical Super Invar struts. In *r*-direction, the vertical mirror should be referenced to the axis of rotation of the spindle. To minimize the thermal loop length between this mirror and the spindle centre, a coupling is made with a Super Invar strut and a capacitive probe as described in the upper metrology frame design.

The product is rotating on the air bearing spindle, and is supposed to be rigidly attached to the mounting table. Although the acquired Professional Instruments BlockHead 10R spindle is specified to have an error motion smaller than 25 nm, it is too much to meet the design error budget ($\delta_{S,r} < 15$ nm, $\delta_{S,z} < 15$ nm, $\delta_{S,\psi} < 0.1$ µrad (3σ)). The error motion will thus have to be measured to determine the product position relative to the reference mirrors with sufficient accuracy.

Ideally, the product position is directly measured relative to the lower metrology frame. The product can be any shape, so measuring to the intermediate body is next best. This body may for instance be provided with a reference edge. The diameter of this edge depends on the product, and some products such as mirrors may not be mounted on an intermediate body at all. Measuring to the edge of the mounting table is thus the most practical solution, provided that the product does not move relative to this edge during a measurement. The edge of the mounting table will obviously not be perfect, so it will have to be calibrated. Due to product specific mass and mounting positions, the edge shape will also vary between measurements.

First, methods of measuring spindle error motion will be briefly discussed, after which the multi-probe method is explained. Next, the design and realization are discussed and experimental results will be given.

4.4.1 Spindle error motion measurement

The error motion of the spindle consists of a synchronous and an asynchronous part (ASME, 1985). The synchronous part is generally repeatable, but may also be dependent on product mass. The asynchronous part, caused by for instance air pressure variations, unbalance and other external excitation, is not repeatable and should thus be monitored continuously.

A probe measuring to a rotating object measures the error motion plus the roundness error of the object. In this case, the rotating object is a reference edge on the table, either as an integral part of the table or as a separate ‘metrology frame’ ring mounted underneath. In either case the edge is probably not sufficiently stable due to the varying loading of the table due to the variable product shape and mass. Preferably, the edge shape is thus determined in-process, before or during each measurement with the product mounted. Several methods exist to separate the object roundness error and the spindle error motion (Marsh et al., 2006).

Compare to a calibrated artefact

Spindle calibration is mostly done by mounting a reference sphere or other artefact with a known form, to which a measurement is performed with (capacitive) sensors. This artefact would have to be mounted over the product before a measurement, to include the deformation caused by the product itself.

Reversal methods

With Donaldson ball reversal (Donaldson, 1972) and Estler face motion reversal (Estler, 1986), a number of revolutions are averaged to obtain the sum of the synchronous error motion and the profile form. This measurement is then repeated with the artefact and probe orientation reversed. Subtracting the two measurements results in an exact solution for the edge form and the synchronous error motion, provided that no other errors are introduced during the reversal.
If this method is to be performed with the product mounted, it would require a separate edge and probe which can be reversed. The form of this edge should remain stable during this operation. Although this is the only method that results in an exact solution, it is not very practical in this case.

Multi-step method

In the multi-step method, the probe remains stationary and the edge is measured under multiple (equidistant) orientations (Chetwynd and Siddall, 1976). Averaging the measurements separates the error motion from the edge form, except for frequencies that are integer multiples of the number of steps. Numerous measurements thus have to be applied to avoid errors from harmonic suppression, especially for objects with a large circumference. Similar to the reversal methods, this method is thus not practical in this case.

Multi-probe method

When multiple probes are placed around the rotating table, the error motion is measured in phase by all the probes, while the form error of the edge is phase shifted with the probe spacing. By Fourier decomposition, the edge profile and error motion can be separated, even for a single revolution (Mitsui, 1982). A minimum of seven capacitive probes are required for this procedure to measure the five degrees of freedom of the spindle and the axial and radial profiles. As with the multi-step method, harmonic suppression occurs at certain frequencies, depending on the chosen probe spacing. Some therefore apply more than seven probes to obtain redundant data to increase the harmonic suppression limit (Zhang et al., 1997).

This method does not require repositioning of the edge and the probes, and can be applied with the product mounted on the table. It may even be applied during measurement of the surface under test. It is thus a true in-process calibration of the edge form of the table. It may, however, suffer from harmonic suppression (Whitehouse, 1976). Each sensor must be individually calibrated, and differences due to mounting must be minimized. This method was further analyzed to assess the applicability and achievable measurement uncertainty.

4.4.2 Multi-probe method

The principle of the multi-probe method will first be explained, followed by the risk of harmonic suppression and the harmonic content of the reference edge. Next, the optimum probe locations are summarized, based on the analysis in Appendix H. Simulations show the suitability of the method. When preparing for testing the method in practice, the spindle was found to show excellent error motion properties. Other parts of the machine have therefore been completed first. Eventually, time did unfortunately not permit the method to be validated in practice.

Principle

A probe measuring to an object rotating on a spindle as shown in Figure 4.41, measures the sum of the error motion and the axial or radial profile (flatness / roundness error). The axial and radial profiles of the object $P_{ax}(\theta)$ and $P_{rad}(\theta)$, respectively, are considered stable during a revolution (typically one second in time).

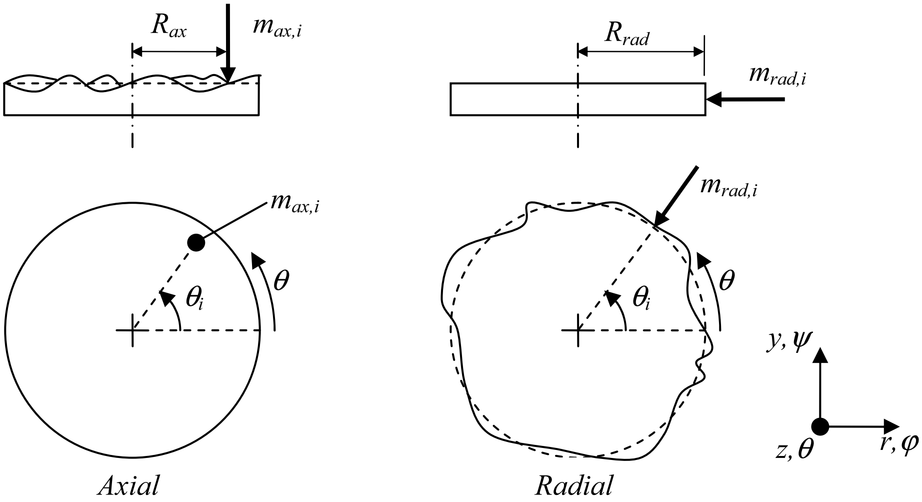

Figure 4.41: Axial and radial probe measuring a profile

The asynchronous error motion varies per revolution, making the error motion a function of the angle θ and time t. For a single revolution however, the error motion can be considered as being only a function of θ. The axial and radial measurement signals $m_{ax,i}(\theta)$ and $m_{rad,i}(\theta)$, of probe located at θ_i and radius $R_{ax,i}$ or $R_{rad,i}$, can now be expressed as:

$$m_{ax,i}(\theta) = P_{ax}(\theta + \theta_i) + z_S(\theta) + \varphi_S(\theta)\sin(\theta_i)R_{ax} - \psi_S(\theta)\cos(\theta_i)R_{ax} \qquad (4.22)$$

$$m_{rad,i}(\theta) = P_{rad}(\theta + \theta_i) + r_S(\theta)\cos(\theta_i) + y_S(\theta)\sin(\theta_i) \qquad (4.23)$$

Besides the rotation θ, there are 7 degrees of freedom in the system: 3 translations, 2 tilts and 2 edge profiles. Applying seven probes provides enough information to solve all 7 variables. Hereto, four axial probes ($i = 1 - 4$ in Figure 4.42) and three radial probes ($i = 5 - 7$) are applied. To prevent thermal expansion of the table being interpreted as radial motion, an 8th probe is added, opposite to probe number 5.

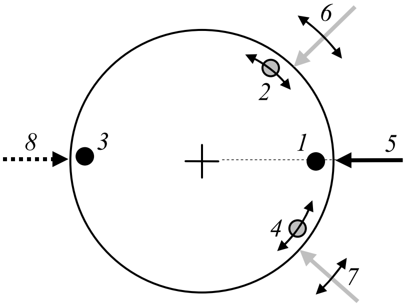

Figure 4.42: Four axial (1-4) and three radial (5-7) probes

The multi-probe error motion reconstruction is shown for the radial profile here. An analogous derivation for the axial direction is shown in Appendix H. The radial measurements $m_1(\theta)$, $m_2(\theta)$ and $m_3(\theta)$ are expressed as:

$$\begin{aligned} m_5(\theta) &= P_{rad}(\theta + \theta_5) + r_S(\theta)\cos(\theta_5) + y_S(\theta)\sin(\theta_5) \\ m_6(\theta) &= P_{rad}(\theta + \theta_6) + r_S(\theta)\cos(\theta_6) + y_S(\theta)\sin(\theta_6) \\ m_7(\theta) &= P_{rad}(\theta + \theta_7) + r_S(\theta)\cos(\theta_7) + y_S(\theta)\sin(\theta_7) \end{aligned} \qquad (4.24)$$

Where P_{rad} is the radial edge profile, r_s is the spindle error motion in r-direction and y_s is the error motion in y-direction. These measurements are multiplied by sum factors f, g and h and then summed to $S_{rad}(\theta)$:

$$\begin{aligned} S_{rad}(\theta) &= fm_5(\theta) + gm_6(\theta) + hm_7(\theta) \\ &= fP_{rad}(\theta+\theta_5) + gP_{rad}(\theta+\theta_6) + hP_{rad}(\theta+\theta_7) \\ &\quad + r_S(\theta)\left(f\cos(\theta_5) + g\cos(\theta_6) + h\cos(\theta_7)\right) \\ &\quad + y_S(\theta)\left(f\sin(\theta_5) + g\sin(\theta_6) + h\sin(\theta_7)\right) \end{aligned} \tag{4.25}$$

The coefficients *f, g* and *h* can now be chosen such that the error motions cancel out. This is the case if the following equations are satisfied:

$$\begin{aligned} & f\cos(\theta_5) + g\cos(\theta_6) + h\cos(\theta_7) = 0 \\ & f\sin(\theta_5) + g\sin(\theta_6) + h\sin(\theta_7) = 0 \\ & \sqrt{\left(f^2+g^2+h^2\right)} = 1 \quad (unit\ vector) \end{aligned} \tag{4.26}$$

The resulting summed measurement now simplifies to (4.27). This is only a function of the radial profile P_{rad}, the probe orientations $\theta_{5\text{-}7}$ and the spindle orientation θ. The error motion is cancelled from the equation.

$$S_{rad}(\theta) = fP_{rad}(\theta+\theta_5) + gP_{rad}(\theta+\theta_6) + hP_{rad}(\theta+\theta_7) \tag{4.27}$$

Since the edge profile is closed, only discrete Fourier terms are present. With harmonic number *k*, the discrete Fourier transform of formula (4.27) is equal to:

$$\begin{aligned} S_{rad}(k) &= fP_{rad}(k)e^{jk\theta_5} + gP_{rad}(k)e^{jk\theta_6} + hP_{rad}(k)e^{jk\theta_7} \\ &= P_{rad}(k)\left(fe^{jk\theta_5} + ge^{jk\theta_6} + he^{jk\theta_7}\right) \end{aligned} \tag{4.28}$$

The Fourier transform of the radial profile can be calculated with:

$$P_{rad}(k) = \frac{S_{rad}(k)}{fe^{jk\theta_5} + ge^{jk\theta_6} + he^{jk\theta_7}} \tag{4.29}$$

By taking the inverse Fourier transform of this profile, $P_{rad}(\theta)$ can be calculated from a single revolution. By phase-shifting and substituting the obtained profiles into the original measurement signals (4.24), the error motion is found.

Harmonic suppression

Three error sources are considered in Appendix H: harmonic suppression, probe noise and probe angular position errors. Only harmonic suppression will be briefly addressed here.

The denominator of equation (4.29) becomes zero for certain combinations of probe positions and harmonics. Physically, this means that this harmonic generates measurement signals of which the mutual phase is such that it cannot be determined whether it is error motion or edge form, as schematically shown in Figure 4.43.

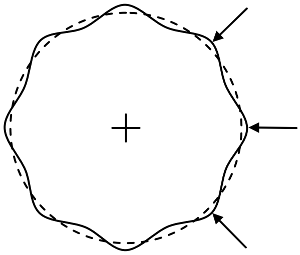

Figure 4.43: Harmonic suppression example

To overcome this problem, one may either choose to leave out these specific harmonics in the reconstruction, or to stop reconstruction before the first suppressed harmonic (k_{limit}) is encountered. All harmonics required to describe the profile and error motion with sufficient accuracy must then be below k_{limit}. Probe locations can be optimized to achieve a high k_{limit}.

Harmonic content of mounting table edge

The diameter of the edge is ∅600 mm and the measurement spot of the probes is ∅1.7 mm. Harmonics up to 1100 upr can thus reliably be measured, above this frequency aliasing may occur.

Axial and radial measurements of the actual edge are shown in Figure 4.44 (left), along with the harmonic content (right). In axial direction the signal is dominated by a second order component, which indicates that the table is warped but level. In radial direction a first order component is visible, which is eccentricity.

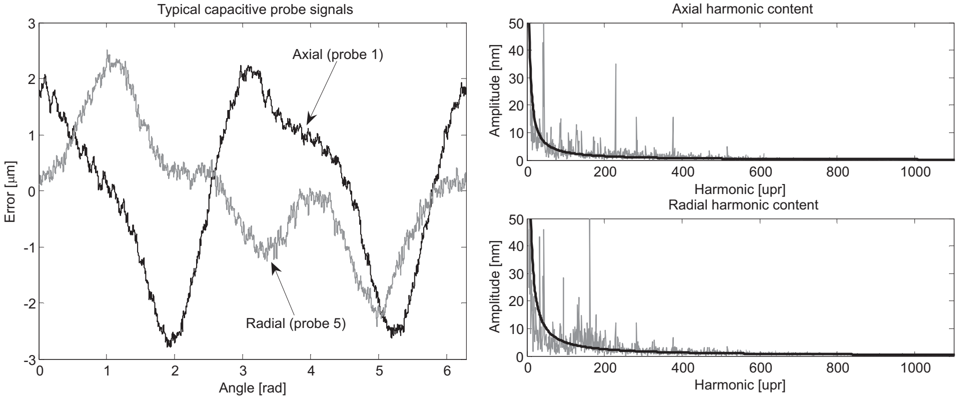

Figure 4.44: Typical measurement signals and harmonic content

This edge form was not yet known during the analysis and simulations of the multi-probe method. It was expected that some low order frequencies would dominate the signal, and that a more or less the other content would be inversely proportional to the harmonic number. A *1/k* function is also shown in Figure 4.44. Generally, this assumption fits the data, but some sharp high order frequencies are present. These probably originate in the properties of the manufacturing machine, such as the number of rolling elements in the bearings. Judging from the above figure, significant content is present up to 600 Hz (3 mm wavelength), but a higher harmonic limit is desirable.

Probe locations

The analysis shown in Appendix H, shows that a smaller angle between the probes allows for a higher achievable harmonic limit. The probe signals will, however, also become correlated. When measuring a sinusoidal profile with amplitude A, harmonic number k and probe spacing $\Delta\theta$, the nominal difference between the two probe signals is:

$$\begin{aligned} &\Delta m(\theta) = A\big(\sin(k\theta) - A\sin(k(\theta-\Delta\theta))\big) \\ &\qquad \textit{with} \quad \sin\alpha - \sin\beta = 2\cos\frac{1}{2}(\alpha+\beta)\cdot\sin\frac{1}{2}(\alpha-\beta) \\ &\Delta m(\theta) = 2A\cos k\left(\theta - \frac{\Delta\theta}{2}\right)\sin\left(k\frac{\Delta\theta}{2}\right) \end{aligned} \tag{4.30}$$

The weakest profile to be distinguished is assumed to be a second order harmonic with 2.5 nm amplitude. The capacitive probes used have a resolution of 0.4 nm rms, therefore the minimum difference between the measurement signals is set to 1 nm. This results in a minimum probe spacing of approximately 12°. The test setup is provided with adjustable mounts to vary the probe positions around this position.

Summarizing from the analysis in Appendix H, the optimum angular probe position has its suppression limit (k_{limit}) at a harmonic above which the harmonics have negligible contribution to the edge form and error motion. This optimization results in angular limits between which the probes physically have to be positioned to not be blind to certain harmonics below k_{limit}. Further, a position must be chosen that has maximum clearance from zero points to obtain minimum alignment sensitivity. Hence, the limits between which the probes have to be positioned must be chosen as far apart as possible. This also eases the physical alignment of the probes. Finally, the cumulative sum of the transfer coefficient harmonics must be minimal to minimize the influence of measurement noise. Judging from the preliminary results, the probes should be positioned near, but not onto, the $\theta_2 = -\theta_4$ and $\theta_6 = -\theta_7$ lines. This should allow for a harmonic limit of 1100 upr.

Simulated results

To test the reconstruction and to estimate the measurement uncertainty, simulations have been performed. In this simulation, edge profiles are generated with a 1/*k* amplitude and random phase content up to a specified limit. The same is done for the error motion in five degrees of freedom. The profile and error motion are sampled at the nominal probe locations to generate simulated probe signals. The above described reconstruction algorithm is then executed to calculate the profile and the error motion. The difference between the nominal input and the simulated results is the error of the method.

The randomly generated edge profile is shown in Figure 4.45 (left). These profiles were generated with 10000 points/rev and a harmonic content up to 1100 upr. The error motion is expected to have less high harmonics due to the averaging effect of the air gap. The error motion shown in Figure 4.45 (right) has harmonics up to 50 upr. Note that the error motion is to be detected in a signal that is two orders of magnitude larger.

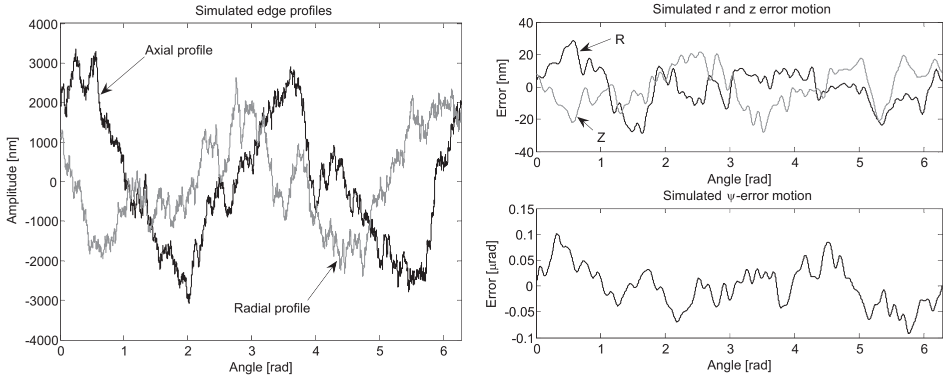

Figure 4.45: Simulated edge profile and error motion

The above profiles and error motion were measured by probes positioned at 12° and -12.25°. These values are based on the analysis of Appendix H. The reconstruction algorithm was first executed without noise and probe misalignment. For probe orientations without harmonic suppression below1100 upr, the results are exact. Next, noise of 0.4 nm rms was added to each probe signal, and a probe misalignment with an uncertainty of 0.0001° was introduced. This high alignment accuracy is expected to be achievable since the probe alignment can be directly derived from the signals due to the large ratio between the profile and the error motion. The reconstructed error motion is compared with the real input of Figure 4.45. The resulting profile reconstruction error and error motion reconstruction error are shown in Figure 4.46.

In this example, the axial and radial profile are measured with an rms error of 0.98 and 0.96 nm. The r, z and ψ-error motion are determined with an rms error of 1.13 nm, 0.89 nm and 2.8 nrad, respectively. Running this simulation with similar parameters shows consistent results.

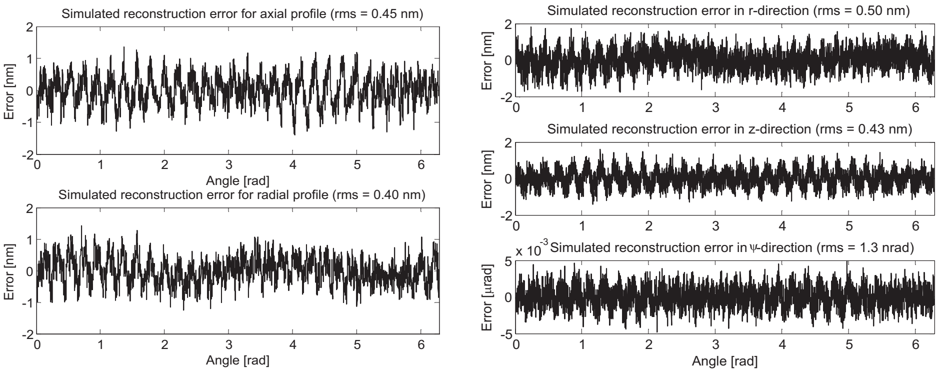

Figure 4.46: Simulated profile and error motion reconstruction error

The simulations show that the multi-probe method is suitable for in-process determination of the spindle error motion. Finding the optimum probe position is still subject of future work. When preparing for testing this method in practice, it was found that the spindle already showed excellent rotation accuracy (section 3.3.5). It was therefore decided to first focus on the rest of the machine. Unfortunately, time did eventually not permit the method to be validated in practice.

4.4.3 Design and realization

The lower metrology frame consists of two steel base plates on which adjustable mounts are placed. These probe brackets can be adjusted to bring the probes into range, and the angular position can be varied. The rotor is grounded to improve the noise level. The whole assembly is protected by a cover.

Probes

The probes used are the Lion Precision C7-C with CPL190 driver modules, specified to have 0.4 nm rms resolution, 10 µm range and 10 kHz bandwidth. The driver modules have an analog +/- 10 V BNC output that is fed into the data acquisition system. The probes are ∅8 mm and 50 mm long and the measurement spot is ∅1.7 mm. Seven probes are used for the multi-probe method; the 8th probe is employed for various measurement tasks during machine assembly, and will finally be applied as an extra radial probe opposite to probe number 5. This allows for determining thermal expansion of the table during measuring, which would otherwise be interpreted as drift of the spindle in positive *r*-direction.

Reference edge

The reference edge is machined on the side of the steel mounting table. For this ∅600 mm disc a roundness of 2.3 µm PV and a flatness of 5.1 µm PV was achieved. With the tilt and eccentricity which are introduced by bolting the steel table to the spindle taken into account, the total indicated readout (TIR) is 5.2 μm in axial direction and 4.8 μm in radial direction. The probes are to be positioned in range to about 1 μm.

Base blocks and brackets

To match the expansion coefficient of the spindle and the mounting table (1), the lower metrology frame is made of similar steel. It consists of two blocks (2 and 3) that are mounted to the granite base (Figure 4.47). The fixation points of the blocks have hinges (4) to create a thermal centre on the measurement plane. The blocks have a square groove (5) that is concentric with the spindle axis. The movable probe brackets (6-11) have two pins that slide through this groove when the orientation is adjusted, to maintain perpendicular alignment and to assure that each probe measures the same track on the axial (12) and radial (13) reference edge. The adjustment range of the probes is ±1°. The axial and radial probe located at zero degrees do not need adjustment, therefore these are mounted to a single bracket (14) which has two pins that fit into a hole and a slot.

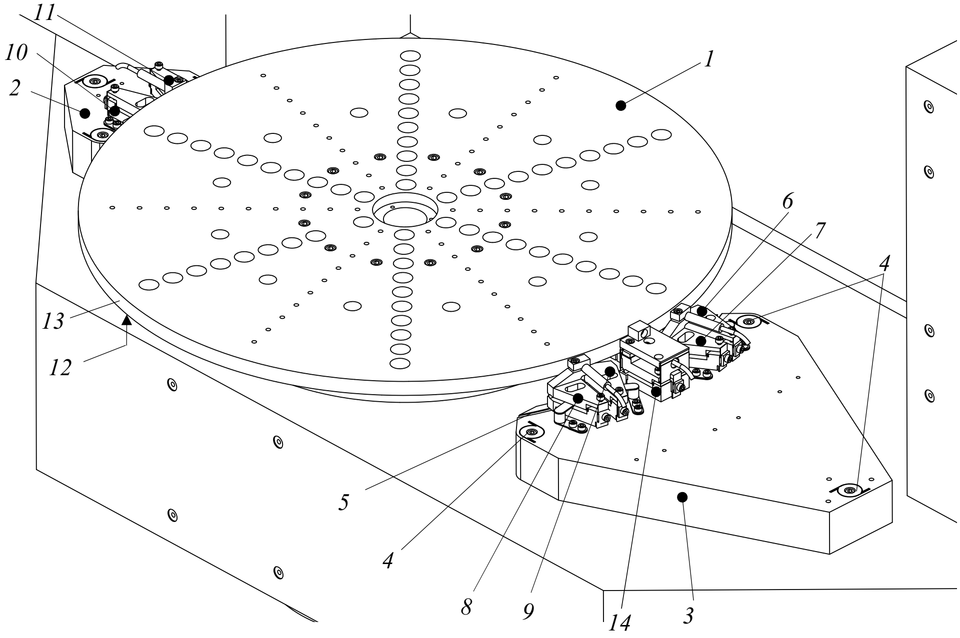

Figure 4.47: Lower metrology frame design

Probe brackets

Figure 4.48 shows the probe brackets in more detail. The movable brackets are constrained in radial and local θ-direction by the two pins in the groove (1). Once in position, they are locked by tightening a central bolt (2), of which the friction torque under the head is diverted to the base plate by a torsionally stiff coupling (3). During alignment and testing of the multi-probe method, the probe location will be changed frequently. Since the probes have an axial measurement range of only 10 µm, they will have to be adjusted many times. To ease adjustment, especially of the axial probes (4) that are hard to reach underneath the mounting table, the bracket has a hinge (5), an adjustment screw (6) and a stroke limit (7). Turning the screw tilts the top part of the bracket to bring the probe into range. A clamp (8) at the backside of the mechanism clamps a plate (9) that locks the mechanism, after which the screw can be loosened. This avoids the instability of the adjustment screw.

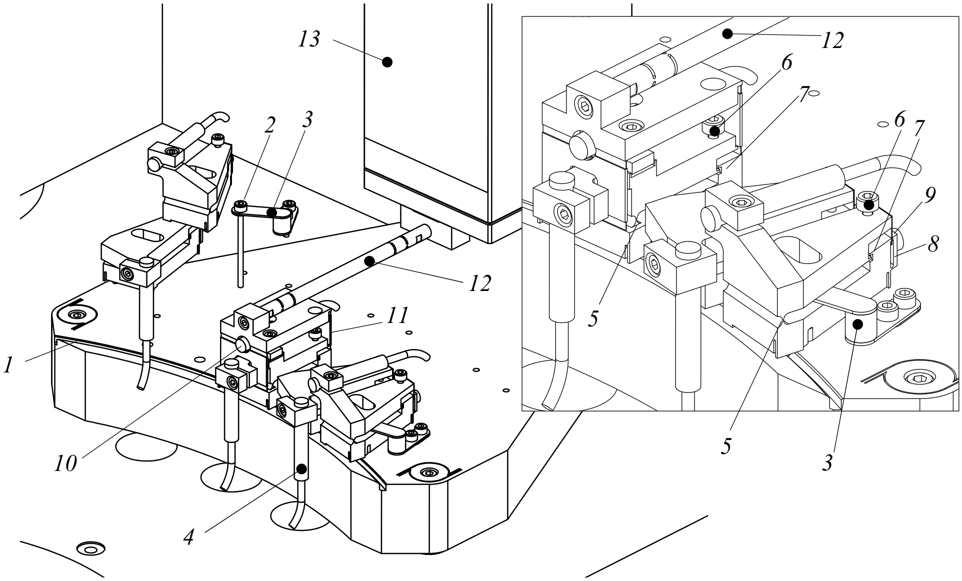

Figure 4.48: Probe brackets

As explained in section 4.3, the upper metrology frame may move in *r*-direction due to bending of the base. To compensate for this, the radial probe (10) in the fixed bracket is mounted on a parallelogram (11). A Super Invar strut (12) connects it to the vertical mirror face (13) on the upper metrology frame. The vertical mirror and radial probe now experience equal shift in *r*-direction, cancelling the effect.

Grounding of the rotor

To achieve optimal performance of the probes, the target should be grounded to the driver unit. Since the spindle rotor is floating on air, no electrical conducting contact is present. A plate with a small bump is therefore pressed lightly onto a plug in the bottom hole of the spindle. Since the contact point is located at the centre line, the relative speed is (almost) zero and thus the friction is negligible. Tests showed no detectable difference of the spindle performance with and without this contact. This grounding significantly reduced the rms noise level from 5.6 nm to 1.9 nm. This is measured with the air pressure turned on, so it also includes air gap variations.

Shielding

Similar to the upper metrology frame, the lower metrology frame is enclosed in a box (Figure 4.36). This is mainly to protect the probes and brackets, and to enclose the reference edge. The covers are connected to the granite base separate from the upper and lower metrology frame.

Realization

The assembled lower metrology frame is shown in Figure 4.49, with and without the shielding, together with a side view of a movable bracket and the parallelogram.

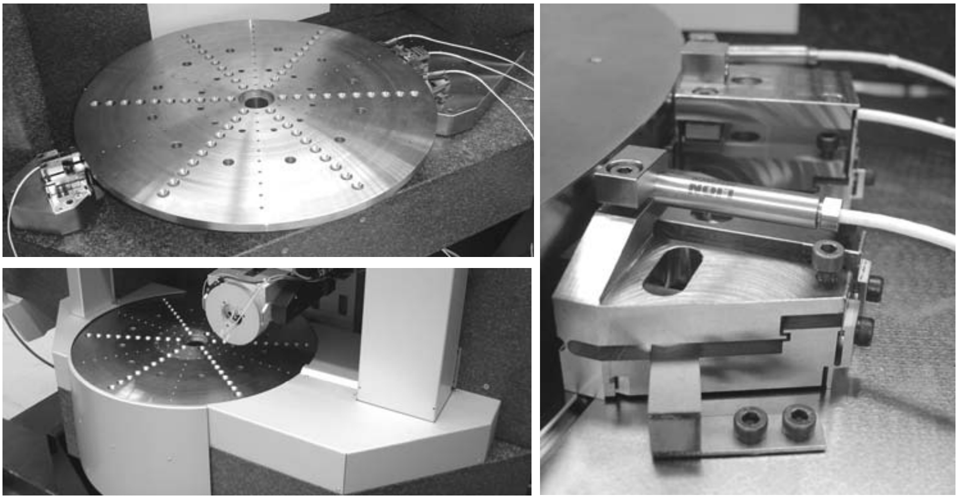

Figure 4.49: Lower metrology frame, probe brackets and shielding

4.5 Metrology system assembly

Figure 4.50 shows the metrology system assembly, with all covers installed. The non-contact probe is already installed in this photograph. The pressure-temperature-humidity (PTH) sensor is situated in the upper right corner of the of the upper metrology frame.

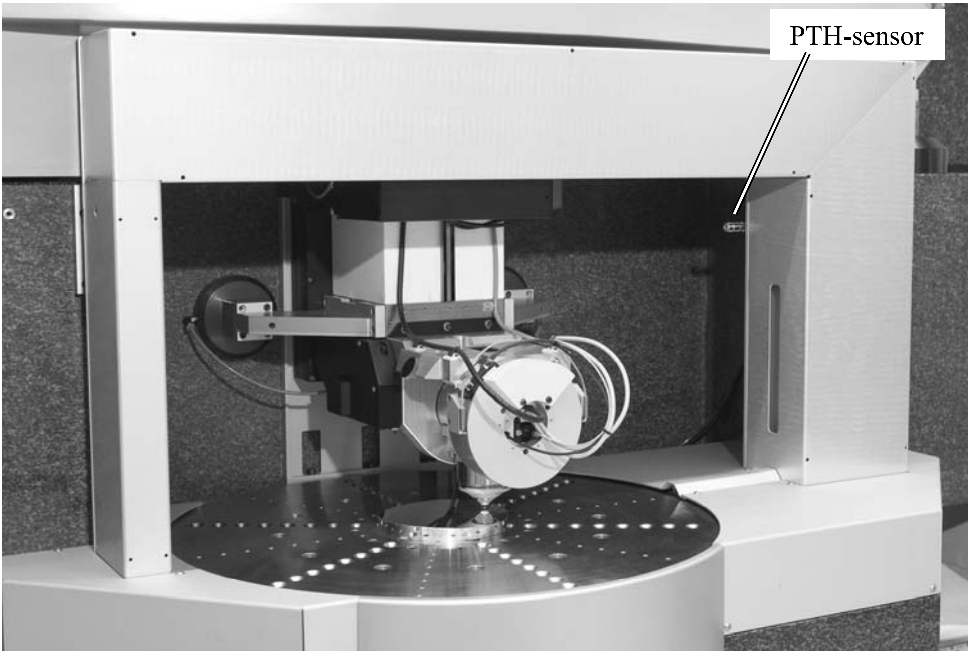

Figure 4.50: Metrology system assembly

4.6 Experiments

In this section, the metrology system stability experiments over 0.1 s and 15 minutes will be shown. The harmonic contents of the measurement error and the displacement is compared. The metrology frame shift compensation mechanism is also tested.

4.6.1 Stability measurements

In section 3.8.2 a test setup was described in which three orthogonal capacitive probes mounted on the spindle measured the displacement of an Invar dummy probe (Figure 3.100). With this setup the stability of the metrology system has also been tested before the optical probe was included in the metrology loop. These tests have been performed with the dummy probe oriented at $\psi = 0°$ and 90°. The results shown below are with the probe at $\psi = 0°$, since this will be the most common orientation.

Figure 4.51 shows the displacement in *z*-direction as measured by the reference capacitive probe and the metrology loop over 0.1 s, sampled at 10 kHz. An offset of 5 nm has been added to the reference probe signal for clarity. The difference between the signals is the part of the displacement that is not measured by the metrology loop. This error has a PV value of 4 nm and an rms value of 0.6 nm.

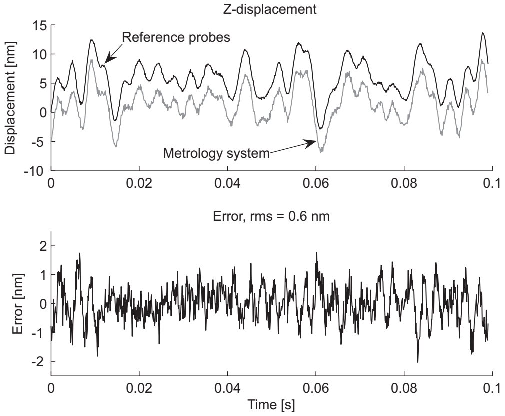

Figure 4.51: Comparison of reference probe and metrology loop in z-direction

Figure 4.52 shows a similar measurement over a period of 15 minutes in *r*, *y* and *z*-direction, sampled at 1 kHz. The drift during this measurement as measured by the reference probes is about 50 nm in *r*, 25 nm in *y* and 85 nm in *r*-direction. These values are an indication of the stability of the motion system with all stages locked. Also note the shock in the nearby workshop at around 10 minutes in *z*-direction.

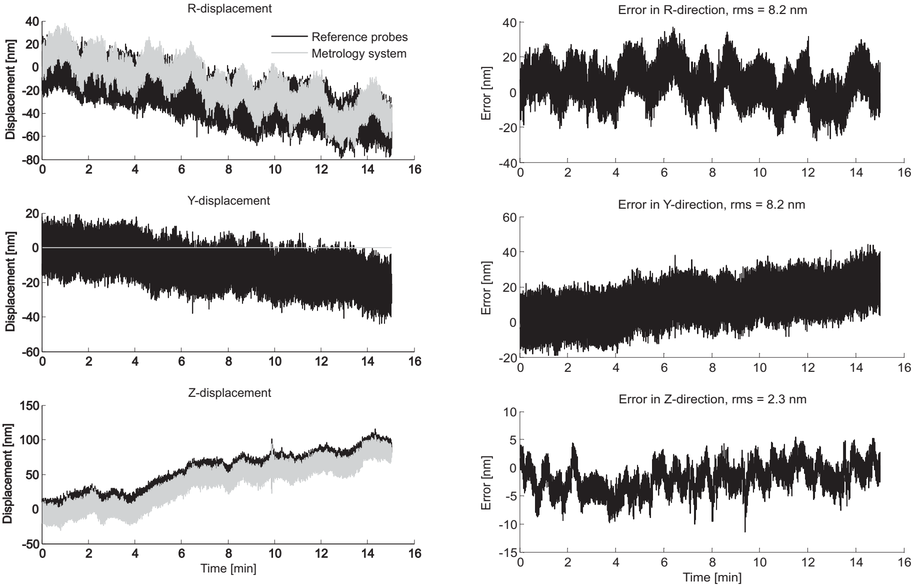

Figure 4.52: r,y,z-displacement measured by reference probes and metrology system

The metrology system measures the displacement of the Ψ-axis and the spindle in *r* and *z*-direction. The difference with the measurements of the reference probes is the error at the probe tip. In these measurements, the refractive index is compensated with a 3rd order polynomial fit. In *r*-direction the faster, uncorrected turbulence and refractive index variations are the main remaining error. The global drift is removed by the metrology loop. The error in *r*-direction is 8.2 nm rms. In *y*-direction the error is equal to the actual displacement, coincidently also 8.2 nm rms including approximately 20 nm of linear drift. In *z*-direction remaining error is 2.3 nm rms, with virtually no remaining drift. The shock around 10 minutes is also compensated for. The remaining fluctuations are probably also turbulence, but with a smaller amplitude than in the *r*-direction due to the shorter air-path.

The harmonic content of a 10 s measurement at 10 kHz is shown in Figure 4.53. The actual displacement as measured by the reference probes shows all the eigenmodes of the motion system, similar to section 3.8.2. The harmonic content of the measurement error is also shown here. In *r* and *z*-direction it can clearly be seen that most of the vibrations are compensated for by the metrology system, especially in the most important *z*-direction. The remaining peak at 278 Hz in *r*-direction is rotation of the Ψ-axis rotor on its brake stiffness, which is too small to be measured by the Ψ-encoder.

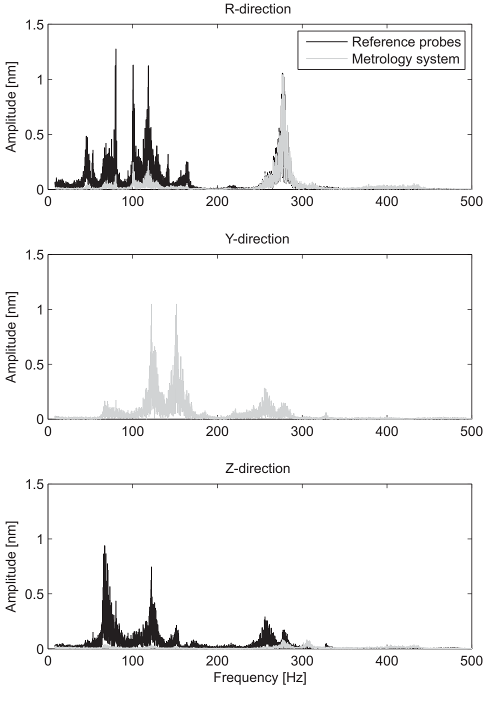

Figure 4.53: Harmonic content of the displacement and the error

4.6.2 Metrology frame shift

As explained in section 3.2.1, the metrology frame may shift in *r*-direction due to bending of the base when the R-stage is moving, or due to thermal expansion of the base. Radial capacitive probe 5 was hereto mounted on an elastic parallelogram and linked to the upper metrology frame via a Super Invar strut. To test this compensation, a force has been applied to the upper metrology frame at the *r*-constraint to shift it in *r*-direction (Figure 4.54). While applying this force, the output of the R-interferometer and the capacitive probe are compared. Little correlation between the error and the displacement can be seen, showing that the compensation works.

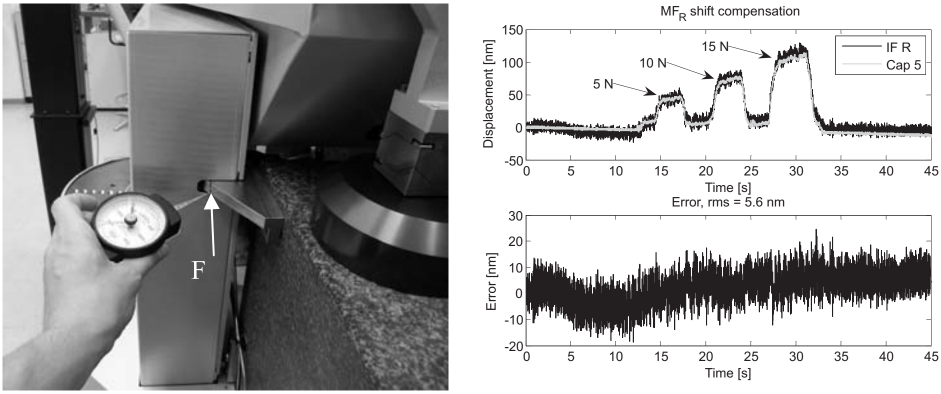

Figure 4.54: Force applied to upper metrology frame and resulting error

When the R-stage is moved through its range, the capacitive probe measures 760 nm displacement (Figure 4.55). In section 3.2.1 a shift of 170 nm was predicted from FEM simulations, but apparently the real shift is larger. The R-stage was moved through its range four times, in which some hysteresis can also be seen. As long as this is mutual for the capacitive probe and the interferometer, this does not cause a measurement error.

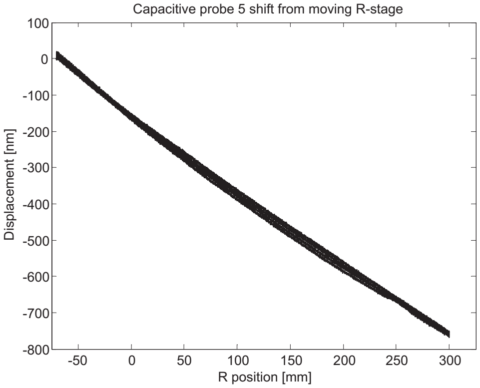

Figure 4.55: Capacitive probe 5 shift due to moving R-stage

4.7 Conclusion

The metrology system measures the position of the probe relative to the product in the six critical directions in the plane of motion of the probe (the measurement plane). The interferometry system measures the Ψ-axis rotor position relative to reference mirrors on the upper metrology frame. A horizontal and vertical interferometer are focussed onto a cylindrical mirror on the face of the Ψ-axis rotor. Due to the reduced sensitivity in tangential direction at the probe tip, the Abbe criterion is still satisfied. Silicon Carbide is the material of choice for the upper metrology frame, due to its excellent thermal and mechanical properties. Mechanical and thermal analysis of this frame shows nanometer-level stabilities under the expected thermal loads. The multi-probe method allows for in-process separation of the spindle reference edge profile and the error motion. Simulations show nanometer level uncertainty, but this has not yet been tested in practice.

Experiments show motion amplitudes in the order of 15 nm PV over 0.1 s, which is compensated to 0.6 nm rms by the metrology system. Over 15 minutes, 80 nm of drift in the most critical in z-direction is compensated to 2.3 nm rms. In the tangential r-direction, the stability is 8.2 nm rms over 15 minutes, just as in the out-of-plane y-direction. Comparing the harmonic content of the error to the displacement clearly shows the eigenfrequencies that are compensated with the metrology system, and those which are not. The upper metrology frame shift in r-direction is measured to be 760 nm, which is cancelled by the compensation mechanism.

At standstill, the metrology system short term stability exceeds the requirements. The long term drift is also small, and can be compensated for in the surface measurement procedure as shown in section 7.2.3. After further experiments with a rotating spindle, moving stages and the optical probe included, a similar conclusion will be drawn in Chapter 7.

Chapter 5

Non-contact probe[1]

The non-contact probe measures the distance between the Ψ-axis rotor and the surface under test. A dual stage design is applied, which has 5 mm range, nanometer resolution and 5 ° unidirectional acceptance angle. This enables the R and Z-stage and Ψ-axis to be stationary during the measurement of a circular track on a freeform surface. The differential confocal method is compactly integrated with an interferometer. The focussing objective is positioned by a flexure guidance with a voice coil actuator. A PSD allows for compensation of the inclination dependent error. A switching motion controller finds the surface and keeps the objective focused onto the surface with nanometer level servo error.

5.1 Concept

The probe must measure the absolute distance to the surface, since the signal is lost for instance when measuring discontinuous surfaces, when performing exploratory probing to verify the coarse surface geometry, or when measuring alignment fiducials. No optical method was found that could do this in a single stage. A two stage concept has therefore been designed, where a short range absolute optical measurement method is kept in focus onto the surface by a 5 mm range servo system (Figure 5.1).

---

[1] *This chapter is largely based on the work of L.A. Cacace. A summary of the design, realization and testing is given here, a detailed description is given in (Cacace, 2009).*

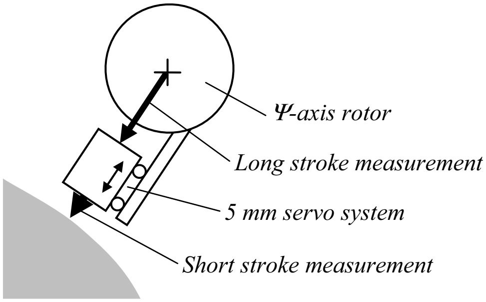

Figure 5.1: Dual stage probe concept

5.1.1 Required probe characteristics

As explained in section 2.2, the axial measurement range should be 5 mm, equal to the maximum peak-to-valley departure from rotational symmetry. The probe will be positioned on a track by the R and Z-stage and the Ψ-axis. These axes will be locked mechanically, so the probe will not be actively controlled perpendicular to local freeform surface slope variations. The acceptance angle should therefore equal the unidirectional maximum local surface slope of -5° to +5°.

Most optical probes are inherently inclination dependent. A slope dependent axial measurement uncertainty (2σ) is therefore specified that is equal to 10 nm when the probe is perpendicular to the surface (for flats, spheres and aspheres), and allowed to increase up to 35 nm at 5° when measuring freeforms. The desired resolution is chosen an order of magnitude smaller, i.e. 1 nm. The required dynamic range is thus $5 \cdot 10^6$.

The intended speed of the spindle is 1 rev/s, which is equal to a circumferential speed of 1.57 m/s at r = 250 mm. To achieve a point spacing of 0.5 mm here, a sample frequency of at least 3 kHz is required.

The reflectivity of the surface may range from 3-4% to (theoretically) 100%, which will result in a factor 25 difference in reflected intensity of the measurement beam. By adjusting the power of the light source to the surface that is measured, optimal signal to noise ratio can be maintained.

The disturbances acting on the servo system are expected to consist of low frequencies (< 10 Hz) with up to mm order amplitude that originate from the form of the surface, and high frequencies with nm - μm order amplitudes that originate from manufacturing machine tool marks and vibrations. The influence of dust and scratches is difficult to predict, and will depend on the response of the measurement method on these scattering elements and on the speed with which they are encountered. The bandwidth of the servo system should either be high to follow these sharp disturbances, or be low to not act and still be in focus after the abnormality has passed. The guidance and actuator are hereto designed for maximum bandwidth, such that both approaches are possible by adjusting the controller software. After all, the goal is to minimize the measurement uncertainty by minimizing the servo error on the surface itself, not on the dust and scratches.

To quantify a minimum required bandwidth, a 10 Hz sinusoidal surface with 1 mm amplitude is assumed. Because the range of the short stroke measurement system is a few micrometers, a desirable servo error of 100 nm is adopted. This requires 10^4 disturbance rejection at 10 Hz. If an average -2 slope is assumed in the open loop frequency response, this gives a desired closed loop bandwidth in the order of 1 kHz.

The probe will be mounted into the Ψ-axis rotor. The maximum probe dimensions are summarized in Figure 5.2. The length of the probe, from the Ψ-axis centre to the probe tip, is chosen to be 100 mm. As explained in 4.2.1, a cylindrical mirror is manufactured onto the face of the Ψ-axis, of which the roundness has to be calibrated. The maximum diameter that can be calibrated at NMi VSL with the required level of accuracy is ∅70 mm. Furthermore, the dimension of the part of the probe that protrudes from the Ψ-axis is limited by the interferometry system at the extreme positions. To be able to insert the probe into the Ψ-axis rotor without disassembling it, the length in *y*-direction is limited to 90 mm by the spacing of the journal bearings of the Ψ-axis stator.

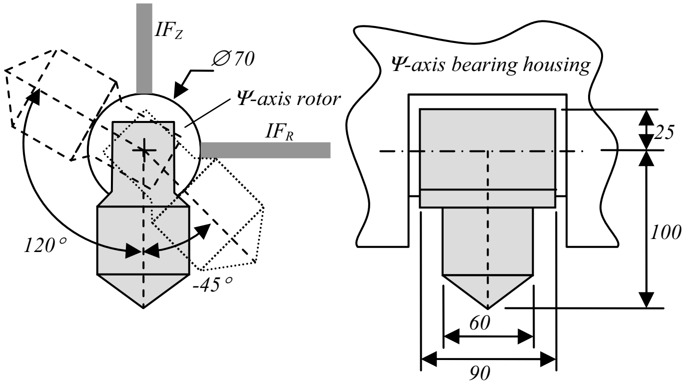

Figure 5.2: Maximum probe dimensions

The spot size of the optical probe will be in the order of a few micrometers, which is small compared to the mm order point spacing. For polished surfaces, no significant harmonic content is expected to be present in the mid- and high spatial frequencies. Aliasing is therefore not expected to be a problem. If mid- or high spatial frequencies are present in the surface, the point spacing should be decreased or the allowed measurement uncertainty must be increased. A high resolution scan may be performed to determine the harmonic content of the surface.

On diamond turned surfaces, the scallop spacing is in the same order of magnitude as the spot size. They may act as cylindrical mirrors and thereby alter the response of the probe. This may reduce the achievable uncertainty. The magnitude of this effect is difficult to predict, and will have to be tested in practice.

5.1.2 Optical absolute distance measurement principles

Several optical distance probe principles were considered, of which an extended overview is given in Appendix I. The main candidates are summarized below.

White-light interferometry

Absolute distance measurement can be done by multiple wavelength or white-light interferometry (Malacara, 2007; Whitehouse, 1994). A sharp interference peak can be detected when the measurement and reference paths of the interferometer have exactly equal optical path length. A repeatability of 0.5 nm is reported in (Deck and De Groot, 1994). In the Mireau setup the intensity peak relates directly to the distance between the surface and the objective, and can thus be used for the feedback of the servo system. The interference peak is very sharp, such that hardly any servo error is allowed. This method is therefore generally applied by scanning through focus point by point to detect the position of the interference peak, rather than to continuously keep it in focus while a surface is moving laterally with the intended high scanning speed.

Triangulation sensors

Triangulation sensors are nominally insensitive to local surface slope for specular surfaces (Gao and Kiyono, 1997; Shiou and Cheng, 2005). The measurement spot can be relatively large, reducing the sensitivity to local surface defects and high spatial frequencies. The measurement spot displaces laterally when the surface is not in nominal focus, which requires software compensation. The blunt layout of this principle is a disadvantage when measuring concave optics.

Chromatic confocal sensors

Chromatic confocal sensors employ an objective designed with large chromatic aberration to disperse a white-light source. The wavelength of the light returning through the pinhole is determined by a spectrometer, and is related to the distance between the surface and the objective by calibration (Molesini et al., 1984). This makes this method principally insensitive to surface reflectivity and surface inclination. The highest reported resolution is 2 nm with 10-20 μm range (www19). The objective used here is 190 mm long and thus relatively heavy to use in a dual stage system.

Focus detectors

In confocal microscopy (Hamilton and Wilson, 1982), a beam is focused onto a surface. The reflection is imaged onto a pinhole. When the intensity coming through the pinhole is maximum, the surface is in best-focus. At this point, the slope of the signal is zero, resulting in zero sensitivity. A better approach is therefore to apply a differential setup, which results in a zero crossing in best-focus. Focus sensors based on confocal and other methods come in a large variety, and were developed for application in optical storage. Several configurations were adapted for distance measurement, such as the critical angle method (Kohno et al., 1988), the Foucault method (Benschop and Van Rosmalen, 1991), the Astigmat method (Fan et al., 2001), the Laser Diode Grating Unit method (Visscher, 1992; Ehrmann and Schindhelm, 1998) and the differential confocal method (Fainman et al., 1982; Tan and Wang, 2002). Some of these methods are combined with an interferometer to increase the range (Dobosz, 1983; Zhang and Cai, 1997; Lu and Li, 2001), but differently from what will be shown later in this chapter. In (Mashimo et al., 1997) an Astigmat is combined with a triangulation sensor to obtain a coarse and fine measurement in one sensor. This does not give the required accuracy over the full range.

The characteristics of the differential confocal method are most suitable for application in the optical probe (see next section). It has a high sensitivity, combined with a relatively long near-linear range. It can be made insensitive to intensity variations in the reflected beam by normalization. It is in principle insensitive to surface tilt in best-focus, and has a rotationally symmetric beam path. The spot size that is required to obtain the required depth resolution is small; in the order of a few micrometers.

5.1.3 Probe concept

The differential confocal method will be described first. Next the addition of a PSD for correction of inclination dependent errors and an interferometer for increasing the range will be explained.

Differential confocal system

The differential confocal principle is shown schematically in Figure 5.3. A Gaussian distributed, linearly polarized laser beam passes through a polarizing beam splitter (PBS) and a quarter wave plate (QWP). The now circularly polarized beam is focused onto the surface by an objective lens with a high NA, such as a CD-player objective. The beam is reflected by the surface and passes through the quarter wave plate again. Its polarization direction has now rotated by 90°, such that it is deflected by the polarizing beamsplitter.

The beam is now split into two equal branches by a non-polarizing beamsplitter (NPBS). A lens with a low NA in each branch creates a focus which is a conjugate of the measurement spot. An undersized pinhole (PH) is inserted in each branch, one just in one front of focus and one just behind the other focus. Behind each pinhole, a photodiode (PD) measure the amount of light passing through the pinhole.

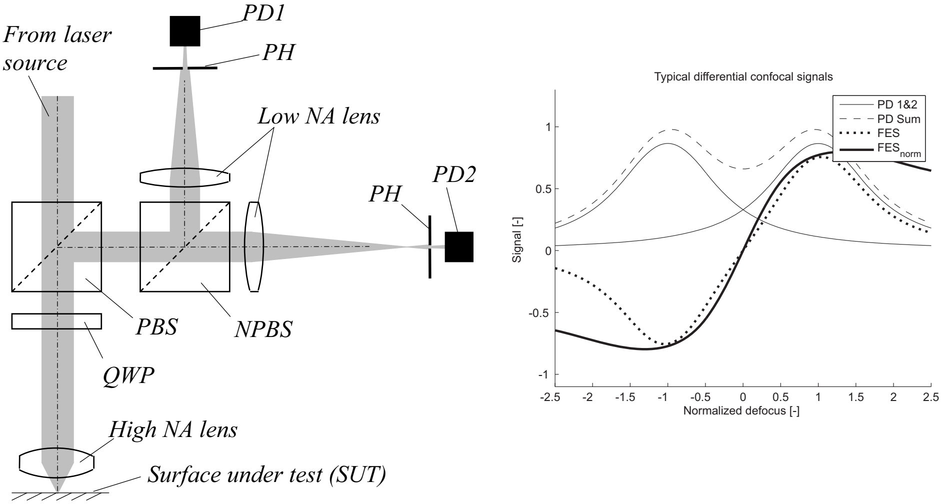

Figure 5.3: Differential confocal system and typical response

When the surface moves towards the objective, both foci move towards their respective photodiodes. This will result in a decrease of the amount of light passing through the pinhole of PD1, and an increase of the amount of light passing through the pinhole of PD2. When the surface is scanned through focus, two Gaussian-like response curves will be measured at the photodiodes, with the spacing between their maximums equal to half the distance between the pinholes (Figure 5.3, right).

Subtracting the signals (5.1) yields the focus error signal (*FES*), and dividing by the sum of the signals yields the normalized focus error signal (*FES$_{norm}$*). Normalization makes the signal insensitive to intensity variations due to changes in laser power, surface reflectivity or common noise in the photodiodes. Both signals are also shown in Figure 5.3.

$$FES = PD1 - PD2 \quad and \quad FES_{norm} = \frac{PD1 - PD2}{PD1 + PD2} \tag{5.1}$$

Both focus error signals have a relatively long linear range with a steep slope and thus high sensitivity. Further, a zero crossing is present where the surface is in best-focus of the objective. This zero crossing can be used to ‘lock’ the probe onto the surface.

Correction of inclination dependent errors

Unidirectional local surface slope can amount up to 5°, which will cause the returned beam to shift by twice the surface slope times the focal distance of the objective. This is shown somewhat exaggerated in Figure 5.4. As a consequence, the beams will have an eccentric intensity distribution relative to the pinholes. The reduced amount of light passing through the pinholes will result in a decreased slope of the focus error signal, but theoretically the location of the zero crossing does not shift. This will thus only result in a measurement error that is a function of the servo error.

Another cause for measurement errors are aberrations in the optics, caused by lens geometry, manufacturing errors and alignment errors. The beam shift will cause it to pass through different parts of the optical system, and will thus be aberrated differently. These may not only result in a changing slope of the focus error signal, but also cause the zero crossing to shift.

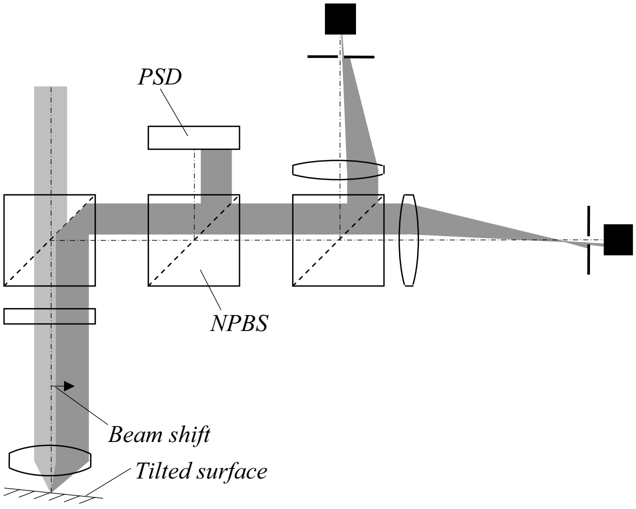

Figure 5.4: Inclination dependent error compensation with a PSD

After a surface is measured, the surface slope can be estimated from the height data and the measurement may be corrected. Due to the small focus spot, local waviness and roughness are expected to contribute to shifting of the returned beam, since the local surface slope at micrometer level may differ from the global surface slope. The returned beam may thus be walking through the aperture with a higher frequency than what would be expected from the surface form alone.

To correct for these inclination dependent errors, a non-polarizing beamsplitter and a two-dimensional Position Sensitive Detector (PSD) are added to the system (see Figure 5.4). This PSD monitors the position of the reflected beam in the aperture while measuring to a tilting surface. Together with a calibration table, the Focus Error Signal can now be corrected after a surface is measured. To generate this calibration table, a known tilt and defocus should be applied simultaneously to the probe, for which no satisfying method has been found in literature yet. A novel calibration procedure has therefore been designed, which is further explained and tested in (Cacace, 2009). The compensation of inclination dependent errors using a PSD is part of a patent application that has been filed on the probe design (Van Amstel et al., 2007).

Increasing the measurement range

The measurement range of the differential confocal principle is in the order of a few micrometers when nanometer uncertainty is required. The entire differential confocal system could be translated over 5 mm, but this would result in a substantial mass and thus little servo bandwidth. Since the beam passing through the objective is collimated when the surface is in focus, the objective alone may also be translated along the optical axis. This significantly reduces the moving mass.

The position of the objective can be measured by an interferometer or a linear scale. An interferometer is the obvious choice, since it adds little moving mass (only a mirror), has high bandwidth and is already available in the machine. As schematically shown in Figure 5.5, this interferometer is measuring parallel to the differential confocal system, to a mirror that is attached to the moving objective.

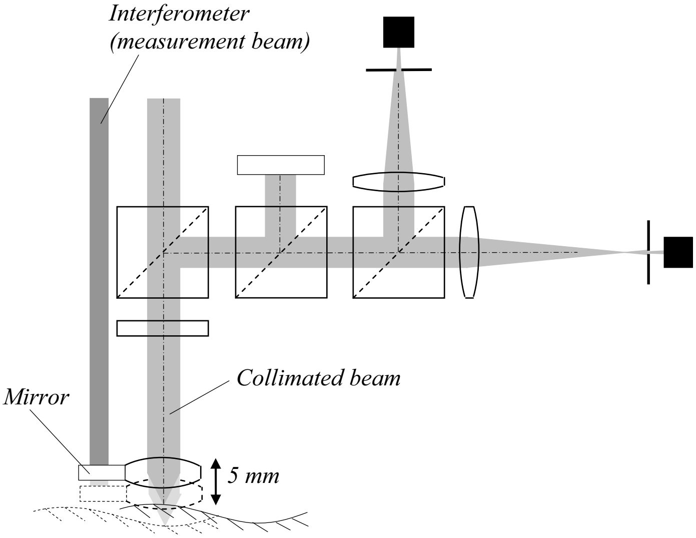

Figure 5.5: Extension of the range by the addition of an interferometer

The zero crossing of the focus error signal can be used as a feedback signal, to servo control the objective to best focus onto the surface. The sum of the focus error signal (the servo error) and the interferometer is now the total distance measured by the probe.

5.1.4 Rough or diffuse surfaces

Although measuring rough surfaces is not a primary goal for the instrument, the advantages of the ability to measure these with the same setup are evident. Some ideas to accomplish this are therefore given here.

When focusing the previously described differential confocal system onto a rough surface, scattering will occur. First of all, this reduces the amount of reflected light, reducing the signal to noise ratio. This can be partially countered by increasing the laser power, the same as is being proposed for measuring transmissive surfaces. The reduced signal to noise ratio may cause the normalization to become unreliable, since the quotient of two weak signals is being calculated.

A second effect is the change in response. In pure reflection, shift of the foci at the pinholes is twice the displacement of the surface. In pure scattering on a diffuse surface, however, this is only proportional. The actual response of the probe will be a combination of the two types of reflection. Due to the scattering, the aperture will also become overfilled, which changes the NA of the beam. A surface specific Focus Error Signal calibration can be conducted on the surface under test, by scanning the objective through focus and using the probe interferometer as a reference.

If this is insufficient, another option may be to use the probe in conventional confocal mode (Hamilton and Wilson, 1982), by only using the signal of one of the photodiodes. The peak intensity is measured when the surface is half the pinhole spacing out of focus. By vibrating the objective around this point, the peak intensity can be detected more robustly than the zero-crossing in differential confocal mode.

This method can be implemented in software, since all the signals will be available in the control and data-acquisition system. Depending on the surface condition, one of the two operation modes can be selected in the software. Obviously, the uncertainty will be larger compared to the differential confocal mode, but it is certainly worth trying to determine whether valuable form information can be collected this way for subsequent processing steps.

5.2 Differential confocal analysis and testing

To explain the working principle of the differential confocal system, a summary of the analytical modelling, testing and optimization as described in (Cacace, 2006) will be given in this section. The response of the differential confocal system is derived analytically using Gaussian beam theory, which will therefore be explained first. Next, the dimensionless focus error signal will be formulated and tested in a test setup, and optimization will be briefly addressed.

5.2.1 Gaussian beam theory

According to geometrical optics, light ideally is focused to a point. To satisfy the law of energy conservation, the irradiance would have to become infinite. Instead, light obeys the laws of diffraction near focus. The diameter of the beam contracts to a finite dimension in focus, from where it starts expanding again (see Figure 5.6, left). For a laser beam with a Gaussian intensity distribution, the distribution in focus is also Gaussian. The radial irradiance distribution is given by (5.2) (O'Shea, 1985), and shown in Figure 5.6 (right):

$$I_D = I_0 \cdot e^{-2\frac{D^2}{D_z^2}} \tag{5.2}$$

Here, D_z is defined as the diameter where the irradiance is $1/e^2$ times the irradiance I_0 at the beam axis. The continuous lines in Figure 5.6 represent these borders, while the dotted lines represent the borders predicted by geometrical optics. These are the asymptotes for the Gaussian approach. For a given location along the optical axis, the irradiance distribution I_D is now given as a function of the diameter D.

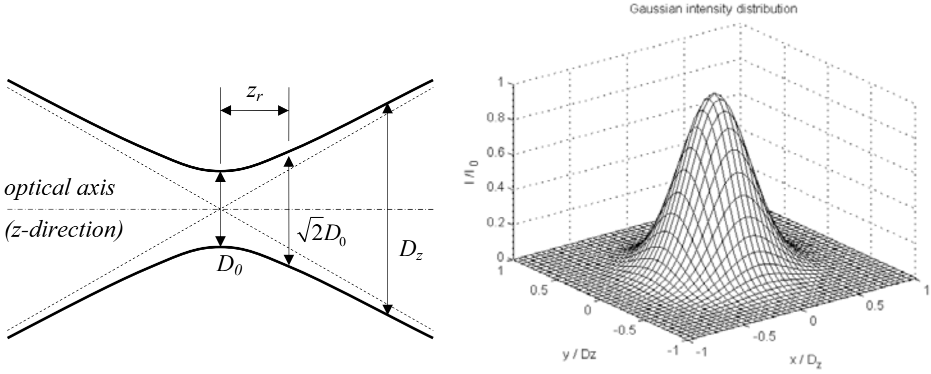

Figure 5.6: Gaussian beam waist and intensity distribution

The region where the beam has the smallest diameter is called the beam waist diameter (D_0). The beam waist extends to the point along the optical axis to a point where the diameter is $\sqrt{2}\cdot D_0$. This distance is called the Rayleigh range (z_r). The divergence between the beams is the angle between the asymptotes (θ). The three beam properties are interdependent. The relation giving D_z at an arbitrary position along the optical axis that is used here is:

$$D_z = D_0\sqrt{1+\left(\frac{z}{z_r}\right)^2} \tag{5.3}$$

5.2.2 Normalized dimensionless focus error signal

The pinholes are placed near the focus in the Gaussian beam, in the image of the surface under test. Here they block part of the light from reaching the photodiodes. By integrating (5.2), the power P_{enc} passing through a circle with diameter D is equal to:

$$P_{enc} = P_{beam}\left(1 - e^{-2\frac{D^2}{D_z^2}}\right) \tag{5.4}$$

The ratio of the encircled power P_{enc} to the total power of the beam P_{beam}, passing through a pinhole with diameter D_{ph} is called the fractional transferred power (FTP), and is given by:

$$FTP = \frac{P_{enc}}{P_{beam}} = \left(1 - e^{-2\frac{D_{ph}^2}{D_z^2}}\right) \tag{5.5}$$

To make the expressions indifferent to the choice of lenses, beam diameter etc, the pinholes are transferred to the object space as shown in Figure 5.7, and parameters are made dimensionless. They are spaced around the surface under test (SUT) at a distance u_{ph}. Displacement of the surface under test effectively displaces the position of the beam waist relative to the pinholes (or vice versa).

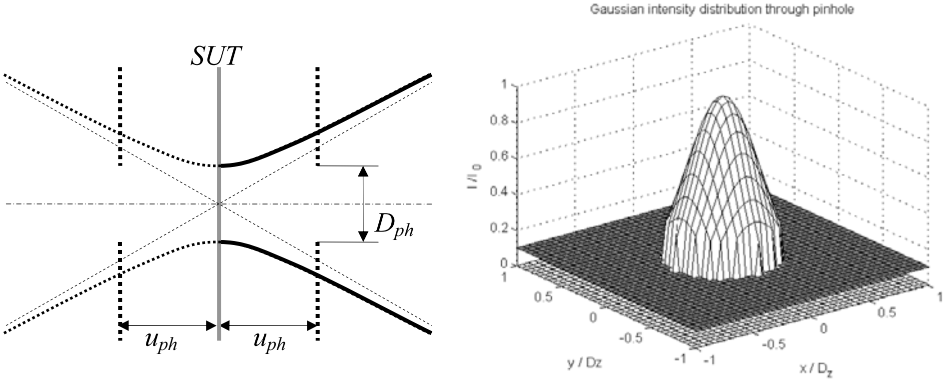

Figure 5.7: Pinholes in object space and profile of beam passing through a pinhole

The parameters D_{ph} and z are made dimensionless by dividing them by the waist diameter (D_0) and the Raleigh range (z_r), respectively:

$$D_{ph,dl} = \frac{D_{ph}}{D_0} \qquad (5.6)$$
$$z_{ph,dl} = \frac{z_{ph}}{z_r}$$

Substitution into (5.5), leads to:

$$FTP = 1 - e^{-2\frac{D_{ph,dl}^2}{1+\left(z_{ph,dl}\right)^2}} \qquad (5.7)$$

Since the light is reflected at the surface under test, an axial displacement u_{SUT} of this surface will result in twice the displacement of the beam waist in image space. The dimensionless distance between the pinholes and the beam waist can thus be written as:

$$\begin{aligned} z_{ph1,dl} &= u_{ph,dl} + 2u_{SUT,dl} \\ z_{ph2,dl} &= -u_{ph,dl} + 2u_{SUT,dl} \end{aligned} \qquad (5.8)$$

Substituting this into (5.7), and subtracting the fractional transferred power of pinhole 1 from pinhole 2, the dimensionless focus error signal FES_{dl} is expressed as (5.9):

$$FES_{dl} = e^{-2\frac{D_{ph,dl}^2}{1+\left(u_{ph,dl}+2u_{SUT,dl}\right)^2}} - e^{-2\frac{D_{ph,dl}^2}{1+\left(-u_{ph,dl}+2u_{SUT,dl}\right)^2}} = e_{1,dl} - e_{2,dl} \qquad (5.9)$$

This signal can be normalized by dividing by the sum of the fractional transferred power of pinhole 1 and 2, giving:

$$FES_{norm,dl} = \frac{e_{1,dl} - e_{2,dl}}{2 - e_{1,dl} - e_{2,dl}} \qquad (5.10)$$

With this model, the effect of the pinhole diameter and offset is shown in Figure 5.8. This figure shows nine combinations of dimensionless pinhole offset and diameter. In the columns, the pinhole diameter is varied, where on the left little power passes through small pinholes, while saturation occurs for large pinholes on the right. On the rows, the varying pinhole offset can be seen from the position of the FTP signals. In combination with the pinhole diameter this leads to very different Focus Error Signals, in signal range, linearity as well as sensitivity at the zero crossing.

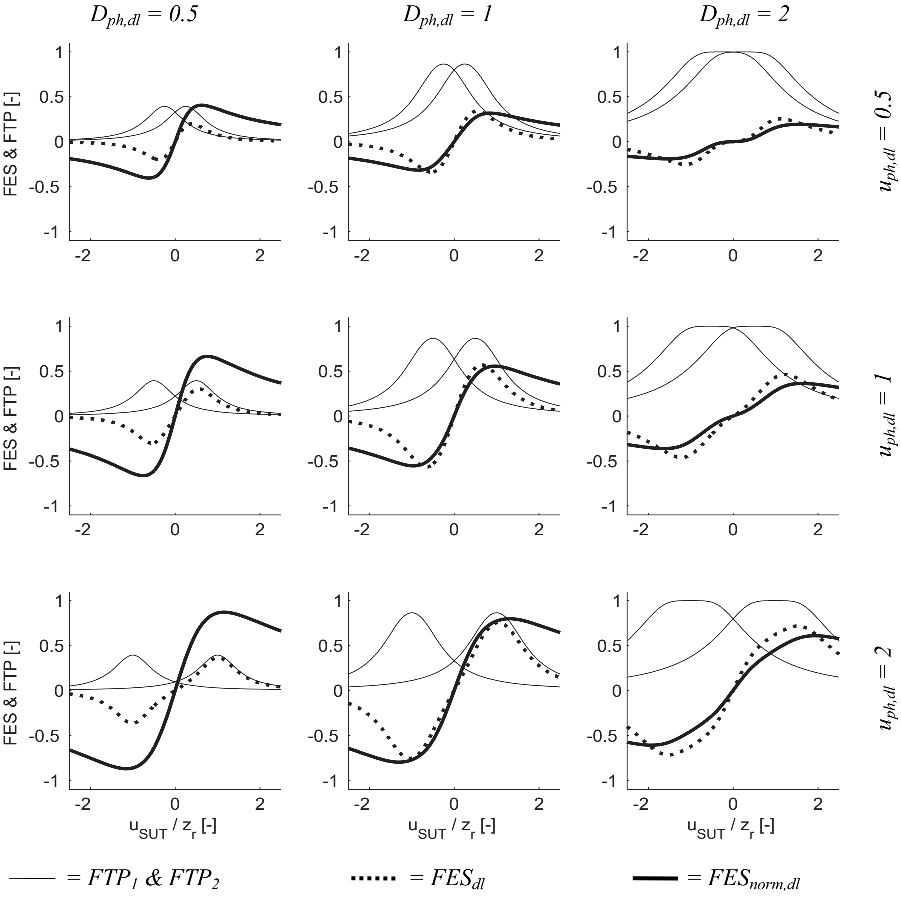

Figure 5.8: Differential confocal response as a function of dimensionless pinhole offset and diameter

5.2.3 Test setup

A test setup was built (Figure 5.9), similar to the schematic of Figure 5.3. The focusing objective is fixed and the PSD for inclination correction and interferometer for the enlarged range are not included. The beam of a HeNe laser (1) is focused onto a mirror (2) by a microscope objective (3). The mirror can be translated through focus by a piezo (4) with internal position feedback by a capacitive sensor. The reflected beam returns to the main optics block (5), where it is split into the two equal branches (6 and 7) in which the pinholes and photodiodes are placed. The photodiode signals are processed by dedicated Philips analog normalization electronics (8). These electronics have a bandwidth of 150 kHz, and are also used in the final probe.

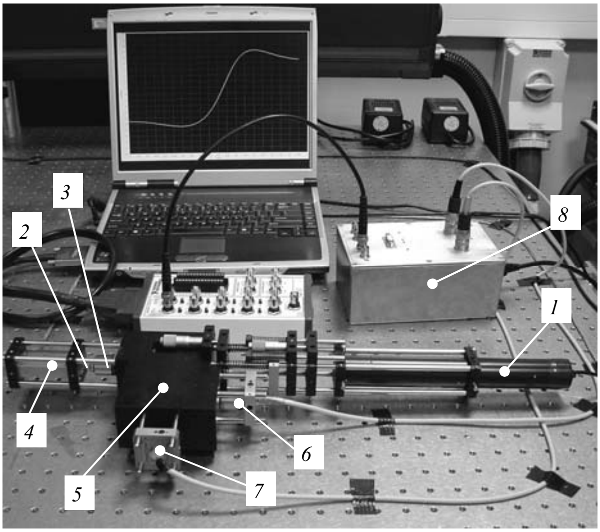

Figure 5.9: Differential confocal test setup

Typical response

Figure 5.10 (left) shows the typical response of the test setup for a pinhole diameter of 20 μm and a pinhole offset in object space of 3 μm. Due to aberrations in the system, the individual photo diode signals are not exactly symmetrical, which causes the fluctuations in the ends of the normalized FES signal. Around the zero crossing, the sensitivity is 12.1 V/μm, the electrical noise level is less than 0.1 nm rms, and the usable near-linear range is approximately 1 μm. With slightly increased range at the cost of some resolution, this differential confocal method is well applicable in the optical probe.

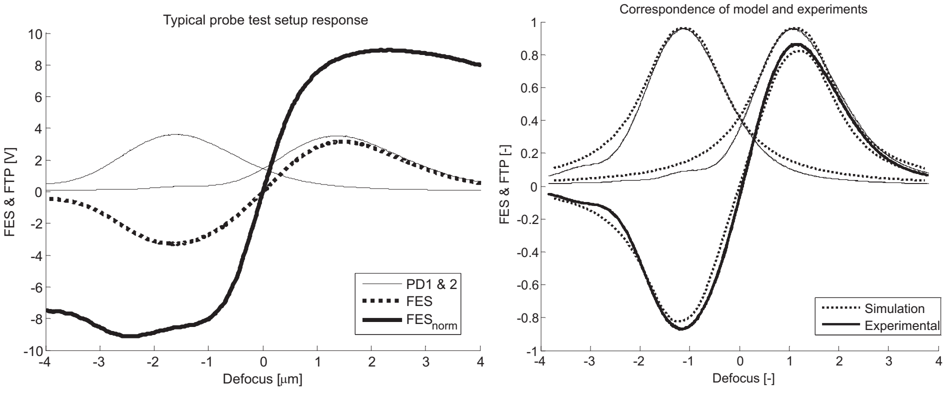

Figure 5.10: Typical test setup response and comparison of model and experiment

The model of formula (5.10) was extended with the properties of the test setup, such as focal lengths and laser power. Figure 5.10 (right) shows the simulated and experimental results for dimensionless pinhole diameter of 1.3 and a dimensionless pinhole offset of 2.2. The diameter of the beam waist is 1.0 μm and the Rayleigh range is 1.3 μm. Without any further fitting, the model matches the experimental results very well.

Interference problem

As the alignment of the test setup improved, an interference problem arose of which an example is shown in Figure 5.11. In this extreme case, the interference even causes the Focus Error Signal to become ambiguous. This is caused by interference of a ghost reflection in a cavity formed by the moving mirror on one side and a parallel plane on the other. The quarter wave plate and polarizing beamsplitter should however prevent this, and the wavelength is not an even portion of the HeNe wavelength.

After eliminating the parallel planes of the beam splitters, it appeared that the other half of the cavity was formed by the laser window. Again, the quarter wave plate and polarizing beamsplitter should prevent light from returning to the laser. Eventually it was found that the large angle of incidence of the outer parts of the circularly polarized beam in combination with polarization dependent reflection of the moving mirror caused the returned beam to be slightly elliptically polarized. This caused some of the light to leak back to the laser and reflect on the laser window or to feedback into the laser. The angle of incidence also explains the wavelength of the interference.

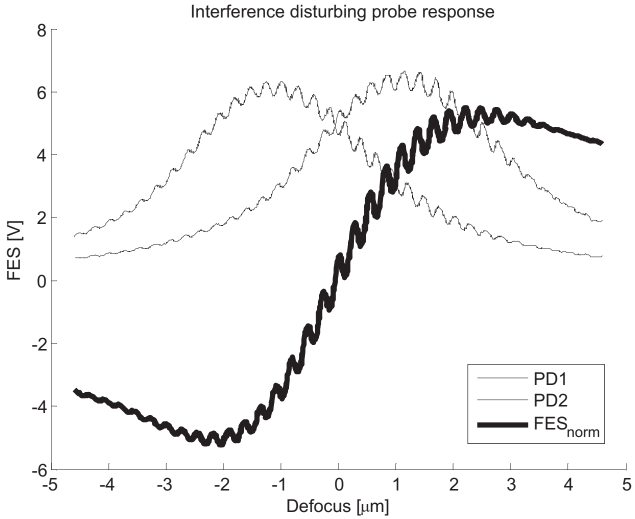

Figure 5.11: Interference problem in probe response

Adding a Faraday isolator after the laser eventually solved the problem. This element acts as an optical diode, which deflects the returned beam leaking through the beamsplitter out of the system. This issue has shown that much care must be taken to prevent ghost reflections in the optical design, since they cause uncorrectable errors or even ambiguities in the FES signal.

5.2.4 Optimization

Six main properties define the performance of the differential confocal system. These are the sensitivity at the zero crossing, the near-linear measurement range, the near-linear optical signal range, the electrical noise level, the electrical dynamic range and the inclination dependent error. These properties are influenced by five parameters of the system: the pinhole diameter, pinhole offset, laser wavelength, laser beam diameter and focal length of the objective lens. Through numerical simulations these parameters are chosen such that the optimal compromise is reached with regard to the specific requirements for the probe as meant in this thesis, as is further described in detail in (Cacace, 2009). The outcome of these calculations and the practical availability of optical components has been used as the input for the optical design.

5.3 Design and realization

The optical design was shown schematically in Figure 5.5. A compact integration of the differential confocal system and the interferometer will be explained first. Next, the design of the optical system, the main optics body and the objective guidance and actuator are explained.

5.3.1 Optical design

The differential confocal system and the displacement measuring interferometer are integrated into one layout, such that they use common optics (Figure 5.12). The differential confocal path (black lines) will be explained first, followed by the interferometer path (gray lines).

The differential confocal laser is delivered to the probe by a fibre and a collimator (1). The beam is deflected towards the surface under test (2) by a right angle prism (3). It then passes through a cube corner (4) of which the top has been removed, and then passes through the central polarizing beam splitter (5) and a quarter wave plate (6). The beam is focused onto the surface under test by a high NA optical storage objective (7). The reflected beam passes the quarter wave plate again and is thus directed to the right by the polarizing beam splitter. Here, a first non-polarizing beam splitter (8) deflects a part of the beam to the PSD (9). The remaining part is split by another non-polarizing beamsplitter (10) to form the two detector branches of the differential confocal system. A mirror (11) is inserted to align the two branches that contain the doublets (12), the pinholes (13) and the photodiodes (14).

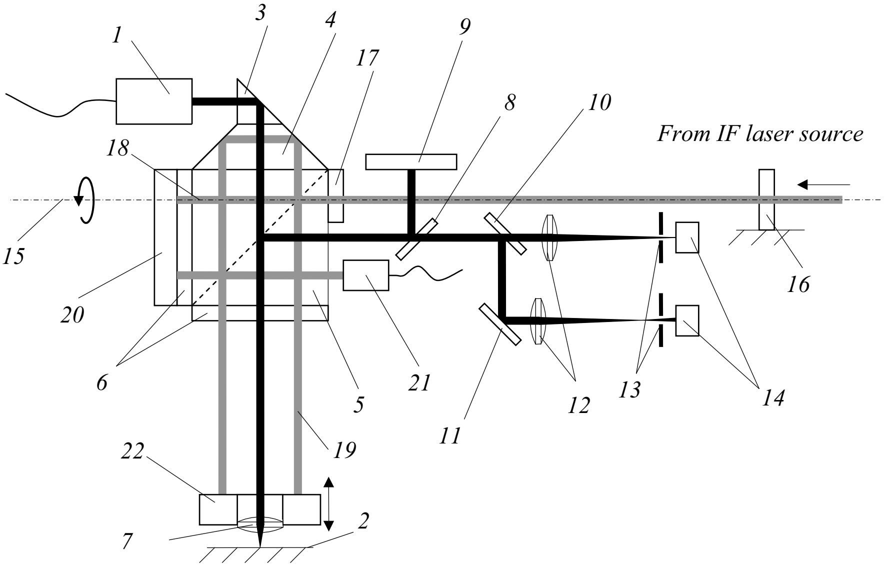

Figure 5.12: Compact integration of differential confocal system and high-stability dual pass interferometer

The interferometer beam comes in from the right, aligned with the rotation axis (15) of the Ψ-axis. A quarter wave plate (16) on the fixed world makes the beam circularly polarized, and a second quarter wave plate (17) on the probe makes the beam linearly polarized again, as explained in section 4.2.2. The beam is then split into a reference part (18) and measurement part (19) by the polarizing beamsplitter (5), which is part of a dual pass high stability interferometer layout (Zanoni, 1989).

The reference beam passes through the beam splitter, through a quarter wave plate (6) onto a mirror (20). The reflected beam again passes the quarter wave plate and is now deflected upwards by the polarizing beamsplitter. After being reflected by the corner cube (4), the beam is deflected towards the quarter wave plate (6) the mirror (19) again, after which it reaches the fibre optic pickup (21).

The measurement beam of the interferometer (18) is deflected down to the moving mirror (22). After being reflected, the beam passes a quarter wave plate (6) again such that it passes through the polarizing beamsplitter and is reflected by the corner cube (4). It then passes to the moving mirror (22) again. After passing through the quarter wave plate and reflecting on the moving mirror, the measurement beam is deflected to the pickup to join the reference beam.

Since both systems operate at (almost) the same wavelength, the anti-reflection and splitter coatings can be optimized for this wavelength. It further results in a compact design that fits the limited space inside the Ψ-axis rotor. Most of the optical components are bonded with index matching adhesive to form a block assembly, to prevent ghost reflections. Further, the dual pass interferometer measures the displacement of the objective without Abbe offset. As will be shown later, it measures over the actuator, eliminating it from the metrology loop. This optical layout is a part of the patent application on the probe design (Van Amstel et al., 2007).

To fit into the Ψ-axis rotor in one piece, the optical layout of Figure 5.12 is folded with two extra prisms (1), as shown in Figure 5.13. Further, several wedges have been added to avoid parallel gap cavities. Further indicated are the fibre and collimator (2), the interferometer supply beam (3), the PSD (4), the differential confocal detector branches (5), the pinholes and photodiodes (6), the main optics block assembly (7), the differential confocal (8) and interferometer (9) beams, the moving mirror and objective (10) and the interferometer pickup (11). The laser source used is a μLS SRT-F fibre coupled diode laser, outputting an adjustable power up to 10 mW at 641.2 nm. Since the beam is highly convergent after exiting the focusing objective, this relatively high laser power causes no safety issues in normal operation.

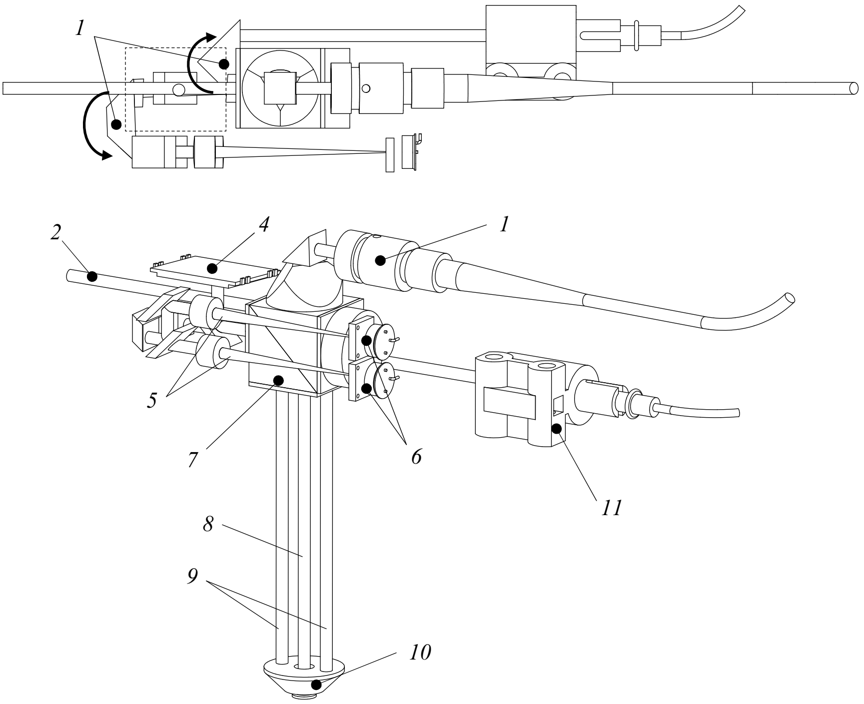

Figure 5.13: Main components of the optical design

5.3.2 Main optics body

Figure 5.14 shows the optics of Figure 5.13 within their housing. The optics block assembly (1) is bonded inside an aluminium block (2) that has many holes and pockets machined into it. The collimator mount (3) is aligned to this block by shimming. Some of the other optical components are aligned using external manipulators while bonding. The non-polarizing beam splitter plates are bonded onto separate pieces (4) that are screwed onto the main block, to be able to remove them during testing and alignment. This is also the case for the detector branches, where the imaging lenses (5), pinholes and photodiodes (6) are attached to a separate detector branch block (7). Alignment of the pinholes is done by sliding them laterally using an external manipulator and then clamping them to the block. The axial adjustment is done by axially sliding and clamping the lens mounts in a fit. This provides sufficient resolution since the alignment is done in magnified image space, giving a linear ratio laterally and a quadratic ratio axially. The cables for the PSD and photodiodes are also shown.

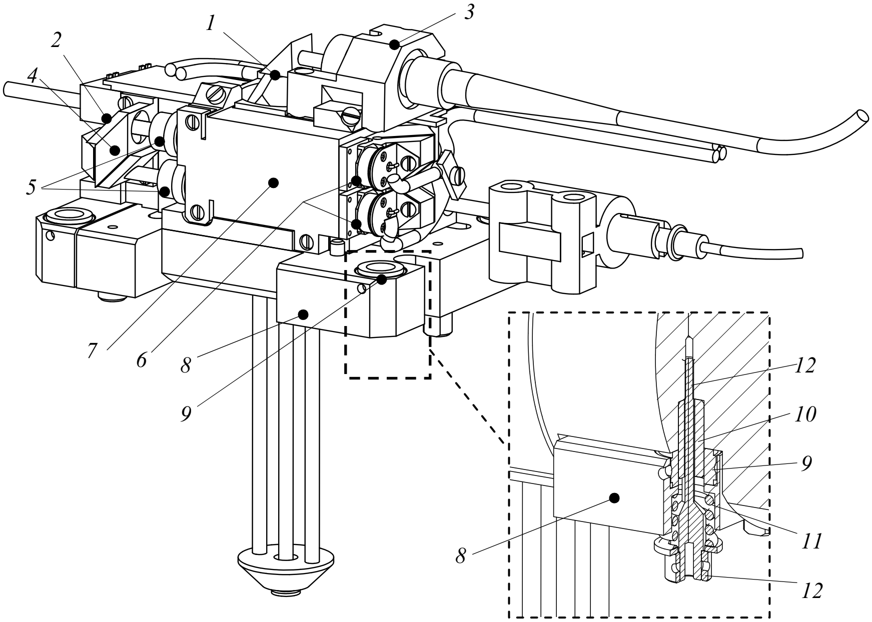

Figure 5.14: Main optics body design

Interface plate

The main body is bonded onto an interface plate (8), which connects to the Ψ-axis. The probe objective guidance is also connected to the bottom of this plate. Four bushings (9) loosely fit into holes in this plate. Three of these hardened steel bushings fit over three dowel pins (10) in the Ψ-axis rotor. The contacts are preloaded by a spring (11), a stud bolt (12) through the hollow dowel pin and a nut (13), using a dedicated tool. A hinge in the interface plate prevents overconstraining. To align the probe perpendicular to the Ψ-axis centre line, the thickness of these bushings is adjusted by lapping. Since the bushings have a loose fit inside the interface plate, the probe can be adjusted in the three in-plane degrees of freedom. Once the probe is aligned, adhesive is inserted around the bushings via holes in the interface plate to lock their position. The probe can now be removed and reinstalled reproducibly on the Ψ-axis.

If other sensors are to be mounted to the Ψ-axis, an interface similar to the interface plate can be applied. If aligned by the same procedure, different probes can be interchanged reproducibly.

Collimator decoupling

The connector of the fibre extends too far to insert the probe into the Ψ-axis rotor in one piece. Initially, it was designed such that the fibre could be decoupled and reinserted after the probe was installed. It appeared that this connection was not reproducible enough to maintain alignment, and furthermore it was wearing rapidly. It was therefore decided to bond the fibre to the collimator and use the fit of the collimator in its elastic clamp as the reproducible connection. Two extra holes were hereto drilled into the already finished Ψ-axis rotor to be able to reach the clamp and tightening screw. A tube was bonded to the fibre that served as a grip and a mechanical stop in axial translation and rotation direction. In the end, this proved to work well.

Realization

Figure 5.15 shows the individual optical components and the assembled block. Most of the components are either modified commercially available parts or parts fabricated to specification.

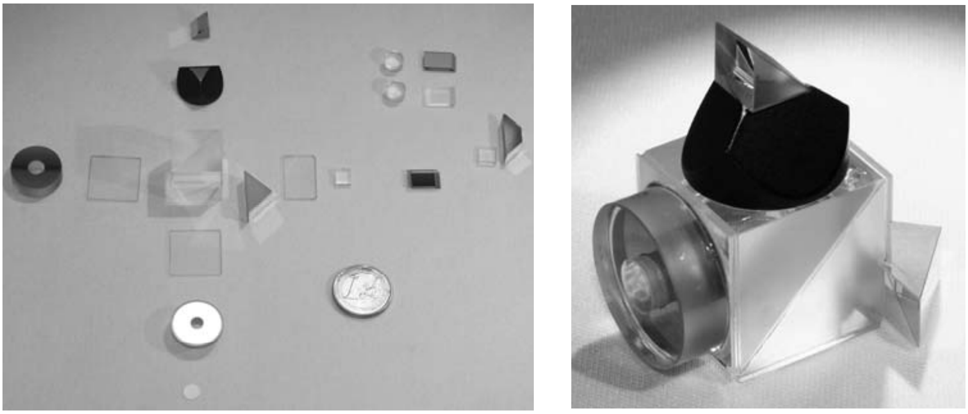

Figure 5.15: Optical components and assembled optics block

Figure 5.16 shows the main body components, which are partially black anodized Aluminium and partially stainless steel. The completed probe main body assembly is also shown, where for instance the beamsplitter plates, detector branch block and collimator can be seen.

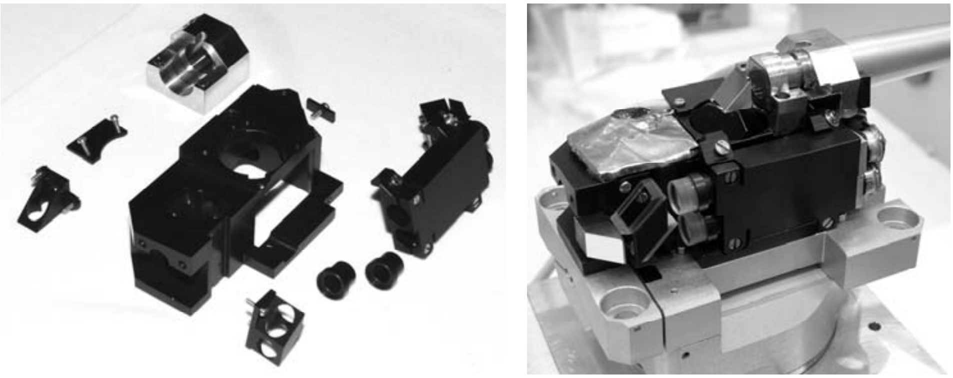

Figure 5.16: Main optics body components and assembled probe main body

5.3.3 Objective guidance and actuator[1]

The guidance moves the objective along a straight line in a repeatable manner over 5 mm range. A repeatability of tens of nanometers is desired for the straightness of motion. Frictionless behaviour is desired to achieve high axial positioning resolution. To achieve high servo bandwidth of the probe, the moving mass should be minimal and the first resonance of the system should be high. A high motor constant in combination with low axial stiffness of the actuator is desired to minimize the power dissipated in the actuator.

Concept

Four types of guidance can be used: a flexure guidance, an air bearing, a rolling element bearing and magnetic bearing. A flexure guidance is free of friction and hysteresis and therefore shows highly repeatable behaviour, and the quality of motion can be in the nanometer range (Rosielle and Reker, 2003; Smith, 2000). It does not require an external power or air supply to operate the guide, other than for axial actuation. Since it is a simple mass spring system, it returns to its equilibrium position when actuation power fails. The 5 mm range of motion is feasible within the required volume. A guidance based on flexures therefore has been designed.

---

[1] *The design of the objective guidance and actuator is largely based on the BSc thesis of S.K. Ravensbergen (Ravensbergen, 2006).*

A Lorentz actuator is preferably applied in this kind of applications. If applied directly onto the moving part, it is non-contact and thus has no friction, wear or hysteresis. For the required stroke of 5 mm, no commutation is required and the magnetic field can be designed such that a highly linear response is obtained.

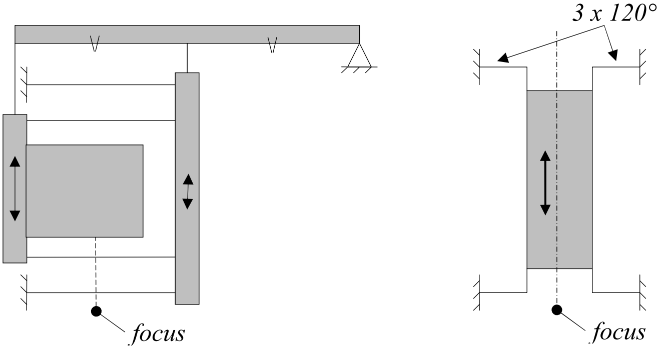

Figure 5.17: Elastic double parallelogram and folded plate spring linear guides

Two types of flexure guide concepts were investigated that can provide the required stroke and straightness of motion: the double parallelogram and the six folded plate spring design, as schematically shown in Figure 5.17. The double parallelogram design applied in (Van Seggelen, 2007) was calibrated by NMi to have nanometer level straightness. The folded leaf spring design is shown to be most suitable for highly dynamic loads in (Broers, 1999).

The circular symmetric design and the absence of a 1:2 lever make the folded plate spring design have the least components. Since each flexural element has to move over the entire stroke, material stress and axial stiffness are higher. The limited out of plane stiffness of the double parallelogram causes the first eigenmode to be lower compared to the folded leaf spring design. A flat Lorentz actuator is applied for the parallelogram and a cylindrical actuator (voice coil) is applied in the six folded leaf spring design. A lower stiffness and smaller actuator volume for the double parallelogram, and higher stiffness but also larger available actuator volume for the folded leaf spring design, coincidentally resulted in similar power dissipation for both designs. The six folded leaf spring design was chosen for its better dynamic behaviour.

Design

The designed guidance and actuator is shown in Figure 5.18. It consists of a top (1) and bottom (2) monolith that contain three folded plate springs, connected by a moving inner ring and a fixed outer ring. The two fixed outer rings are spaced by the magnet yoke (3), and the inner rings are connected by a tube (4). Six folded plate springs make the assembly overconstrained in the rotation about the centre line, but in this case this acceptable since the two monoliths are bonded on two a cylindrical fit on the magnet yoke. A cone (5) is connected to the tube that carries the coil carrier and coil (6) of the actuator. The objective and interferometer mirror (7) are bonded to the lower moving inner ring, and a cover (8) protects the plate springs. An adapter (9) is bonded to the top outer ring to connect the actuator to the probe main body via bushings and dowel pins, similar to Figure 5.14.

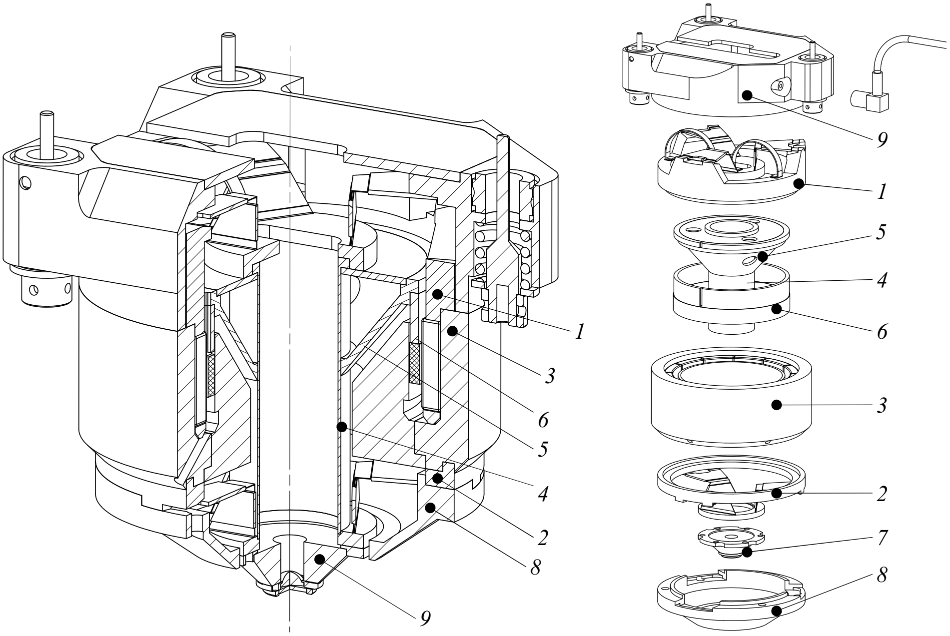

Figure 5.18:Objective guidance and actuator design

Elastic guidance properties

For flexure mechanisms the allowable strain ($\sigma_{0,2}/E$) should be maximized to achieve maximum stroke with minimal actuation force. For dynamically moving plate spring mechanisms in particular, the maximum stroke and eigenfrequency of the hinge elements is proportional to $\sigma_{0,2}/\sqrt{E\rho}$. For both cases, Ti 6Al 4V ($E = 114$ GPa, $\rho = 4430$ kg/m^3, $\sigma_{0,2} = 880$ MPa) is a most suitable material, as also shown in the material comparison in (Boneschanscher, 1995).

For an operating lifetime of 10 years, the estimated maximum amount of cycles is 10^8. To prevent failure from fatigue, the allowable stress σ_{max} should be kept below 500 MPa. The thinned parts of the plate spring are 0.09 mm thick and 2.7 mm long, which gives an axial stiffness c_{ax} of the system of 1.3 N/mm, and a radial stiffness of $c_{rad} = 3.6 \cdot 10^6$ N/m. The maximum occurring stress at 2.5 mm axial displacement is 320 MPa. The flexures are manufactured by wire EDM and are shown in Figure 5.19.

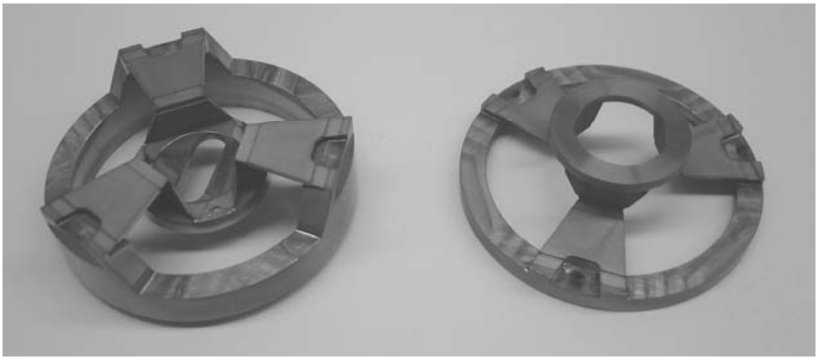

Figure 5.19: Monolithic flexure elements with three folded leaf springs

With the tube, cone, coil and interferometer mirror attached to this guidance, the total moving mass is 46 g. The axial eigenmode with the servo switched off is calculated to be 28 Hz, and the first disturbing resonance is torsion around the centre line at 1.4 kHz (Figure 5.20). This is caused by the relatively large inertia of the actuator coil. The second eigenmode is translation of the lower part at 1.7 kHz. The first resonance in the plate springs occurs at 2 kHz.

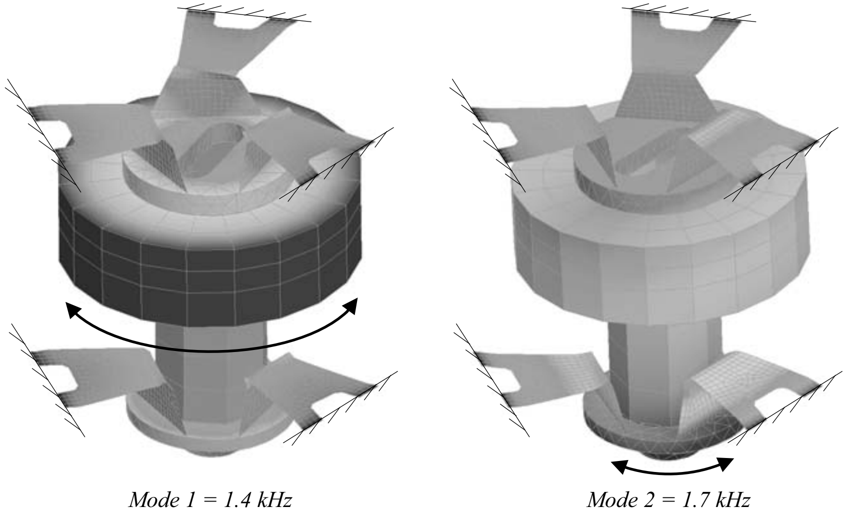

Mode 1 = 1.4 kHz

Mode 2 = 1.7 kHz

Figure 5.20: Eigenmodes of the objective guidance

Actuator

The actuator should provide a maximum motor constant within the available volume to minimize power dissipation. With the guidance stiffness of 1.3 N/mm, the maximum static force F_c is 3.25 N. The moving mass is 46 g, giving a gravity induced deflection when the probe is vertical of 0.35 mm. The probe zero point will be chosen in the equilibrium position. Reaching the upmost position thus requires 3.6 N. To minimize the power dissipation, the probe zero point may be made dependent on the orientation of the Ψ-axis.

The actuator force constant k_F is equal to (5.11), where I is the current, B is the flux density in the air gap, D is the diameter of the coil and n is the number of windings.

$$k_F = \frac{F}{I} = B \cdot l = B \cdot \pi D \cdot n \tag{5.11}$$

The actuator motor constant (k_m) is given by (5.12), with the coil volume V and the resistivity ρ_c of the winding material.

$$k_m = \sqrt{\frac{F^2}{P}} = \sqrt{\frac{B^2 V}{\rho_c}} \tag{5.12}$$

The magnetic circuit and coil dimensions were optimized using Ansoft Maxwell®. As shown in Figure 5.21, the obtained flux density B in the air gap is 0.8 T, using NeFeB magnets with a coercivity of $8.6 \cdot 10^5$ H (www5) and an Armco yoke with a saturation limit of 2.15 T (www4). The coil diameter is ∅ 44 mm with a cross section of 1.9 x 6.2 mm. The wire diameter is 0.45 mm and the number of windings is 50, giving an effective copper volume of 1100 mm^3 and a fill ratio of 68%. The resistivity of copper is $16.7 \cdot 10^{-9}$ Ωm. Substituting these actuator properties into (5.10) and (5.12) gives a theoretical force constant of 5.5 N/A and a motor constant of 6.5 N/√W.

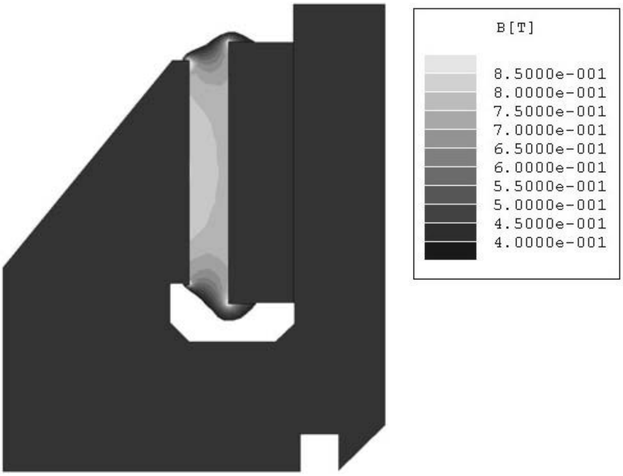

Figure 5.21: Probe actuator magnetic field

The required actuator force consists of the spring force F_c, the gravity force F_g and the acceleration force F_a. For sinusoidal motion with amplitude A_{PV}, and frequency f the total force as a function of time and ψ is given by:

$$\begin{aligned} F(t,\psi) &= F_c(t) + F_g(\psi) + F_a(t) = \\ &= c_{ax}\frac{A_{PV}}{2}\sin\left(2\pi f t\right) + m_p g\cos(\psi) - m_p\frac{A_{PV}}{2}4\pi^2 f^2\sin\left(2\pi f t\right) = \\ &= \left(c_{ax} - m_p 4\pi^2 f^2\right)\frac{A_{PV}}{2}\sin\left(2\pi f t\right) + m_p g\cos(\psi) \end{aligned} \tag{5.13}$$

$$F_{mean} = \frac{1}{2}\sqrt{3}\left(c_{ax} - m_p 4\pi^2 f^2\right)\frac{A_{PV}}{2} + m_p g\cos(\psi) \tag{5.14}$$

The coil resistance was measured to be 0.75 Ω and the motor force constant was measured to vary between 5 and 6 N/A, depending on the position. Figure 5.22 shows the required mean actuator force as a function of the frequency and amplitude as calculated with (5.14). This force is limited by the maximum amplifier current of 2 A, to show what the actuator is theoretically capable of. These frequency and amplitude combinations will, however, not occur in practice. The dip in the required force around the resonance can also be seen. The power dissipated in the coil windings is shown in the second figure. Generally, power dissipation will be less than 50 mW.

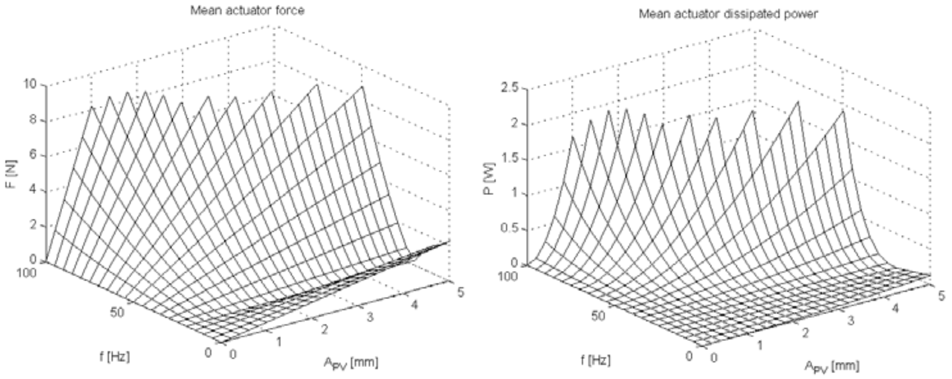

Figure 5.22: Actuator force and power dissipation

Figure 5.23 shows the power dissipation for a constant position, which is 125 mW for 2.5 mm away from equilibrium.

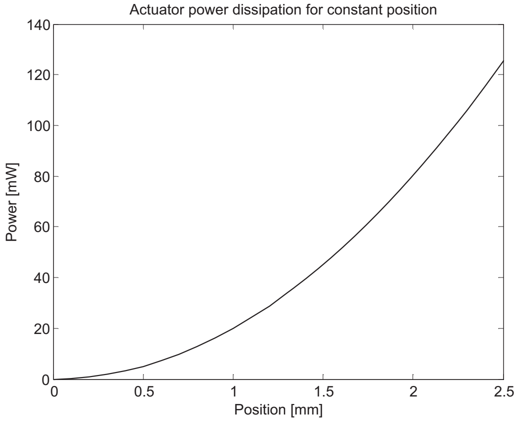

Figure 5.23: Power dissipation for constant position

The thermal conductivity from the coil to the rest of the actuator is minimal due to the adhesive layer, small surface area and ceramic coil carrier that separate it from the metal parts. Supposing the coil can thus only loose the dissipated power to the surrounding air, the temperature increase is given by:

$$q = h\,A_S\,\Delta T \tag{5.15}$$

When continuously retracted or extended to the maximum position, 125 mW is dissipated. The surface area A_s of the coil is $1.7 \cdot 10^{-3}$ m^2, and the transfer coefficient is assumed to be 5 W/m^2K. This gives a temperature increase of 14.7 K, so the coil can not be overheated this way. With the specific heat of copper of 390 J/kgK and the copper mass of mass of 9.8 g, this temperature is reached in about 7.5 minutes.
During normal operation, the dissipation will be much less. When moving with 1 mm PV amplitude and 5 Hz, the dissipation is 3 mW. During a 15 minute measurement this would give a worst case temperature increase of 0.7 K, when still neglecting the cooling effect of the movement and the conduction to the rest of the actuator.

Realization

Figure 5.24 shows the objective guidance components, and the completed assembly. A close up of the interferometer mirror and the focusing objective is also shown. A Teflon ring surrounds the objective to protect it from accidentally contacting a surface.

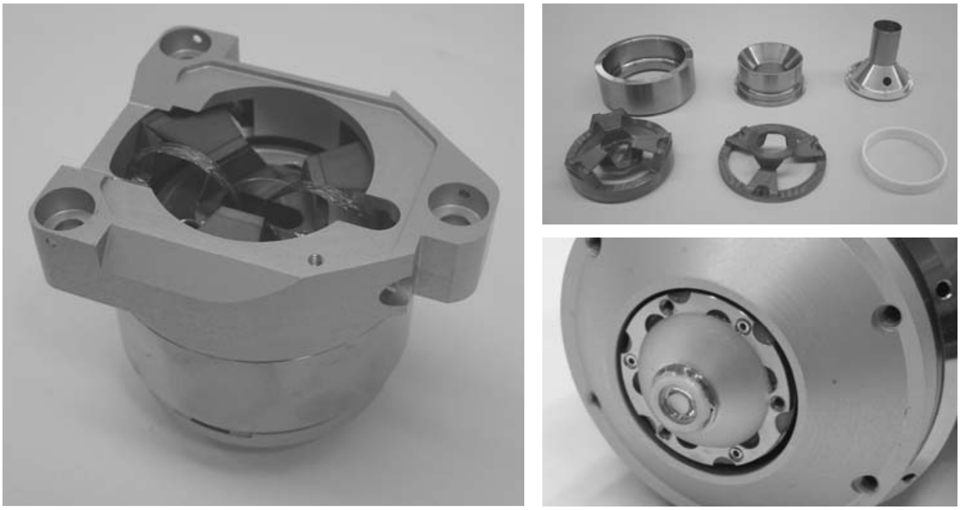

Figure 5.24: Objective guidance and actuator

Experiments

Figure 5.25 shows the force – displacement diagram of the actuator. The stiffness around the zero crossing is 0.71 N/mm, where 1.3 N/m was calculated. Due to the relatively large stroke, the stiffness is quite nonlinear. The asymmetry in the curve for positive and negative displacement is probably due to internal stresses in the flexures, giving negative stiffness to the assembly. Around the zero crossing, the hysteresis is approximately 18 µm. This may be caused by small friction in the braided litzes or by magnetic hysteresis.

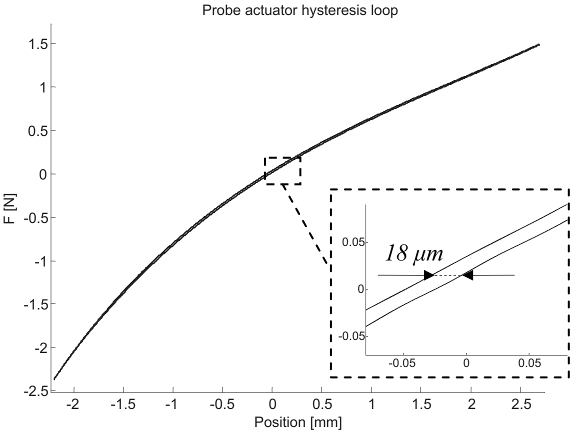

Figure 5.25: Probe actuator hysteresis loop

Figure 5.26 shows the plant frequency response from the probe actuator to the interferometer, where the power is in m/N. Since the motor constant and the guidance stiffness vary over the range, measurements were taken around force offsets of 1.1, 0, –1.1 and –2.2 N. A mass-spring model was fit to the measured frequency response with the highest process sensitivity (1.1 N), to design a robust actuator controller. After the axial resonance between 18 and 31 Hz, the actuator shows almost pure mass behaviour (-2 slope). A small unexpected anti-resonance resonance occurs around 290 Hz, which is probably the φ-rotation resonance of the Ψ-axis on its kinematic mount. The second and third resonance occur close together at 1670 and 1750 Hz. The FEM analysis showed 1400 and 1700 Hz, so especially the second resonance is higher.

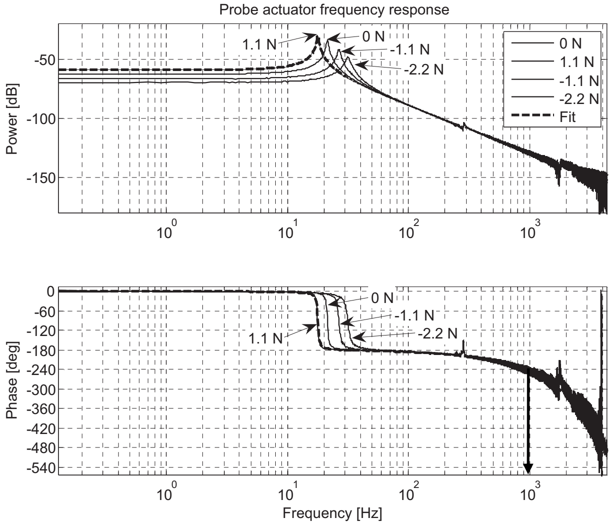

Figure 5.26: Probe actuator frequency response

After the rigid body resonance, the phase goes to -180° and than decreases further due to the delay in the electronics. The resonances hardly cause a phase lag, so the achievable bandwidth will mainly be determined by the delay. Assuming 30° phase margin, the achievable bandwidth can be 900 Hz with a standard PID controller. The implemented controller has a bandwidth of 100 Hz.

The tilt error motion of the guidance was measured by attaching a mirror to the front and measuring its tilt with an autocollimator (see Figure 5.27, left). As shown in Figure 5.27 (right), tilts up to 225 μrad occur in α and 70 μrad in β, which are substantially larger than expected (see section 2.3.1 for coordinate system definition). The repeatability of the tilt is 5 μrad, which is as expected for an elastic mechanism, and can thus well be compensated for. The relatively large tilt error may be due to the plate springs being misaligned in the monoliths, dirt between the fitting, internal stresses or the overconstraining with the 6th plate spring.

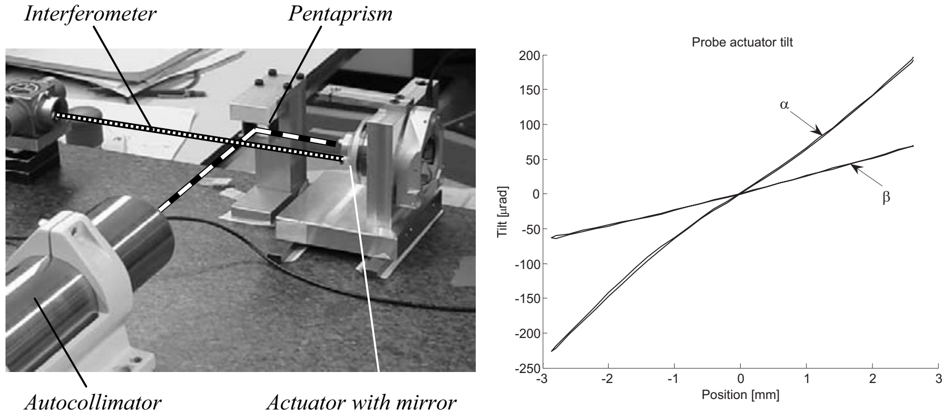

Figure 5.27: Probe actuator tilt measurement setup and results

5.4 Probe assembly

The probe is shown in Figure 5.28. The mass is 1 kg, and the outer dimensions are 65 x 90 x 125 mm. The connecting cables are the laser fibre, the actuator cable, a PSD signal cable and one cable for both photodiode signals.

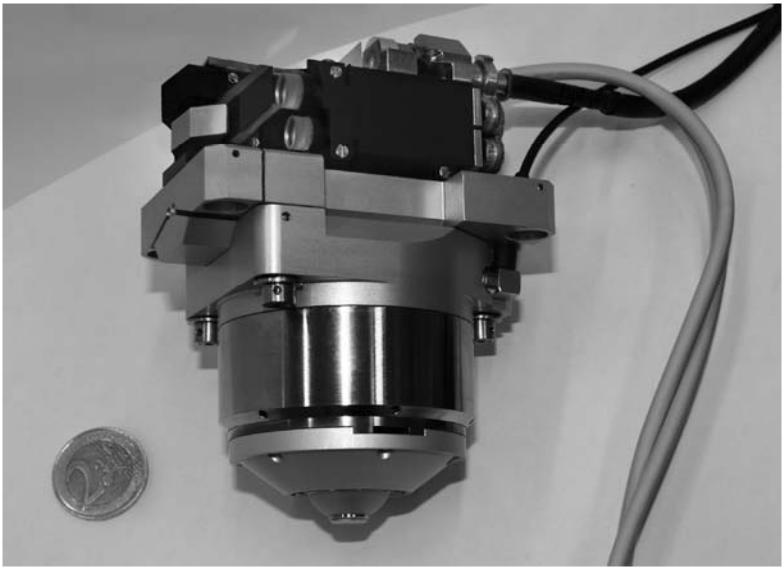

Figure 5.28: Probe assembly

The probe electronics consist of two signal processing boards. These process the low current signals coming from the photodiodes and the PSD, and must therefore be positioned close to the probe to minimize the capacity of the cable. The boards are mounted inside the Z-stage preload frame, as shown in Figure 5.29. From here, ±10 V coax cables feed the signals to the data acquisition system.

Figure 5.29: Probe electronics inside Z-stage preload frame

5.5 Experiments

This section describes the main test results of the differential confocal system and PSD, before installation into the machine. Tests that include the interferometer (stability tests and surface measurements) will be described in section 7.2, as a part of the complete machine testing. Tests of the actuator and guidance were already described in section 5.3.3. The sensitivity, range and linearity of the Focus Error Signal are shown first, followed by the repeatability, the noise level and the PSD signals.

These tests were performed on the probe just after completion, when alignment was optimal. After these tests, the probe collimator mount unfortunately had to be removed and realigned, along with some other components. The final probe configuration is slightly different compared to the stand-alone test results as shown in this section.

Focus Error Signal

The Focus Error Signal has been tested by locking the probe actuator, and scanning a mirror attached to a piezo through focus while measuring its displacement with a capacitive probe. Figure 5.30 shows the individual pinhole signals, the sum signal and the normalized Focus Error Signal. The intensity difference at maximum of the individual pinhole signals is mainly caused by uneven splitting of the beamsplitter plate. The FES sensitivity at the zero crossing is 6.1 V/µm. The 16 bits data acquisition electronics have 0.3 mV resolution, giving an electronic displacement resolution of 0.05 nm. The usable measurement range is chosen from -2.5 to 1.5 µm, giving a total range of 4 µm. The sensitivity variation in this range is substantial, but the repeatability remains sufficient to meet the uncertainty requirements. The FES controller must be robust enough to remain stable over the entire curve.

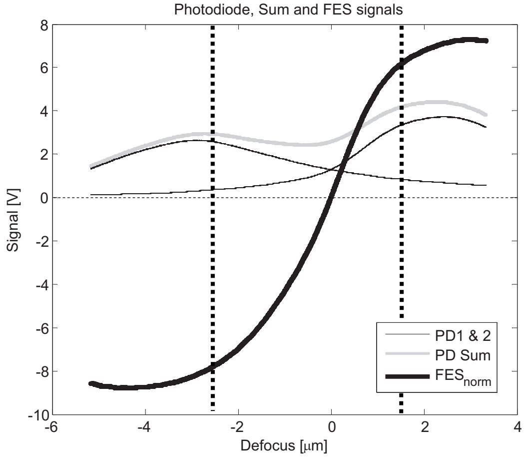

Figure 5.30: Probe differential confocal signals

FES noise level

To test the noise level, a mirror was rigidly attached to the guidance such that it is in focus of the differential confocal system. Data was recorded at 200 kHz, without and with an analog 10 kHz low-pass filter. Without the filter, the system bandwidth is 150 kHz and has an rms noise level of 0.31 nm. With the filter, the rms noise level is 0.17 nm.

FES repeatability

To test the repeatability of the FES signal, 55 FES curves were recorded by scanning the piezo through focus. A 13th order polynomial was then fit through the data, as if it were a calibration curve. Figure 5.31 (left) shows the deviation of the 55 FES curves from this fit. As can be seen, a ghost interference is still present in the system that causes an interferometric disturbance similar to the one described in section 5.2.3. The amplitude is much lower now, so the minimization of the parallel plane cavities in the optical design has paid off. It is expected that due to minor changes in the system, the interference will shift such that this remaining interference can not be calibrated and compensated for. The rms departure from the fit curve is 1.9 nm.

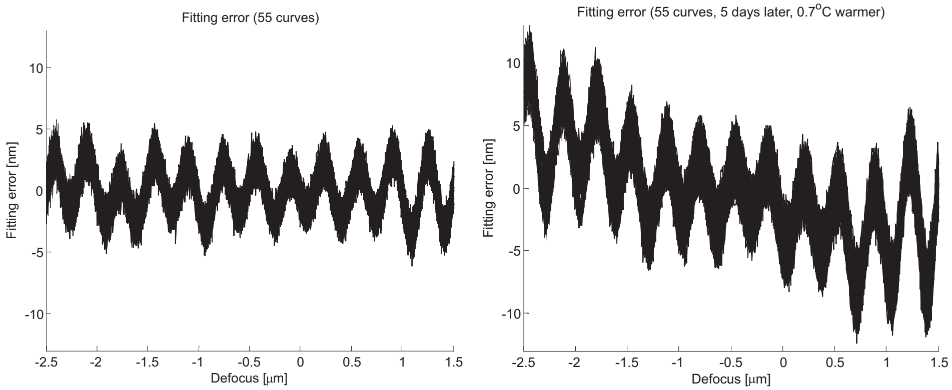

Figure 5.31: Departure from 13th order fit

Five days later, 55 FES curves were recorded again. The temperature was 0.7 K higher and the laser and electronics had been on for just one minute. Figure 5.31 (right) shows the difference of these curves with the polynomial fit of 5 days earlier. Again, a periodic disturbance can be seen, combined with a small sensitivity change. The difference with the polynomial fit is 4.1 nm rms. The periodic disturbance has shifted slightly, and can not be calibrated for. The repeatability of the Focus Error Signal is therefore equal to this 4.1 nm rms.

PSD signals

The PSD signals are shown in Figure 5.32. While scanning through focus, the X and Y signals should ideally be constant, but a ghost interference causes some fluctuation. The sensitivity is 1.24°/V in X and Y. In X direction the fluctuation over the full range is largest with 0.12 V, which is equivalent to 0.15°. In Y direction this is smaller with 0.04 V or 0.05°. Over the full axial range, the surface slope from 0° to 5° can thus be measured in 33 and 100 steps in X and Y direction, respectively. As will be shown later, the servo error is relatively small, such that only a small part of the range is used, typically in the order of 100 nm. The uncertainty in the slope measurement will therefore be lower. For now, a 6σ error of 0.15° is assumed for further estimations of the achievable correction uncertainty. This is equal to 0.025° rms.

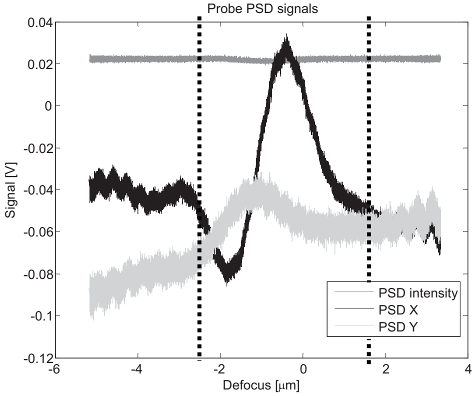

Figure 5.32: PSD signals

The actual inclination dependent error will be shown in (Cacace, 2009). Preliminary measurement results show a maximum best-focus shift of 550 nm at 5°. A tilt measurement error of 0.025° rms may therefore result in a distance measurement error in the order of 3 nm rms. Although somewhat speculative, this order of magnitude is well within the required uncertainty. It is therefore expected that the required total expanded uncertainty of 35 nm at 5° can be met.

5.6 Installation and alignment on machine

The Ψ-axis is aligned perpendicular to the measurement plane as explained in section 3.7. The probe must now be mounted into the Ψ-axis rotor such that the actuator motion direction is parallel to the measurement plane, and that the probe focal point coincides with the measurement plane. As explained in section 5.3.2 the alignment of the probe relative to the Ψ-axis is adjusted by lapping the four bushings that fit over the dowel pins.

The probe actuator is removed to align the probe parallel to the measurement plane. The actuator was aligned parallel to the differential confocal laser beam during the probe assembly. This beam is now pointed down onto a PSD that is fixed onto the spindle. The X and Y direction of the PSD are aligned to the measurement plane by moving the R-stage and adjusting the orientation of the spindle until the measured *y*-displacement is minimal. Next, the Z-stage is moved up and down and the orientation of the Ψ-axis is adjusted until pure *y*-translation remains. The φ-orientation of the probe can now be calculated, and the thickness of the shims can be adjusted. This procedure was iterated a few times until a φ-alignment of 46 μrad was obtained.

Next, the probe actuator was installed and the objective was focused onto the PSD. By moving the R-stage and rotating the spindle, the *y*-offset was determined. The probe was then shifted in y-direction until the circle measured by the PSD was minimal. The probe is now aligned. The alignment is fixed by inserting adhesive to lock the bushings in place, as described in section 5.3.2. Here, a y-offset of 7 µm was finally obtained, which is within the range of the fine-adjustment strut of the Ψ-axis mount (section 3.6.4). Further centring with a PSD resulted in sub-µm y-offset. Figure 5.33 shows the probe installed on the machine, reflected in a toric mirror.

Figure 5.33: Probe installed on machine

5.7 Motion control [1]

First, the controller scheme will be explained. Next, the surface lock procedure will be shown. This section closes with the measured FES frequency response and a typical servo error example.

Controller scheme

The probe motion controller consists of a plant P and three separate controllers C as shown in Figure 5.34. The plant P is the complete probe, which has one input and two outputs: the actuator force (F), the interferometer (IF) and the Focus Error Signal (FES), respectively. The first controller is a feedforward force controller (C_F), the

---

[1] *The motion control design and experiments are the work of G.F.IJ. Kramer of TNO.*

second is a feedback controller on the interferometer (C_{IF}), and the third is a feedback controller using the Focus Error Signal (C_{FES}). The machine control software operates a switch between the controllers. The input of the system is either a force *F* when in force control, a position setpoint *S* that is translated to a third order profile by a trajectory generator (TG) when in interferometer control, or the Focus Error Signal when in FES control.

The probe actuator is a mass-spring system, with a non-linear force-displacement characteristic as shown in Figure 5.25. The interferometer output is proportional to the objective position. The FES output is proportional to the position of the surface relative to best-focus, but is independent of the position of the guidance. By applying the force linearizing gain (FL), the system is converted to a pure mass system, such that both controllers only have to act on outside disturbances and the residual spring force. This FL gain is a static polynomial that is fit to Figure 5.25. This feedback system is unstable, and is stabilized by either the interferometer or FES controller. To smoothly switch between interferometer and FES control, a sample & hold (SH) block is activated and the controller states are reset when switching. The SH value is equal to the fitting error in the FL gain and the dynamic force of that moment.

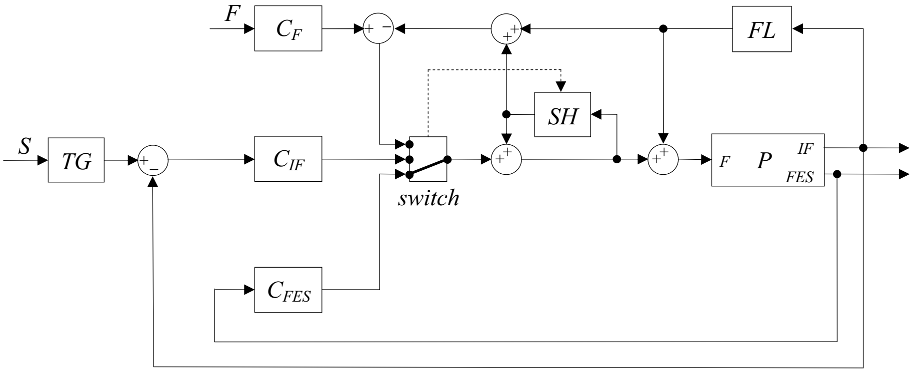

Figure 5.34: Probe control scheme

When the interferometer is not homed and no surface is in focus, the probe is actuated by an open loop current controller. This is a unit gain controller that has been extended with a second order profile generator to smooth the force profile between setpoint changes. The force linearizing and sample-and-hold signal are already present in the loop, and therefore subtracted from the output of C_F.

Nulling the probe

At startup, the probe is nulled onto the nulling target. A force of 3 N is hereto applied by the force controller first, to pull the probe against its rubber end-stops. The approximate position of the guidance is now known, and the interferometer is reset with this position. The probe force is set back to 0 N, releasing the probe to its equilibrium position. Next, the controller is switched to interferometer control and a setpoint of +2.5 mm is given. This retracts the probe almost to the end-stops. To lock the probe onto the nulling target, a setpoint of –2.5 mm is given, which extends the probe to the opposite extreme position. While extending, the FES_{norm} and PD_{Sum} signals are monitored and the interferometer control is switched to FES control when the target is in focus. Detecting this focus will be explained in the next paragraph. With the probe focused onto the nulling target, the interferometer is reset again, but this time with the exact calibrated distance between the Ψ-axis centre and the nulling target.

Locking on to a surface

Figure 5.35 (left) shows the FES_{norm} and PD_{Sum} signals as measured on a Zerodur optical flat from -0.5 mm to +0.5 mm around best-focus. The right figure is zoomed around focus between -20 to +20 μm. The FES_{norm} signal nominally does not change with the surface reflectivity due to the normalization, but the PD_{Sum} signal does. The thresholds are therefore surface specific.

When approaching focus (from right to left in the figures), five regions can be distinguished: *blind*, *far*, *ok*, *near* and again *blind*. In the *blind* region, the PD_{Sum} signal is close to zero and the FES_{norm} signal is unreliable. Here it can not be determined in which direction best-focus is.

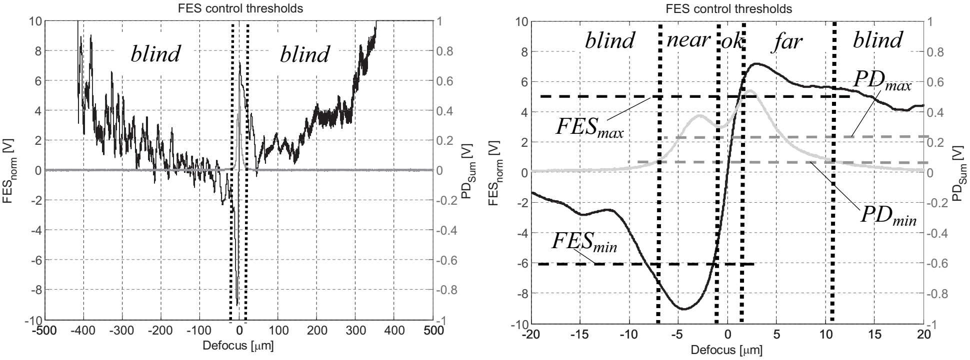

Figure 5.35: FES control thresholds measured on Zerodur

When further approaching focus, the PD_{Sum} signal increases, just as the FES_{norm} signal. When $PD_{Sum} > PD_{min}$ and $FES_{norm} > FES_{max}$, it can be unambiguously determined that the objective is too *far* from the surface. Next, the FES_{norm} signal decreases onto the near-linear measurement range. When $PD_{Sum} > PD_{min}$ and $FES_{min} < FES_{norm} < FES_{max}$, the surface is in the *ok* measurement range of the differential confocal system. Continuing, the FES_{norm} signal crosses FES_{min}, where it can be unambiguously determined that one too close to the surface (*near*). PD_{Sum} finally becomes smaller than PD_{min}, where it can no longer be determined in which direction best-focus is.

When locking on to the surface, the actuator is extended until the *ok* region is detected. Then, the probe is locked on to the surface by switching the interferometer control to FES control. When the *far* or *near* region is entered from the *ok* region, the controller applies maximum force to get back to best-focus. If the *blind* region is entered, the probe is immediately retracted to the +2.5 mm position by the interferometer controller to avoid contacting the surface.

FES frequency response

The frequency response of the interferometer and FES loop are different, and thus require a different controller design. To determine the FES frequency response, the probe was focussed onto a surface with the interferometer control loop. Noise was then inserted into this loop, and the FES output was recorded. The interferometer controller was calculated out from the loop to obtain the FES plant frequency response. Ideally, a weak interferometer controller is used to minimize the influence on the response, but the FES range is so small that this was not possible. The low frequency results, especially around the resonance, are therefore not reliable. The measurement of Figure 5.36 were taken with the actuator at +1 mm. Similar to the frequency response of the actuator and interferometer (Figure 5.26), the response is position dependent. Above the resonance, where the data is reliable, the behaviour is pure mass-like and thus no longer position dependent. The first parasitic resonance for the FES control loop is around 1700 Hz. The anti-resonance around 290 Hz that was present in the interferometer loop does not occur in the FES loop, confirming that this is the φ-rotation resonance of the Ψ-axis on its kinematic mount.

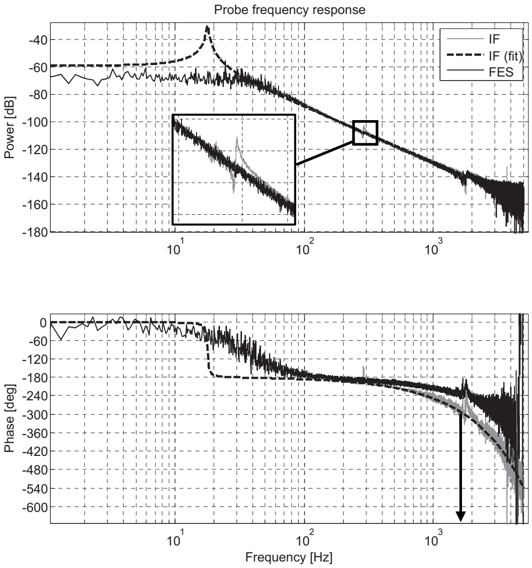

Figure 5.36: Probe interferometer and FES plant frequency response

The bandwidth of the FES electronics is higher and the delay is less compared to the interferometer loop. The phase decreases less rapidly. With a phase margin of 30°, the bandwidth for this loop may be up to 1600 Hz, provided that a differential compensator can be applied at this frequency without causing instabilities due to noise amplification.

Typical servo error

For the current FES controller, robustness is preferred above bandwidth. The controller is currently tuned for 250 Hz bandwidth. Figure 5.37 (left) shows a typical servo error at standstill. A 50 Hz disturbance is present in the actuator signal, which translates into about 16 nm PV servo error. This motion is also measured by the interferometer and therefore does not translate to measurement error.
Figure 5.37 (right) shows the typical servo error for a 1.6 mm tilted surface at 1 rev/s. A periodic servo error with about 275 nm PV can be seen, with sharp spikes superimposed. The encircled spikes have a duration of a few samples and are caused by dust or scratches. These can clearly be recognized and are filtered from the data. Two other spikes per revolution can also be seen (indicated by the arrows), that are probably caused by the hysteresis in the actuator.

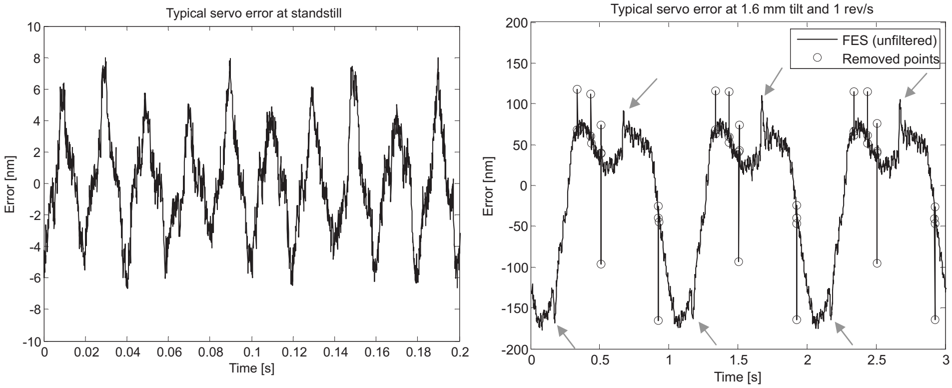

Figure 5.37: Typical servo errors at standstill and with 1.6 mm tilt at 1 rev/s

The measurement uncertainty decreases with a smaller servo error. In future work, the probe controller bandwidth can hereto be increased. Since the response to dust and scratches will then also become stronger, one may have to make the emergency switching of the controller more robust. Since measuring circular tracks gives highly repeatable servo errors, learning control may further be applied per measured track, especially for heavily freeform surfaces.

5.8 Conclusion

An optical probe has been designed, realized and tested. It consists of a compact integration of the differential confocal method and a dual pass interferometer. The differential confocal method has been modelled, tested and optimized. The range of the system realized is 4 µm and the noise level is 0.17 nm rms. The repeatability over the full range is 4.1 nm rms. A PSD is added for compensation of the inclination dependent error. Preliminary measurement results show a tilt dependency of about 550 nm at 5°, which may be compensated to nanometer level uncertainty.

A flexure guidance with voice coil actuator straightguides the focusing objective and interferometer mirror, increasing the range to 5 mm. In interferometer and FES control, a bandwidth of respectively 900 and 1600 Hz is possible. A switching controller has been designed that is capable of automated searching and locking on to a surface under test.

In Chapter 7 the performance of the probe will be shown when measuring a surface. Based on these experiments and the results shown in this chapter, it is expected that the probe will meet its requirements after further calibration. Further design details and calibration of the inclination dependent error can be found in (Cacace, 2009).

Chapter 6

Electronics and software[1]

The electronics and software are designed to safely operate the 5 axes of the machine and to acquire the signals of all measurement channels. The electronics cabinet contains a dSPACE real-time processor with many in and outputs, control units for all 5 axes, a safety control unit, a probe laser unit and an interferometry interface. The software consists of three main elements: the trajectory planning, the machine control and the data processing. Emphasis has been on the machine control, in order to safely operate the machine manually. Several pre-programmed functions have been implemented to facilitate this. A basic measurement script can further be programmed off-line to perform an automated measurement. The data processing software converts the raw data to a surface point cloud to determine repeatability and flatness of the tilted flat measurements as shown in Chapter 7.

6.1 Electronics

The electronics cabinet is shown in Figure 6.1. It consists of seven sub-systems: the dSPACE real-time data-acquisition and processing system with various in- and output connector panels, the R, Z, θ amplifier unit, the Ψ-axis and probe actuator amplifier unit, the interferometer interface, the probe laser unit and the safety control unit. The pressure-temperature-humidity (PTH) sensor electronics and PC are also shown.

---

[1] *This chapter gives a summary of the custom electronics as largely developed by M.H.C. Janssen of TU/e GTD and software as developed by G.F.IJ. Kramer of TNO.*

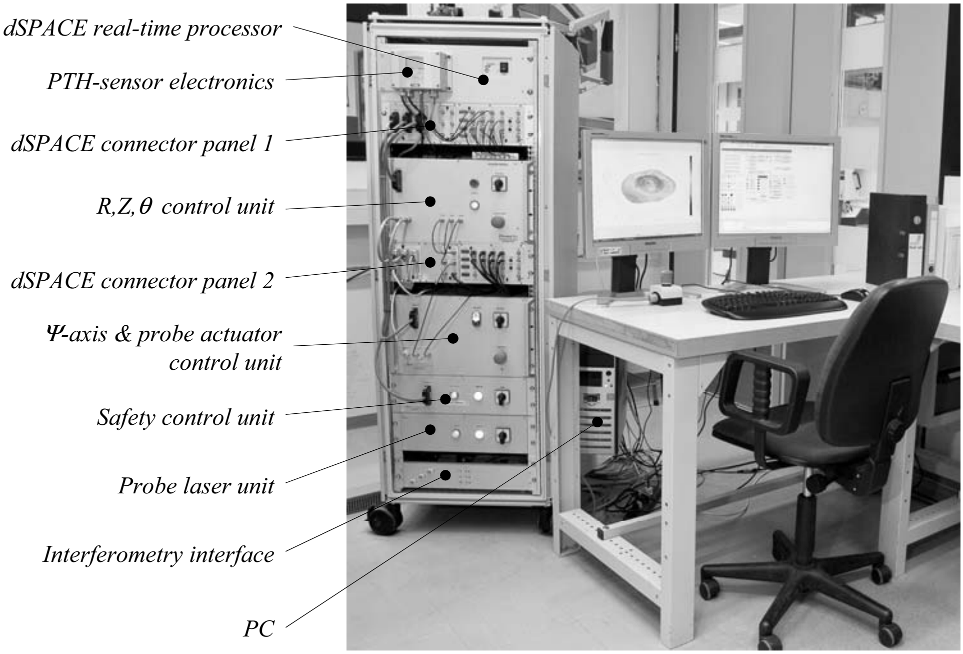

Figure 6.1: Electronics overview

dSPACE real-time processor and connector panels

A dSPACE real-time processing system was selected for the main control system platform, mainly for its flexibility and high allowable number of in- and outputs. Control software is written in Matlab Simulink, converted to c-code and uploaded to the stand-alone real-time processor. A graphical user interface can be made in ControlDesk.

The dSPACE system has 2 x 16 high-speed parallel ADC inputs, 2 x 6 DAC outputs, 6 analog encoder inputs and 2 x 96 digital I/O channels. All channels operate via a sample-and-hold trigger to ensure synchronization of the data. The achievable sample rate depends on the amount of software running on the real-time-processor. After some optimization, a sample rate of 10 kHz was achieved.

R, Z, θ control unit[1]

This unit contains the electronics required to operate the R and Z-stages and the spindle. It hereto has three ELMO 3-phase PWM amplifiers, a 24 V and 80 V power supply and two Heidenhain encoder splitters. This unit also operates the brake solenoid valves and monitors the status of the limit switches. The amplifiers operate

---

[1] *The R, Z, θ-control unit has been designed and built by Eltromat BV.*

in linear amplification mode and receive their setpoint as a ±10 V signal from the dSPACE DAC output. The R and Z-amplifiers use a split-off linear scale signal for the commutation. The spindle has Hall sensors and a separate lower resolution Renishaw encoder for the commutation interpolation; the high-resolution Heidenhain encoder is fed directly into the dSPACE system. The logic of this unit operates on the 24 V power supply and is active when the power is on. The 80 V power supply that drives the motors is activated separately by a button on the front, and is immediately disabled in case of an emergency.

Ψ-axis and probe control unit

The Ψ-axis electronics are similar to the R and Z-stages, with an ELMO 3-phase PWM amplifier, a Heidenhain splitter, a 42 V and 24 V power supply, brake signal and limit switch input. The probe amplifier is a custom analog linear amplifier[1] with a bandwidth of 50 kHz, operating on two power supplies for + and – 28 V and a (variable) maximum output of 2 A. A custom amplifier was designed here to achieve high bandwidth and to achieve better response around the zero current output, compared to PWM amplifiers. The probe amplifier setpoint and Ψ-axis brake output are relayed through the Safety control unit as will be explained later. Similarly to the R, Z, θ-unit, the 42 V power stage is turned off when an emergency occurs. The probe amplifier is not disabled, since the actuator must stay retracted in this case.

Safety Control unit

The control software on the dSPACE processor monitors the safety status of the machine, and performs a controlled emergency action if necessary. This mainly concerns retracting the probe if the FES signal is lost, or braking the stages in case of a large servo error or an activated inner limit switch. This software may, however, stop responding, causing the motor setpoint and brake outputs to become undefined. This may in turn cause stage runaway and in worst case a severe machine crash.

A PLC in the Safety Control Unit therefore monitors the vital functions of the machine. It monitors a TTL heartbeat signal from the dSPACE software, checks for the presence of air pressure and acts on the emergency button. If one of these shows an error, the power supplies to the R and Z-stage, spindle and Ψ-axis amplifiers are disabled, and the R-stage and Ψ-axis brakes are enabled. The power to the probe amplifier is not disabled, but its setpoint is now switched to the PLC, which generates an emergency retract trajectory. Simultaneously, the Z-stage is lifted by increasing the pressure to the weight compensation, as described in section 3.4.5. It is locked mechanically in the top position. The spindle brake is not enabled since it is not designed to brake the rotor at full speed. Since there is about 10 minutes of air supply left in the pressure vessel, the spindle is let to slow down by itself.

---

[1] *Designed by M.H.C. Janssen of TU/e GTD.*

All this is activated by disabling the power to solenoid valves. If electrical power fails, the same action is thus evoked, apart from retracting the probe and keeping the spindle brake open.

Probe laser unit

The probe laser is a variable power diode laser that is coupled to the probe collimator via a fibre. The probe laser unit holds the laser source, laser driver, Peltier cooler driver and power supply. The laser power setpoint is coming from a dSPACE DAC output, and the laser status is reported back via a voltage level to an ADC input. A red light on the front indicates whether the laser is on.

Interferometry interface

The Agilent N1231B interferometer counter board is installed in a PCI slot of the PC. This slot serves as a power supply and for settings modifications. The measurement signals are outputted via three parallel 40 bit digital signals. Of these 40 bits, 32 are the actual counter and the remainder are used for status, resetting and triggering. The Interferometry interface unit splits these 3 x 40 channels into the three 32 bit counters that are fed into three 32 bit digital I/O inputs of the dSPACE system, and combines the remaining status, reset and trigger bits of the three axis to feed them into a fourth digital I/O channel.

6.2 Software

Three main software parts can be distinguished (Figure 6.2). The first part is the trajectory planning, where the surface design data (XYZ, polynomials, Zernike etc.) is combined with the user specified measurement parameters such as track spacing, speed, and number of revolutions to average, to derive the machine setpoints. The machine control part (2) first executes a machine startup routine to home the axes and null the interferometers. The motion control software is then ready to execute the off-line created setpoint list, during which it continuously monitors machine safety. While performing the measurement, the raw data is outputted and recorded on a harddisk. The data processing software (3) converts the raw data to surface coordinates and applies refractive index correction, averaging of revolutions and calibration compensation. Next, the obtained surface form is compared to the design and the measurement results are generated.

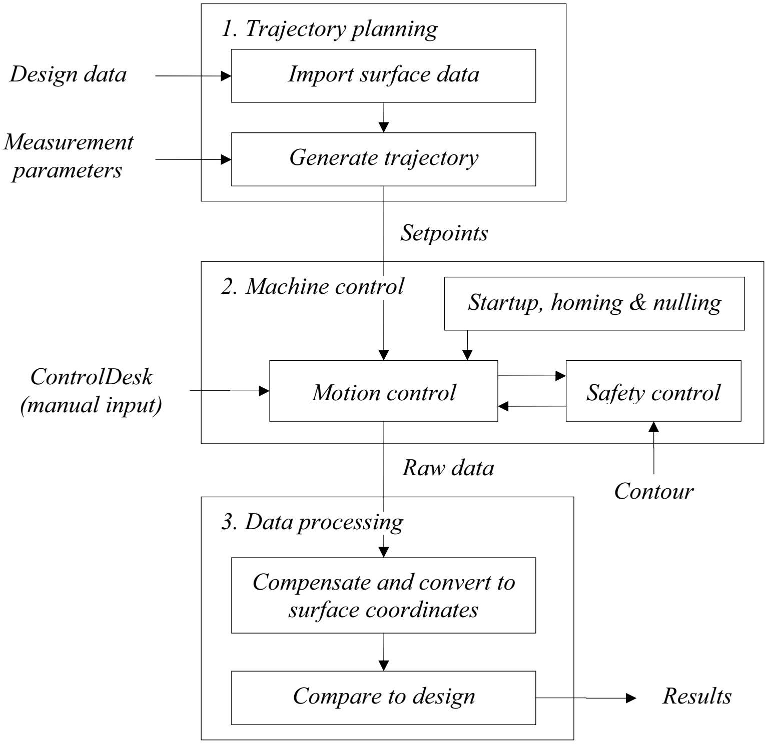

Figure 6.2: Software outline design

The main scope of this project is to demonstrate the repeatability of the machine, which will be done by measuring a tilted flat. Emphasis has therefore been on the development of the machine control software part, such that the machine can be safely operated. The conversion to surface coordinates is also performed, but no calibration data has yet been taken into account. Since only a tilted flat will be measured, no extensive surface fitting algorithm has been developed yet. Especially for the ‘import surface data’ and ‘compare to design’ parts, commercial software may be available (www12, 23, 25).

The current functionality of the three software parts will be explained in more detail in the next paragraphs. An extensive description of the software conceptual design can be found in (Henselmans et al., 2008).

Trajectory planning

This software part will import the surface design data and generate the machine setpoints for an automated measurement, based on user specified measurement parameters. The design data can for example be in polynomial, aspherical constants, Zernike, XYZ or CAD format. The user parameters can be measurement type (e.g. circular scan, radial scans, spiral scan or high-resolution scan), and the desired speed, point spacing etc. Although this part of the software determines the usability of the machine to a large extend, it is not in the scope of this project. It will either be gradually developed when the machine is in use, or it will be adapted from a commercially available software package.

As will be described in the next paragraph, the machine can be controlled manually from a graphical ControlDesk user interface, from which setpoints can be given and some pre-programmed sequences can be executed by pushing a button or entering a setpoint. To perform an automated measurement, a program can be composed in Matlab, based on a set of functions that execute these same commands. The machine control executes these commands as a function of time, while the data acquisition system samples the data.

Machine control

The machine control software part continuously runs on the real-time processor, waiting for and executing external commands. The control loops are written in Matlab Simulink®, and the safety control part is written using Matlab Stateflow®. It holds its position, either locked or in closed loop control, until a new command is given.

Commands can come from the ControlDesk user interface (Figure 6.3) or from an off-line programmed measurement script. Given the real position and desired position it generates a third order profile for each axis for each new setpoint. A contour of the surface under test must be provided by the user, relative to which the motion profile is checked to avoid collisions[1]. Next the five motion controllers execute each profile for each axis, while monitoring the speed, the servo error and the limit switches.

Some often used sequences can be initiated by pushing a button. This includes an automated *homing* sequence that must be performed after machine startup. Since the stage positions are unknown at startup, each axis is moved to find the reference markers on the encoders and linear scales in a safe way. Another sequence is *machine parking*, in which the machine goes to the upper right position, the Ψ-axis goes to the 120° position and all axes are locked. A *probe homing* button re-zeros the probe interferometer with the probe focused on the nulling target. When a surface is in range of the probe, a *toggle surface lock* button extends the probe and switches to FES control when the surface is in focus.

---

[1] *The traject generator and checker are developed by IME Technologies.*

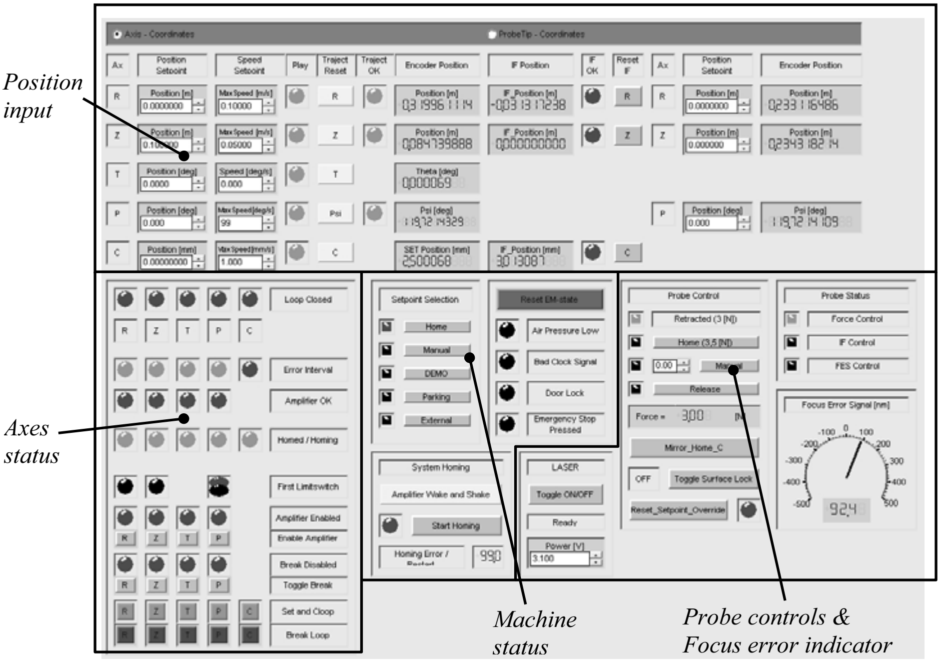

R: Position [m] 0.0000000; MaxSpeed [m/s] 0.10000; Position [m] 0,31996 1114; IF_Position [m] -0,03 13 17238; Position [m] 0.0000000; Position [m] 0,233 1 16486

Z: Position [m] 0.100000; MaxSpeed [m/s] 0.05000; Position [m] 0,084739888; IF_Position [m] 0,000000000; Position [m] 0.000000; Position [m] 0,2343 182 14

T: Position [deg] 0.0000; Speed [deg/s] 0.000; Theta [deg] 0,000069

P: Position [deg] 0.000; MaxSpeed[deg/s] 99; Psi [deg] 1 19,72 14329; Position [deg] 0.000; Psi [deg] 1 19,72 14 109

C: Position [mm] 0.00000000; MaxSpeed[mm/s] 1.000; SET Position [mm] 2500068; IF_Position [mm] 30 13087

Homing Error / Restart 99,0

Power [V] 3.100

0.00

Force = 3,00 [N]

92,4

Figure 6.3: Machine control user interface

Besides checking each trajectory, the machine control software also continuously monitors other safety indicators. It acts on the inner limit switches, air pressure failure, servo error and overspeed, by breaking the control loop of an axis and enabling the brakes. When the probe looses focus, it is immediately retracted to avoid collisions. Only when the software stops responding, similar actions are performed by the safety control unit electronics.

Surfaces with non-circular circumferences can be measured in two ways. Indexing the spindle is easiest to implement, but also the slowest. In this method the probe is focused onto the surface, while the spindle is moving back and forth. A square surface for instance requires this for each corner. Two diagonal scans can be performed first to eliminate the drift during this procedure, as will be shown in section 7.2.3.

A faster method is to rotate the spindle continuously, and intermittently operating the probe in FES and interferometer control. When the probe reaches the edge of the surface, the position of the objective is controlled by the interferometer, which positions it to where the surface of the next edge will be. This requires a priori micrometer accuracy knowledge of the surface to be feedforwarded to the probe, for instance obtained by performing a coarse measurement with the first method. The risk of damaging the probe this way is evident; much attention must thus be paid to safety here.

Data processing

During a measurement, the machine outputs the raw data of all measurement channels. This data is stored as a time trace on the harddisk of the pc and is processed off-line, after the measurement is completed. The data processing flow scheme is shown in Figure 6.4. The input signals used to compute the surface coordinate point cloud are the 8 capacitive probes, the spindle and Ψ-axis encoders, the R, Z and probe interferometers, the air pressure, temperature and humidity, and the Focus Error Signal and PSD signals of the probe.

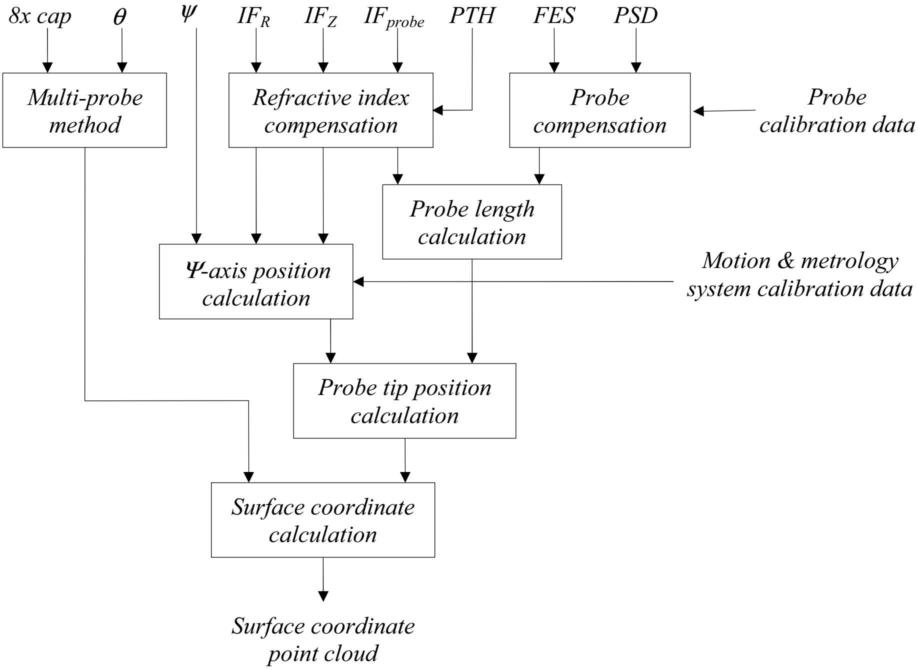

Figure 6.4: Data processing flow scheme

With the 8 capacitive probe signals and θ encoder, the product position relative to the metrology frame is calculated. As shown in section 4.4.2, this will eventually be done by applying the multi-probe method, but this method has not been implemented yet. The reference edge profile is for now determined by averaging the capacitive probe signals of several revolutions. The synchronous spindle error motion is ignored this way, but this error is currently much smaller than other remaining error sources, and does not influence the repeatability measurements. The asynchronous error motion is determined by subtracting the averaged edge profile from the capacitive probe signals. The interferometer signals are compensated for the refractive index with the pressure, temperature and humidity signals. The R and Z-interferometer and the Ψ-axis encoder give the Ψ-axis rotor position. Motion and metrology system calibration data, such as stage tilt and mirror flatness is not yet taken into account, again because this does not influence the repeatability.

The probe FES signal is not yet compensated for the inclination dependency, also because this does not influence the repeatability. The FES signal is combined with the probe interferometer to obtain the probe length. This probe length added to the Ψ-axis position and orientation results in the ‘point of contact’ between the probe and the surface, relative to the metrology frame. This point of contact is then corrected for the product position to obtain the true surface coordinate point cloud.

The data acquisition system is sample based. The signals are therefore interpolated to equidistant θ, to eliminate the effect of spindle speed variations. The obtained equidistant circumferential signals are also interpolated in radial direction to compensate for probe position variations during the measurement of the tracks. The resulting data is in a fixed grid, which can be averaged or compared to measurements or fits that have the same datagrid.

To calculate the repeatability of the machine, several surface measurements are averaged, and each individual measurement is compared with this average to compute the rms difference. To calculate the flatness of the surface, a basic fitting algorithm generates an ideal flat for the same datagrid. This fit is subtracted from the data to obtain the surface flatness as measured by the machine.

Chapter 7

Machine validation

The machine assembly consists of the motion system, metrology system, non-contact probe, electronics and software, as described and tested in the preceding chapters. The machine performance is tested by stability, single track and full surface measurements, focussing on repeatability. Calibration techniques have been taken along in the design to assure traceability. Based on the measurements, the achievable uncertainty after calibration is estimated.

7.1 Machine assembly

In the previous chapters the concept, design, analysis, realization and testing of the elements of the machine have been explained. The machine prototype is shown in Figure 7.1. The dimensions of the machine are 2.1 x 1.8 x 1.8 m, and the mass is approximately 3500 kg. The motion system has a parallel bearing setup with the Z-stage aligned directly to a vertical base plane. Separate position and preload frames have been applied throughout, and the motors, brakes and weight compensation are aligned with the centre of gravity of the stages. The metrology system consists of an interferometry system that directly measures the displacement of the Ψ-axis rotor relative to a Silicon Carbide metrology frame. Capacitive probes measure the error motion of the spindle. The optical probe consists of a compact integration of a differential confocal system with inclination dependency compensation and an interferometer for increasing the measurement range. The machine control allows for execution of measurement scripts, and measurement results are generated by data processing software. Intermediate test results have been shown in the previous chapters. In the coming sections, the overall machine performance will be demonstrated.

Figure 7.1: Non-contact freeform optics measurement machine prototype

7.2 Machine validation

Several experiments have been conducted to test the machine performance. This section describes the stability, the repeatability of a single track and full surface measurement of a tilted flat.

In the following test results, no calibration data has been taken into account yet. The multi-probe method has also not been applied yet for the spindle error motion measurement. One error source that has been compensated for is the data delay on several measurement signals. With the capacitive probe experiment as described in section 4.6, all bodies in the metrology loop may be assumed rigid, or connected with high stiffness. Applying an impulse to one of these bodies should thus give an in phase response on all measurement channels. This way, it was determined that the interferometers and spindle encoder require a delay of 80 µs and 180 µs, respectively. These delays are taken into account in the off-line data processing software.

7.2.1 Stability measurements

In section 4.6, stability measurements were described before the optical probe was installed on the machine. By using an Invar dummy probe with 3 orthogonal faces and 3 capacitive probes, the stability over 15 minutes in the *r*, *y* and *z*-direction was determined to be 8.2 nm rms in *r* and *y*, and 2.3 nm rms in *z*-direction. The error over 0.1 s was 0.6 nm rms. The drift in *r* and *z*-direction was negligible.

Similar experiments have been performed with the completed machine. A ∅100 mm Zerodur optical flat has been mounted on the spindle (see Figure 7.2, left). The optical probe is focussed onto this surface, with the Z-stage positioned such that the probe actuator is at its equilibrium position. The tangential stability can not be measured this way, but this is now of lesser importance since this is a less-critical direction (see section 2.3.2).

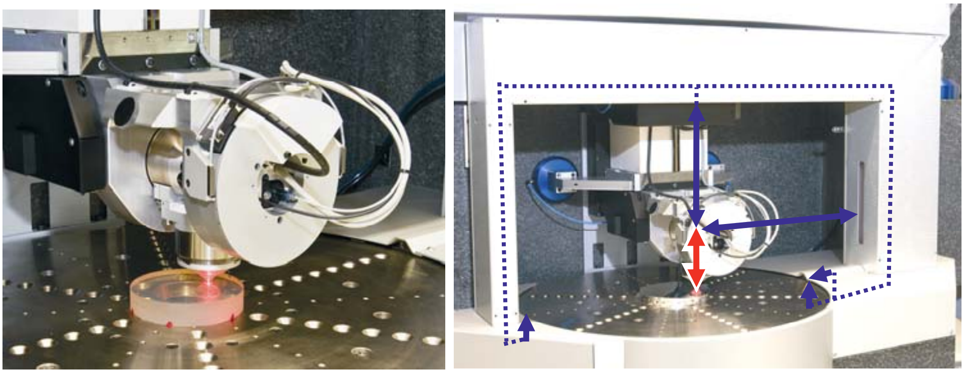

Figure 7.2: Probe focused on Zerodur flat and metrology loop

The metrology loop consists of three sections (Figure 7.2, right): the metrology system, the optical probe and the product. The metrology system in turn is built from the interferometry system, the metrology frame, the capacitive probes and the mounting table. Assuming that the product position on the table is stable, the sum of the metrology loop and the optical probe should be constant. These experiments have been performed for 0.1 s to determine the noise level, for 15 minutes to see the typical drift during a measurement, and for 12 hours to see the typical day to day variation.

Figure 7.3 (left) shows the displacement measured by the metrology system and the probe over a period of 0.1 s, sampled at 10 kHz. An offset of 5 nm has been added for clarity. With all stages locked (including the spindle), a PV motion in *z*-direction of 15 nm can be seen. The difference between the displacement measured by the metrology system and the probe is also shown, and is 0.88 nm rms.

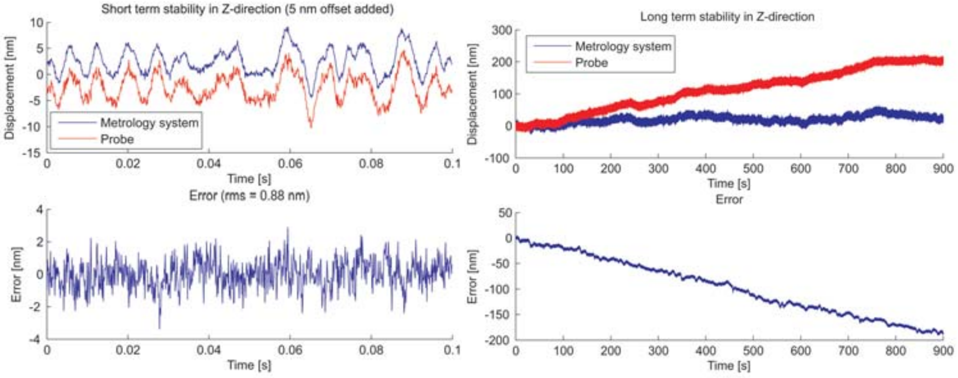

Figure 7.3: Stability in z-direction for 0.1 second and 15 minutes

Figure 7.3 (right) shows the same measurement over a period of 15 minutes, sampled at 1 kHz. A more or less linear drift can be seen of almost 200 nm/15 min. In the experiments with the reference capacitive probes (section 4.6), hardly any drift was observed. The cause is thus either the optical probe or different thermal conditions between the two experiments. The temperature was recorded during both experiments, but these showed no large temperature fluctuations. The temperature history, however, is more important than the temperature during the actual measurement, due to the large time constant of the machine. As will be shown in section 7.2.3, much of the drift can be compensated for in the measurement procedure.

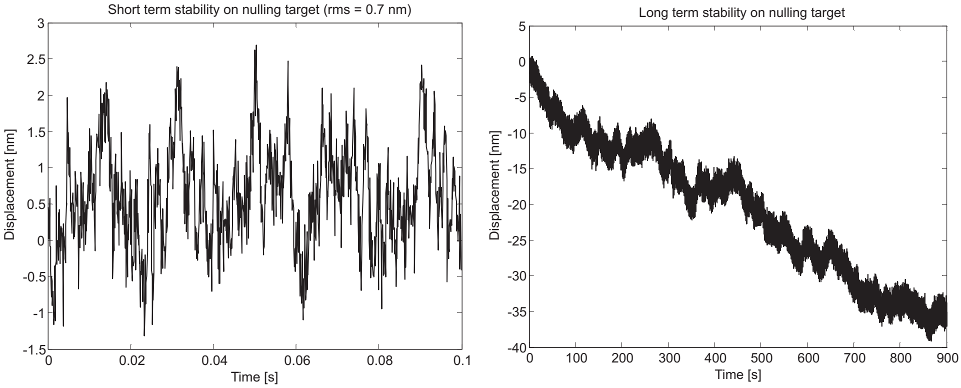

Figure 7.4: Stability with probe focused on nulling target

Two experiments have been conducted to find the source of the drift. First, the probe was focussed onto the nulling target to shorten the metrology loop. This now consists of only the Ψ-axis bearing housing, the bearing and the probe. Figure 7.4 shows the distance measured by the probe over a period of 0.1 s and 15 minutes. As expected for the shorter metrology loop, the noise level of 0.7 nm rms is lower than in Figure 7.3. A typical drift of 35 nm/15 min was observed during several subsequent measurements. The probe is therefore not thought to be the main source of the 200 nm/15 min drift of Figure 7.3.

The second experiment was an overnight stability measurement with the probe measuring to the Zerodur flat again, for a duration of 12 hours to also include the temperature history. Figure 7.5 shows the measurements of the metrology system and the probe, the error and the temperature. During the experiment, the temperature drops 0.6 °C, and the displacement measured by the metrology system and the probe is clearly correlated to this.

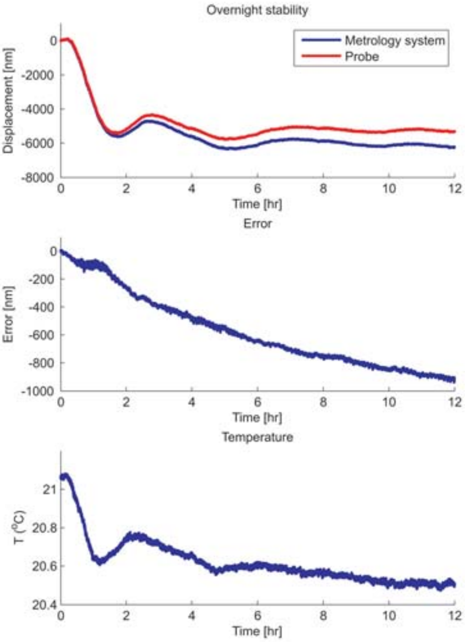

Figure 7.5: Overnight stability in z-direction

The total resulting displacement is around 6 µm and the error is approximately 900 nm. The error increases more or less linearly rather than with the actual temperature curve, and is thus caused by a part of the loop with a very large time constant; i.e. the base block. At the end of the experiment, the temperature has been more or less stable for several hours, but the error is still increasing. A measurement done after this experiment would thus result in a steadily increasing error at a constant temperature.

As already mentioned, slow drifts as observed in the previous experiments are not a problem in surface measurements, since they can be compensated for in the measurement procedure.

7.2.2 Single track measurements

To test the effects of a moving surface, such as roughness, turbulence and probe servo action, a single track was measured at different speeds. The speeds used are 60°/s and 360°/s, at a radius of 40 mm. This gives 42 mm/s and 251 mm/s tangential scanning speed at the probe tip, respectively. The sample rate was 1 kHz, giving 6000 and 1000 points/rev. The surface was tilted by 1 mm, giving a 1 mm PV sine as the measured surface profile. Figure 7.6 shows the error of 10 revolutions compared to the mean of these 10 revolutions.

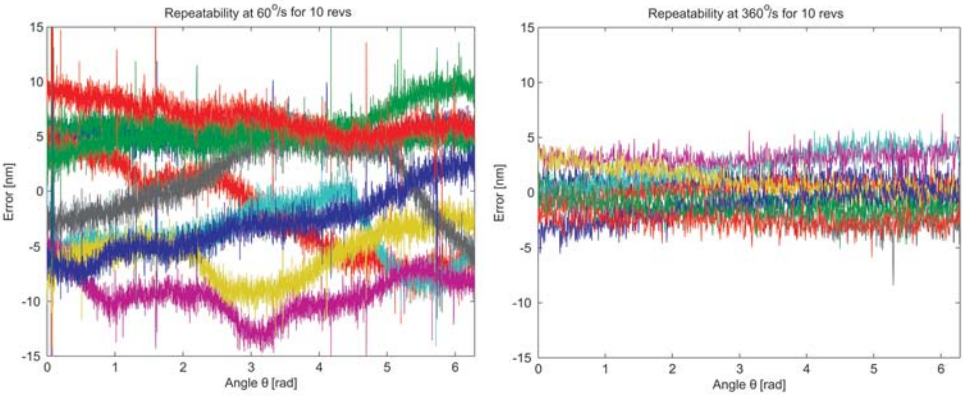

Figure 7.6: Repeatability of 10 tracks at 60°/s and 360°/s

The benefit of fast measurement on the repeatability is clearly visible. As seen in the earlier experiments, turbulence in the interferometers typically causes fluctuations with a duration of several seconds. At 60°/s this causes errors within one revolution, hence the variation in form of the measured profiles. At 360°/s errors within one revolution are small, hence the profile errors are straight but with some offset. The repeatability of the 1 mm sine measurements is 25 nm PV at 60°/s and 10 nm PV at 360°/s, which will both be well within the requirements after averaging.

Similar experiments have been performed on the 1 mm tilted flat for 15 minutes as well, measuring 150 and 900 revolutions, respectively. Figure 7.7 shows the error relative to the mean of the first 10 revolutions. Similar to Figure 7.6, the higher measurement speed produces less variation between subsequent revolutions. After some time, a sine shaped error appears in both measurements, which can be caused by an amplitude or phase change relative to the first 10 revolutions. Physically this can be caused by a tilt or rotation shift of the product on the table, or drift of the probe relative to the product in *r* or *y*-direction. For both measurements, all error profiles are within a band of 45 nm PV. Also note the recurring spikes in the left figure, caused by a dust particle or a scratch. Further note that drift as shown in Figure 7.3 did not occur during these measurements. Apparently, the temperature history was such that the machine was stable during these measurements.

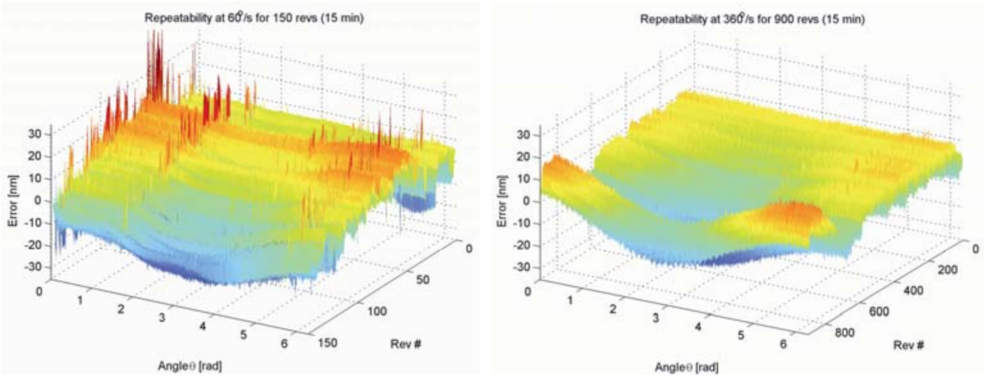

Figure 7.7: Repeatability of 15 minutes of track measurements at 60°/s and 360°/s

7.2.3 Surface measurements

The next step in the machine validation is the measurement of a full surface. Again, the ∅100 mm Zerodur optical flat will be measured. The flatness of this surface was measured interferometrically at NMi VSL to be 44 ± 20 nm PV over a ∅95 mm aperture (Figure 7.8). The rms value is 7.1 nm.

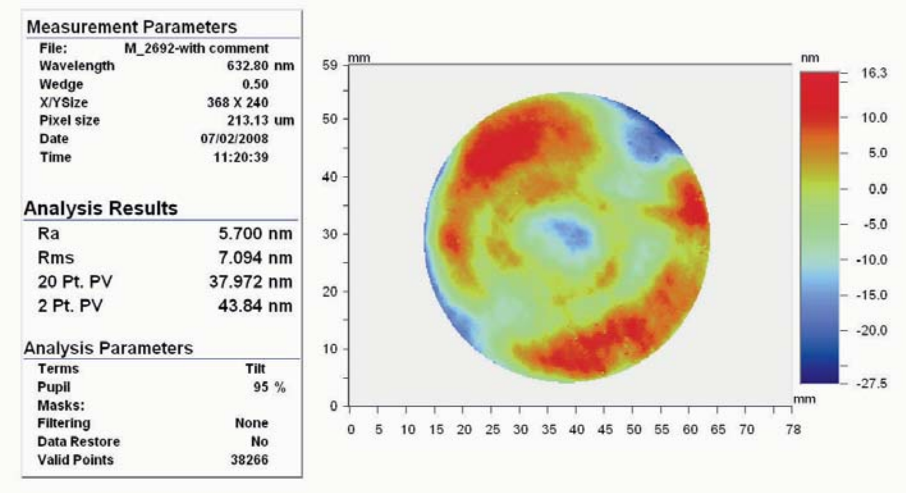

Measurement Parameters

File:	M_2692-with comment
Wavelength	632.80 nm
Wedge	0.50
X/YSize	368 X 240
Pixel size	213.13 um
Date	07/02/2008
Time	11:20:39

Analysis Results

Ra	5.700 nm
Rms	7.094 nm
20 Pt. PV	37.972 nm
2 Pt. PV	43.84 nm

Analysis Parameters

Terms	Tilt
Pupil	95 %
Masks:	
Filtering	None
Data Restore	No
Valid Points	38266

Figure 7.8: NMi VSL calibration result of Zerodur optical flat

This surface will be measured multiple times to determine the repeatability. This will be calculated by determining the average rms error of the individual measurements relative to the average of the whole series. Measurements will first be performed with the surface (almost) flat on the table, with a tilt of 13 μm. Next, 2 shims will be added to obtain a tilt of 1.6 mm (1.14°).

Although some error sources have not been calibrated yet and the calibration data that already is available has not been taken into account yet, the flatness error of the surface as measured by the machine will be calculated, to give a first estimate of the current measurement uncertainty by comparison with the result of Figure 7.8.

Measurement procedure

The following measurements are performed automatically using a pre-programmed measurement script. The sequence starts with zeroing the probe onto the nulling target. Next the probe moves to the edge of the surface, with the spindle at θ = 0°. For drift compensation, four radial scans are obtained by moving the R-stage back and forth twice at a speed of 20 mm/s. This is repeated with the spindle at θ = 90°. Since this surface is only 100 mm in diameter, the radial scan can be taken over the full diameter to obtain extra data on the repeatability of the radial scans.

Next, the spindle speed is set to 360°/s. The R-stage is positioned on the outer track, and the brake is enabled. Five revolutions are acquired, after which the R-stage is moved to the next track. A track spacing of 1 mm is used. When the R-stage arrives at the spindle centre, the spindle is stopped at θ = 0° and the radial scanning procedure is repeated.

Drift compensation

The measurement of all circular tracks takes about 6 minutes, so drift accumulates between measuring the outer and the inner track. Five circular tracks are measured in 5 s, and are averaged to obtain the circular profile at a certain radial position. Drift during measurement of such a profile is negligible as already shown in Figure 7.6. It is therefore assumed that each average circular profile is exact, but that the vertical position of the profile is offset by the drift.

The radial scans take only 4 s per scan, so the drift will be small here and four scans are averaged. The z-position of each circular profile at θ = 0° and θ = 90° is now compared with the radial scans at this position. The difference is the drift that occurred during the circular measurements. This difference is subtracted from the vertical position of each profile to obtain the drift compensated surface measurement.

This procedure is demonstrated by an example measurement of a 13 μm tilted flat. Figure 7.9 (top) shows the radial height measurements at θ = 0° and θ = 90°. The bottom figures show the same profile with a linear fit removed, and the filtered average interpolated to the radial positions of the circular tracks. Some drift has occurred between the first and second series of scans, but the measured profile repeats well.

The profiles at 0° and 90° are quite different. These profiles consist of the flatness of the surface under test (different at 0° and 90°), and a common component of the flatness of the horizontal reference mirror. This common component can be calculated with a reversal (Evans et al., 1996), but this calibration has not been performed yet.

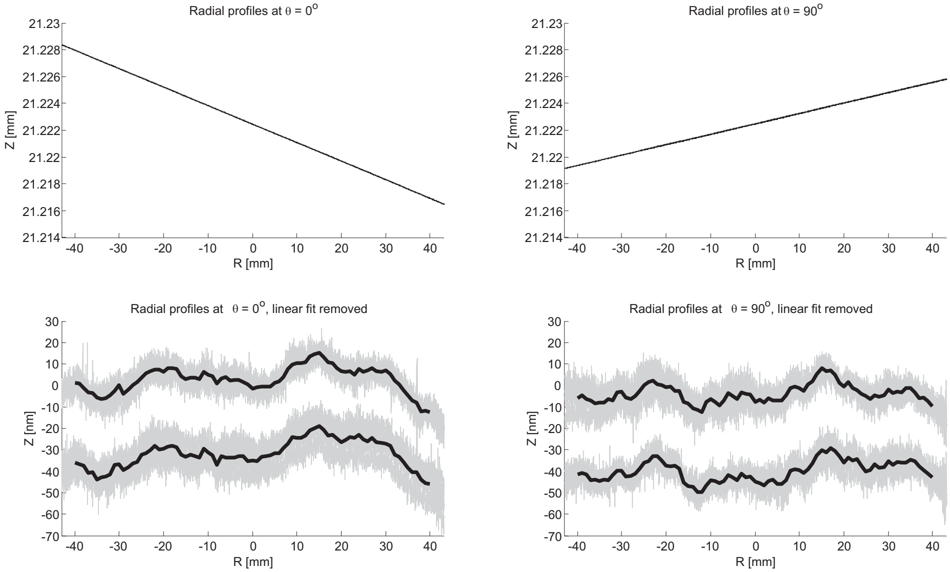

Figure 7.9: Radial scans at $\theta = 0°$ and $\theta = 90°$

The measured radial profiles from before and after the circular measurements are averaged, and compared to the outcome of the circular scans at θ = 0° and θ = 90°. The difference is shown in Figure 7.10. The difference between the profiles is very similar, and is averaged again to obtain the drift offset per circular track for the compensation. The result of this drift compensation on the repeatability of the surface measurements will be shown in the next sections.

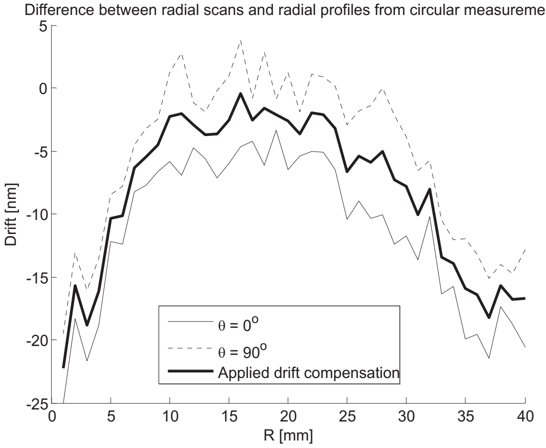

Figure 7.10: Drift calculated from profiles at $\theta = 0°$ and $\theta = 90°$

13 μm tilted flat measurement

Figure 7.11 shows the surface being measured and the surface measurement result. This surface has been measured 3 times, at 1 revolution per second and with a track spacing of 1 mm. Five revolutions are averaged per track. The total measurement time from start to finish is 11 minutes. The sample rate is 1 kHz, giving 1000 points per revolution. Especially near the centre this gives a very high data point density, which has not been reduced yet. Further, only spikes have been removed and no noise filtering has been applied to the circular tracks. The following presented results are therefore almost raw data.

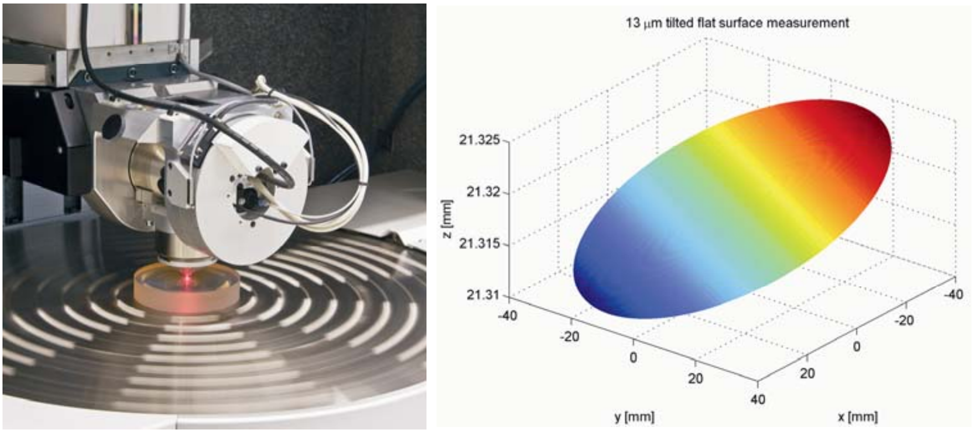

Figure 7.11: Measurement of the optical flat and the surface measurement result

To calculate the repeatability, the three measurements are averaged and the error of each individual measurement relative to this average surface is determined. This is first done without the drift compensation, with the results as shown in the top graphs of Figure 7.12. The error relative to the average surface without the drift compensation is 7.8, 4.1 and 9.3 nm rms, respectively. The rotationally symmetric component caused by the drift can clearly be seen. The drift compensation profile shown in Figure 7.10 belongs to measurement 3.

The error of the drift compensated surfaces, relative to their average, is 1.9, 2.2 and 2.3 nm, respectively. The rotationally symmetric component has almost completely been removed, leaving mainly noise. The average repeatability of these three measurements is 2.1 nm rms.

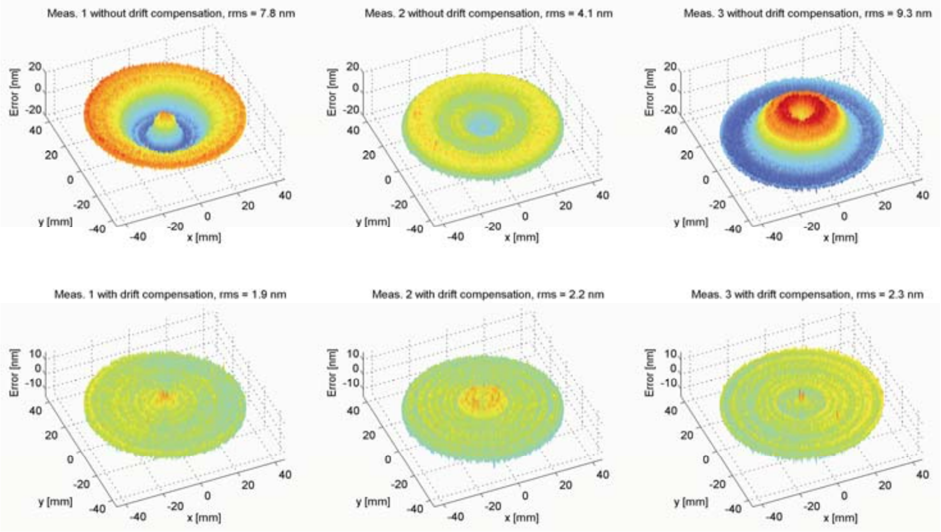

Figure 7.12: Repeatability without (top) and with (bottom) drift compensation

By subtracting a perfect flat from the result of Figure 7.11, the flatness error of the surface as measured by the (uncalibrated) machine is obtained. The rms flatness error of the three measurements is 8, 8.5 and 9.4 nm, respectively. The PV value is about 50 nm. Measurement 2 is shown in Figure 7.13. No quantitative comparison has yet been made with the NMi calibration measurement (Figure 7.8), but the PV and rms value is very similar and resemblance in the form can also be seen. For this surface, the measurement uncertainty requirement of 30 nm (2σ, or 15 nm rms) is thus met, even with the uncalibrated machine.

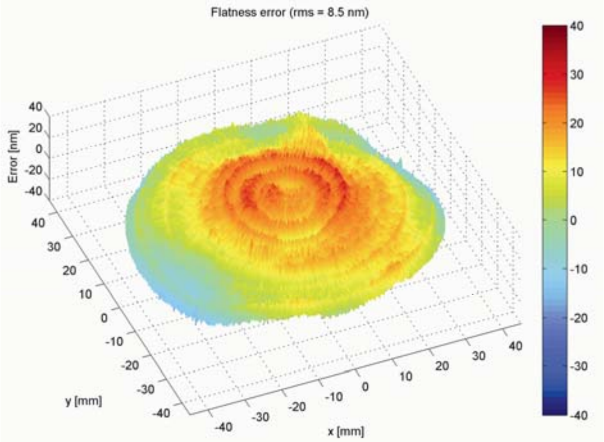

Figure 7.13: Flatness error for 13 μm tilted flat

1.6 mm tilted flat measurement

The previous measurements were done with very little tilt, thereby excluding errors caused by the probe tilt dependency and servo errors. The next measurements are therefore done on a surface with 1.6 mm tilt (1.14°). The surface was measured 10 times, spread over one day. The measurement and drift compensation procedure is equal to the one described earlier. The repeatability results are very similar to those presented for the 13 μm tilted flat, again consisting mainly of noise. The values vary from 2.6 to 4.5 nm rms, with a mean of 3.4 nm.

The flatness error is shown in Figure 7.14. The flatness error measured in the 10 measurements varies from 13 to 15 nm rms, with a mean of 13.9 nm. A clear measurement artefact is, however, visible at the centre.

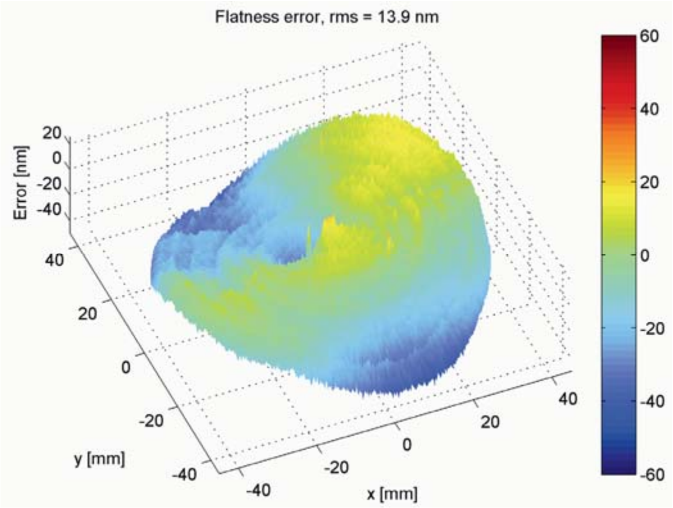

Figure 7.14: Flatness error for 1.6 mm tilted flat

This peak at the centre is caused by the tilt dependency of the probe, which is not yet calibrated and compensated for. This tilt dependency causes the probe to measure height changes in case of pure surface tilt, as is the case at the centre of rotation. Around the surface centre this results in the discontinuity that is visible in the centre of the figure. The preliminary calibration results of the tilt dependency show a large difference in the magnitude of the error for the tilt in α and β-direction. This may cause the warp in the figure. Nevertheless, the uncertainty requirement of 15 nm rms is again met, be it with some clear measurement artefacts. When the probe inclination dependency calibration has been implemented, it is expected that the uncertainty can be well below the requirement for this relatively heavily freeform surface.

7.3 Calibration and nulling

Besides tilted flats and off-centred spheres, very little traceable freeforms with the required uncertainty are available to calibrate the systematic errors of the machine. Traceability must therefore be provided by calibrating all error sources of the metrology loop, either individually or in groups. To ensure calibratability of the machine, a calibration plan has been made together with NMi VSL during the concept design of the machine (Henselmans et al., 2005). In this plan, error sources are identified and calibration strategies are explained. Some of these are rather straightforward, coming from general CMM calibration techniques. Some are worth mentioning since they influenced the design.

The nominal spindle axis of rotation is chosen as the reference of the machine. To determine the alignment of the reference mirrors of the metrology frame relative to the spindle, autocollimator measurements as described in section 4.3.5 are performed. These required a through central hole in the spindle.

The flatness of the horizontal reference mirror can be calibrated by measuring a straightedge or optical flat on the machine. The probe is hereto to be oriented vertically. To calibrate the vertical reference mirror, a similar technique may be applied, or a reference cylinder may be measured. This requires the probe to be oriented horizontally. Initially only +45° to – 45° degrees was required for convex to concave optics, so the range of the Ψ-axis had to be extended to +90°.

The uncertainty of the probe length is the main error source in the measurement of the absolute radius of curvature of a convex or concave surface. The interferometer of the probe must thus be nulled such that this length is constant. A nulling target has hereto been added to the Ψ-axis bearing housing, and the range of the Ψ-axis was further increased to +120° to reach this target. Calibration of the probe length is now to be done once with a concave reference sphere with a radius of curvature of 100 mm, such that the R- and Z-stage can be stationary.

Nulling of the Z-interferometer is not very critical since an error here only produces a height offset of the surface. The R-interferometer should be nulled such that the probe focus coincides with the spindle centre on the table. With a contact probe, this could be done by measuring a cylinder with known diameter, but with an optical probe sideways measurements are not possible.
Two solutions may be applied. The first requires a PSD to be mounted on the spindle, on which the probe is focused. Provided that the probe tip coincides properly with the

measurement plane (section 5.6), the radius of the circle that appears when rotating the spindle is equal to the *r*-position.
A solution that does not require extra electronics and cables is to use the PSD that is already available in the probe. If a lens and mirror assembly are mounted in the hole in the spindle centre, the probe can be positioned such that the focus is coincident with the focus of the lens (schematically shown in Figure 7.15). The differential confocal part and interferometer of the probe are not shown for clarity.

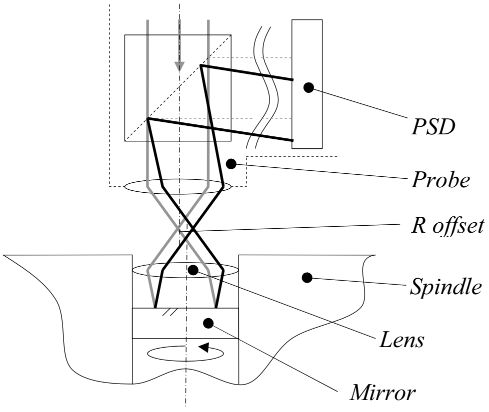

Figure 7.15: Probe centring with lens and mirror on spindle

A lateral offset produces a shift on the probe PSD. By rotating the spindle and minimizing the circle radius that appears on the PSD makes the method insensitive to eccentricity of the lens assembly. Such a target has not been implemented yet, but a recess is provided in the mounting table to do so. Essentially this is thus a 3D nulling target for an optical probe.

A calibration method for calibrating the tilt dependency of the probe has also been designed. This calibration method allows for traceable testing due to the uncoupling of tilt and displacement of the target. It is especially useful since it can be applied on-machine. This new method is further explained in (Cacace, 2009).

Although some calibration measurements have been performed, such as the stage tilt measurements (section 3.8.3) and the Ψ-axis mirror roundness (section 3.6.1), this data has not yet been taken into account in the surface measurement results presented in the previous section. Since only a tilted flat was measured, some of the error sources did not effect the measurement yet. For future measurements, especially when the Ψ-axis is to be actuated because the surface slope exceeds 5°, calibrations such as the probe length have to be performed first.

7.4 Achievable uncertainty estimation

An estimate will be made in this section of the achievable measurement uncertainty after all calibrations have been performed, based on the results presented in this chapter. The repeatability of 2-4 nm rms is such that it is expected to be only a small part of the actual measurement uncertainty. The main part of the uncertainty will be determined by the uncertainties of the calibrations. In section 2.3.3 (Figure 2.12) a measurement task specific uncertainty was estimated, based on estimates of individual error sources. Two main variables were identified here, being the diameter of the surface and the local surface slope.

For a surface of 100 mm diameter and no local surface slope, an expanded uncertainty of 22.6 nm (11.3 nm rms) was predicted (section 2.3.3). Based on a qualitative comparison of the 13 μm tilted flat, the measured flatness (PV and rms) resembles the NMi calibration values very well, without any calibration. Calibration for convex and concave surfaces, for which the Ψ-axis and Z-stage also need to be actuated, can be performed with well known spherical artefacts. It is therefore expected that the achievable uncertainty for surfaces with little local slope (aspheres and slightly freeform surfaces), may eventually be measured with uncertainties as predicted or even better.

For a 100 mm diameter surface with 1.1° of local slope, the expanded uncertainty was budgeted to be 23.4 nm. For surfaces up to 500 mm and with 5° of local slope, an expanded uncertainty of 55 nm was predicted. As shown in section 5.5, the inclination dependent error of the probe may be compensated to the order of 3 nm rms, or 6 nm expanded uncertainty. Based on the above approximations, the required form measurement uncertainty for highly freeform surfaces may thus also be met, provided that the novel probe calibration method can be performed with the expected uncertainty.

The repeatability is not limiting for the achievable uncertainty. All considered, it is expected that the uncertainty estimation of Figure 2.12 is realistic, and may even be surpassed provided that all calibrations can be done with their expected level of accuracy.

7.5 Conclusion

The performance of the machine assembly has been tested by stability, single track and full surface measurements. The measurements focus on repeatability, since this is a key condition before achieving low measurement uncertainty by calibration. The measurements are performed on a ∅100 mm optical flat, which was calibrated by NMi to be flat within 7 nm rms and about 40 nm PV.

At standstill, the measured displacement due to vibrations is 15 nm PV over 0.1 s. This is compensated by the separate metrology system to 0.9 nm rms, confirming the advantage of the separate short metrology loop. Over 15 minutes, the drift is 200 nm, which is clearly correlated to the thermal history of the base as was shown with a 12 hour measurement.
When measuring a single track on a flat tilted by 1 mm, the advantage of speed was demonstrated. At 60°/s, interferometer air turbulence is the main error source, resulting in a spread of 25 nm PV. At 360°/s this reduces to 10 nm PV.
For the full surface measurements, a measurement procedure was implemented which measures the radial profile before and after the circular tracks, to compensate for drift. This procedure improves the repeatability of a flat tilted by 13 μm from 4 – 9 nm rms to about 2 nm rms. Similar measurements of a 1.6 mm tilted flat show an average repeatability of 3.4 nm over 10 measurements.
Although no calibration data has been taken into account yet, the measured flatness deviation of the 13 μm tilted flat of 8-9 nm rms and 50 nm PV already matches the NMi measured flatness very well. For the 1.6 mm tilted flat, the inclination dependency of the probe causes a clearly visible measurement artefact that can be compensated for with the built-in PSD. Nevertheless, the measured flatness is 13 nm rms, compared to 7 nm rms measured by NMi.

Calibration techniques for providing traceability to the machine have been taken into account early in the design, including a novel calibration technique for the probe tilt dependency.

The measurement results exceed the expectations, especially since they are basically raw data. Future calibrations and development of control and data-processing software will certainly further improve these results. The desired measurement uncertainty is therefore certainly expected to be achievable.

Chapter 8

Conclusion and recommendations

In the previous chapters, the design, realization and testing of a non-contact measurement machine for freeform optics has been shown. This chapter will recapitulate the main conclusions. In the recommendations, subjects of future work are described, consisting of further experiments, calibrations and software.

8.1 Conclusion

The performance of high-precision optical systems using spherical optics is limited by aberrations. By applying aspherical and freeform optics, the geometrical aberrations can be reduced or eliminated while at the same time also reducing the required number of components, the size and the weight of the system. New manufacturing techniques enable creation of high-precision freeform surfaces. Suitable metrology (high accuracy, universal, non-contact, large measurement volume and short measurement time) is key in the manufacturing and application of these surfaces, but not yet available. In this thesis, the design, realization and testing of a new metrology instrument is described, capable of universal, non-contact and fast measurement of freeform optics up to ∅500 mm, with an uncertainty of 30 nm (2σ).

Machine concept

A cylindrical scanning setup with an optical distance probe has been designed. This concept is non-contact, universal and fast. With a probe with 5 mm range, circular tracks on freeform surfaces can be measured rapidly with minimal dynamics. By applying a metrology frame relative to which the position of the probe and the product are measured, most stage errors are eliminated from the metrology loop. Because the probe is oriented perpendicular to the aspherical best-fit of the surface, the sensitivity to tangential errors is reduced. This allows for the metrology system to be 2D. The machine design can be split into three parts: the motion system, the metrology system and: the non-contact probe.

Motion system

The motion system positions the probe relative to the product in 4 degrees of freedom. The product is mounted on an air bearing spindle (θ), and the probe is positioned over it in radial (r), vertical (z) and inclination (ψ) direction by the R-stage, Z-stage and Ψ-axis, respectively. The motion system provides a sub-µm repeatable plane of motion to the probe. The Z-stage is hereto aligned to a vertical plane of the granite base using three air bearings, to obtain a parallel bearing stage configuration. To minimize distortions and hysteresis, the stages have separate position and preload frames. Direct drive motors and high resolution optical scales and encoders are used for positioning. Mechanical brakes are applied while measuring a track, to minimize power dissipation and to exclude encoder, amplifier and EMC noise. The motors, brakes and weight compensation are aligned to the centres of gravity of the R and Z-stage. Stabilizing controllers have been designed based on frequency response measurements.

When locked, the noise level at the probe tip in *r, y* and *z*-direction is 6.8, 4.8 and 4.4 nm rms, respectively. The first eigenmodes are at 46, 122 and 67 Hz, respectively. The tilt error of the Z-stage over the full range of motion has been calibrated with NMi VSL to be 7.5, 8.6 and 34.2 µrad in φ, ψ and θ-direction respectively.

The low noise level and high eigenfrequency in *y*-direction, and the low tilt error in φ and θ-direction are contributed to the parallel bearing setup. Compared to a stacked design, the higher stiffness comes at the cost of higher moving mass and a more intricate design. This especially holds for the separate preload frames, which are to achieve similarly high eigenfrequencies as the position frames. Much of the displacement in *r* and *z*-direction is compensated for by the metrology system.

Metrology system

The metrology system measures the position of the probe relative to the product in the six critical directions in the plane of motion of the probe (the measurement plane). By focussing a vertical and horizontal interferometer onto the Ψ-axis rotor, the displacement of the probe is measured relative to the reference mirrors on the upper metrology frame. Due to the reduced sensitivity in tangential direction at the probe tip, the Abbe criterion is still satisfied. Silicon Carbide is the material of choice for the upper metrology frame, due to its excellent thermal and mechanical properties. Mechanical and thermal analysis of this frame shows nanometer-level stabilities under the expected thermal loads. Simulations of the multi-probe method show capabilities of in process separation of the spindle reference edge profile and the spindle error motion with sub-nanometer uncertainty. This method has not been validated in practice yet.

Experiments show motion amplitudes in the order of 15 nm PV over 0.1 s, which is compensated to 0.6 nm rms by the metrology system. Over 15 minutes, 80 nm of drift in the most critical in z-direction is compensated to 2.3 nm rms. In the tangential r-direction, the stability is 8.2 nm rms over 15 minutes, just as in the out-of-plane y-direction. Comparing the harmonic content of the error to the displacement clearly shows the eigenfrequencies that are compensated with the metrology system, and those which are not. The upper metrology frame shift in r-direction from R-stage movement is measured to be 760 nm, which is cancelled by the compensation mechanism.

Non-contact probe

The non-contact probe measures the distance between the Ψ-axis rotor and the surface under test. A dual stage design is applied, which has 5 mm range, nanometer resolution and 5° unidirectional acceptance angle. This enables the R and Z-stage and Ψ-axis to be stationary during the measurement of a circular track on a freeform surface. The design consists of a compact integration of the differential confocal method with an interferometer. The differential confocal method has been modelled, tested and optimized. The range of the system realized is 4 μm and the noise level is 0.17 nm rms. The repeatability over the full range is 4.1 nm rms. The focussing objective is positioned by a flexure guidance with a voice coil actuator. A switching motion controller finds the surface and keeps the objective focused onto it with some tens of nanometers servo error. In interferometer and FES control, a bandwidth of respectively 900 and 1600 Hz is possible. A PSD allows for compensation of the inclination dependent error. Preliminary measurement results show a tilt dependency of about 550 nm at 5°, which may be compensated to nanometer level uncertainty in the off-line data processing.

Electronics and software

The electronics and software are designed to safely operate the 5 axes of the machine and to acquire the signals of all measurement channels. The electronics cabinet contains a real-time processor with many in and outputs, control units for all 5 axes, a safety control unit, a probe laser unit and an interferometry interface. The software consists of three main elements: the trajectory planning, the machine control and the data processing. Emphasis has been on the machine control, in order to safely validate the machine performance and perform basic data-processing.

Machine validation

The performance of the machine assembly has been tested by stability, single track and full surface measurements. The measurements focus on repeatability, since this is a key condition before achieving low measurement uncertainty by calibration. The measurements are performed on a ∅100 mm optical flat, which was calibrated by NMi to be flat within 7 nm rms and about 40 nm PV.

At standstill, the measured displacement due to vibrations is 15 nm PV over 0.1 s. This is compensated by the separate metrology system to 0.9 nm rms, confirming the advantage of the separate short metrology loop. When measuring a single track on a flat tilted by 1 mm, the advantage of speed was demonstrated. At 60°/s, interferometer turbulence is the main error source, resulting in a spread of 25 nm PV. At 360°/s this reduces to 10 nm PV. For the full surface measurements, a measurement procedure was implemented which measures the radial profile before and after the circular tracks, to compensate for drift. This procedure results in a repeatability of about 2 nm rms. Similar measurements of a 1.6 mm tilted flat show an average repeatability of 3.4 nm over 10 measurements. Although no calibration data has been taken into account yet, the measured flatness deviation of the 13 μm tilted flat of 8-9 nm rms and 50 nm PV already matches the NMi VSL measured flatness well. For the 1.6 mm tilted flat, the inclination dependency of the probe causes a clearly visible measurement artefact that can be compensated for with the built-in PSD. Nevertheless, the measured flatness is 13 nm rms, compared to 7 nm rms measured by NMi.

Calibration techniques for providing traceability to the machine have been taken into account early in the design, including a novel calibration technique for the probe tilt dependency.

Conclusion

A new non-contact measurement machine prototype for freeform optics has been developed. The characteristics desired for a high-end, single piece, freeform optics production environment (high accuracy, universal, non-contact, large measurement volume and short measurement time) have been incorporated into one instrument. The validation measurement results exceed the expectations, especially since they are basically raw data. Future calibrations and development of control and data-processing software will certainly further improve these results.

8.2 Recommendations

For the fully functional prototype to be applied in freeform optics research and manufacturing, some subjects require further attention:

Positioning accuracy

The positioning accuracy of the stages is not critical due to the non-contact nature of the measurement. The controllers of the stages have been designed for robustness, not yet for minimal positioning error. To make use of the full positioning capability enabled by the air-bearings, direct-drive motors and optical scales, the controllers should be further tuned. This may be applied to explore the high-resolution scanning possibility of the machine.

The braking of the stages currently is a successive operation, in which the controller is turned off and the solenoid valve of the brake piston is opened. In the delay of this sequence, the stages are free floating masses that move away from the desired position. Leaving the controller on until the brake is closed may lead to saturation of the integrator in the controller. A more sophisticated switching scheme should therefore be designed, for instance by switching to an intermediate PD controller when applying the brake.

For the Z-stage, the remaining friction of the weight compensation is expected to be limiting for the positioning resolution. Re-alignment may improve this. Otherwise, the friction may be modelled and compensated for in the controller.

Probe response for various materials

The probe sum signal varies with surface reflectivity. The laser power may be adjusted to prevent saturation of the photodiodes, but the controller thresholds (Figure 5.35) also have to be adapted. Optimum setup data for various materials may be collected in a software library, such that the correct probe setup can be easily selected in software from for instance a pull-down menu.

Diamond turned surfaces contain scallops with a width of the same order of magnitude as the probe focal spot. Test must be performed to research the influence on the measurement uncertainty and the controller stability. Perhaps a specific controller setup must be designed. The pores of Silicon Carbide currently cause the probe to jump to safety retract mode. A specific controller setup that is forgiving for a momentary loss of signal may hereto be developed. These specific controller setups may be linked to the pull-down menu described before.

Due to the normalization, the FES signal nominally does not depend on the reflectivity. This must be verified, and surface specific calibrated FES curves may be stored in the same library mentioned before. The FES curve may also be calibrated in process for each surface under test by comparing it with the probe interferometer.

Rough surfaces may be measurable with the probe (section 5.1.4). This may either require only threshold and controller adaptation, or to operate the probe in conventional confocal mode. Since this would result in a machine that can be applied throughout the optics production process, it is certainly worth investigating.

Calibration for traceability

In the validation chapter, the repeatability of the machine has been demonstrated. Repeatability is key in achieving low measurement uncertainty through calibration. Several calibration measurements have already been performed (stage tilt calibration, Ψ-axis mirror roundness), which can readily be implemented in the data processing. Some further calibrations have to be performed to provide traceability to NMi standards to the instrument.

The probe length, which is determined by the distance between the Ψ-axis centre line and the nulling target, must be calibrated. This can be done by measuring a 100 mm radius concave reference test plate. This calibration is required when surfaces are measured for which the Ψ-axis is to be actuated.

The flatness and alignment of the horizontal and vertical reference mirror can be calibrated by a reversal with an optical flat. This calibration is required for large surfaces and surfaces with large height differences.

When measuring freeform surfaces, the compensation of the probe inclination dependency should be applied. The calibration procedure and results will be explained in (Cacace 2009).

For freeform surfaces with large local slope, the probe tip y-position should be calibrated as a function of r, z, ψ and c (the probe actuator position). This is a comprehensive procedure, required to reach the ultimate measurement uncertainty on heavily freeform surfaces.

To prevent systematic errors from being overlooked, a final cross-check with NMi VSL of a more complex form than the optical flat can be done. An eccentrically mounted sphere can be measured on the machine and on the NMi interferometer, or a heavily freeform surface may be measured on a high accuracy CMM.

Software

As explained in Chapter 6, especially the trajectory planning and the data-processing require further development. Much is to be gained in this area, since the software determines the usability of the machine. It must be further investigated whether commercially available software can be adapted or elements incorporated. User friendly software is key in acceptance and common application of the machine in a workshop environment. This will encourage continuation of the development and exploration of the full potential of the machine.

References

(Abbe, 1890)
Abbe, E., '*Meßapparate für Physiker*', Zeitschrift Für Instrumentenkunde, Vol. 10, pp.446 – 448, 1890

(Aerts, 2007)
Aerts, C.A.L., '*Brake and Ψ-axis of NANOMEFOS*', MSc Thesis, Technische Universiteit Eindhoven, DCT 2007.051, 2007

(Agilent, 2002)
Agilent Technologies, '*Laser and optics user's manual*', product number: 05517-90045, 2002

(Allen et al., 1990)
Allen, L., Angel, R., Mangus, J.D., Rodney, G., Shannon, R.R., Spoelhof, C.P., '*The Hubble space telescope optical systems failure report*', NASA Technical Report NASA-TM-103443, 1990

(Allen et al., 2006)
Allen, Y.Y., Huang, C., Klocke, F., Brecher, C., Pongs, G., Winterschladen, M., Demmer, A., Lange, S., Bergs, T., Merz, M., Niehaus, F., '*Development of a compression moulding process for three-dimensional tailored free-form glass optics*', Applied Optics, Volume 45, No. 25, pp. 6511 – 6518, September 2006

(Anderson and Burge, 1995)
Anderson, D.S., Burge, J.H., '*Swing-arm profilometry of aspherics*', Proc. of SPIE, Vol. 2536, pp 169 – 179, 1995

(ASME, 1985)
American Society of Mechanical Engineers, *'Axis of rotation – Methods for Specifying and testing'*, American National standard, ANSI/ASME B89.3.4M, 1985

(ASML, 2004)
ASML Optics WaveFront Newsletter, October 2004

(ASPE, 2004)
Proceedings of ASPE Winter Topical Meeting on *'Free-form optics: Design, Fabrication, Metrology and Assembly'*, editors: Dow, T.A., Garrard, K.P., Sohn, A., Ohl, R.G., 2004

(Assoufid et al., 2001)
Assoufid, L., Hignette, O., Howells, M., Irick, S., Lammert, H., Takacs, P., '*Future metrology needs for synchrotron radiation grazing-incidence optics*', Nuclear instruments and methods in Phys. Res. A, 467 – 468, pp. 267 – 270, 2001

(Atad-Ettedgui et al., 2006)
Atad-Ettedgui, E., Peacocke, T., Montgomery, D., Gostick, D., McGregor, H., Cliff, M., '*Opto-mechanical design of SCUBA-2*', Proceedings of SPIE, Optomechanical Technologies for Astronomy, Volume 6273, 2006

(Beaucamp et al., 2004)
Beaucamp, A.T.H., Freeman, R., Morton, R., Walker, D.D., '*Metrology software support for free-form optics manufacturing*', Proceedings of SPIE, Current developments in lens design and optical engineering V, Volume 5523, pp. 281 – 289, 2004

(Becker and Heynacher, 1987)
Becker, K., Heynacher, E., '*M400 – A coordinate measuring machine with 10 nm resolution*', Proc. of SPIE, Vol. 802, pp. 209 – 216, 1987

(Beckstette, 2008)
Beckstette, K.F., '*Trends in aspheres and freeform optics*', presented at OptoNet Workshop, 2008

(Bejan, 1993)
Bejan, A., '*Heat transfer*', John Wiley & Sons, ISBN 0-471-50290-1, 1993

(Benschop and Van Rosmalen, 1991)
Benschop, J., van Rosmalen, G., '*Confocal compact scanning optical microscope based on compact disc technology*', Applied Optics, Volume 30, No. 10, pp. 1179 - 1184, 1991

(Birch and Downs, 1993)
Birch, K.P, Downs, M.J., '*An updated Edlén equation for the refractive index of air*', Metrologia, Vol. 30, pp. 155-162, 1993

(Bobroff, 1987)
Bobroff, N., 'Residual errors in laser interferometry from air turbulence and nonlinearity', Applied Optics, Volume 26, No. 13, pp. 2676 – 2682, 1987

(Bockman, 1996)
Bockman, J.J., 'Method and interferometric apparatus for measuring changes in displacement of an object in a rotating reference frame', Patent US5677768, 1996

(Boneschanscher, 1995)
Boneschanscher, M.N., '*Elastische geleidingen, een literatuurstudie*', TNO-report TPD-HOI-RPT-950076, 1995, in Dutch

(Breyer and Pressel, 1991)
Breyer, K.H., Pressel, H.G., '*Paving the way to thermally stable coordinate measuring machines*', Progress in precision engineering: proc. of the 6th international precision engineering seminar, pp. 56 – 76, 1991

(Broers, 1999)
Broers, S.B., 'Ontwerp van een draaibank met elastische geleidingen voor fabricage van niet-rotatiesymmetrische lenzen', MSc Thesis, Technische Universiteit Eindhoven, 1999, in Dutch

(Bryan, 1979)
Bryan, J.B., 'Design and construction of an ultra precision 84 inch diamond turning machine', Precision Engineering, Volume 1, Issue 1, pp. 13-17, 1979

(Bryan and Carter, 1979)
Bryan, J.B., Carter, D.L., '*Design of a new error-corrected co-ordinate measuring machine*', Precision Engineering, Volume 1, Issue 3, pp. 125-128, July 1979

(Bryan, 1984)
Bryan, J.B., '*The power of deterministic thinking in machine tool accuracy*', The first International Machine Tool Engineers Conference, Japan, Lawrence Livermore National Laboratory Report UCRL-91531, 1984

(Bryan, 1990)
Bryan, J.B., '*International status of thermal error research (1990)*', Annals of CIRP, Vol. 39/2, pp. 645 – 656, 1990

(Burge and Wyant, 2004)
Burge, J.H., Wyant, J.C., 'Use of Computer Generated Holograms for Testing Aspheric Optics', Proc. of ASPE Winter Topical Meeting on 'Free-form optics: Design, Fabrication, Metrology and Assembly', pp. 45 - 50, 2004

(Cacace, 2006)
Cacace, L.A., *'Development of a nanometer accuracy non-contact probe for NANOMEFOS'*, MSc Thesis, Technische Universiteit Eindhoven, nr. DCT 2006.032, 2006

(Cacace et al., 2007)
Cacace, L.A., Van Amstel, W.D., Henselmans, R., De Man, H., Rosielle, P.C.J.N., 'Development of a new differential confocal optical probe with nanometer

accuracy at large acceptance angles for measurement of free-form aspherics', Proc. of the 7th Euspen Annual conference, pp. 168 – 171, 2007

(Cacace, 2009)
Cacace, L.A., 'An Optical Distance Sensor: Tilt robust differential confocal measurement with mm range and nm uncertainty', PhD Thesis, Technische Universiteit Eindhoven, to be published in 2009

(Callender et al., 2006)
Callender, M.J., Efstathiou, A., King, C.W., Walker, D.D., Gee, A.E., Lewis, A.J., Oldfield, S., Steel, R.M., *'A Swing Arm Profilometer for Large Telescope Mirror Element Metrology'*, Proc. of SPIE, Vol. 6273, 2006

(Chambure et al., 1999)
Chambure, D. de, Lainé, R., Katwijk, K. van, Kletzkine, P. *'XMM's X-ray telescopes'*, ESA Bulletin 100, December 1999

(Chang et al., 1997)
Chang, Y.C., Sasian, J., Greivenkamp, J., *'Determining the character of aspheric surfaces'*, Convergence Newsletter, Centre for Optics Manufacturing, University of Rochester, Volume 5, No. 4, July/August 1997

(Chetwynd and Siddall, 1976)
Chetwynd, D.G., Siddall, G.J., *'Improving the accuracy of roundness measurement'*, J. of Physics E: Scientific Instruments, Vol. 9, pp. 537 – 544, 1976

(Cosijns, 2004)
Cosijns, S.J.A.G., '*Displacement laser interferometry with sub-nanometer uncertainty*', PhD Thesis, Technische Universiteit Eindhoven, ISBN 90-386-2656-8, 2004

(Deck and De Groot, 1994)
Deck, L., de Groot, P., '*High-speed noncontact profiler based on scanning white-light interferometry*', Applied Optics, Vol. 33, No. 31, pp. 7334 – 7338, 1994

(Dobosz, 1983)
Dobosz, M., '*Optical profilometer: a practical approximate method of analysis*', Applied Optics, Vol. 22, No. 24, pp. 3983 – 3987, 1983

(Donaldson, 1972)
Donaldson, R.R., 'A simple method for separating spindle error from test ball roundness error', Annals of CIRP, Vol. 21/1, pp. 125 – 126, 1972

(Donaldson and Patterson, 1983)
Donaldson, R.R., Patterson, S.R., '*Design and construction of a large, vertical axis diamond turning machine*', Proc. of SPIE, 27th International technical symposium and instrument display, August 1983

(Dörband and Seitz, 2001)
Dörband, B., Seitz, G., '*Interferometric testing of optical surfaces at its current limit*', Optik 112, No. 9, pp. 392 – 398, 2001

(Dumas et al., 2004)
Dumas, P.R., Fleig, J., Forbes, G.W., Golini, D., Kordonski, W.I., Murphy, P.E., Shorey, A.B., Tricard, M., '*Flexible polishing and metrology solutions for free-form optics*', Proc. of ASPE Winter Topical Meeting on *'Free-form optics: Design, Fabrication, Metrology and Assembly'*, pp. 39 – 44, 2004

(Duparré et al., 2002)
Duparré, A., Ferre-Borrull, J., Gliech, S., Notni, G., Steinert, J., Bennet, J.M., 'Surface characterization techniques for determining the root-mean-square roughness and power spectral densities of optical components', Applied Optics, Volume 41, No. 1, pp. 154 – 171, January 2002

(Edlén, 1966)
Edlén, B., '*The refractive index of air*', Metrologia, Vol. 2/ 2, pp. 71 – 80, 1966

(Ehrmann and Schindhelm, 1998)
Ehrmann, K., Ho, A., Schindhelm, K., '*A 3D optical profilometer using a compact disc reading head*', Meas. Sci. Technol., Volume 9, pp. 1259 – 1265, 1998

(Estler, 1985)
Estler, W.T., '*High-accuracy displacement interferometry in air*', Applied Optics, Volume 24, No. 6, pp. 808 – 815, 1985

(Estler, 1986)
Estler, W.T, described in (Evans, 1996) but first derived and described at the 1986 SME Precision Machining Workshop,

(Euspen, 2009)
Euspen Special Interest Group meeting on '*Structured and freeform surfaces*', Edinburgh, Februari 2009

(Evans et al., 1996)
Evans, C.J., Hocken, R.J., Estler, W.T., '*Self-calibration: Reversal, Redundancy, Error Separation, and 'Absolute testing'*, Annals of CIRP, Vol. 45/2, pp. 617 – 634, 1996

(Fainman et al., 1982)
Fainman, Y., Lenz, E., Shamir, J., '*Optical profilometer: a new method for high sensitivity and wide dynamic range*', Applied Optics, Vol. 21, No. 17, pp. 3200 – 3208, 1982

(Fan et al., 2001)
Fan, K.C., Chu, C.L, Mou, J.I., '*Development of a low-cost autofocusing probe for profile measurement*', Meas. Sci. Technol., Volume 12, 2137 – 2146, 2001

(Frank et al., 2005)
Frank, T., Theska, R., Lotz, M., Hackel, T., Höhne, G., '*Weight compensation mechanisms for ultra high precision vertical positioning*', Proceedings of 5th Euspen Annual conference, pp. 429 – 432, 2005

(Frost et al., 2003)
Frost, F., Fechner, R., Ziberi, B. Flamm, D., Schindler, A., '*Large area smoothing of optical surfaces by low-energy ion beams*', Thin Solid Films, Volume 459, Issues 1-2, pp. 100-105, July 2004

(Gao and Kiyono, 1997)
Gao, W., Kiyono, S., 'Development of an optical probe for profile measurement of mirror surfaces', Opt. Eng. 36(12), pp. 3360 – 3366, 1997

(Garrard et al., 2005)
Garrard, K., Bruegge, T., Hoffman, J., Dow, T., Sohn, A., '*Design tools for freeform optics*', Proceedings of SPIE, Volume 5874, pp. 1-11, 2005

(Geckeler and Weingärtner, 2002)
Geckeler, R.D., Weingärtner, I., '*Sub-nm topography measurement by deflectometry: flatness standard and wafer nanotopography*', Proc. of the 3rd Euspen Int. conference, pp. 497 – 500, 2002

(Gilmozzi and Spiromilio, 2007)
Gilmozzi, R. Spiromilio, J., '*The European Extremely Large Telescope (E-ELT)*', ESO 'The Messenger' No. 127, March 2007, pp. 11 – 19, 2007

(Grejda, 2002)
Grejda, R.D., 'Use and calibration of ultraprecision axes of rotation with nanometer level metrology', PhD Thesis, Pennsylvania State University, 2002

(Hamilton and Wilson, 1982)
Hamilton, D.K., Wilson, T., '*Surface profile measurement using the confocal microscope*', J. of Appl. Phys., Volume 53 (7), pp. 5320 – 5322, 1982

(Hansen et al., 2006)
Hansen, H.N., Carneiro, K., Haitjema, H., De Chiffre, L., '*Dimensional micro and nano metrology*', Annals of the CIRP, Vol. 55/2, pp. 721 – 733, 2006

(Hecht, 1998)
Hecht, E., *'Optics'*, 3rd Edition, Addison-Wesley, ISBN 0-201-30425-2, 1998

(Hemschoote et al., 2004)
Hemschoote, D., Vleugels, P., Qian, J., Van Brussel, H., Reynaerts, D., '*An Abbe-compliant 3D-measurement concept based on linear scales*', Proceedings of 4th Euspen Annual conference, pp. 336 – 337, 2004

(Henselmans, 2003)
Henselmans, R., '*Ontwerp van een contactloze meetmachine voor free-form optische oppervlakken*', MSc Thesis, Technische Universiteit Eindhoven, nr. PE-2003-117, 2003, in Dutch

(Henselmans and Rosielle, 2004)
Henselmans, R., Rosielle, P.C.J.N., '*Free-form optical surface measuring apparatus and method*', Patent EP1668318, 2004

(Henselmans et al., 2004)
Henselmans, R., Rosielle, P.C.J.N., Kappelhof, J.P., *'NANOMEFOS – Nanometer Accuracy Non-contact Measurement of Freeform Optical Surfaces'*, Proceedings of ASPE Winter Topical Meeting, pp. 97 - 101, 2004

(Henselmans et al., 2005)
Henselmans, R., Bergmans, R., Kotte, G., '*NANOMEFOS Calibration plan*', Internal design report, Technische Universiteit Eindhoven, 2005

(Henselmans et al., 2005a)
Henselmans, R., Rosielle, N., Steinbuch, M., Saunders, I., Bergmans, R., *'Design of a measurement machine for the universal non-contact measurement of large free-form optics with 30 nm uncertainty'*, Proc. of SPIE Optical Manufacturing and Testing VI, 2005

(Henselmans et al., 2005b)
Henselmans, R., Rosielle, P.C.J.N., Steinbuch, M., Saunders, I.J., *'Nanometer Accuracy Non-contact Measurement of Freeform Optical Surfaces*, Philips Precision Technology Conference, pp. 117 – 121, 2005

(Henselmans, 2007)
Henselmans, R., ‘NANOMEFOS – Nanometer Accuracy Non-contact Measurement of Freeform Optical Surfaces’, Berliner Glas Technology Day on Aspheres, 2007

(Henselmans et al., 2007)
Henselmans, R., Cacace, L.A., Rosielle, P.C.J.N., Steinbuch, M., ‘Design and realization of a measurement machine for the universal non-contact measurement of large freeform optics with 30 nm uncertainty’, Proc. of the 7th Euspen Annual conference, pp. 13 - 16, 2007

(Henselmans, 2008)
Henselmans, R., ‘NANOMEFOS: Design, realization and testing of a measurement machine for freeform optics’, 1st Aachen Precision Days, Fraunhofer IPT, 2008

(Henselmans et al., 2008)
Henselmans, R., Kramer, G., Beaucamp, A., King, C., Ponudurai, K., ‘*NANOMEFOS Software development*’, Internal design report, Technische Universiteit Eindhoven, 2008

(Henselmans et al., 2008a)
Henselmans, R., Cacace, L.A., Rosielle, N., Steinbuch, ‘Design, realization and testing of the NANOMEFOS non-contact measurement machine for freeform optics’, ASPE Annual meeting, 2008

(Heynacher, 1979)
Heynacher, E., ‘Aspheric Optics – How they are made and why they are needed’, Phys. Technol., Vol.10, 1979

(Holota, 2008)
Holota, W., ‘Aspheres and freeform optics for astronomical instrumentation’, presented at OptoNet Workshop, 2008

(Holster, 1967)
Holster, P.L., ‘*Gaslagers met uitwendige drukbron*’, P.T. Werktuigbouw, vol. 22, No. 9, pp. 363 – 370, No. 10, pp. 415 – 425, No. 26, pp. 1105, 1967, in Dutch

(Hughes et al., 2000)
Hughes, E.B., Wilson, A, Peggs, G.N., ‘*Design of a high-accuracy CMM based on multi-lateration techniques*’, Annals of CIRP , Vol. 49/1, pp. 391 – 394, 2000

(ISO, 2006)
International Organization for Standardization, standard ISO 10110, 'Optics and photonics – Preparation of drawings for optical elements and systems', 2006

(Jäger et al., 2001)
Jäger, G., Manske, E., Hausotte, T., '*Nanopositioning and Measuring Machine*', Proc. of 2nd Euspen Int. Conference, pp. 290 – 293, 2001

(Johnson, 1985)
Johnson, K.L., '*Contact mechanics*', Cambridge University Press, ISBN 0-521-34796-3, 1985

(Johnstone et al., 2004)
Johnstone, E., Schluchter, C., Ray, A.B., '*Wavefront metrology errors*', Proc. of Euspen International conference, pp. 348-349, 2004

(Karow, 1993)
Karow, H.H., '*Fabrication methods for precision optics*', Wiley Interscience, ISBN 0-471-51222-2, 1993

(Knarren, 2003)
Knarren, B.A.W.H., '*Application of optical fibres in precision heterodyne laser interferometry*', PhD Thesis, Technische Universiteit Eindhoven, ISBN 90-386-3044-1, 2003

(Knauer et al., 2004)
Knauer, M.C., Kaminski, J., Häusler, G., '*Phase Measuring Deflectometry: a new approach to measure specular free-form surfaces*', Proc. of SPIE, Vol. 5457, pp. 366 – 376, 2004

(Kohno et al., 1988)
Kohno, T., Ozawa, N., Miyamoto, K., Musha, T., '*High precision optical surface sensor*', Applied Optics, Volume 27 (1), pp. 103 – 108, 1988

(Kunzmann et al., 1993)
Kunzmann, H., Pfeifer, T., Flügge., J., '*Scales vs. interferometers – performance and comparison of two measuring systems*', Annals of the CIRP, Volume 42/2, pp. 753 – 767, 1993

(Laan et al., 2000)
Laan, E.C., De Vries, J., Kruizinga, B., Visser, H., Levelt, P.F., Van den Oord, G.H.J., Maelkki, A., Leppelmeier, G.W., Hilsenrath, E., *'Ozone monitoring with the OMI instrument'*, Proceedings of SPIE, Imaging and Spectrometry VI, Volume 4132, pp. 334-343, 2000

(Lu and Li, 2001)
Lu, S., Li, Z., *'A composite probe for surface topography measurement'*, Int. J. of Adv. Manuf. Technol., Volume 18, pp. 831 – 835, 2001

(Machkour et al., 2006)
Machkour-Deshayes, N., Stoup, J., Lu, Z.Q., Soons, J., Griesmann, U., Polvani, R., '*Form-Profiling of optics using the geometry measuring machine and the M-48 CMM at NIST*', Journal of Research of the National Institute of Standards and Technology, Vol. 111, No. 5, pp. 373 – 384, 2006

(Mahajan, 1991)
Mahajan, V.N. '*Aberration theory made simple*', Bellingham, ISBN 0-8194-0536-1, 1991

(Malacara, 2007)
Malacara, D., '*Optical shop testing*', Wiley-Interscience, ISBN 978-0-470135-96-9, 2007

(Marsh et al., 2006)
Marsh, E., Couey, J., Vallance, R., '*Nanometer-level comparison of three error motion separation techniques*', Transactions of the ASME, Vol. 128, pp. 180 – 187, 2006

(Martin et al., 2003)
Martin, H.M., Allen, R.G., Burge, J.H., Dettmann, L.R., Ketelsen, D.A., Miller, S.M., Sasian, J.M., '*Fabrication of mirrors for the Magellan telescopes and the Large Binocular Telescope*', Proc. of SPIE, Vol. 4837, pp. 609 – 618, 2003

(Mashimo et al., 1997)
Mashimo, K., Nakamura, T., Tanimura, Y., 'Development of optical noncontact sensor for measurement of three-dimensional profiles using depolarized components of scattered light', Opt. Eng., Volume 36(1), pp. 227- 234, 1997

(MIL-PRF-13830B, 1997)
Performance specification: 'Optical components for fire control instruments, general specification governing the manufacture, assembly, and inspection of', 1997

(Mitsui, 1982)
Mitsui, K., 'Development of a new measuring method for spindle rotation accuracy by three points method', Proc. of the 23rd MTDR, pp. 115 – 121, 1982

(Molesini et al., 1984)
Molesini, G., Pedrini, G., Poggi, P., Quercioli, F., '*Focus-wavelength encoded optical profilometer',* Opt. Comm., Volume 49, no. 4, pp. 229 – 233, 1984

(NIST, 2008)
National Institute of Standards and Technology (NIST), '*Programs of the Manufacturing Engineering Laboratory',* March 2008

(OptoNet, 2006)
OptoNet Workshop on 'Ultrapräzisionsbearbeitung von Asphären, Freiformflächen und Mikrostrukturen', Jena, 2006

(OptoNet, 2008)
OptoNet Workshop on 'Ultraprecision manufacturing of freeforms and microstructures', Jena, 2008

(O'Shea, 1985)
O'Shea, D.C., '*Elements of modern optical design*', Jonh Wiley & Sons, ISBN 0-47107796-8, 1985

(Plummer, 1982)
Plummer, W.T., '*Unusual optics of the Polaroid SX-70 Land camera*', Applied Optics, Volume 21, No. 2, pp. 196 – 202, January 1982

(Qian et al., 1995)
Qian, S., Jark, W., Takacs, P., 'The penta-prism LTP: A long-trace-profiler with stationary optical head and moving penta prisma', Rev. Sci. Instrum. 66, pp. 2562 – 2569, 1995

(Ravensbergen, 2006)
Ravensbergen, S.K., '*Probe guidance and focus drive for the NANOMEFOS optical sensor*', BSc Thesis, Technische Universiteit Eindhoven, nr. DCT 2006.127, 2006

(Ries and Muschaweck, 2002)
Ries, H., Muschaweck, J., '*Tailored freeform optical surfaces*', J. Opt. Soc. Am. A, Volume 19, No. 3, pp. 590 – 594, March 2002

(Rosielle and Reker, 2002)
Rosielle, P.C.J.N., Reker, E.A.G., '*Constructieprincipes 1*', Lecture notes 4007, Technische Universiteit Eindhoven, 2002, in Dutch

(Ruijl, 2001)
Ruijl, T.A.M., 'Ultra Precision Coordinate Measuring Machine – Design, Calibration and Error Compensation', PhD Thesis, Technische Universiteit Delft, ISBN 90-6464-287-7, 2001

(Saunders et al., 2005)
Saunders, I.J., Ploeg, L., Dorrepaal, M., Van Venrooy, B., '*Fabrication and metrology of freeform aluminium mirrors for the SCUBA-2 instrument*', Proceedings of SPIE, Optical Manufacturing and Testing VI, Volume 5869, 2005

(Savio et al., 2007)
Savio, E., De Chiffre, L., Schmitt, R., '*Metrology of freeform shaped parts*', Annals of the CIRP, Volume 56/2, pp. 810 – 835, 2007

(Schellekens et al., 1998)
Schellekens, P., Rosielle, N., Vermeulen, H., Vermeulen, M., Wetzels, S., Pril, W., '*Design for precision: current status and trends*', Annals of the CIRP, Volume 47/2, pp. 557 – 586, 1998

(Schuhmann, 2007)
Schuhmann, R., '*Aspheres in Optical Design – Chances and Limits*', Berliner Glas Technology Day on Aspheres, 2007

(Schulz and Weingärtner, 2002)
Schulz, M., Weingärtner, I., '*Free-form measurement with high lateral resolution*', Proc. of the 3rd Euspen Int. conference, pp. 621 – 624, 2002

(Schwenke et al., 2002)
Schwenke, H., Neuschaefer-Rube, U., Pfeifer, T., Kunzmann, H., '*Optical methods for Dimensional Metrology in Production Engineering*', Annals of the CIRP, Volume 51/2, pp. 685 – 699, 2002

(Shiou and Cheng, 2005)
Shiou, F.J., Cheng, W.Y., '*Development of an innovative multi-detector laser triangulation probe*', Proc. of IEEE Int. conf on Mechatronics, pp. 318 - 322, 2005

(Slocum et al., 2003)
Slocum, A., Basaran, M., Cortesi, R., Hart, J.A., '*Linear motion carriage with aerostatic bearings preloaded by inclined iron core linear electric motor*', Precision Engineering, Volume 27, pp. 382 – 394, 2003

(Smith, 2000)
Smith, S.T., '*Flexures: Elements of elastic mechanisms*', Taylor & Francis, ISBN 90-5699-261-9, 2000

(Szwedowicz, 2006)
Szwedowicz, K.K., '3D-deflectometry: fast nanotopography measurement for the semiconductor industry', PhD Thesis, Technische Universiteit Eindhoven, 2006

(Takeuchi et al., 2004)
Takeuchi, H., Yosizumi, K., Tsutsumi, H., '*Ultrahigh accurate 3-D profilometer using atomic force probe of measuring nanometer*', Proceedings of ASPE Winter Topical Meeting on Free-form optics: Design, Fabrication, Metrology and Assembly, pp. 102 – 107, 2004

(Tan and Wang, 2002)
Tan, J., Wang, F., 'Theoretical analysis and property study of optical focus detection based on differential confocal microscopy', Meas. Sci. Technol., Volume 13, pp. 1289 – 1293, 2002

(Thompson, 1989)
Thompson, D.C., '*The design of an ultra-precision CNC measuring machine*', Annals of the CIRP, Volume 38/1, pp. 501 – 504, 1989

(Ulrich et al., 2003)
Ulrich, W., Rostalski, H.J., Hudyma, R., '*The development of dioptric projection lenses for deep ultraviolet lithography*', Optical review, Volume 10, No. 4, pp. 233 – 240, 2003

(Youngworth et al., 2005)
Youngworth, R.N., Gallagher, B.B., Stamper, B.L., '*An overview of power spectral density (PSD) calculations*', Proceedings of SPIE, Optical Manufacturing and Testing VI, Volume 5869, pp. 206 – 216, 2005

(Van Amstel et al., 2007)
Van Amstel, D., Cacace. L.A., Henselmans, R., '*Optical sensor with tilt error correction',* 2007, published in EPB 2008/47, nr 1992905, 2008

(Van Beek, 2006)
Van Beek, A., '*Advanced engineering design: Lifetime performance and reliability*', Technische Universiteit Delft, ISBN 90-810406-1-8, 2006

(Van der Beek et al., 2002)
Van der Beek, N.A.J., Amstel, W.D. van, Kaathoven, D. van, Potze, W., Vermeulen, O.T.J., Breukers, M., '*Deflectometry on aspheric surfaces: a new approach and generic solution for measuring 'free form' aspheres*', Proc. of the 3rd Euspen Int. conference, pp. 657 – 660, 2002

(Van der Lee et al., 2003)
Van der Lee, N., Kappelhof, P., Hamelinck, R., '*Flexure based alignment mechanisms: Design, development and application*', Proc. of SPIE, Vol. 5176, , pp. 94 – 107, 2003

(Van Eijk, 1985)
Van Eijk, J., '*On the design of plate-spring mechanisms*', PhD Thesis, Technische Universiteit Delft, 1985

(Van Seggelen, 2007)
Van Seggelen, J.K., 'NanoCMM – A 3D Coordinate Measuring Machine with low moving mass for measuring small products in array with nanometer uncertainty', PhD Thesis, Technische Universiteit Eindhoven, ISBN 90-386-2629-0, 2007

(Van Veggel, 2007)
Van Veggel, A.M.A., '*The basic angle monitoring system: picometer stability with Silicon Carbide optics*', PhD Thesis, Technische Universiteit Eindhoven, ISBN 978-90-386-0874-7, 2007

(Van Venrooy and Ploeg, 2005)
Van Venrooy, B., Ploeg, L., TNO I&T, *Personal communication*, 2005

(Vermeulen, J., 1999)
Vermeulen, J.P.M.B., '*Ceramic Optical Diamond Turning Machine – Design and Development*', PhD Thesis, Technische Universiteit Eindhoven, ISBN 90-5282-954-3, 1999

(Vermeulen, M., 1999)
Vermeulen, M.M.P.A., '*High-Precision 3D-Coordinate Measuring Machine – Design and Prototype-Development*', PhD Thesis, Technische Universiteit Eindhoven, ISBN 90-386-2631-2, 1999

(Visscher, 1992)
Visscher, M., 'The measurement of the film thickness and the roughness deformation of lubricated elastomers', PhD Thesis, Technische Universiteit Eindhoven, 1992

(Walker et al., 2001)
Walker, D.D., Brooks, D., Freeman, R., King, A., McCavana, G., Morton, R., Riley, D., Simms, J., '*The first aspheric form and texture results from a production machine embodying the precession process*', Proc. of SPIE 46th Annual Meeting, San Diego, Vol. 4451, pp. 267 – 276, 2001

(Wanders, 2006)
Wanders, G., '*Advanced techniques in freeform manufacturing*', presented at OptoNet Workshop, 2006

(Weckenmann et al., 2006)
Weckenmann, A., Peggs, G., Hoffmann, J., '*Probing systems for dimensional micro- and nano-metrology*', Meas. Sci. Technol. 17, pp. 504 – 509, 2006

(Welford, 1986)
Welford, W.T., '*Aberrations of optical systems*', Hilger, ISBN 0-95274-564-8, 1986

(Whitehouse, 1976)
Whitehouse, D.J., 'Some theoretical aspects of error separation techniques in surface metrology', J. of Physics E, Vol. 9, 1976

(Whitehouse, 1994)
Whitehouse, D.J., '*Handbook of surface metrology'*, Bristol: Institute of Physics, ISBN 0-7503-0039-6, 1994

(Winsor et al., 2004)
Winsor, R., Ohl, R. Connelly, J.A., MacKentry, J.W., '*Optical design of an Infrared Mutli-Object Spectrometer utilizing free-form optical surface*', Proc. ASPE Winter Topical Meeting on Free-form optics: Design, Fabrication, Metrology and Assembly, pp. 79-83, 2004

(Zänkert, 2008)
Zänkert, J., '*Freeform optics for display technologies*', Presented at OptoNet Workshop, 2008

(Zanoni, 1989)
Zanoni, C., 'Differential interferometer arrangements for distance and angle measurements: principles, advantages and applications', VDI Berichte, nr 749, pp. 93 – 106, 1989

(Zhang et al., 1997)
Zhang, G.X., Zhang, Y.H., Yang, S.M., Li, Z., '*A Multipoint method for spindle error motion measurement*', Annals of CIRP, Vol. 46/1, pp. 441 – 445, 1997

(Zhang and Cai, 1997)
Zhang, J., Cai, L., '*Profilometry using an optical stylus with interferometric readout*', Meas. Sci. Technol., Volume 8, pp. 546 – 549, 1997

Websites:

www1 en.wikipedia.org/wiki/Black_body#Radiation_emitted_by_a_human_body
www2 www.aerotech.com
www3 www.airbearings.com
www4 www.aksteelbv.com
www5 www.bakkermagnetics.com
www6 www.botechbv.com
www7 www.coorstek.com
www8 www.heidenhain.com
www9 www.ibspe.com ⇒ Isara
www10 www.lionprecision.com
www11 www.matweb.com
www12 www.metrologic.fr
www13 www.newwayairbearings.com
www14 www.nanotech.com
www15 www.precitech.com
www16 www.qedmrf.com
www17 www.sios.de ⇒ nmm
www18 www.spiroflex.com (formerly known as Tensator)
www19 www.stilsa.com
www20 www.taylor-hobson.com ⇒ PGI 1240
www21 www.tecnotion.com
www22 www.zeeko.co.uk
www23 www.zeeko.co.uk ⇒ Metrology Toolkit
www24 www.zeiss.com
www25 www.zeiss.com ⇒ Holos NT
www26 www.zygo.com ⇒ VeriFire

Appendix A

Current fabrication methods

This appendix describes the current fabrication methods for aspherical and freeform optics. First, the limitations of classical polishing methods will be explained, after which the freeform manufacturing process chain will be shown. Next, diamond turning and local polishing techniques are explained.

Classical polishing

A unique feature of spherical surfaces is that a convex and concave spherical part with the same radius can be brought into full contact in any orientation. High accuracy spherical optical surfaces have been produced for centuries by simple tools such as shown in Figure A.1 (Karow, 1993). The surfaces are polished by randomly moving the spherical tool over a spherical glass part with the same radius, separated by an abrasive. Although the tool is not perfectly spherical, the random motion evens out this error, resulting in a highly spherical surfaces. By attaching multiple small lenses to a pitch or spot block, many elements can be produced in one run.

Parabolic surfaces have been generated with these techniques by varying the tool speed and dwell time as a function of the radial position. General aspherical and freeform surfaces can, however, not be produced using these methods.

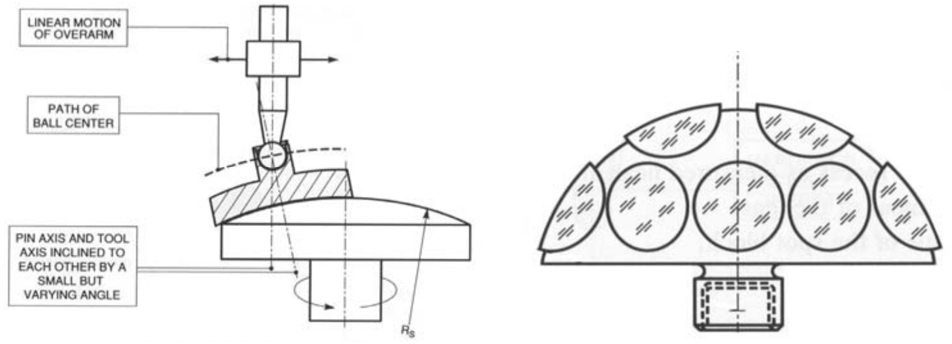

Figure A.1: Polishing of spherical optics (left) and spot block (right) (Karow, 1993)

Process chain

Aspherical and freeform optics are generally manufactured according to the process steps of Figure A.2. The machining methods are different for ductile and brittle materials. A blank is pre-machined first by conventional 5-axis milling or grinding machines, and then coarsely measured by a spherometer or a CMM. The surface is now within a few tens of micrometers of the desired form, but still opaque. The surface is given optical quality by fine-machining, after which a precision measurement is performed. The surface is now re-machined to correct the form error. This process is iterated until the desired form is obtained, after which a coating may be applied.

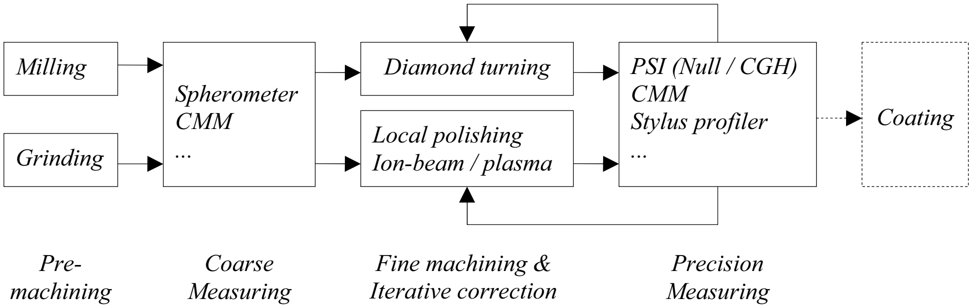

Figure A.2: General aspherical and freeform optics process chain

Diamond turning

Non-ferro metals and some ceramics can be diamond turned. Aspheres with any cross-section can be generated relatively easy this way. For freeforms, the diamond tool is actuated during each revolution by a slow- or fast-tool servo (Wanders, 2006). The resulting surface form is determined by the guidance errors, servo errors and tool wear. Since these errors are to some extend reproducible, they can be compensated for by correcting the tool path with measurement data. In diamond machining, about 10 µm has to be removed from the entire surface in each subsequent cut, so local correction is not possible. The whole surface has to be machined again. This iterative process is repeated until the desired surface form is obtained.

In Figure A.3 a Precitech Nanoform 350 diamond turning machine is shown that is present at the TNO Optical Workshop. On this particular machine, an air bearing LVDT probe has been added to perform on-machine measurements. The machine controls have hereto been adapted to allow for indexing of the spindle, which results in a cylindrical CMM setup. With this contact probe, a 500 mm diameter surface can be measured in several hours, with an uncertainty of approximately 2-5 µm. Despite the long measurement time and moderate accuracy, this method does provide useful information without dismounting the product.

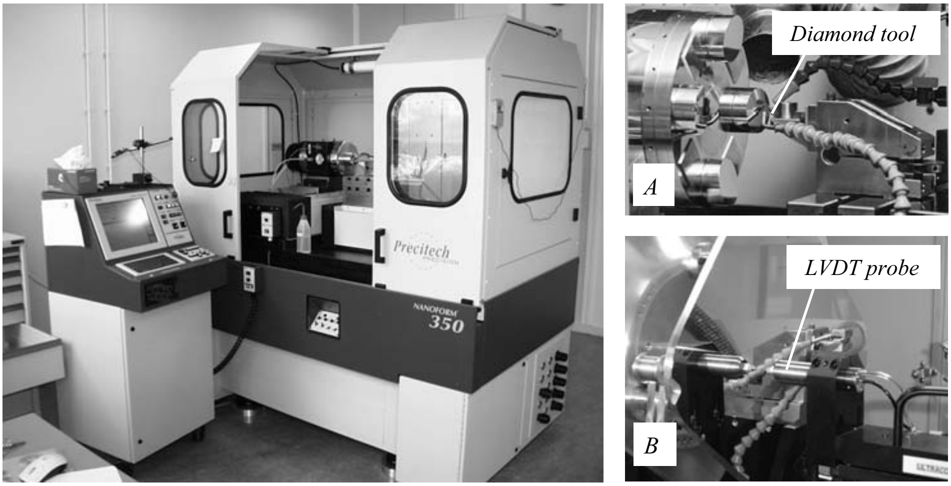

Figure A.3: The Precitech Nanoform 350 diamond turning machine at TNO, manufacturing of off-axis parts (A), and on-machine LVDT probe (B)

Local polishing and ion beam / plasma machining

Grinding causes sub-surface damage, which are micro-cracks up to tens of micrometers deep. This layer first has to be polished away. After the first precision measurement, local polishing techniques are applied to correct the form. Examples are the Zeeko Precessions^{tm} process (Walker et al., 2001), the QED Magneto Rheological Finishing technique (Dumas et al., 2004) or ion-beam and plasma machining (Frost et al., 2001). These local polishing techniques have a typical influence function, which allows for deterministic material removal. With the real and desired form, combined with the characteristic influence function of the method, the machining path (dwell time, speed, pressure etc.) can be determined. Currently, these deterministic polishing techniques predict material removal to approximately 90% accuracy (Walker et al., 2001). To obtain the desired surface form, an iterative loop of measuring and local corrective machining is required.

For optics up to 200 mm and 500 mm, standard universal production equipment is commercially available (www14, 15, 16, 22). For the larger mirrors, dedicated instruments have been built (Martin et al., 2003).

In Figure A.4 (left) a Zeeko IRP 600 polishing robot is shown that is present at the TNO Optical Workshop. This machine polishes locally, either with a Fluid Jet setup, or with a rotating inflatable bonnet (Figure A.4, right).

Figure A.4: Zeeko polishing robot (with FJP setup) at TNO, and classical bonnet polishing close-up

Appendix B

Current metrology methods

In every fabrication process, the achievable result is only as good as the measurement method. For a high-end, single piece, freeform optics production environment, important characteristics of a measurement method are high accuracy, universal, non-contact, large measurement volume and short measurement time. Many techniques, experimental as well as commercial, exist for measuring optics. In this appendix, an overview of the existing methods will be given with respect to the mentioned characteristics.

A recent overview of measuring general freeform surfaces, ranging from car body parts to turbine blades to optics, is given by (Savio et al., 2007). Figure B.1 shows the parts and measurement methods discussed in this paper in a Stedman diagram. The surfaces as meant in this thesis are situated in the dotted area.

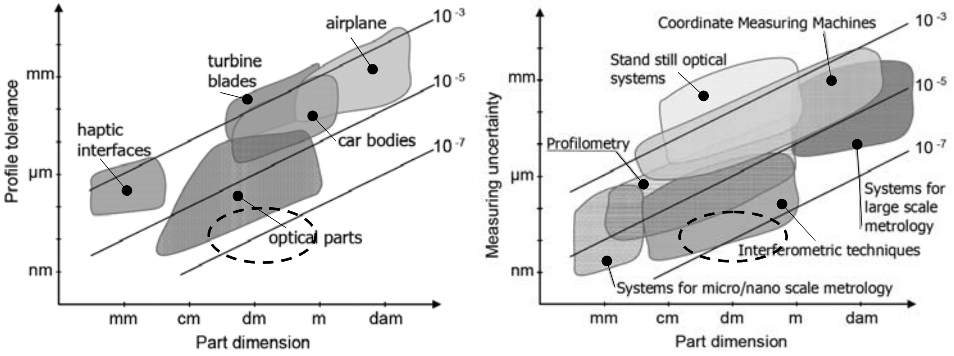

Figure B.1: General freeform parts and measurement methods (source: Savio, 2007)

Methods specifically suitable for measuring freeform optics can be divided into *'imaging'* and *'scanning'* techniques, and will be further explained in the next sections.

B.1 Imaging techniques

Imaging techniques measure the surface as a whole at once, and are therefore fast and non-contact. Phase-Shifting Interferometry, Null/CGH tests, Stitching interferometry and fringe projection will be discussed.

Phase- Shifting Interferometry

With a Fizeau interferometer, an interferogram is produced by combining the reflected wavefront of a reference surface and the wavefront coming from the surface to be measured (Figure B.2, left). The distance between the fringes of the interferogram represents exactly one wavelength optical path difference (OPD) between the beams, and thus half a wavelength departure between the reference surface and the surface to be measured.

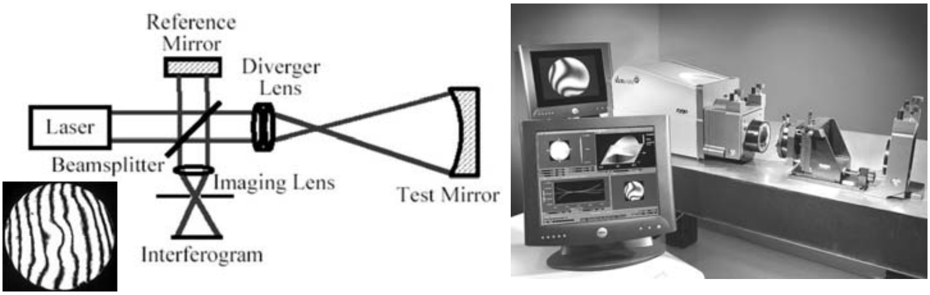

Figure B.2: Schematic Fizeau interferometer setup (left) and Phase-shifting Interferometer (right, source: www26)

By applying phase-shifting, the direction of the height difference can be derived. Phase-Shifting Interferometry (Figure B.2, right) currently is the work horse for measuring flat and spherical optics. An extensive overview of many interferometry based techniques is given in (Malacara, 2007). The entire surface is imaged at once, measuring it in seconds without contact. With a calibrated reference surface and proper measurement conditions, uncertainty can be of (sub)nanometer order (Dörband and Seitz, 2001). Apertures are generally around 100 mm, but some larger setups exist.

When the departure between the reference and test surface increases, the number of fringes also increases. With a 1k x 1k CCD, up to a few hundred fringes can be resolved, which limits the departure from spherical to some tens of micrometers.

Null correctors and Computer Generated Holograms

When measuring an asphere or freeform with too much departure from the reference wavefront, the reference can be matched to the surface under test by using a correction element such as a null lens or Computer Generated Hologram (CGH) (Burge and Wyant, 2004), as schematically shown in Figure B.3. These elements have to be specially designed and manufactured for each specific surface shape.

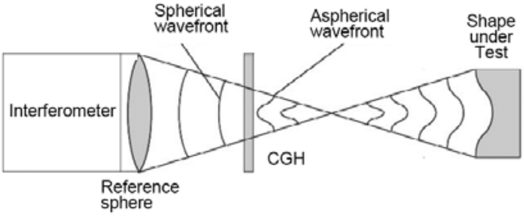

Figure B.3: Schematic principle of a CGH (source: (Savio, 2007))

Traceability of the measurement is hard to obtain, since the correction elements cannot be calibrated and alignment is crucial. This method is therefore mainly applicable for large series or optics where tool cost is of secondary interest.

Stitching

Another way of reducing the number of fringes on the detector is by decreasing the aperture. By imaging multiple sub-apertures of the surface (Figure B.4), and numerically stitching these together, a complete surface area measurement can be obtained (Dumas et al., 2004). When the departure is in the order of millimeters, the amount of sub-apertures that is required increases rapidly, along with the measurement time. The absolute dimension (scale), position and tilt of each sub-aperture must be known accurately to prevent stitching errors. This limits the applicability for parts with large departure from spherical.

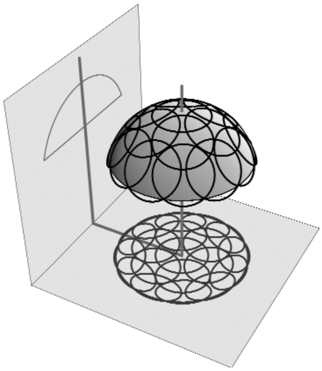

Figure B.4: Stitching interferometry principle (source: www16)

Fringe projection

In this method, fringes are projected from a tv-screen onto a surface under test (Figure B.5). The slope variation over the surface causes variation in the distance between the fringes, as recorded by a camera. By phase-shifting the fringes, the surface slope direction is deduced, and translated to a height profile. This method is mainly being applied for progressive spectacle glasses. An absolute height measurement uncertainty of 200 µm and a measured curvature variation of 0.01 dpt (20 nm over 3 mm) are reported (Knauer et al., 2004).

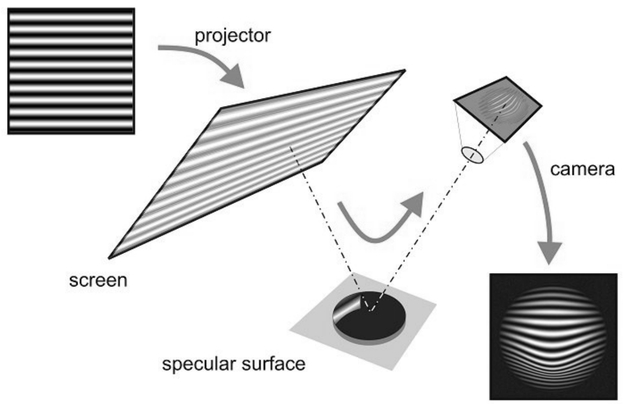

Figure B.5: Fringe projection (Knauer et al., 2004)

B.2 Scanning techniques

Scanning methods measure a surface point by point, making them universal and scalable to the required measurement volume. Stylus profilometers, Coordinate Measuring Machines, Swing arm profilometers and slope and curvature measurement systems will be discussed.

Stylus profilometers

A stylus profilometer (Figure B.6) performs a 2D line scan with a diamond or ruby tipped stylus (Whitehouse, 1994). This is currently the most commonly applied method for measuring aspheres. For measuring freeforms, a transverse stage is added. In 2D mode, the uncertainty can be in the order of several tens of nanometers.

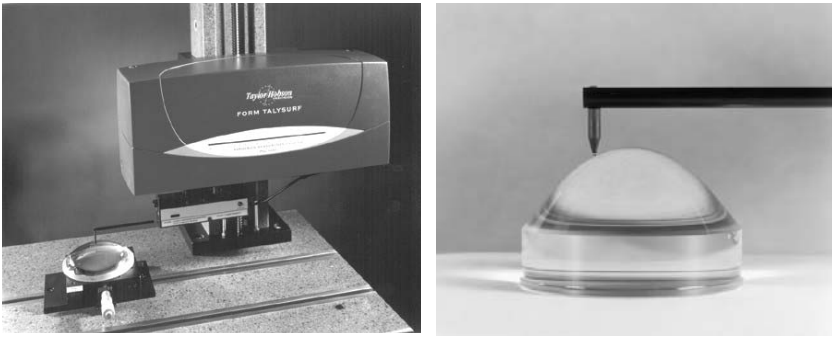

Figure B.6: Stylus profilometer (www20)

The measurement length is limited to about 200 mm, and the vertically allowed sag is in the order of 20 mm. The contact stylus requires slow scanning speeds (~10 mm/s) and has the risk of damaging the surface. Transverse inclined surfaces further give rise to torsional deflection errors in the stylus arm and bending of the stylus itself.

Coordinate Measuring Machines

True 3D measurements are done with a coordinate measuring machine (CMM). A touch trigger probe is brought into contact with the surface under test, and the position of the three orthogonal axes and the readout of the probe are recorded. Conventional portal CMMs (Figure B.7), have a large measurement volume combined with micrometer order uncertainty. These are currently the most applied instruments for measuring freeform parts.

Figure B.7: Coordinate Measuring Machine (www24)

Conventional portal CMMs are limited by Abbe errors (Abbe, 1890). In (Vermeulen, M., 1999) and (Van Seggelen, 2007), intermediate bodies are introduced in the guidance setup to keep the linear scales aligned to the probe tip, eliminating the Abbe offset in the horizontal plane (Figure B.8). The Zeiss F25 (www24) is a follow up of (Vermeulen, M., 1999).

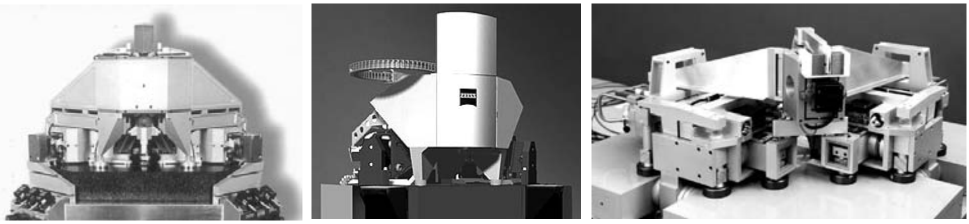

Figure B.8: Scale based CMMs without Abbe offset in the horizontal plane (from left to right: (Vermeulen, M, 1999), (www24) and (Van Seggelen, 2007)

In (Ruijl, 2001; Jäger et al., 2001) laser interferometers are used that are orthogonally aligned to a stationary probe tip, and are measuring to a moving mirror block on which the product is mounted (Figure B.9). These machines are commercialized by IBS PE (www9) and SIOS (www17), respectively. In (Becker and Heynacher, 1987) fixed reference mirrors are applied and the laser interferometers emanate from the moving probe. These setups all meet the Abbe principle in the 3 orthogonal directions. The measurement volume is mainly limited by the size of the reference mirrors. The measurement volume of these CMMs is generally less than 1 dm^3, and uncertainties in the order of several tens of nanometers are reported. The CMM of (Becker and Heynacher, 1987) has a measurement volume of 400x600x200 mm.

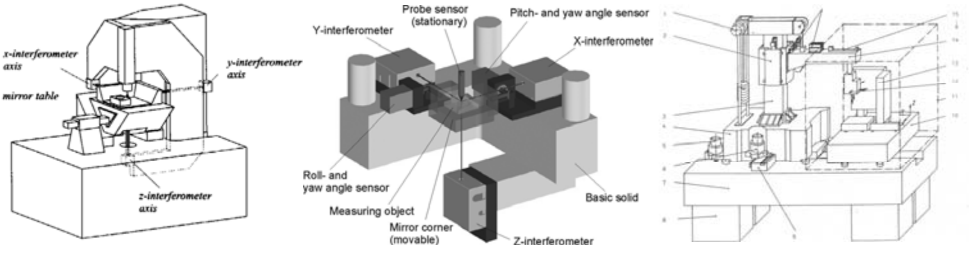

Figure B.9: CMMs with laser interferometry (from left to right: (Ruijl, 2001), (Jäger et al., 2001) and (Becker and Heynacher, 1987))

Contact trigger probes (Weckenmann et al., 2006) are employed to detect the surface, since the orthogonal setup makes application of an optical non-contact probe difficult for surfaces with slopes of more than a few degrees. In (Takeuchi et al., 2004) an

Atomic Force Probe is used (Figure B.10), in combination with interferometers and stationary reference mirrors. It is kept at a constant distance from the surface, resulting in a semi-contact measurement. A vertical interferometer measures the vertical displacement of the probe relative to a horizontal reference mirror.

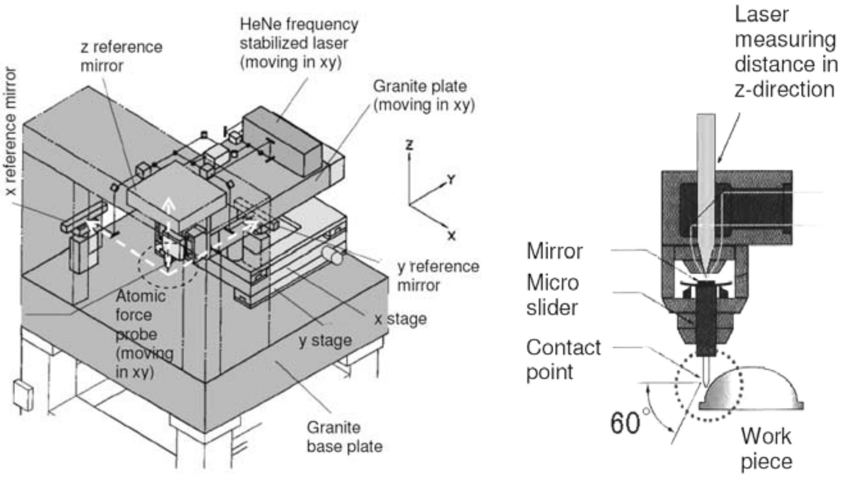

Figure B.10: CMM with AFM probe (Takeuchi et al., 2004)

Although the surface is not contacted, scanning speeds are still limited to mm/s, leading to measurement times of many hours for large surfaces. Due to the orthogonal setup, measurement uncertainty rapidly increases with surface inclination (Figure B.10, right). This machine is available with a measurement volume of 400 x 400 x 90 mm, and has a specified measurement uncertainty of around 0.3 µm when measuring to 45° inclined surfaces.

Swing arm profilometers

All CMMs described above have orthogonal axes of motion and can therefore not keep the probe perpendicular to inclined surfaces. For spherical surfaces this can be realized with a swing-arm or polar setup (Figure B.11). Here the product is mounted on a rotation stage. The probe is mounted to an arm that can be rotated on another rotation stage, such that the probe is coaxial with the centre line of the product at the zero position. When the centre lines of both rotation stages intersect at the centre of curvature of the surface to be measured, the probe describes a circle that coincides with the surface and stays perpendicular to it.

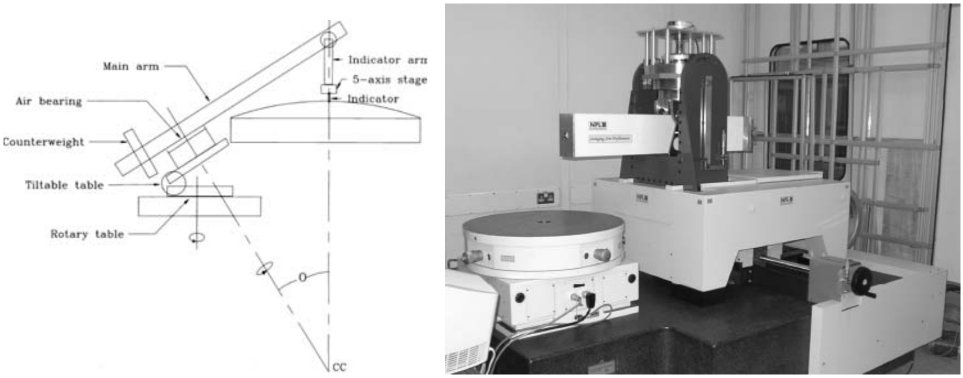

Figure B.11: Swing arm schematic (Anderson and Burge, 1995) and setup (Callender et al., 2006)

The orientation of the rotation axis of the arm has to be aligned to the centre of curvature of the product. This alignment is difficult since the probe is to be aligned with a non-physical point in space. During scanning, the arm is subject to varying gravitational deflection. Swing-arm profilometry is applied by (Anderson and Burge, 1995) and (Callender et al., 2006) for measurement of telescope primary mirrors and mirror segments.

Slope measurement

Slope measurement with a miniature autocollimator, also called a deflectometer, is applied in (Van der Beek et al., 2002, Szwedowicz, 2006). An autocollimator and moving pentaprism are used in a Long Trace Profiler (Qian et al., 1995) for measuring synchrotron optics. The surface slope relative to the sensor is measured, which inherently requires the tilt of the sensor to be known accurately. By integrating the inclination data, the surface form is obtained. Measurement noise and other non-repeatable errors are eliminated by using a multi-path integration algorithm. Systematic errors in inclination as well as positioning of the sensor have to be calibrated. A full scan of the surface must always be made; quickly measuring some points for alignment or checking is not possible, due to the required integration.

Slope difference and Curvature measurement

Slope difference measurement (Geckeler and Weingärtner, 2002) and curvature scanning (Schulz and Weingärtner, 2002; Machkour et al., 2006) determine surface form from integrating surface slope difference and local curvature, respectively. These two properties can be measured independently from an outside reference. Although the location of the measurement points on the surface must be known, this somewhat relaxes the requirements for the positioning system of the sensor. Similar to slope measurement, a full surface scan must always be made. The slope difference method of PTB is mainly applied for flat surfaces and uses an autocollimator and a moving pentaprism as a sensor. The curvature scanning method of PTB and NIST utilizes a miniature interferometer which is mounted on a positioning system. Measuring freeform surfaces with millimetre order departure from spherical requires sensors with a much larger dynamic range.

B.3 Conclusion

Many commercial and experimental techniques exist that can be used for measuring optics. No single method yet incorporates the five characteristics (high accuracy, universal, non-contact, large measurement volume and short measurement time) desired for measuring single piece high precision freeform surfaces as described in section 1.1.3. This lack of a suitable metrology method is currently holding back the common application of high-precision aspherical and freeform optics.

Appendix C

Brake stiffness calculation

During measurement of the circular tracks, the stages are locked mechanically. The stiffness of the brake callipers and the contact is calculated and tested in this appendix, based on (Aerts, 2007).

The stiffness of the brake (Figure C.1, left) is determined by the shear stiffness of the hinge, but the hinge also has to withstand the tensile reaction force of the clamping force. Two wide half cross-hinges (hinge 1) are therefore applied that are attached to the fixed centre piece. For maximum hinge shear stiffness, relatively short and thick hinge plates are used. To cope with the high resulting stresses, 34CrNiMo6 is used with a yield stress of 900 N/mm^2.

The rotation stiffness of this hinge can be calculated with (Van Eijk, 1985; Boneschanscher, 1995):

$$k_\psi = 2\frac{EI}{l}(12\lambda^2 + 1) \quad with \quad \lambda = \frac{1}{2} + \frac{R}{l} \tag{C.1}$$

$$\sigma_\psi = \psi\frac{Eh}{2l}(1 + 6|\lambda|) \tag{C.2}$$

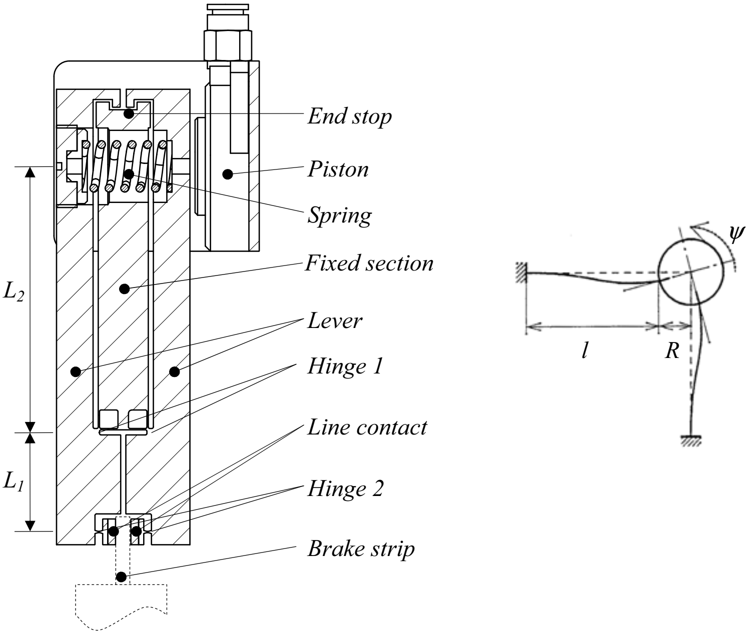

Figure C.1: Brake calliper and cross hinge

With the plate spring thickness h of 0.25 mm, the length l of 3 mm and the width w of 80 mm, the resulting bending stiffness per lever is 55 Nm/rad. The lever ratio is 2.5 with an upper length L_1 of 50 mm and a lower length L_2 of 20 mm (see Figure C.1). To open the clamp 0.2 mm requires a rotation of 0.01 rad and thus 11 N at the piston. The maximum occurring stress in this rotation is 333 N/mm^2. The spring is preloaded with 80 N, which delivers a force of 200 N at the contact. This force results in a tensile stress in hinge 1 of 12 N/mm^2.

The stiffness of the clamp is composed of the shear and bending stiffness of hinge 1, given by (C.3) and (C.4), the shear stiffness of hinge 2 (C.7) and the contact stiffness. With a width w_1 of 80 mm, the shear stiffness of hinge 1 is equal to $1.0 \cdot 10^9$ N/m:

$$c_{1,shear} = \frac{2 G h w_1}{l} \qquad \text{C.3)}$$

Similarly, the bending stiffness of hinge 1 at the contact is $1.8 \cdot 10^9$ N/m:

$$c_{1,bend} = \frac{E h w_1^3}{12 L_1^2 l} \qquad \text{C.4)}$$

The shear stiffness of hinge 2 can be calculated by approximating the hinge with an equivalent beam element. With the hinge hole diameter D being 3 mm and the hinge width w_2 being 20 mm, the stiffness is equal to $3.7\cdot10^{8}$ N/m.

$$c_{2,shear} = \frac{G\,w_2}{1.2}\sqrt{\frac{h}{D}} \tag{C.5}$$

The properties of the line contact can be calculated with formulas (C.6) – (C.13) (Johnson, 1985). With Young's modulus E and Poisson's ratio ν, the contact modulus E_c is equal to (C.6). The brake strip material is stainless steel ($E = 2\cdot10^{11}$ N/m^2, $\nu = 0.3$) and the cylinder contacts are manufactured from Tungsten Carbide ($E = 6\cdot10^{11}$ N/m^2, $\nu = 0.3$), giving a contact modulus of $1.6\cdot10^{11}$ N/m^2.

$$\frac{1}{E_c} = \frac{1-\nu_1^2}{E_1} + \frac{1-\nu_2^2}{E_2} \tag{C.6}$$

With the local radius of curvature R of 15 mm, the contact radius R_c also is 15 mm (C.7).

$$\frac{1}{R_c} = \frac{1}{R_1} + \frac{1}{R_2} \tag{C.7}$$

The clamping force F is 200 N over 5 mm contact length, giving a line load P of $1\cdot10^{4}$ N/m. The half width b of the contact is calculated with (C.8), and is in this case equal to 68 µm:

$$b = \sqrt{\frac{4PR_c}{\pi E_c}} \tag{C.8}$$

The Hertzian contact stress σ_{Hz} (C.9) is 374 N/mm^2. The maximum shear stress is equal to 0.3 times the Hertzian contact stress (Johnson, 1985), or 112 N/mm^2, which is sufficiently lower than 58% of the yield strength of the strip material.

$$\sigma_{Hz} = \sqrt{\frac{PE_c}{\pi R_c}} \tag{C.9}$$

To calculate the tangential stiffness, the contact is approximated with an elliptical contact with major radius a and minor radius b. The contact shear modulus G_c is calculated with (5.12) and equal to $3.4\cdot10^{10}$ N/m^2.

$$\frac{1}{G_c}=\frac{2-\nu_1}{G_1}+\frac{2-\nu_2}{G_2} \tag{C.10}$$

With friction coefficient μ and tangential force T, the tangential displacement δ is equal to:

$$\delta=\frac{3\mu F}{16aG_c}\left\{1-\left(1-\frac{T}{\mu F}\right)^{\frac{2}{3}}\right\}\Phi \tag{C.11}$$

The tangential stiffness of the contact $c_{t,contact}$ is now given by:

$$c_{t,contact}=8aG_c\left(1-\frac{T}{\mu F}\right)^{\frac{1}{3}}\frac{1}{\Phi} \tag{C.12}$$

Where the correction factor Φ is equal to:

$$\Phi\cong\begin{cases}1+\left(1.4-0.8\nu\right)\log\left(\dfrac{a}{b}\right) & for \quad T\,//\,b\\ 1 & for \quad a=b\\ 1+\left(1.4+0.8\nu\right)\log\left(\dfrac{a}{b}\right) & for \quad T\,//\,a\end{cases} \tag{C.13}$$

The half contact width a is equal to 2.5 mm, and the friction coefficient μ is estimated to be 0.1. Figure C.2 shows the tangential stiffness of a single contact. For small disturbing forces, the tangential stiffness is equal to $2.4\cdot10^8$ N.

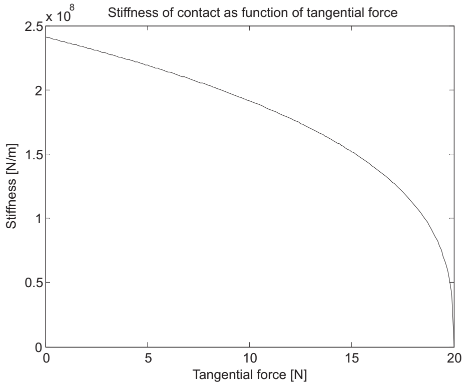

Figure C.2: Tangential stiffness of brake contact

The total static stiffness of the two arms of the brake clamp is a series combination of the stiffness calculated in (C.3) – (C.5) and the contact stiffness (C.12). With the above calculated results, the total brake stiffness c_{brake} is equal to $2.4 \cdot 10^{8}$ N/m.

$$\frac{1}{c_{brake}} = \frac{1}{2c_{1,s}} + \frac{1}{2c_{1,b}} + \frac{1}{2c_{2,s}} + \frac{1}{2c_{contact}} \tag{C.14}$$

The tangential displacement as a function of a tangential force was already given in (C.11). When this force is increased up to T_1 and is then decreased to T again, the displacement for the decreasing force is given by:

$$\delta_d = \frac{3\mu P}{16 a G_c}\left\{ 2\left(1 - \frac{T_1 - T}{2\mu P}\right)^{\frac{2}{3}} - \left(1 - \frac{T_1}{\mu P}\right)^{\frac{2}{3}} - 1 \right\}\Phi \tag{C.14}$$

Setting the force T to zero gives the hysteresis half width δ_h of the contact after being loaded up to T_1:

$$\delta_h = \frac{3\mu P}{16 a G_c}\left\{ \frac{1}{18}\left(\frac{T_1}{\mu P}\right)^{2} + \frac{1}{27}\left(\frac{T_1}{\mu P}\right)^{3} \right\}\Phi \tag{C.16}$$

Figure C.3 shows the hysteresis curves of a single contact after being loaded to 5, 10, 15 and 20 N. This gives a hysteresis of 0.5, 2.6, 8.1 and 32 nm respectively.

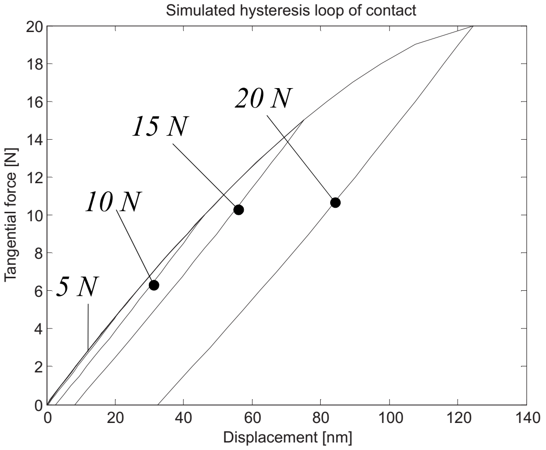

Figure C.3: Hysteresis of brake contact

The stiffness and hysteresis were tested in a test setup (Figure C.4). The stiffness was measured to be $5 \cdot 10^7$ N/m, which is significantly lower than expected. Examination showed that the supposed 'rigid' world of the experiment has a stiffness similar to the brake. Since the mounting stiffness is difficult to improve, this measured stiffness of $5 \cdot 10^7$ N/m will be used for further calculations in the coming sections.

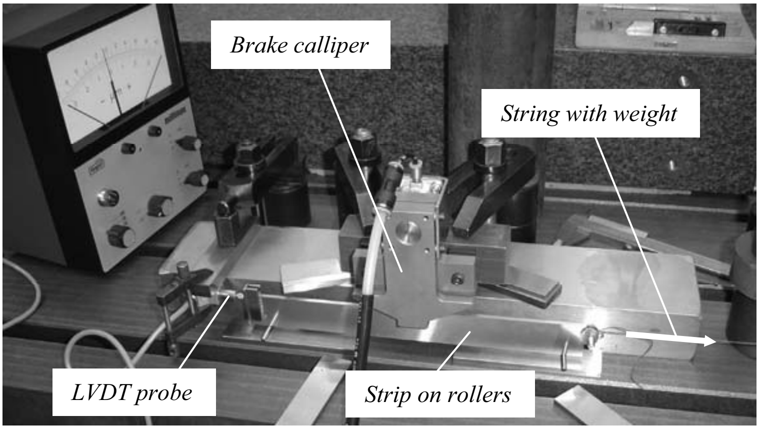

Figure C.4: Brake test setup

Macro-slip will occur at around 20 N, and the small amounts of hysteresis are difficult to measure. The amount of hysteresis certainly was not larger than the calculated values. These tests were repeated with the R-stage of the machine, on air bearings and with a more sensitive linear encoder, but no repeatable hysteresis loop could be measured. The hysteresis of the brake is thus sufficiently low.

Appendix D

Intermediate body concept

To allow for quick and reproducible changing between manufacturing and measurement machine, the product may be mounted to an intermediate body. This minimizes alignment and product handling. A conceptual design is given in this appendix.

Six rows of the M5 holes in the product mounting table start with a conical section. A sphere (1 in Figure D.1) can be bolted into this conical seat. An intermediate body with three axial (2) and three tangential contact points (3) on 3 teeth (4) may now be placed onto the machine with a few micrometers repeatability. A ring (5) with 3 springs (6) can be mounted over the contact points to provide a constant preload force on the contacts. Providing the manufacturing machines with a similar interface may allow for fast changing between measuring and machining with minimal intermediate alignment. It also prevents handling the product and the associated thermal disturbance.

As explained in Appendix A, diamond turning requires a minimal depth of cut of several micrometers, and lateral positioning of a polishing pad is only accurate to up to some hundredth of a millimeter. Reproducibility is therefore not extremely critical. Reference fiducials may further be placed on the intermediate body to obtain the surface position relative to the intermediate body or to verify alignment.

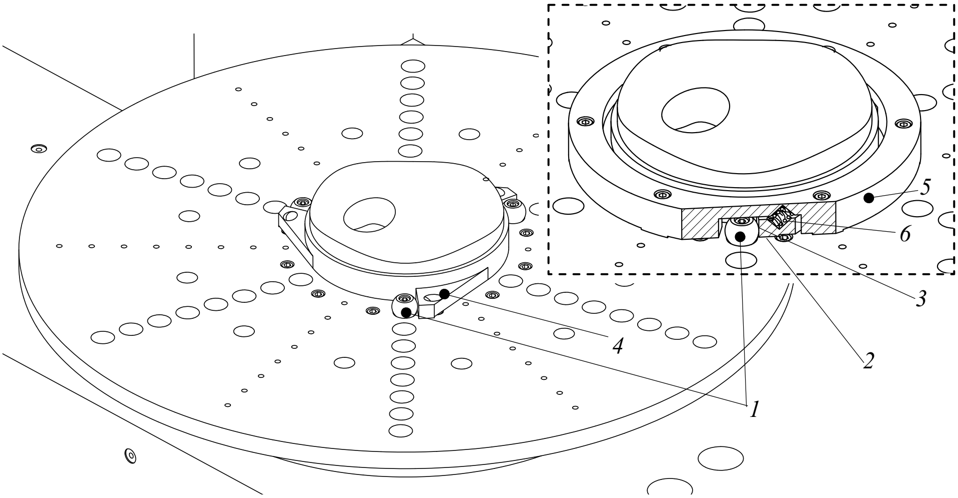

Figure D.1: Intermediate body concept

Appendix E

Motion system stiffness and eigenfrequencies

During assembly, intermediate stiffness tests have been done. The first part of this appendix describes the results and the differences with the calculated values. Next, the eigenfrequency results of section 3.8.2 are analyzed and differences with the calculations are explained.

E.1 Stiffness measurements

The stiffness of the motion system has been measured for several components. The bearing properties were already measured in a separate test setup (section 3.1.2). In the machine, a mean air gap of 10 µm at a supply pressure of 5.5 bar was measured, showing that all bearings operate properly.

The stiffness of the R-brake has been measured by pushing a force gauge against the side of the stage, while measuring the displacement with the R-stage encoder. A stiffness of $4 \cdot 10^7$ N/m was determined this way. The stiffness of the brake alone was measured to be $5 \cdot 10^7$ N/m, and some stiffness is lost in the connection between the brake strip and the R-stage position frame. With the total stage mass of 275 kg, the measured stiffness should give an eigenfrequency in *r*-direction of 60 Hz.

The vertical stiffness at the Z-brake mounting point, i.e. the structural loop including the R-stage position frame bending stiffness and the vertical bearings stiffness, was measured by setting mass on top of the R-stage, while measuring the displacement at the read-head arm mounting point. A stiffness of $4.4 \cdot 10^7$ N/m was measured. The Z-brake stiffness is $5 \cdot 10^7$ N/m, so the vertical stiffness at the clamping point is $2.3 \cdot 10^7$ N/m.

To measure the entire vertical structural loop from probe tip to base, weights were applied on the top of the Alumina tube and the displacement was measured at the probe tip. This way, the Z-brake stiffness, R-stage position frame bending stiffness and R-stage bearings stiffness and all connections are in the loop. The measured stiffness is $1.8 \cdot 10^7$ N/m, which gives a vertical resonance at 73 Hz for the 85 kg vertically moving mass.

To measure the stiffness in y-direction at the Z-stage lower interface, onto which the Ψ-axis mount is bolted, a force gauge was pushed against this interface while the displacement was measured with a capacitive probe. The measured stiffness was $2.1 \cdot 10^7$ N/m. A part of this stiffness is the connection between the bearing bridge and the interface, which was measured to be $5.3 \cdot 10^7$ N/m.
The probe and Ψ-axis are connected to this interface on the Z-stage position frame. The Z-stage force frame has its own connection to the bearings, so this is not taken into account here. The top bearing is taken as the rotation point here, since most of the mass is concentrated around the lower bearings. The inertia of the Z-stage, excluding the force frame, is 7.6 kgm^2, and 11.4 kgm^2 when rotating around the top bearing. The distance between the interface and the top bearing is 595 mm, so the tilting stiffness around the top bearing is equal to $7.5 \cdot 10^6$ Nm/rad. This gives an eigenfrequency of 129 Hz which is mainly present in y and slightly in z-direction

During assembly of the Ψ-axis bearing, the stiffness of a single thrust bearing was measured to be $1.8 \cdot 10^8$ N/m. The calculated stiffness is $1.2 \cdot 10^8$ N/m, so the slightly smaller air gap also gives higher stiffness. The air gap of the Ψ-axis radial bearing was measured by shutting off the air and measuring the radial displacement. The lift was measured to be 4.5 µm, but about 2 µm roundness error is present in the bearing ring. The average air gap is probably slightly smaller than the desired 7 µm, which may also explain the higher stiffness.

E.2 Eigenfrequency measurements

Figure E.1 shows the harmonic content of the measurements as shown in section 3.8. The most significant peaks are numbered. The source of each peak is investigated and differences with the calculated values are explained.

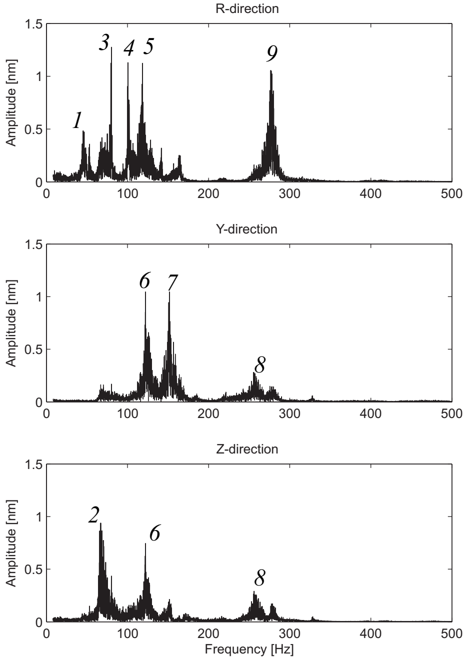

Figure E.1: Harmonic content of relative probe tip to spindle displacement

Initially, much higher vibration levels were found. After investigating this, it appeared that the air supply line that supplied the stages was too thin, resulting in very turbulent flow. The acoustic noise from this flow excited the preload frame resonances, which in turn excited the position frames. After increasing the tube diameter, most of the noise was removed.

By turning the air of individual stages on and off, and by blocking the air to individual bearings, it was attempted to address each frequency;

1. ***46 Hz in R.*** This is the whole stage assembly (275 kg) resonating on the R-brake stiffness. 68 Hz was estimated and 60 Hz was calculated from the stiffness measurement.
2. ***67 Hz in Z.*** This is the Z-stage resonating on the vertical structural loop stiffness. Here, 91 Hz was calculated theoretically and 73 Hz was calculated from the stiffness measurements.

3. – 5. ***80 Hz, 100 Hz and 118 Hz in R.*** These are probably 1st and 2nd resonances of the R-stage preload frame and the 1st resonance of the Z-stage preload frame, which were calculated at 68, 73 and 84 Hz. These particular resonances evoke reaction forces in R-direction or cause rotation around θ. As explained in section 3.4.2 and 3.5.2, these frequencies were expected to be increased by the stiffness and damping of the preload pistons. As shown in section 4.6

(Figure 4.53), some of this error is not corrected by the metrology frame, indicating that some ψ-rotation may also be present that is not measured due to the Abbe offset in this direction.

6. ***122 Hz in Y and Z.*** This frequency is the Z-stage position frame with Ψ-axis assembly, rotating in φ-direction on the stiffness of the bridge. A frequency of 129 Hz was calculated here. As also shown in the amplitude, the main motion is in y-direction, and the amplitude in z-direction is smaller.
7. ***152 Hz in Y.*** The source of this resonance is not sure yet, but most likely it is a vertical resonance in the Z-stage preload frame that rotates the Z-stage in φ-direction.
8. ***256 Hz in Y and Z.*** This resonance is probably rigid body rotation of the Z-stage in φ-direction, which was estimated to be 259 Hz.
9. ***276 Hz in R.*** This resonance is rotation of the Ψ-axis rotor and probe in ψ-direction on the stiffness of the Ψ-brake. The resonance was estimated at 356 Hz, but a softer preload spring had to be used for this calliper to be able to open the brake. This also reduces the tangential stiffness of the contacts.

Appendix F

Interferometer shielding experiments

Air turbulence causes local variations of the refractive index, which causes errors in the interferometer measurement signals. This appendix describes tests that have been done on the machine to determine the optimum shielding configuration.

To compensate for slow refractive index variations (the weather), a Pressure-Temperature-Humidity sensor is used, with which the momentary refractive index is calculated. Faster and local fluctuations coming from turbulence can not be compensated with this sensor. Several forms of interferometer shielding are discussed in section 4.2.3. Some (atmospheric) configurations have been tested on the machine to determine the required level of shielding.

The basic noise level of the unenclosed R-interferometer was determined first. To see the effect of the rotating spindle, it was rotated with 1 rev/s. No significant increase in the interferometer noise was detected.

Figure F.1 shows photographs of the test setups for measuring the effect of a tent to enclose the metrology system volume, a tube around the R-interferometer and a box around both interferometers. The stability is measured for 15 minutes, in a setup with 3 capacitive probes similar to Figure 3.100. In each experiment, the PTH-sensor is inside the enclosed volume.

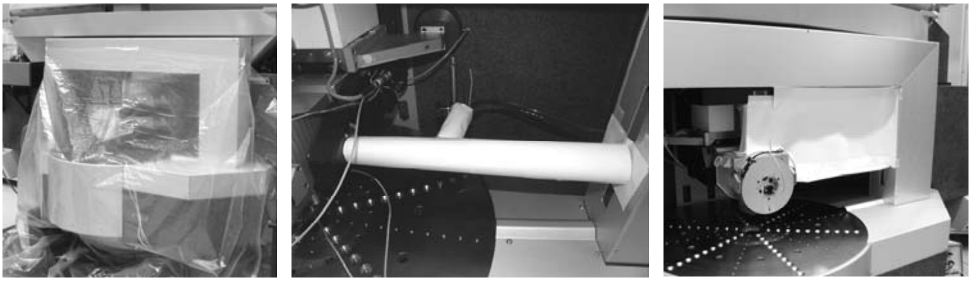

Tent *Tube with sensor inside* *Box with sensor inside*

Figure F.1: Interferometer shielding test setups

Figure F.2 shows the typical R-interferometer signals, and the resulting measurement error after compensation for the local refractive index variation. The detrended signals are shown, to exclude thermal drift during the measurements. Enclosing the metrology frame volume with a tent clearly reduces the sharpness of the fluctuations. Enclosing the beam with a tube or a box further reduces these fluctuations, but attenuates the slow fluctuations (minutes). These are also measured by the PTH-sensor, but the correlation is insufficient to fully compensate for them. The easiest solution, the enclosure of the entire metrology system volume, gives the best results. In these tests, this was done by a tent, but a polycarbonate enclosure with doors has eventually been added.

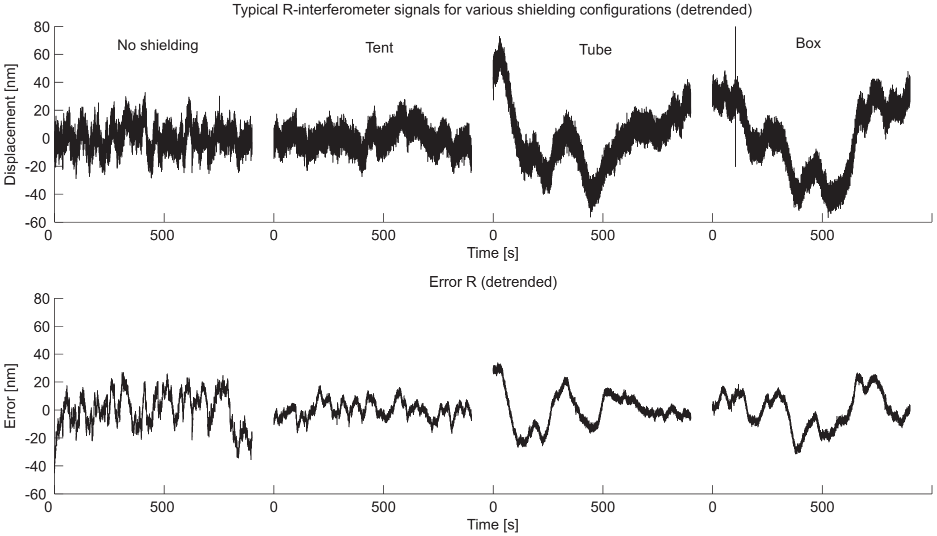

Figure F.2: Typical interferometer signals for different shielding configurations

Appendix G

Upper metrology frame thermal analysis

Section 4.3.2 shows the thermal analysis results of the Upper Metrology Frame. In this analysis, the beam deflection is calculated analytically with the temperature gradient of the beam, as described in the first part of this appendix. The influence of time dependent heat loads on the frame has been analyzed using a FEM model, for which the describing thermal equations are given in the second part of this appendix.

G.1 Beam deflection

A beam (Figure G.1) has a temperature T_0 on the top side, and a temperature $T_0 + dT$ on the bottom. The length of the top side is L_0, and the length of the bottom side is $L_0 + dL$.

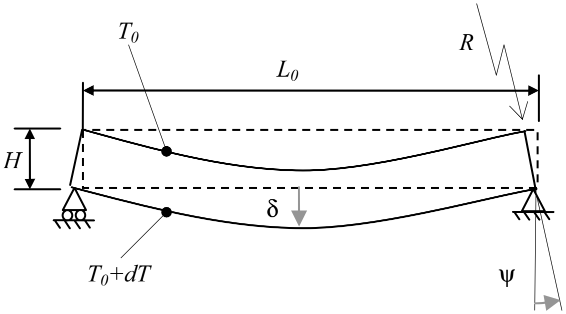

Figure G.1: Beam deflection from vertical thermal gradient

The length difference between the top and bottom side is equal to:

$$dL = \alpha \cdot L_0 \cdot dT \tag{G.1}$$

Approximating the beam as the segment of a circle with inner radius *R* and outer radius *R*+*H*, the length of the top is given by:

$$L_0 = 2\psi R \tag{G.2}$$

And the bottom by:

$$L_0 + dL = 2\psi\left(R + H\right) \tag{G.3}$$

Substituting (G.2) and (G.3) in (G.1), gives ψ as a function of *dL*:

$$\begin{aligned} 2\psi R + dL &= 2\psi R + 2\psi H \\ dL &= 2\psi H \\ \psi &= \frac{dL}{2H} \end{aligned} \tag{G.4}$$

The cosine of ψ is equal to:

$$\cos\left(\psi\right) = \frac{R + H - \delta}{R + H} \tag{G.5}$$

Replacing the cosine with the small angle approximation gives:

$$\begin{aligned} 1 - \frac{\psi^2}{2} &= \frac{R + H - \delta}{R + H} = 1 - \frac{\delta}{R + H} \\ \delta &= \frac{\psi^2}{2}\left(R + H\right) \end{aligned} \tag{G.6}$$

From (G.2), *R* is given by:

$$R = \frac{L_0}{2\psi} \tag{G.7}$$

Substituting this into (G.6), results in:

$$\delta = \frac{\psi^2}{2}\left(\frac{L_0}{2\psi} + H\right) = \frac{L_0\psi}{4} + \frac{\psi^2 H}{2} \tag{G.8}$$

Substituting (G.4) and supposing *dL* much smaller than *L* gives:

$$\delta = \frac{dL\left(L_0 + dL\right)}{8H} \approx \frac{L_0^2}{8H} \cdot \alpha \cdot dT \tag{G.9}$$

G.2 FEM model

To simulate the transient behaviour of the upper metrology frame, a Finite Element Model was made in Matlab Simulink. The metrology frame consists of an outer shield, an air layer and the frame itself. Wall elements consisting of a shield, air layer and frame are indicated by subscripts *s*, *a* and *f*, respectively.

For each element, the energy balance equations are formulated (Bejan, 1993). The element's time dependent temperature *dT/dt* is calculated from the heat transfer rate *q*, the density ρ, the volume *V* and the specific heat c_p (G.10).

$$q = \rho V c_p \frac{dT}{dt} \tag{G.10}$$

The heat lost to convection is calculated with the convection coefficient *h*, the surface area *A*, and the temperature difference *dT (G.11)*.

$$q = h A dT \tag{G.11}$$

The heat transfer from conduction to the neighbouring elements is a function of the area A, the thickness t and the thermal conductivity k of the conducting element (G.12).

$$q = \frac{A}{t} k \, dT \tag{G.12}$$

A wall element consisting of shield, air layer and frame is shown in Figure G.2. The dots represent the point mass of each element, and are coupled by thermal resistances.

The heat transfer into and out of each element via convection and conduction is also indicated.

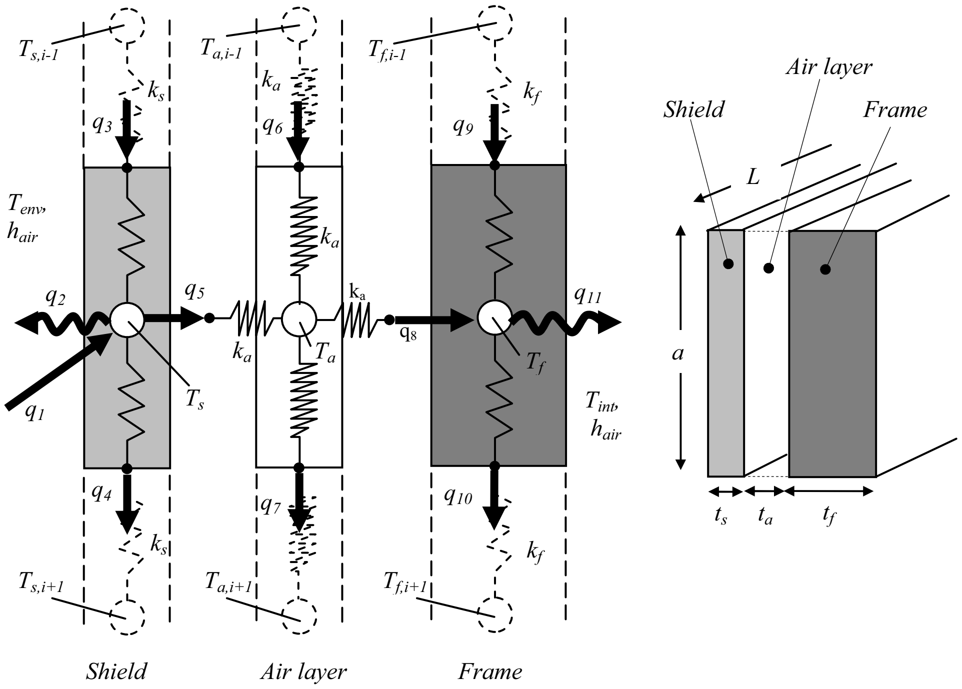

Figure G.2: Wall element model

The temperature of the shield (*s*), air layer (*a*) and frame (*f*) elements is:

$$\begin{aligned}\frac{dT_{s,i}}{dt}&=\frac{1}{m_s\,c_{p,s}}(q_1-q_2+q_3-q_4-q_5)\\ \frac{dT_{a,i}}{dt}&=\frac{1}{m_a\,c_{p,a}}(q_5+q_6-q_7-q_8)\\ \frac{dT_{f,i}}{dt}&=\frac{1}{m_f\,c_{p,f}}(q_8+q_9-q_{10}-q_{11})\end{aligned}\tag{G.13}$$

The energy transfer rates q_1 to q_{11} are given by (G.14). Here, L is the length of the element (equal to the beam length), t is the thickness and a is the height, as also indicated in Figure G.2.

$$\begin{aligned}
q_1 &= q_{in} & q_7 &= \frac{L t_a k_a}{a}(T_{a,i} - T_{a,i+1}) \\
q_2 &= h_{air}\, a L (T_{s,i} - T_{env}) & q_8 &= \frac{2 L a k_a}{t_a}(T_{a,i} - T_{f,i}) \\
q_3 &= \frac{L t_s k_s}{a}(T_{s,i-1} - T_{s,i}) & q_9 &= \frac{L t_f k_f}{a}(T_{f,i-1} - T_{f,i}) \\
q_4 &= \frac{L t_s k_s}{a}(T_{s,i} - T_{s,i+1}) & q_{10} &= \frac{L t_f k_f}{a}(T_{f,i} - T_{f,i+1}) \\
q_5 &= \frac{2 L a k_a}{t_a}(T_{s,i} - T_{a,i}) & q_{11} &= h_{air}\, a L (T_{f,i} - T_{\text{int}}) \\
q_6 &= \frac{L t_a k_a}{a}(T_{a,i-1} - T_{a,i}) & &
\end{aligned} \tag{G.14}$$

Similar to the above, corner elements and elements without a shield can be composed. With these elements a model as shown in Figure 4.24 is made. By using the temperature of the neighbouring elements, the heat transfer into and out of the element and the temperature of the element is calculated. This way, the influence of operators and environmental temperature fluctuations from the air conditioning has been determined. The results are shown in section 4.3.2.

Appendix H

Multi-probe method

In section 4.4.2 the multi-probe method was shown for the radial direction. This appendix will start with an analogous derivation for the axial direction. To optimize the location of the probes, the error sensitivity is analyzed. An optimization for the achievable harmonic suppression limit is shown, on the basis of which simulations are performed.

H.1 Axial profile reconstruction

Analogous to the derivation in 4.4.2, the axial profile can be reconstructed. The measurement signal of an axial probe is:

$$m_{ax,i}(\theta) = P_{ax}(\theta + \theta_i) + z_S(\theta) + \varphi_S(\theta)\sin(\theta_i)R_{ax} - \psi_S(\theta)\cos(\theta_i)R_{ax} \tag{H.1}$$

The four axial probe signals can be combined in a matrix $\vec{M}_{ax}(\theta)$.

$$\vec{M}_{ax}(\theta) = \begin{bmatrix} m_1(\theta) \\ m_2(\theta) \\ m_3(\theta) \\ m_4(\theta) \end{bmatrix} \tag{H.2}$$

With:

$$\begin{aligned}
m_1(\theta) &= P_{ax}(\theta+\theta_1) + z_S(\theta) + \varphi_S(\theta)\sin(\theta_1)R_{ax} - \psi_S(\theta)\cos(\theta_1)R_{ax} \\
m_2(\theta) &= P_{ax}(\theta+\theta_2) + z_S(\theta) + \varphi_S(\theta)\sin(\theta_2)R_{ax} - \psi_S(\theta)\cos(\theta_2)R_{ax} \\
m_3(\theta) &= P_{ax}(\theta+\theta_3) + z_S(\theta) + \varphi_S(\theta)\sin(\theta_3)R_{ax} - \psi_S(\theta)\cos(\theta_3)R_{ax} \\
m_4(\theta) &= P_{ax}(\theta+\theta_4) + z_S(\theta) + \varphi_S(\theta)\sin(\theta_4)R_{ax} - \psi_S(\theta)\cos(\theta_4)R_{ax}
\end{aligned} \tag{H.3}$$

The measurement signals are multiplied by sum factors *a*, *b*, *c* and *d* and summed to obtain the sum signal $S_{ax}(\theta)$. In matrix form with unit vector $\vec{u}_{ax}$:

$$S_{ax}(\theta) = \vec{M}_{ax}^T(\theta)\vec{u}_{ax} \quad with \quad \vec{u}_{ax} = \begin{bmatrix} a \\ b \\ c \\ d \end{bmatrix} \tag{H.4}$$

The summed measurement signal now becomes:

$$\begin{aligned}
S_{ax}(\theta) &= am_1(\theta) + bm_2(\theta) + cm_3(\theta) + dm_4(\theta) \\
&= aP_{ax}(\theta+\theta_1) + bP_{ax}(\theta+\theta_2) + cP_{ax}(\theta+\theta_3) + dP_{ax}(\theta+\theta_4) \\
&\quad + z_S(\theta)(a+b+c+d) \\
&\quad + \varphi_S(\theta)\left(a\sin(\theta_1) + b\sin(\theta_2) + c\sin(\theta_3) + d\sin(\theta_4)\right)R_{ax} \\
&\quad - \psi_S(\theta)\left(a\cos(\theta_1) + b\cos(\theta_2) + c\cos(\theta_3) + d\cos(\theta_4)\right)
\end{aligned} \tag{H.5}$$

The coefficients *a* – *d* of the unit vectors can now be chosen such that the error motion cancels out. This is the case if the following set of equations is satisfied:

$$\begin{aligned}
&a+b+c+d = 0 \\
&a\sin(\theta_1) + b\sin(\theta_2) + c\sin(\theta_3) + d\sin(\theta_4) = 0 \\
&a\cos(\theta_1) + b\cos(\theta_2) + c\cos(\theta_3) + d\cos(\theta_4) = 0 \\
&\sqrt{\left(a^2+b^2+c^2+d^2\right)} = 1 \quad (unit\ vector)
\end{aligned} \tag{H.6}$$

The resulting summed measurements now become:

$$S_{ax}(\theta) = aP_{ax}(\theta+\theta_1) + bP_{ax}(\theta+\theta_2) + cP_{ax}(\theta+\theta_3) + dP_{ax}(\theta+\theta_4) \tag{H.7}$$

Since the edge profile is closed, only discrete Fourier terms are present. Asynchronous error motion can contain a continuous frequency spectrum, but this has fallen out of the equation. The discrete Fourier transform of formula (H.7) is equal to:

$$\begin{aligned} S_{ax}(k) &= aP_{ax}(k)e^{jk\theta_1} + bP_{ax}(k)e^{jk\theta_2} + cP_{ax}(k)e^{jk\theta_3} + dP_{ax}(k)e^{jk\theta_4} \\ &= P_{ax}(k)\left(ae^{jk\theta_1} + be^{jk\theta_2} + ce^{jk\theta_3} + de^{jk\theta_4}\right) \end{aligned} \tag{H.8}$$

The Fourier transforms of the axial profile $P_{ax}(k)$ can now be calculated with (H.9).

$$P_{ax}(k) = \frac{S_{ax}(k)}{ae^{jk\theta_1} + be^{jk\theta_2} + ce^{jk\theta_3} + de^{jk\theta_4}} \tag{H.9}$$

By taking the inverse Fourier transform of this profile, $P_{ax}(\theta)$ can be calculated from a single revolution. By phase-shifting and substituting the obtained profile into the original measurement signals (H.3), the axial and tilt error motion of the spindle is obtained.

As explained in 4.4.2, harmonic suppression occurs if the denominator of (H.9) becomes zero for certain combinations of θ_i and harmonic k. For calculation of k_{limit} in the next section, a complex transfer coefficient $h_{ax}(k)$ is defined according to (H.10):

$$h_{ax}(k) = \frac{1}{ae^{jk\theta_1} + be^{jk\theta_2} + ce^{jk\theta_3} + de^{jk\theta_4}} \tag{H.10}$$

For the error analysis in the next section, it is convenient to write (H.9) in matrix form. A phase vector $\vec{e}$ can be defined as:

$$\vec{e}_{ax}(k) = \begin{bmatrix} e^{jk\theta_1} \\ e^{jk\theta_2} \\ e^{jk\theta_3} \\ e^{jk\theta_4} \end{bmatrix} \tag{H.11}$$

The Fourier transforms of the summed measurement signals of equation (H.8) can now be written as:

$$S_{ax}(k) = \vec{M}_{ax}^{T}(k)\vec{u}_{ax} = P_{ax}(k)\vec{e}_{ax}(k)^{T}\vec{u}_{ax} \tag{H.12}$$

Giving (H.13) with a complex transfer coefficient column $\vec{H}_{ax}(k)$:

$$
\begin{aligned}
&P_{ax}(k) = \vec{M}_{ax}^T(k)\,\vec{u}_{ax}\left(\vec{e}_{ax}(k)^T\,\vec{u}_{ax}\right)^{-1} = \vec{M}_{ax}^T(k)\,\vec{H}_{ax}(k) \\
&\mathit{with}\quad \vec{H}_{ax}(k) = \vec{u}_{ax}\left(\vec{e}_{ax}(k)^T\,\vec{u}_{ax}\right)^{-1}
\end{aligned}
\tag{H.13}
$$

H.2 Analysis

The following analysis is similar for the axial and radial direction, the *ax* and *rad* subscripts are therefore omitted. This analysis is performed in the frequency domain. For clarity, the *(k)* is also left out.

Three error sources are considered when optimizing the probe position: harmonic suppression, sensor noise and probe angular position errors. Harmonic suppression is caused by the denominator of (H.9) becoming zero for certain combinations of probe locations and harmonic number, and is discussed in section 4.4.2. This is equal to the transfer coefficient $h_{ax}(k)$ going to infinity.

To investigate the influence of sensor noise and probe angular position error on the final measurement error, the profiles, measurement signals and transfer coefficients can be decomposed into a true component (subscript *t*) and an error component (subscript *e*), expressed as (H.14).

$$
\begin{aligned}
P &= P_t + P_e \\
\vec{M} &= \vec{M}_t + \vec{M}_e \\
\vec{H} &= \vec{H}_t + \vec{H}_e
\end{aligned}
\tag{H.14}
$$

With which equation (H.13) can be written as:

$$
\begin{aligned}
P_t + P_e &= \left(\vec{M}_t^T + \vec{M}_e^T\right)\left(\vec{H}_t + \vec{H}_e\right) \\
&= \vec{M}_t^T\vec{H}_t + \vec{M}_t^T\vec{H}_e + \vec{M}_e^T\vec{H}_t + \vec{M}_e^T\vec{H}_e
\end{aligned}
\tag{H.15}
$$

With the exact solution being:

$$
P_t = \vec{M}_t^T\vec{H}_t \tag{H.16}
$$

The Fourier transform of the profile reconstruction error is expressed as equation (H.17), stating that this error is equal to the true measurement times the error of the transfer coefficient, plus the measurement error times the total transfer coefficient.

$$P_e = \vec{M}_t^T \vec{H}_e + \vec{M}_e^T \left(\vec{H}_t + \vec{H}_e\right) = \vec{M}_t^T \vec{H}_e + \vec{M}_e^T \vec{H} \tag{H.17}$$

To minimize the profile reconstruction error, the components of equation (H.17) should thus be minimized. In other words:

1. The true measurement signal is multiplied by the error of the transfer coefficient. The amplitude of the measurement signal must thus be kept small, i.e. the edge must be as round/flat as possible and the error motion must be small. Due to the harmonic suppression, large lower order harmonics are preferred above smaller high frequencies. Generally, the edge form will determine the amplitude (*A*) of the measurement signal for the combination of an air bearing and the dimensions of the mounting table:

$$\left|\vec{M}_t\right| \approx \left|A_{edge}\right| \tag{H.18}$$

2. $\vec{H}$ is only a function of *k* and θ_i, and since *k* are only positive integers, the error of the transfer coefficient can only be a function of the probe angular position error $\theta_{e,i}$. This is the accuracy with which the probe angles are known. Since the edge profile mainly determines the measurement signal, the probe positions can be accurately determined sampling the edge with a high sample rate and calculating the shift for which the difference between two measurement signals is minimal. The sum of the probe angles must further comply with the closure principle.
   The sensitivity of the transfer coefficient to angular probe errors can be calculated with $d\vec{H}/d\theta_i$. For small deviations, the change of the transfer coefficient is given by equation (H.19), and thus scales linearly with the probe angular position error.

$$\left|\vec{H}_e\right| \approx \left|\frac{d\vec{H}_t}{d\theta_i}\right| \cdot \theta_{e,i} \tag{H.19}$$

   The amplitude of the measurement signals decreases rapidly with the harmonic number (see Figure 4.44). The angular sensitivity must thus especially be minimized for low order harmonics. Generally, the sensitivity will increase for probe locations that are close to a suppressed harmonic.

3. When the probes are calibrated, the measurement error may be assumed to be only noise. When this noise is supposed to be purely white, the amplitude in the Fourier domain is a constant, $\vec{n}$:

$$\left|\vec{M}_e\right| \approx \vec{n} \tag{H.20}$$

It must further be noted that when multiple revolutions are averaged, the contribution of the sensor noise and the asynchronous error motion ultimately goes to zero. The averaged measurement signals then consist of only the profile plus the synchronous error motion. Performing the above described reconstruction on this data also results in a correct solution of the profile *P(θ)*, with which the synchronous and asynchronous error motion are then determined again. This procedure may yield a lower uncertainty if enough measurements have been acquired.

4. The measurement error $\vec{M}_e$ is multiplied by the total transfer coefficient $\vec{H}$. When the error of the transfer coefficient is supposed to be small compared to the true value,

$$\vec{H} \approx \vec{H}_t \tag{H.21}$$

The amplitude of $\vec{H}_t$ should thus be minimized by choosing the optimum angular probe positions. Since the measurement error is assumed to have a constant amplitude per measurement signal and per harmonic, the cumulative sum per harmonic of the cumulative sum of the components of $\vec{H}_t$ must be minimized by choosing the optimum angular probe positions.

Substituting equation (H.18) – (H.21) into equation (H.17), and re-introducing the (k) to indicate the Fourier domain, gives:

$$P_e(k) \sim \left|A_{edge}(k)\right| \cdot \left|\frac{d\vec{H}_t(k)}{d\theta_i}\right| \cdot \theta_{e,i} + \vec{n}\,\vec{H}_t(k) \tag{H.22}$$

The profile reconstruction error thus is the sum of two components. The first component is the roundness / flatness of the table (A_{edge}) times the alignment sensitivity of the transfer coefficient, times the alignment error. The second component is the noise times the transfer coefficient. The optimum probe position is the position where (H.21) is minimal over the range of harmonics.

Summarizing, the optimum angular probe position has its suppression limit (k_{limit}) at a harmonic above which the remaining harmonics have negligible contribution to the edge form and error motion. This optimization results in angular limits between which the probes physically have to be positioned to not be blind to certain harmonics below k_{limit}. Further, a position must be chosen that has maximum clearance from zero points to obtain minimum alignment sensitivity. Hence, the limits between which the probes have to be positioned must be chosen as far apart as possible. This also eases the physical alignment of the probes. Finally, the cumulative sum of the transfer coefficient at each harmonic must be minimal to minimize the influence of measurement noise.

H.3 Optimization

To find the optimum probe location (see Figure 4.42), it will first be attempted to find angular probe positions where no harmonic suppression occurs. Next, one can search within the suitable areas to the position where the error in the profile reconstruction is lowest (H.22).

For an arbitrary axial probe orientation of θ_2 = 66° and θ_4 = -15°, the magnitude of the complex transfer coefficient $h_{ax}(k)$ is shown in Figure H.1 (top). After a few near-zeros, a hard zero is encountered at k = 180 upr.

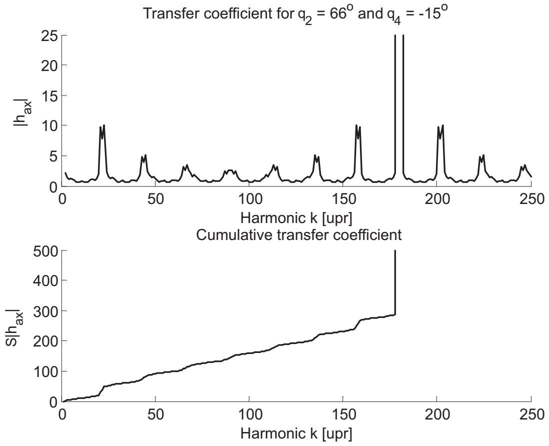

Figure H.1: Transfer coefficient magnitude for arbitrary probe orientation

To compare the different probe locations, the cumulative transfer coefficient (H.23) is calculated for all combinations of θ_2 and θ_4, as shown in Figure H.1 (bottom).

$$\sum_{1}^{k} \left| h_{ax}(k) \right| \tag{H.23}$$

Figure H.2 (left) shows the value of the cumulative transfer coefficient, where dark areas indicate a low cumulative value and light areas indicate (near) zeros. Figure H.2 (middle) shows the same result up to k = 100. The required spatial resolution quickly increases with the harmonic number, and with that also the calculation time.

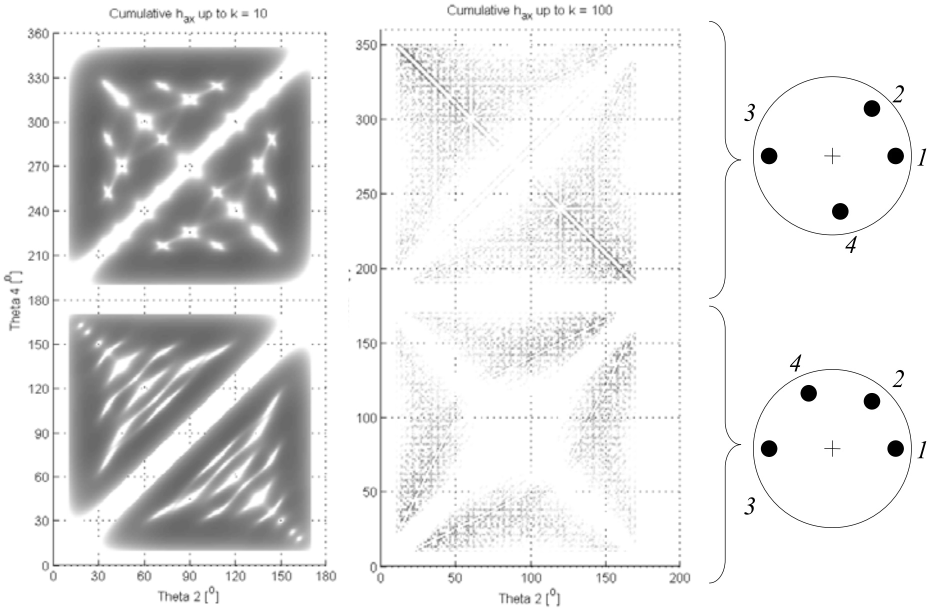

Figure H.2: Cumulative transfer coefficient up to k = 10 upr

Based on Figure H.2 and some further calculations, it was decided that choosing the probe locations close to the minimum probe spacing would yield the highest k_{limit}. Figure H.3 shows this calculated for an area around 12° ± 1° up to k = 100 upr (left), 500 upr (middle) and 1100 upr (right). The value of the cumulative transfer coefficient is lowest at the dark area. The vertical scale is not equal for the figures. Two optimum lines are present just next to $\theta_2 = -\theta_4$. When the probes are positioned to within 0.1°, no harmonic suppression occurs, even up to the highest measurable harmonic of 1100 upr. For the simulations, optimum locations of $\theta_2 = 12°$ and $\theta_4 = -12.25°$ have been used (indicated by white marker).

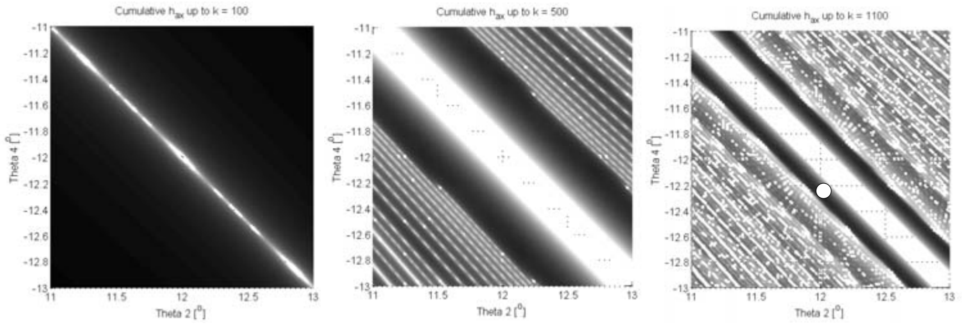

Figure H.3: Cumulative axial transfer coefficient for 100, 500 and 1100 upr

Following an analogous route, the possible probe locations in the radial direction were also determined, as shown in Figure H.4. Although the radial configuration is very different from the axial configuration, the results are remarkably similar.

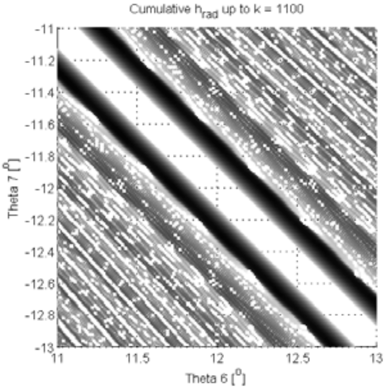

Figure H.4: Cumulative radial transfer coefficient at k = 1100 upr

To determine the optimum position within the areas of Figure H.3 (right) and Figure H.4, equation (H.22) should be minimized. This has not yet been done due to time constraints. Instead, the uncertainty has been simulated by using optimum probe locations in a simulation as shown in 4.4.2. Here, it was shown that sub-nanometer uncertainty can be achieved, provided that the probe angles are known with sufficient accuracy.

Appendix I

Optical distance measurement principles

The non-contact probe is a dual stage design, in which the short stroke is an optical absolute distance measurement method. This appendix gives an overview of principles and shows whether they are suitable for application in the non-contact probe design.

White-light interferometry

Absolute distance measurement can be done by multiple wavelength or white-light interferometry (Malacara, 2007; Whitehouse, 1994). A white light source (WL in Figure I.1, left) is hereto focussed onto the surface by a Mireau objective (MO). This objective consists of a beamsplitter (BS) and reference mirror (M). When the optical path length between the reference and measurement path is exactly equal, a sharp interference peak is detected, as shown in Figure I.1 (right). A repeatability of 0.5 nm is reported in (Deck and De Groot, 1994).

In this Mireau setup, the intensity peak relates directly to the distance between the surface and the objective, and can thus be used for the feedback of the servo system. The interference peak is very sharp, such that hardly any servo error is allowed. This method is therefore generally applied by scanning through focus per measurement point to detect the position of the interference peak, rather than to continuously keep it in focus while a surface is moving laterally with the intended high scanning speed.

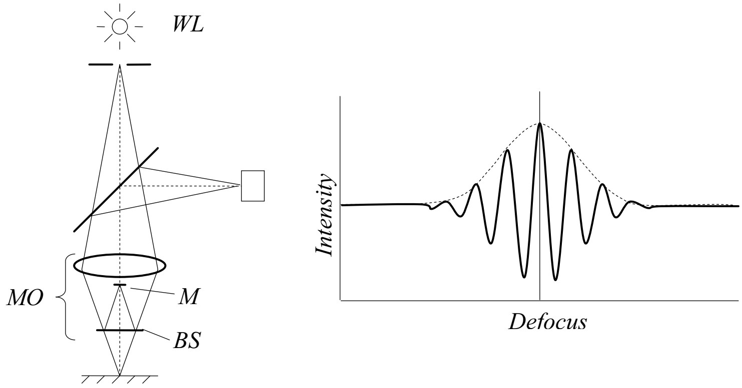

Figure I.1: White light interference principle

Triangulation sensors

In triangulation setups for specular surfaces (Gao and Kiyono, 1997; Shiou and Cheng, 2005), a point source (S) is focused onto the surface as shown in Figure I.2. The reflected image is focused onto a PSD. The spot position on the detector depends on the height of the surface. Surface tilt nominally does not influence the measurement. The measurement spot can be relatively large, reducing the sensitivity to local surface defects and high spatial frequencies. The measurement spot displaces laterally when the surface is not in nominal focus, which requires software compensation when measuring on locally inclined surfaces. The blunt layout of this principle is a disadvantage when measuring concave optics.

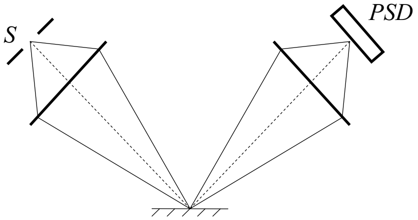

Figure I.2: Triangulation principle

Confocal microscopy

In confocal microscopy (Hamilton and Wilson, 1982), a point source (S in Figure I.3) is focused onto a surface. The reflection is imaged onto a pinhole (P). If the surface is in focus, all light passes through the pinhole, onto a detector. The response is a Gaussian function of the position of the surface. When the intensity coming through the pinhole is maximum, the surface is in best-focus. At this point, the slope of the signal is zero, resulting in zero sensitivity. The peak intensity is sensitive to intensity variations in the reflected beam, for instance due to reflectivity variation of the surface under test or source power fluctuations. Best focus is therefore mainly detected by continuously scanning or vibrating the objective (O) through focus.

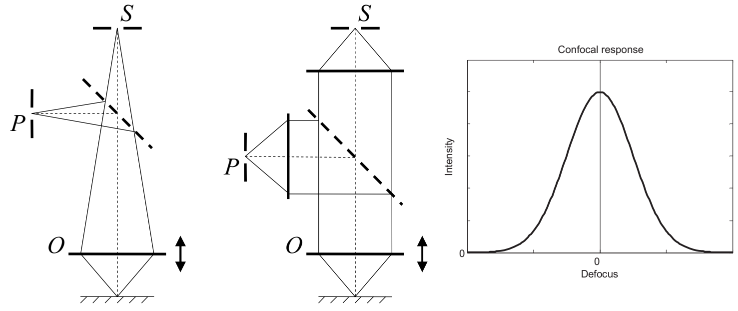

Figure I.3: Confocal microscopy principle

Chromatic confocal sensors

Chromatic confocal sensors employ an objective (O in Figure I.4) designed with large chromatic aberration to disperse a white-light source (WL). The wavelength of the light returning through the pinhole (P) is determined by a spectrometer (SM), and is related to the distance between the surface and the objective by calibration (Molesini et al., 1984). This makes this method principally insensitive to surface reflectivity and surface inclination. The highest reported resolution is 2 nm with 10-20 μm range (www19). The objective used here is 190 mm long and thus relatively heavy to use in a dual stage system.

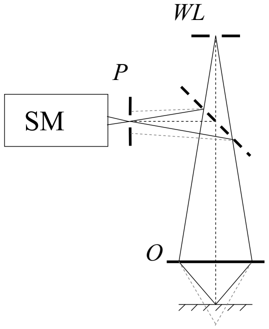

Figure I.4: Chromatic confocal principle

Focus detectors

To avoid the sensitivity to intensity variations, differential (normalized) systems have been developed. These give a focus error signal that is an S-curve with a steep slope and a zero crossing in best-focus. Focus sensors based on confocal and other methods come in a large variety, and were mainly developed for application in optical storage.

They measure axial distance for track focusing and tilt in one direction for track following. The axial Focus Error Signal is obtained by the dividing the sum of the difference signals of the photodiode pairs (PD) by the sum of all signals (I.1), as shown in the (Figure I.5, left):

$$FES = \frac{(I_1 - I_2) + (I_4 - I_3)}{I_1 + I_2 + I_4 + I_3} \qquad (I.1)$$

In the Foucault method (Benschop and Van Rosmalen, 1991) of Figure I.5, the beam reflected by the surface is focussed onto two photodiode pairs by a lens and a double wedge (W). In best-focus, the spots are positioned on the splits between the photodiodes, such that all measure equal intensity. When out of focus, the spots shift outwards or inwards, giving an unbalance within each photodiode pair. In the Laser Diode Grating Unit method, as applied by (Visscher, 1992) and (Ehrmann and Schindhelm, 1998), a similar effect is created by a grating (G).

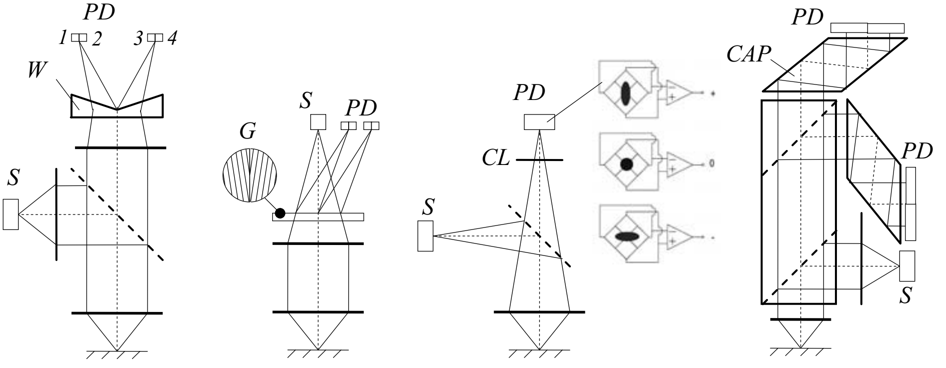

Foucault *LDGU* *Astigmat* *Critical Angle*

Figure I.5:Focus detector principles

In the Astigmat method (Fan et al., 2001) the reflected beam passes through a cylinder lens (CL) that introduces astigmatism to the beam. The beam is focused onto a quadrant detector (see Figure I.5), on which the balance between the photodiodes shifts when the surface moves through focus.

In the critical angle method (Kohno et al., 1988) the reflected beam enters a critical angle prism (CAP). Via double total internal reflection, the beam reaches a photodiode pair (PD). When the surface moves through focus, the divergence of the beam changes. This causes light to leak from the system at the critical angle prism, which results in the unbalance on the photodiode pairs.

The differential confocal method (Fainman et al., 1982; Tan and Wang, 2002) is also a focus detection method. This method is selected for the optical probe, and is explained in detail in section 5.1.3.

Dankwoord

Na een zwangerschap van meer dan 7 jaar (incl. het afstuderen), is de bevalling nu dan eindelijk voltooid. Het is een gezonde tweeling geworden van 3500 kg en 2.1x1.8x1.8 m, en 730 g en 24x17x2 cm. In deze periode heb ik het voorrecht en het genoegen gehad om met vele mensen samen te mogen werken. Hun enthousiasme en vakmanschap heb ik als zeer inspirerend, motiverend, leerzaam en vooral als ontzettend leuk ervaren. Hoewel ik nooit volledig kan zijn, wil ik een woord van dank richten aan de volgende mensen:

Beste Nick, je hebt me begeleid van mijn eerste stage in 2001 tot en met de (aanstaande) promotie. Dat is bijna 30% van mijn leven! Aan jouw steun, enthousiasme, creativiteit, kennis, tijd en (waar nodig) kritiek, heb ik enorm veel te danken!

Beste Maarten, jij biedt je promovendi een prachtige omgeving om zich te ontplooien, met aanstekelijk enthousiasme, inhoudelijke begeleiding, vrijheid voor eigen initiatief en op de IWO’s samen met Nick opbeurende woorden in moeilijke tijden.

Beste Lennino, eerst als afstudeerder en later met je bedrijf AC Optomechanix, heb jij met een enorme drive, late uren, vreugde bij de successen en doorzettingsvermogen bij de tegenslagen de probe-klus weten te klaren. We hebben veel plezier gehad en veel van elkaar geleerd. Ik wens je veel sterkte met je proefschrift en van harte succes met je bedrijf!

Beste Geerten, met lange dagen en een grote (maar onzichtbare) hoeveelheid code heb jij de machine tot leven gebracht, zodat we op de valreep zelfs Hoofdstuk 7 nog hebben kunnen vullen. Altijd secuur, geduldig en constructief; hopelijk zetten we deze plezierige samenwerking als collega’s weer voort bij een volgend project!

Zo ongeveer iedereen van de Gemeenschappelijke Technische Dienst heeft wel een steentje bijgedragen aan de realisatie van de machine. In het bijzonder wil ik Michiel, Peter, Rinus en Erwin noemen. Michiel en Peter, met bewondering en enige jaloezie heb ik vaak naar jullie vakmanschap staan kijken. Jullie hebben aan een half woord genoeg en krijgen het onmogelijke steeds weer voor elkaar. Rinus, jij hebt samen met je collega’s alle elektronica tot een veilig en werkend geheel gemaakt, en die werktuigbouwers telkens weer geduldig van uitleg voorzien. Erwin, jij was de brug tussen het ontwerp en de fabricage. Meer dan eens heb ik het vermoeden gehad een voorkeursbehandeling te krijgen in de planning. Heren van het twee-wekelijks overleg (inclusief Lennino en Geerten), jullie enthousiasme en de toewijding waren mij een waar genoegen!

Toen ik in 2002 mijn afstudeeropdracht bij het toenmalige TNO TPD begon, was ik nog behoorlijk nat achter mijn flaporen. Pieter en Jacob Jan, ondanks dit wilden jullie met mij een promotieproject starten. Dank voor deze kans! Aan jullie inspirerende visie heb ik een prachtige ervaring en een uitdagende baan te danken.
Velen van TNO hebben de afgelopen jaren bijgedragen aan het project, zowel op projectmanagement, ontwerp als optische fabricage. In het bijzonder wil ik noemen: Ian, Guido, Marcel, Henri, Reinder, Johan, Ellart, Bert, Harry, Leon, Leo, Mariët, Bart, Dick, Andries en de heren van de Optische Vervaardiging en natuurlijk de afdeling Precision Motion Systems. Ik zie er naar uit met jullie aan uitdagende nieuwe projecten te gaan werken!

Rob, Gerard en jullie collega's van het NMi VSL, dank voor de metrologische expertise. Gerard, met jouw enthousiaste, gedegen en geduldige aanpak hebben we mooie resultaten geboekt. Voor de toekomstige kalibraties zullen we vast weer een beroep op jullie doen.

Corné en Simon wil ik bedanken voor hun afstudeer- en stagebijdrage. Jullie hebben de kans om iets te ontwerpen dat ook gebouwd werd met veel enthousiasme gegrepen, en goed meegedraaid in het project. Jullie waren voor mij ook een leerzame ervaring.

Lou, Eddy en Casper van het IOP Precisie Technologie wil ik bedanken, net als de leden van de Begeleidingscommissie. De halfjaarlijkse bijeenkomsten boden een goed punt om naar toe te werken en een frisse blik uit de buitenwereld op het project. Een bijzonder woord van dank gaat uit naar Wim van Amstel voor zijn wijze raad en hulp bij de probe-ontwikkeling.

I would further like to thank Prof. Rob Munnig Schmidt (TU Delft), Prof. John Compter (TU/e) and Prof. Paul Shore (Cranfield University) of the reading committee for their useful comments and their efforts to read this somewhat bulky thesis.

Beste Roger, al sinds onze tweede stage lopen we parallel. Zo ongeveer alle ideeën (goede en slechte) hebben we besproken, en successen en tegenspoed meteen gedeeld. Je bent een fijne vriend geworden, en blijft gelukkig ook weer collega! Succes met jouw laatste loodjes.

Ook de andere lab- en DCT-genoten wil ik bedanken voor alle gezelligheid. In het bijzonder wil ik hierbij Eef, Gerrit, Ruud, Lia, Caroline en Petra nog vermelden.

Lieve pap en mam, dankzij jullie sta ik waar ik nu sta. Bedankt voor jullie onvoorwaardelijke steun, interesse, aanmoediging, kansen, vrijheid en goede raad. Het is een beetje afgezaagd, maar het dekt de lading het best: Bedankt voor alles! Ook Wardje en de rest van de (schoon)familie, van harte bedankt voor jullie steun en interesse.

Dan mijn vrienden en vriendinnen. Met ‘de groep’ hebben we zo ongeveer sinds de basisschool de tijd al doorstaan, anderen gaan terug tot het begin van de universiteit. De afgelopen tijd heb ik te vaak verstek laten gaan. Dank voor alle bier, lol en afleiding; jullie zijn een fijne fundering.

En als laatste dan mijn lieve Lian. Gelukkig zou je het in mijn plaats hetzelfde hebben aangepakt, anders zou je dit niet al die jaren volgehouden hebben. Zonder jou als maatje was me dit niet gelukt. Vanaf nu wordt het nog fijner samen!

Rens Henselmans
Dordrecht, februari 2009

Curriculum Vitae

Rens Henselmans was born on March 17, 1979 in Gouda, the Netherlands. After finishing Atheneum in 1997 (Cum Laude) at the 'Dongemond College' in Raamsdonksveer, he studied Mechanical Engineering at the Technische Universiteit Eindhoven. In 2003 he graduated (With Honours) within the Constructions & Mechanisms Group on the conceptual design of a non-contact measurement machine for freeform optics, carried out at TNO TPD. From 2004 to 2009 he continued the design and realization of this machine in a PhD project, of which the results are presented in this thesis. He is now employed by the Precision Motion Systems department of TNO Science & Industry.